Conference Proceedings of the Society for Experimental Mechanics Series

Nikolaos Dervilis *Editor*

Special Topics in Structural Dynamics, Volume 6

Proceedings of the 35th IMAC, A Conference and Exposition on Structural Dynamics 2017

Springer

Conference Proceedings of the Society for Experimental Mechanics Series

Nikolaos Dervilis
Editor

Special Topics in Structural Dynamics, Volume 6

Proceedings of the 35th IMAC, A Conference and Exposition on Structural Dynamics 2017

Springer

Editor
Nikolaos Dervilis
University of Sheffield
Sheffield, UK

ISSN 2191-5644 ISSN 2191-5652 (electronic)
Conference Proceedings of the Society for Experimental Mechanics Series
ISBN 978-3-319-53840-2 ISBN 978-3-319-53841-9 (eBook)
DOI 10.1007/978-3-319-53841-9

Library of Congress Control Number: 2017936948

Printed on acid-free paper

This Springer imprint is published by Springer Nature
The registered company is Springer International Publishing AG
The registered company address is: Gewerbestrasse 11, 6330 Cham, Switzerland

Preface

Special Topics in Structural Dynamics represents one of ten volumes of technical papers presented at the 35th IMAC, A Conference and Exposition on Structural Dynamics, organized by the Society for Experimental Mechanics, and held in Garden Grove, California, January 30–February 2, 2017. The full proceedings also include volumes on Nonlinear Dynamics; Dynamics of Civil Structures; Model Validation and Uncertainty Quantification; Dynamics of Coupled Structures; Sensors and Instrumentation; Structural Health Monitoring & Damage Detection; Rotating Machinery, Hybrid Test Methods, Vibro-Acoustics and Laser Vibrometry; Shock & Vibration, Aircraft/Aerospace and Energy Harvesting, and Topics in Modal Analysis & Testing.

Each collection presents early findings from experimental and computational investigations on an important area within Structural Dynamics. Special Topics in Structural Dynamics represents papers on enabling technologies for General Dynamics in both Modal Analysis Measurements, & System Identification; and Damage Detection.

The organizers would like to thank the authors, presenters, session organizers, and session chairs for their participation in this track.

Sheffield, UK — Nikolaos Dervilis

Contents

Chapter 1
Harmonic Forcing of a Two-Segment Euler-Bernoulli Beam

Arnaldo J. Mazzei and Richard A. Scott

Abstract This study is on the forced motions of non-homogeneous elastic beams. Euler-Bernoulli theory is employed and applied to a two-segment configuration subject to harmonic forcing. The objective is to determine the frequency response function for the system. Two different solution strategies are used. In the first, analytic solutions are derived for the differential equations for each segment. The constants involved are determined using boundary and interface continuity conditions. The response, at a given location, can be obtained as a function of forcing frequency (FRF). The procedure is unwieldy. Moreover, determining particular integrals can be difficult for arbitrary spatial variations. An alternative method is developed wherein material and geometric discontinuities are modeled by continuously varying functions (here logistic functions). This results in a single differential equation with variable coefficients, which is solved numerically, for specific parameter values, using MAPLE®. The numerical solutions are compared to the baseline analytical approach for constant spatial dependencies. For validation purposes an assumed-modes solution is also developed. For a free-fixed boundary conditions example good agreement between the numerical methods and the analytical approach is found, lending assurance to the continuous variation model. Fixed-fixed boundary conditions are also treated and again good agreement is found.

Keywords Beams with layered cells • Layered structures resonances

Nomenclature

A	Area of the beam cross section (A_i, area of i-cell)
B_i	Constants
E	Young's modulus (E_i, Young's modulus of i-cell)
F	External forcing (spatial function, F_i, acting on i-cell)
f	External transverse force per unit length acting on the beam (f_i, acting on i-cell)
$H(x)$	Logistic function
I	Area moment of inertia of the beam cross section (I_i, moment of inertia of i-cell)
L	Length of the beam (L_i, length of i-cell)
R	Spatial function, (for assumed solution, R_i on i-cell)
t	Time
w	Beam transversal displacement
xyz	Inertial reference system (coordinates x , y , z)
Y	Non-dimensional beam displacement in the y (transverse) direction
ν	Non-dimensional frequency ($\nu = \lambda^2$)
ρ	Mass density (ρ_i, density of i-cell)
ξ	Non-dimensional spatial coordinate
τ	Non-dimensional time
ω	Frequency of harmonic excitation
Ω_0	Reference frequency

A.J. Mazzei (✉)
Department of Mechanical Engineering, C. S. Mott Engineering and Science Center, Kettering University, 1700 University Avenue, Flint, MI 48504, USA
e-mail: amazzei@kettering.edu

R.A. Scott
University of Michigan, Herbert H. Dow Building, 2300 Hayward, Ann Arbor, MI 48109, USA

N. Dervilis (ed.), *Special Topics in Structural Dynamics, Volume 6*, Conference Proceedings of the Society for Experimental Mechanics Series, DOI 10.1007/978-3-319-53841-9_1

1.1 Introduction

This work is an extension of one given in reference [1] in which the determination of the bending natural frequencies of beams whose properties vary along the length was sought. Of interest were beams with different materials and varying cross-sections, which were layered in cells and could be uniform or not.

In reference [1] an approach was discussed, in which the discrete cell properties were modeled by continuously varying functions, specifically logistic functions, which had the considerable advantage of working with a single differential equation (albeit one with variable coefficients). Natural frequencies could be calculated via a forced motion strategy by means of MAPLE®'s ODE[1] solver.

There are several references on vibrations of layered beams. For example reference [2], where free vibrations of stepped Timoshenko beams were treated via a Lagrange multiplier formalism. Results compared well with values obtained using other analytical methods. In reference [3] Euler-Bernoulli stepped beams were studied via exact and FEM approaches. FEM results using non-integer polynomials shape functions [4] compared well with exact solutions. General studies on media with discrete layers have been given, for example, in references [5–8]. Note that finite difference approaches to the dynamics of non-homogeneous media can be found in reference [9].

Here the objective is to determine the frequency response functions (FRF) of such beams. Euler-Bernoulli theory is used for a two-segment configuration under harmonic forcing. Analytic solutions can be obtained for each segment, for specific conditions, and the response calculated at a given location, thus providing the FRFs. But the procedure is unwieldy and particular solutions to the differential equations can be difficult to obtain for arbitrary spatial variations. The alternate approach utilized involves modeling material and geometric discontinuities by continuously varying functions. This results in a single differential equation with variable coefficients, which is solved numerically. These are compared to analytical solutions for constant spatial dependencies. An assumed-modes solution is also developed for validation purposes.

1.2 Basic Problem

In this study Euler-Bernoulli beam theory is used. The equation of motion is given below and Fig. 1.1 exhibits the underlying variables.

$$\frac{\partial^2}{\partial x^2}\left(E(x)I(x)\frac{\partial^2 w(x,t)}{\partial x^2}\right)+\rho(x)A(x)\frac{\partial^2 w(x,t)}{\partial t^2}=f(x,t) \tag{1.1}$$

In the derivation of Eq. (1.1) no assumption was made in relation to the material type, therefore it can be either a homogeneous or a non-homogeneous material.

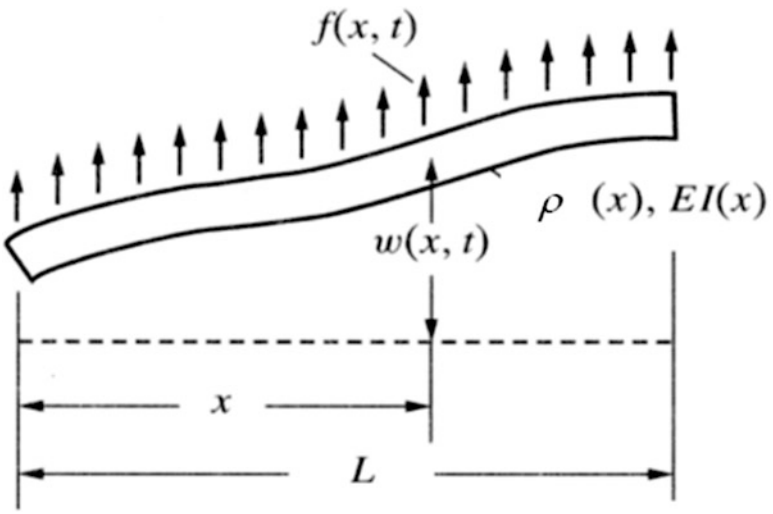

Fig. 1.1 Beam element

[1] www.maplesoft.com.

The layered configuration discussed here is a two-cell beam. Strategies for obtaining the steady state response, due to harmonic forcing, are investigated in the following.

1.3 Analytical Approach

In this section analytic solutions are sought using standard beam theory.

Consider the beam shown in Fig. 1.2 which is composed by two cells of different materials.

The transversal displacement equation of motion for each segment ("*i-th*" segment) is:

$$\frac{\partial^2}{\partial x^2}\left(E_i(x)I_i(x)\frac{\partial^2 w_i\left(x,t\right)}{\partial x^2}\right)+\rho_i(x)A_i(x)\frac{\partial^2 w_i\left(x,t\right)}{\partial t^2}=f_i\left(x,t\right),i=1,2... \tag{1.2}$$

where f_i are external transverse forces per unit length.

For harmonic forcing with frequency ω:

$$f_i\left(x,t\right)=F_i(x)\sin\left(\omega t\right) \tag{1.3}$$

Assuming solutions of the form:

$$w_i\left(x,t\right)=R_i(x)\sin\left(\omega t\right) \tag{1.4}$$

leads to

$$\frac{d^2}{dx^2}\left(E_iI_i\frac{d^2R_i(x)}{dx^2}\right)-\rho_iA_i\omega^2R_i(x)=F_i(x) \tag{1.5}$$

For A_i, ρ_i, I_i and E_i constant in each segment:

$$\frac{d^4R_i(x)}{dx^4}-\frac{\rho_iA_i}{E_iI_i}\omega^2R_i(x)=\frac{F_i(x)}{E_iI_i} \tag{1.6}$$

Define ${\gamma_i}^4=\frac{\rho_iA_i}{E_iI_i}\omega^2$ and $P_i(x)=\frac{F_i(x)}{E_iI_i}$, then for each segment:

$$\frac{d^4R_i(x)}{dx^4}-{\gamma_i}^4R_i(x)=P_i(x) \tag{1.7}$$

General solutions to the linear differential equation (1.7) can be written as:

$$R_i(x)=R_{ih}(x)+R_{ip}(x) \tag{1.8}$$

where $R_{ih}(x)$ are the general solutions to the homogeneous equations and $R_{ip}(x)$ are "particular integrals".

For Eq. (1.7),

$$R_{1h}(x)=B_1\cosh\left(\gamma_1x\right)+B_2\sinh\left(\gamma_1x\right)+B_3\cos\left(\gamma_1x\right)+B_4\sin\left(\gamma_1x\right) \tag{1.9}$$

$$R_{2h}(x)=B_5\cosh\left(\gamma_2x\right)+B_6\sinh\left(\gamma_2x\right)+B_7\cos\left(\gamma_2x\right)+B_8\sin\left(\gamma_2x\right) \tag{1.10}$$

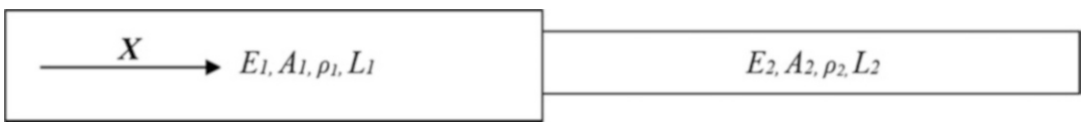

Fig. 1.2 Layered beam

For arbitrary forcing $P_i(x)$, finding tractable particular integrals can pose a problem (this is treated later numerically). In the following two examples are considered.

1.3.1 Constant Spatial Force

Here attention is restricted to constant spatial forcing: $P_1(x) = P_{1,0}$, $P_2(x) = P_{2,0}$; $P_{1,0}$, $P_{2,0}$ constants.

Then

$$R_{1p}(x) = -\frac{P_{1,0}}{{\gamma_1}^4} \tag{1.11}$$

$$R_{2p}(x) = -\frac{P_{2,0}}{{\gamma_2}^4} \tag{1.12}$$

Now the general solutions can be written:

$$R_1(x) = B_1 \cosh(\gamma_1 x) + B_2 \sinh(\gamma_1 x) + B_3 \cos(\gamma_1 x) + B_4 \sin(\gamma_1 x) - \frac{P_{1,0}}{{\gamma_1}^4} \tag{1.13}$$

$$R_2(x) = B_5 \cosh(\gamma_2 x) + B_6 \sinh(\gamma_2 x) + B_7 \cos(\gamma_2 x) + B_8 \sin(\gamma_2 x) - \frac{P_{2,0}}{{\gamma_2}^4} \tag{1.14}$$

The overall analytic solution requires that the boundary conditions be defined. Two sets are considered below.

1.3.1.1 Free-Fixed Boundary Conditions

For these conditions the moment and shear free end at $x = 0$ gives: $\left.\frac{d^2R_1(x)}{dx^2}\right|_{x=0} = 0$ and $\left.\frac{d^3R_1(x)}{dx^3}\right|_{x=0} = 0$, which, from Eq. (1.13), leads to $B_1 = B_3$ and $B_2 = B_4$. Then Eq. (1.13) becomes:

$$R_1(x) = B_1(\cosh(\gamma_1 x) + \cos(\gamma_1 x)) + B_2(\sinh(\gamma_1 x) + \sin(\gamma_1 x)) - \frac{P_{1,0}}{{\gamma_1}^4} \tag{1.15}$$

The remaining constants involved in the solutions can be determined as follows. The boundary condition at the other end (fixed) gives: $R_2(x) = 0$ and $\left.\frac{dR_2(x)}{dx}\right|_{x=L} = 0, x = L$ $(L = L_1 + L_2)$. Interface continuity conditions give: $R_1(x) = R_2(x), x = L_1$ (displacement continuity), $\frac{dR_1(x)}{dx} = \frac{dR_2(x)}{dx}, x = L_1$(slope continuity), $E_1I_1\frac{d^2R_1(x)}{dx^2} = E_2I_2\frac{d^2R_2(x)}{dx^2}, x = L_1$(moment continuity) and $E_1I_1\frac{d^3R_1(x)}{dx^3} = E_2I_2\frac{d^3R_2(x)}{dx^3}, x = L_1$(shear continuity). The conditions lead to a system of algebraic equations:

$$\begin{aligned}
&B_5\cosh(\gamma_2 L) + B_6\sinh(\gamma_2 L) + B_7\cos(\gamma_2 L) + B_8\sin(\gamma_2 L) = \tfrac{P_{2,0}}{{\gamma_2}^4}\\
&B_5\sinh(\gamma_2 L) + B_6\cosh(\gamma_2 L) - B_7\sin(\gamma_2 L) + B_8\cos(\gamma_2 L) = 0\\
&B_1(\cosh(\gamma_1 L_1) + \cos(\gamma_1 L_1)) + B_2(\sinh(\gamma_1 L_1) + \sin(\gamma_1 L_1)) - \tfrac{P_{1,0}}{{\gamma_1}^4} =\\
&B_5\cosh(\gamma_2 L_1) + B_6\sinh(\gamma_2 L_1) + B_7\cos(\gamma_2 L_1) + B_8\sin(\gamma_2 L_1) - \tfrac{P_{2,0}}{{\gamma_2}^4}\\
&B_1(\sinh(\gamma_1 L_1)\gamma_1 - \sin(\gamma_1 L_1)\gamma_1) + B_2(\cosh(\gamma_1 L_1)\gamma_1 + \cos(\gamma_1 L_1)\gamma_1) =\\
&B_5\sinh(\gamma_2 L_1)\gamma_2 + B_6\cosh(\gamma_2 L_1)\gamma_2 - B_7\sin(\gamma_2 L_1)\gamma_2 + B_8\cos(\gamma_2 L_1)\gamma_2\\
&B_1\left(\cosh(\gamma_1 L_1){\gamma_1}^2 - \cos(\gamma_1 L_1){\gamma_1}^2\right) + B_2\left(\sinh(\gamma_1 L_1){\gamma_1}^2 - \sin(\gamma_1 L_1){\gamma_1}^2\right) =\\
&\tfrac{E_2I_2}{E_1I_1}\left(B_5\cosh(\gamma_2 L_1){\gamma_2}^2 + B_6\sinh(\gamma_2 L_1){\gamma_2}^2 - B_7\cos(\gamma_2 L_1){\gamma_2}^2 - B_8\sin(\gamma_2 L_1){\gamma_2}^2\right)\\
&B_1\left(\sinh(\gamma_1 L_1){\gamma_1}^3 + \sin(\gamma_1 L_1){\gamma_1}^3\right) + B_2\left(\cosh(\gamma_1 L_1){\gamma_1}^3 - \cos(\gamma_1 L_1){\gamma_1}^3\right) =\\
&\tfrac{E_2I_2}{E_1I_1}\left(B_5\sinh(\gamma_2 L_1){\gamma_2}^3 + B_6\cosh(\gamma_2 L_1){\gamma_2}^3 + B_7\sin(\gamma_2 L_1){\gamma_2}^3 - B_8\cos(\gamma_2 L_1){\gamma_2}^3\right)
\end{aligned} \tag{1.16}$$

from which B_1, B_2, B_5, B_6, B_7 and B_8 can be determined.

In non-dimensional matrix form the complete set of equations is given by:

$$\begin{bmatrix} 1 & 0 & -1 & 0 & 0 & 0 & 0 & 0 \\ 0 & 1 & 0 & -1 & 0 & 0 & 0 & 0 \\ 0 & 0 & 0 & 0 & \cosh(\gamma_r\lambda) & \sinh(\gamma_r\lambda) & \cos(\gamma_r\lambda) & \sin(\gamma_r\lambda) \\ 0 & 0 & 0 & 0 & \sinh(\gamma_r\lambda) & \cosh(\gamma_r\lambda) & -\sin(\gamma_r\lambda) & \cos(\gamma_r\lambda) \\ \cosh\left(\frac{\lambda}{1+\alpha}\right) & \sinh\left(\frac{\lambda}{1+\alpha}\right) & \cos\left(\frac{\lambda}{1+\alpha}\right) & \sin\left(\frac{\lambda}{1+\alpha}\right) & -\cosh\left(\frac{\gamma_r\lambda}{1+\alpha}\right) & -\sinh\left(\frac{\gamma_r\lambda}{1+\alpha}\right) & -\cos\left(\frac{\gamma_r\lambda}{1+\alpha}\right) & -\sin\left(\frac{\gamma_r\lambda}{1+\alpha}\right) \\ \sinh\left(\frac{\lambda}{1+\alpha}\right) & \cosh\left(\frac{\lambda}{1+\alpha}\right) & -\sin\left(\frac{\lambda}{1+\alpha}\right) & \cos\left(\frac{\lambda}{1+\alpha}\right) & -\gamma_r\sinh\left(\frac{\gamma_r\lambda}{1+\alpha}\right) & -\gamma_r\cosh\left(\frac{\gamma_r\lambda}{1+\alpha}\right) & \gamma_r\sin\left(\frac{\gamma_r\lambda}{1+\alpha}\right) & -\gamma_r\cos\left(\frac{\gamma_r\lambda}{1+\alpha}\right) \\ \cosh\left(\frac{\lambda}{1+\alpha}\right) & \sinh\left(\frac{\lambda}{1+\alpha}\right) & -\cos\left(\frac{\lambda}{1+\alpha}\right) & -\sin\left(\frac{\lambda}{1+\alpha}\right) & -E_rI_r{\gamma_r}^2\cosh\left(\frac{\gamma_r\lambda}{1+\alpha}\right) & -E_rI_r{\gamma_r}^2\sinh\left(\frac{\gamma_r\lambda}{1+\alpha}\right) & E_rI_r{\gamma_r}^2\cos\left(\frac{\gamma_r\lambda}{1+\alpha}\right) & E_rI_r{\gamma_r}^2\sin\left(\frac{\gamma_r\lambda}{1+\alpha}\right) \\ \sinh\left(\frac{\lambda}{1+\alpha}\right) & \cosh\left(\frac{\lambda}{1+\alpha}\right) & \sin\left(\frac{\lambda}{1+\alpha}\right) & -\cos\left(\frac{\lambda}{1+\alpha}\right) & -E_rI_r{\gamma_r}^3\sinh\left(\frac{\gamma_r\lambda}{1+\alpha}\right) & -E_rI_r{\gamma_r}^3\cosh\left(\frac{\gamma_r\lambda}{1+\alpha}\right) & -E_rI_r{\gamma_r}^3\sin\left(\frac{\gamma_r\lambda}{1+\alpha}\right) & E_rI_r{\gamma_r}^3\cos\left(\frac{\gamma_r\lambda}{1+\alpha}\right) \end{bmatrix} \begin{bmatrix} b_1 \\ b_2 \\ b_3 \\ b_4 \\ b_5 \\ b_6 \\ b_7 \\ b_8 \end{bmatrix} = \begin{bmatrix} 0 \\ 0 \\ \frac{1}{{\gamma_r}^4} \\ 0 \\ \left(1-\frac{1}{{\gamma_r}^4}\right) \\ 0 \\ 0 \\ 0 \end{bmatrix} \frac{Q_0}{\lambda^4}$$

$$\equiv [\mathrm{A}]\{\mathrm{B}\} = \{\mathrm{F}\} \tag{1.17}$$

where $b_i = \frac{B_i}{L}$, $L_2 = \alpha L_1$, $L = (1+\alpha)L_1$, $\lambda = \gamma_1 L$,$\gamma_r = \frac{\gamma_2}{\gamma_1}$, $I_r = \frac{I_2}{I_1}$, $E_r = \frac{E_2}{E_1}$, $Q_0 = P_0 L^3$ and $P_{1,0} = P_{2,0} = P_0$.

Note that natural frequencies can found on setting the determinant of [A] to zero.

1.3.1.2 Fixed-Fixed Boundary Conditions

For these conditions the fixed end at $x = 0$ gives: $R_1(x) = 0$ and $\left.\frac{dR_1(x)}{dx}\right|_{x=0} = 0$, which, from Eq. (1.13), leads to $B_1 + B_3 = \frac{P_{1,0}}{\gamma_1^4}$ and $B_2 = -B_4$. Following the procedure described above leads to the following non-dimensional system of equations for the unknowns coefficients (non-dimensional matrix form):

$$\begin{bmatrix} 1 & 0 & 1 & 0 & 0 & 0 & 0 & 0 \\ 0 & 1 & 0 & 1 & 0 & 0 & 0 & 0 \\ 0 & 0 & 0 & 0 & \cosh(\gamma_r\lambda) & \sinh(\gamma_r\lambda) & \cos(\gamma_r\lambda) & \sin(\gamma_r\lambda) \\ 0 & 0 & 0 & 0 & \sinh(\gamma_r\lambda) & \cosh(\gamma_r\lambda) & -\sin(\gamma_r\lambda) & \cos(\gamma_r\lambda) \\ \cosh\left(\frac{\lambda}{1+\alpha}\right) & \sinh\left(\frac{\lambda}{1+\alpha}\right) & \cos\left(\frac{\lambda}{1+\alpha}\right) & \sin\left(\frac{\lambda}{1+\alpha}\right) & -\cosh\left(\frac{\gamma_r\lambda}{1+\alpha}\right) & -\sinh\left(\frac{\gamma_r\lambda}{1+\alpha}\right) & -\cos\left(\frac{\gamma_r\lambda}{1+\alpha}\right) & -\sin\left(\frac{\gamma_r\lambda}{1+\alpha}\right) \\ \sinh\left(\frac{\lambda}{1+\alpha}\right) & \cosh\left(\frac{\lambda}{1+\alpha}\right) & -\sin\left(\frac{\lambda}{1+\alpha}\right) & \cos\left(\frac{\lambda}{1+\alpha}\right) & -\gamma_r\sinh\left(\frac{\gamma_r\lambda}{1+\alpha}\right) & -\gamma_r\cosh\left(\frac{\gamma_r\lambda}{1+\alpha}\right) & \gamma_r\sin\left(\frac{\gamma_r\lambda}{1+\alpha}\right) & -\gamma_r\cos\left(\frac{\gamma_r\lambda}{1+\alpha}\right) \\ \cosh\left(\frac{\lambda}{1+\alpha}\right) & \sinh\left(\frac{\lambda}{1+\alpha}\right) & -\cos\left(\frac{\lambda}{1+\alpha}\right) & -\sin\left(\frac{\lambda}{1+\alpha}\right) & -E_rI_r{\gamma_r}^2\cosh\left(\frac{\gamma_r\lambda}{1+\alpha}\right) & -E_rI_r{\gamma_r}^2\sinh\left(\frac{\gamma_r\lambda}{1+\alpha}\right) & E_rI_r{\gamma_r}^2\cos\left(\frac{\gamma_r\lambda}{1+\alpha}\right) & E_rI_r{\gamma_r}^2\sin\left(\frac{\gamma_r\lambda}{1+\alpha}\right) \\ \sinh\left(\frac{\lambda}{1+\alpha}\right) & \cosh\left(\frac{\lambda}{1+\alpha}\right) & \sin\left(\frac{\lambda}{1+\alpha}\right) & -\cos\left(\frac{\lambda}{1+\alpha}\right) & -E_rI_r{\gamma_r}^3\sinh\left(\frac{\gamma_r\lambda}{1+\alpha}\right) & -E_rI_r{\gamma_r}^3\cosh\left(\frac{\gamma_r\lambda}{1+\alpha}\right) & -E_rI_r{\gamma_r}^3\sin\left(\frac{\gamma_r\lambda}{1+\alpha}\right) & E_rI_r{\gamma_r}^3\cos\left(\frac{\gamma_r\lambda}{1+\alpha}\right) \end{bmatrix} \begin{bmatrix} b_1 \\ b_2 \\ b_3 \\ b_4 \\ b_5 \\ b_6 \\ b_7 \\ b_8 \end{bmatrix} = \begin{bmatrix} 1 \\ 0 \\ \frac{1}{{\gamma_r}^4} \\ 0 \\ \left(1-\frac{1}{{\gamma_r}^4}\right) \\ 0 \\ 0 \\ 0 \end{bmatrix} \frac{Q_0}{\lambda^4}$$

$$\equiv [\mathrm{A}]\{\mathrm{B}\} = \{\mathrm{F}\} \tag{1.18}$$

1.4 Continuous Variation Model

Here the transitions from one material to another are approximated via logistic functions (step functions are not used since they would generate numerical complications because of the singular derivatives):

$$H(x) \approx \frac{1}{2} + \frac{1}{2}\tanh(Kx) = \frac{1}{1+e^{-2Kx}} \tag{1.19}$$

Note that in Eq. (1.19) a larger K corresponds to a sharper transition at $x = 0$.

A non-dimensional version of the equation of motion can be obtained by taking:

$\tau = \Omega_0 t$, $\xi = {x}/{L}$, $Y(\xi,\tau) = w(x,t){\Omega_0}/{L}$, $\nu = {\omega}/{\Omega_0}$, $I(x) = I_1H_2(K\xi) = I_1f_2(\xi)$, $A(x) = A_1H_4(K\xi) = A_1f_4(\xi)$, $E(x) = E_1H_1(K\xi) = E_1f_1(\xi)$, $\rho(x) = \rho_1H_3(K\xi) = \rho_1f_3(\xi)$. ($H_i$, logistic functions.)

Substituting these into Eq. (1.1) leads to:

$$\frac{\partial^2}{\partial\xi^2}\left(f_1(\xi)f_2(\xi)\frac{\partial^2 Y(\xi,\tau)}{\partial\xi^2}\right) + \frac{\lambda^4}{\nu^2}f_3(\xi)f_4(\xi)\frac{\partial^2 Y(\xi,\tau)}{\partial\tau^2} = g(\xi,\tau) \tag{1.20}$$

Ω_0 is a reference frequency, which is set to $\Omega_0 = \sqrt{\frac{E_1 I_1}{\rho_1 A_1 L^4}}$. This gives: $\lambda^4 = (\gamma_1 L)^4 = \left(\frac{\rho_1 A_1 L^4 \omega^2}{E_1 I_1}\right) = \nu^2$and $g(\xi, \tau) = \frac{L^3 \Omega_0}{E_1 I_1} f(x, t)$.

Analytic solutions may not be feasible for Eq. (1.20). Here the following approach is adopted. Given the material layout (stacked cells) and cross section variation, i.e., $f_1(\xi)$, $f_3(\xi)$, $f_2(\xi)$ and $f_4(\xi)$, a MAPLE® routine is developed for obtaining numerical approximations to the frequency response function (FRF) of the system. The equation is subjected to a harmonic forcing function, for example $g(\xi, \tau) = F(\xi) \sin(\nu\tau)$, and response amplitudes are monitored for different values of ν.

An approach described by the authors in reference [10] can also be utilized for extracting resonances and amplitudes. In Eq. (1.20) vibration frequencies can be calculated by assuming $Y(\xi, \tau) = S(\xi) \sin(\nu\tau)$ and harmonic forcing $g(\xi, \tau) = F(\xi) \sin(\nu\tau)$. This leads to:

$$\frac{d^2}{d\xi^2}\left(f_1(\xi) f_2(\xi) \frac{d^2 S(\xi)}{d\xi^2}\right) - \lambda^4 f_3(\xi) f_4(\xi) S(\xi) = F(\xi) \tag{1.21}$$

where, it should be noted that $\nu^2 = \lambda^4$.

In this case the strategy consists of using MAPLE®'s two-point boundary value solver to solve a forced motion problem. A constant value for the forcing function F is assumed and the frequency λ is varied. By observing the mid-span deflection of the beam, the resonant frequency can be found on noting where an abrupt change in sign occurs. Higher modes can be obtained by extending the search range.

1.5 Numerical Examples

Consider the beam shown in Fig. 1.2 and assume the following materials: Aluminum ($E_1 = 71$ *GPa*, $\rho_1 = 2710$ *kg/m*^{3}) and Silicon Carbide ($E_2 = 210$ *GPa*, $\rho_2 = 3100$ *kg/m*^{3}). These values are taken from a basic paper in the field [11].

1.5.1 Free-Fixed Boundary Conditions

For the free-fixed case and taking $\alpha = 1 (L_2 = L_1)$, the determinant of [A] in Eq. (1.17) leads to the following values for the first two non-dimensional natural frequencies: $\lambda_1 = 2.3967$ and $\lambda_2 = 5.2342$. (The following parameters apply: $\gamma_r = 0.7886$, $E_r = 2.9577$, $A_r = A_2/A_1 = 1.00$, $\rho_r = \rho_2/\rho_1 = 1.1481$, $Q_0 = 1.00$.)

For this case the non-dimensional version of Eq. (1.15) is given by:

$$R_1(\xi) = b_1(\cosh(\lambda\xi) + \cos(\lambda\xi)) + b_2(\sinh(\lambda\xi) + \sin(\lambda_1\xi)) - \frac{Q_0}{\lambda^4} \tag{1.22}$$

Setting $\xi = 0.50$ (beam mid-span) and using b_1 and b_2 from Eq. (1.17), amplitudes can be calculated for different values of the frequency λ.

Using Eq. (1.22) the frequency response function spanning the first two natural frequencies for the mid-point of the beam is shown in Fig. 1.3.

For the continuous variation model and this uniform beam, the non-dimensional logistic functions and cross-section functions can be written, for example, as (see Fig. 1.4):

$$\begin{array}{l} f_1(\xi) = 1 + \frac{E_2 - E_1}{E_1}\left(\frac{1}{2} + \frac{1}{2}\tanh\left(500\left(\xi - \frac{1}{2}\right)\right)\right), f_2(\xi) = 1 \\ f_3(\xi) = 1 + \frac{\rho_2 - \rho_1}{\rho_1}\left(\frac{1}{2} + \frac{1}{2}\tanh\left(500\left(\xi - \frac{1}{2}\right)\right)\right), \ f_4(\xi) = 1 \end{array} \tag{1.23}$$

Assuming a value of *1* for the external forcing and using the approach given in reference [10], the resultant deflections are plotted bellow for two distinct values of the frequency λ.

The resonance frequencies are taken to occur at $\lambda = 2.40$ and $\lambda = 5.25$ as seen in Figs. 1.5 and 1.6, respectively.

Amplitudes for the response at the center of the beam can be monitored from Eq. (1.21). This approach leads to the numerical FRF shown in Fig. 1.7.

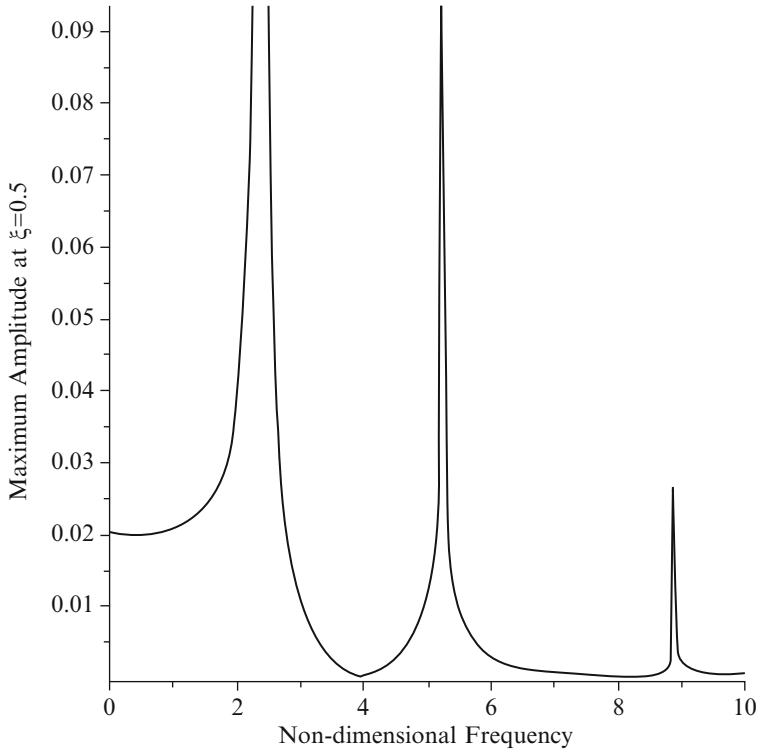

Fig. 1.3 FRF for non-homogeneous beam mid-point—Free/Fixed

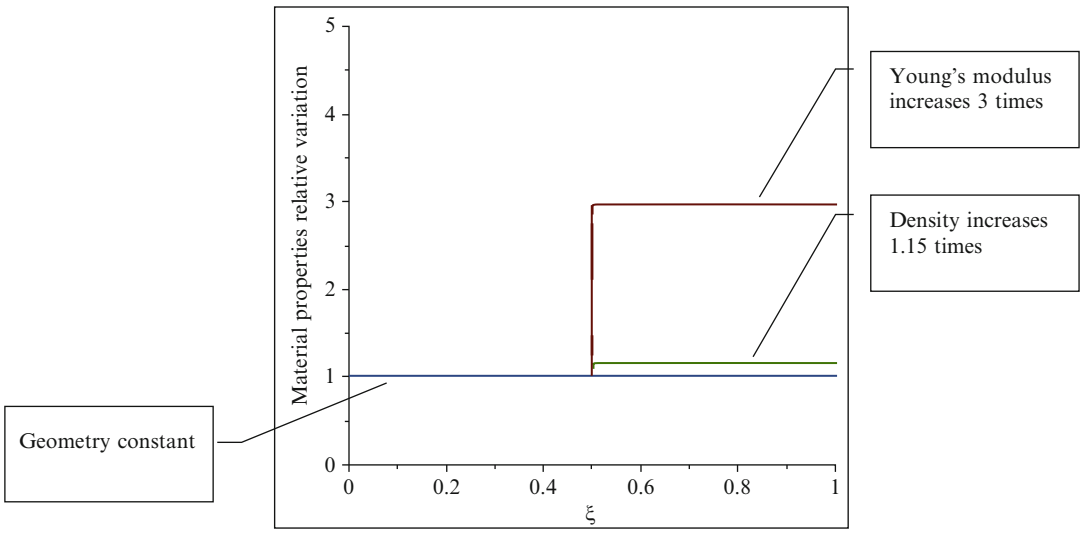

Fig. 1.4 Relative properties variation for two-cell beam

The figure shows an overlap of the numerical results and the results from the analytical approach, Eq. (1.22). It is seen that good agreement is obtained, the first two resonances are captured and the amplitude values correspond well.

Next the FRF is obtained via solutions to Eq. (1.20). The results are shown in Fig. 1.8.

It is seen in the overlap that the PDE solutions lead to a reasonable approximation to the FRF for this case. The first resonance is captured within 12% but the second resonance is not. Obtaining better results from MAPLE® would require considerable more effort and is not pursued here in view of the other successful approaches.

For validation purposes, an assumed mode method is pursued in the following. The solution to Eq. (1.1) is assumed to have the form of a Rayleigh-Ritz expansion:

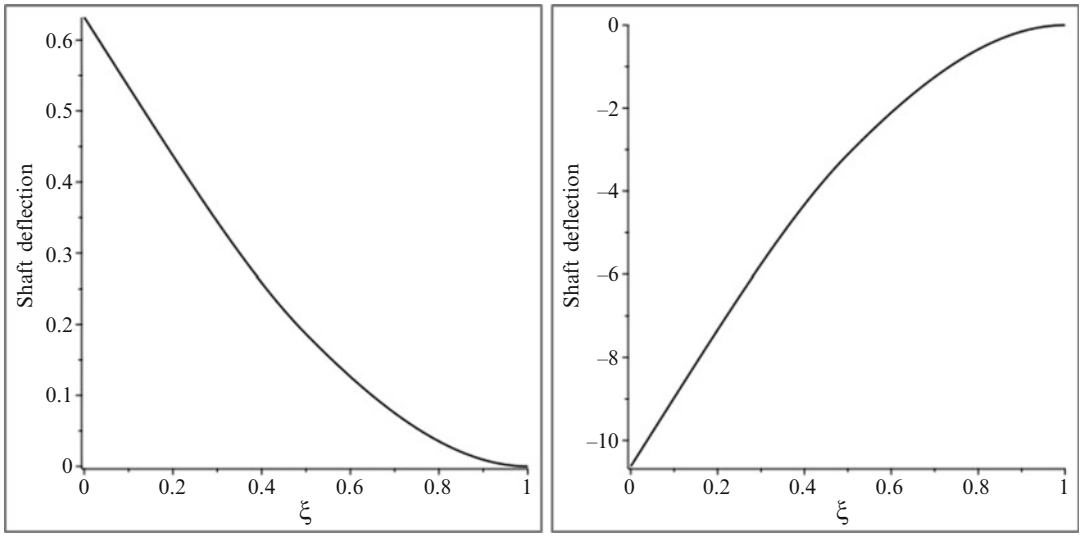

Fig. 1.5 Beam deflections for distinct values of λ–Free-Fixed: first resonance

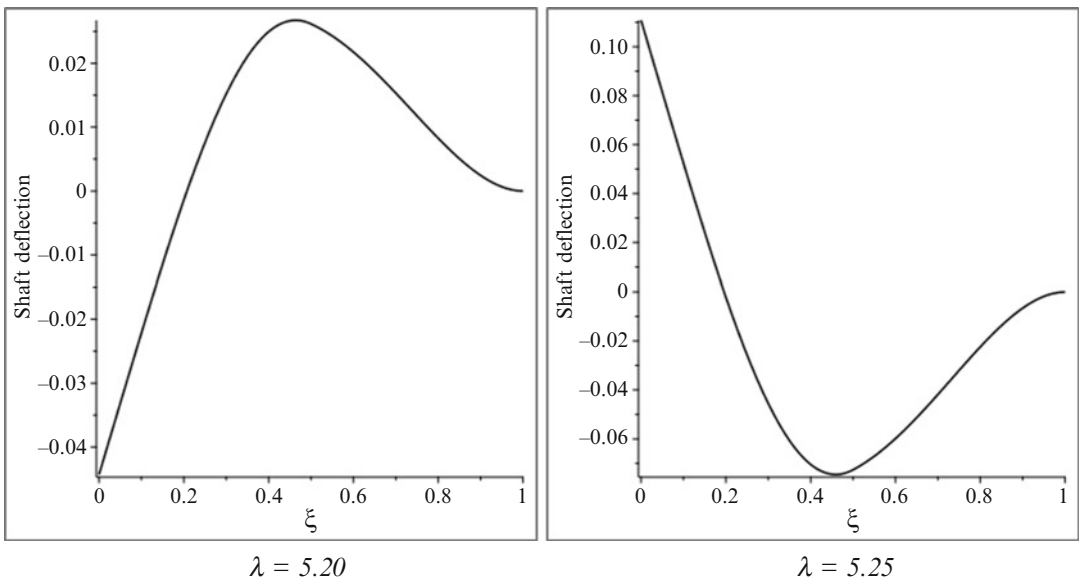

Fig. 1.6 Beam deflections for distinct values of λ–Free-Fixed: second resonance

$$w(x,t) = \sum_{i=1}^{n} \alpha_i(t)\varphi_i(x) \tag{1.24}$$

where the generalized coordinates α_i, in the linear combination of shape functions φ_i, are functions of time.

The shape functions φ_i must be chosen so they form a linearly independent set that possess derivatives up to the order appearing in the strain energy expression for the problem. They also must satisfy the prescribed boundary conditions.

Substituting Eq. (1.24) into the appropriate expressions for the kinetic and strain energy, and using Lagrange's equations, leads to a set of n differential equations for the generalized coordinates α_i.

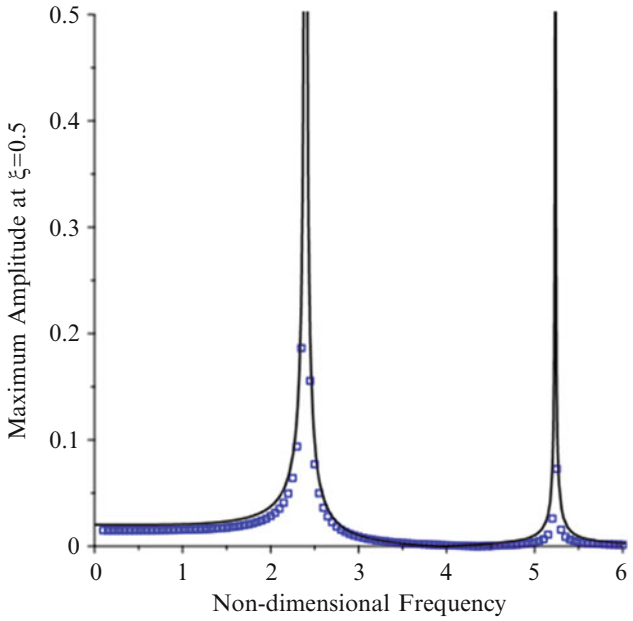

Fig. 1.7 Results comparison—numerical and analytical approaches (ODE)—Free/Fixed

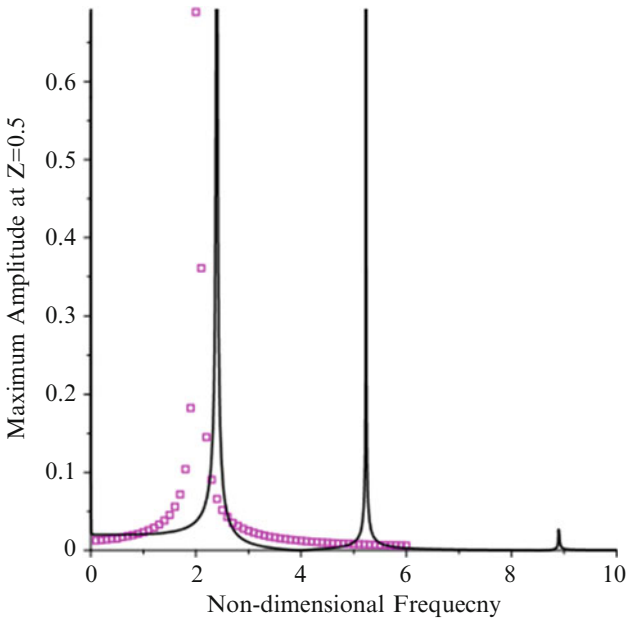

Fig. 1.8 Results comparison—numerical and analytical approaches (PDE)—Free/Fixed

For the problem at hand, the discrete non-dimensional mass and stiffness matrices, for the differential equations set, can be obtained from:

$$m_{i,j} = \int_0^{\frac{1}{2}} \varphi_i(x)\,\varphi_j(x)\,dx + A_r\rho_r \int_{\frac{1}{2}}^{1} \varphi_i(x)\,\varphi_j(x)\,dx, k_{i,j} = \int_0^{\frac{1}{2}} \varphi_i''(x)\,\varphi_j''(x)\,dx + E_r I_r \int_{\frac{1}{2}}^{1} \varphi_i''(x)\,\varphi_j''(x)\,dx \tag{1.25}$$

If the external transverse loads are taken to be sinusoidal with frequency ν, the following expression for calculating the generalized external forces can be used:

$$p_i = \left[\int_0^{\frac{1}{2}} f_1 \varphi_i(x)\, dx + \int_{\frac{1}{2}}^{1} f_2 \varphi_i(x)\, dx \right] \sin(\nu\tau) \tag{1.26}$$

where f_i is the amplitude of the force acting on the i-segment.

The natural frequencies can then be evaluated via an eigenvalue problem and the system response to external forcing estimated via modal analysis. The procedure is tackled using MAPLE®.

As a first approach, non-dimensional mode shapes for a homogenous cantilever beam are used for the shape functions set. They can be written as:

$$\varphi_i(x) = N_i \left\{ \left[\cos(\beta_i) + \cosh(\beta_i) \right] [\sin(\beta_i (1-\xi)) - \sinh(\beta_i (1-\xi))] + [\sin(\beta_i) + \sinh(\beta_i)] \right.$$
$$\left. [\cosh(\beta_i (1-\xi)) - \cos(\beta_i (1-\xi))] \right\} \tag{1.27}$$

where N_i is a normalization parameter and $\beta_1 = 1.875, \beta_2 = 4.694, \beta_k = (2k-1)\frac{\pi}{2}, k = 3, ..., n$. The normalization parameters are taken to be the inverse of the magnitude of the maximum values of the shape functions in the interval $\xi = 0..1$.

Using $i = 3, f_1 = 1$ and $f_2 = 1$, the discrete differential equations of motion for the generalized coordinates α_i are:

$$\begin{bmatrix} 0.2518 & 0.0053 & 0.0053 \\ 0.0053 & 0.2659 & 0.0192 \\ 0.0053 & 0.0192 & 0.4670 \end{bmatrix} \begin{bmatrix} \ddot{\alpha}_1(t) \\ \ddot{\alpha}_2(t) \\ \ddot{\alpha}_3(t) \end{bmatrix} + \begin{bmatrix} 8.8339 & 5.5380 & -16.0001 \\ 5.5380 & 254.1732 & 351.7299 \\ -16.0001 & 351.7299 & 3255.3629 \end{bmatrix} \begin{bmatrix} \alpha_1(t) \\ \alpha_2(t) \\ \alpha_3(t) \end{bmatrix} = \begin{bmatrix} 0.3915 \\ 0.2170 \\ 0.1678 \end{bmatrix} \sin(\nu\tau) \tag{1.28}$$

The natural frequencies are calculated as $\lambda = 2.41$ and $\lambda = 5.33$.

Following the procedure, the Rayleigh-Ritz approximation for the steady state response is obtained. Setting an arbitrary non-dimensional time $\tau = 100$, for example, and monitoring the amplitudes at $\xi = 0.5$, for distinct values of the excitation frequency ν, leads to the results shown in Fig. 1.9.

The figure shows an overlap of the assumed modes results and the analytic results (solid line). It can be seen that very good agreement is obtained in terms of frequencies and FRFs for the first two resonances.

In the search for better convergence in the higher modes, one can increase the number of shape functions utilized in the approach. However, this increases the complexity of the numerical calculations in the algorithm developed, due to the presence of increasingly more complex trigonometric and hyperbolic functions in the integrals of Eqs. (1.25) and (1.26).

An alternative is to use polynomial shape functions. This is discussed next.

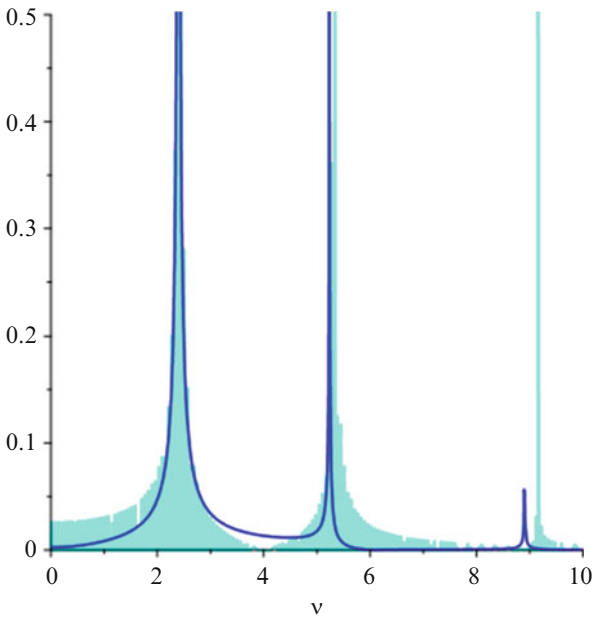

Fig. 1.9 Results comparison—assumed modes and analytical approaches—Free/Fixed

In this case, the shape functions φ_i are taken to be beam characteristic orthogonal polynomials, with each polynomial satisfying the prescribed boundary conditions of the problem. They are generated by the Gram-Schmidt process [12] as demonstrated by Bhat [13].

The first polynomial is taken to satisfy the two boundary conditions at the fixed end and to have the following form (free-fixed non-dimensional homogeneous beam static deflection under distributed load):

$$\varphi_1(x) = s_1\left(x^4 - 5x^3 + 15x^2 - 19x + 8\right) \tag{1.29}$$

The constant s_1 is chosen such that:

$$\int_0^1 (\varphi_k(x))^2 dx = 1 \tag{1.30}$$

The remainder polynomials are generated by the Gram-Schmidt approach. In addition, the set is also normalized as described above. For example, an approximation with three polynomials gives:

$$\begin{aligned}
\varphi_1(x) &= 0.1250x^4 - 0.6250x^3 + 1.8750x^2 - 2.3750x + 1.0000 \\
\varphi_2(x) &= 5.4569\,(x - .1538)\left(0.2959x^4 - 1.4797x^3 + 4.4391x^2 - 5.6228x + 2.3675\right) \\
\varphi_3(x) &= 29.5510\,(x - 0.3238)\,(x - 0.1539)\left(0.2959x^4 - 1.4797x^3 + 4.4391x^2 - 5.6228x + 2.3675\right) - \\
&\quad 0.1556x^4 + 0.7780x^3 - 2.3341x^2 + 2.9565x - 1.2448
\end{aligned} \tag{1.31}$$

which leads to the following discrete differential equations of motion for the generalized coordinates α_i:

$$\begin{bmatrix} 0.1790 & 0.0034 & 0.0041 \\ 0.0034 & 0.5489 & 0.0248 \\ 0.0041 & 0.0248 & 0.5702 \end{bmatrix} \begin{bmatrix} \ddot{\alpha}_1(t) \\ \ddot{\alpha}_2(t) \\ \ddot{\alpha}_3(t) \end{bmatrix} + \begin{bmatrix} 9.3374 & -54.7945 & 114.6766 \\ -54.7945 & 963.8044 & -2147.8536 \\ 114.6766 & -2147.8536 & 9888.9234 \end{bmatrix} \begin{bmatrix} \alpha_1(t) \\ \alpha_2(t) \\ \alpha_3(t) \end{bmatrix} = \begin{bmatrix} 0.3063 \\ 0.3333 \\ 0.2276 \end{bmatrix} \sin(\nu\tau) \tag{1.32}$$

The natural frequencies are calculated as $\lambda = 2.42$ and $\lambda = 5.41$.

Following the procedure and using the same non-dimensional time $\tau = 100$, monitoring the amplitudes at $\xi = 0.5$ leads to the results shown in Fig. 1.10.

The overlap of the assumed modes and the analytic results (solid line) shows that good agreement is obtained for the first two frequencies and FRFs.

Figure 1.11 shows results using six polynomials. The natural frequencies are calculated as $\lambda = 2.41$ and $\lambda = 5.31$.

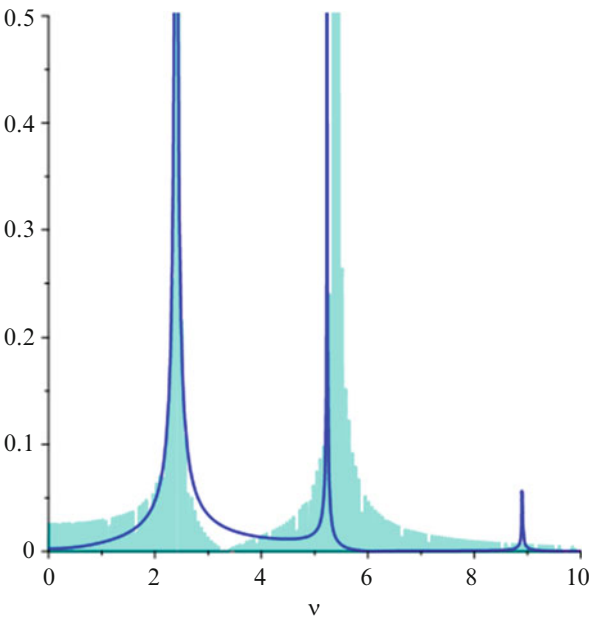

Fig. 1.10 Results comparison—assumed modes three polynomials and analytical approaches—Free/Fixed

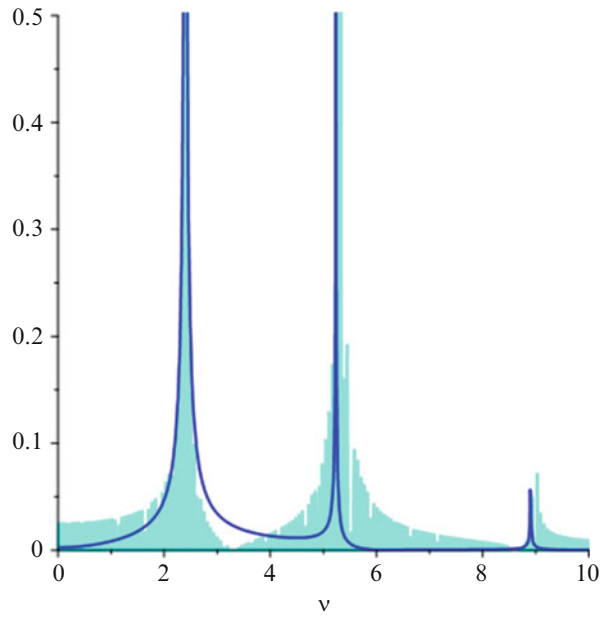

Fig. 1.11 Results comparison—assumed modes six polynomials and analytical approaches—Free/Fixed

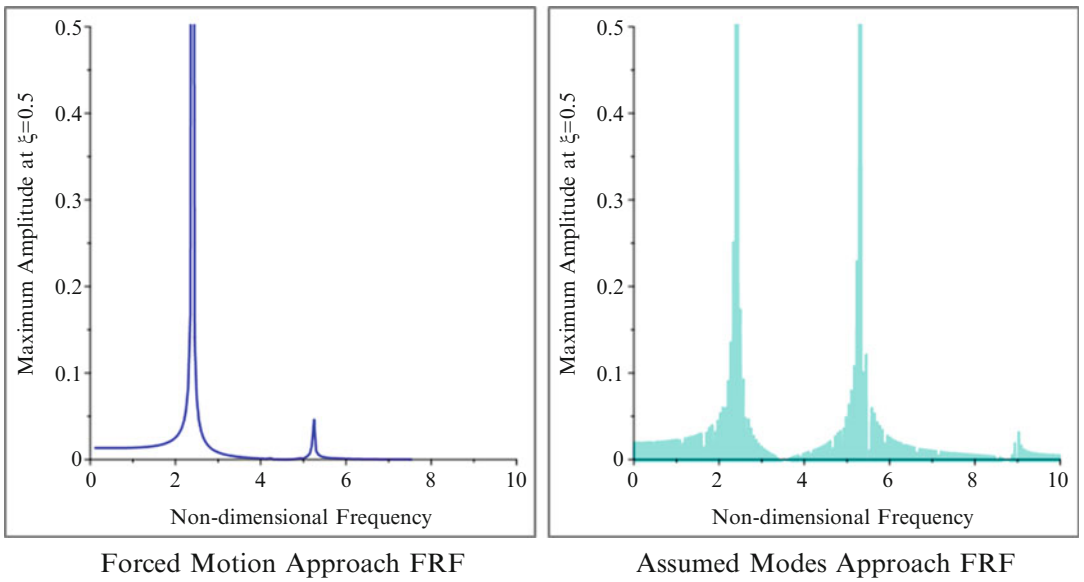

Fig. 1.12 FRF for varying spatial functions—Free/Fixed

The overlap shows better agreement and demonstrates convergence of the approach.

Consider next an example in which the spatial force variations are such that the particular integrals in Eq. (1.8) are intractable analytically. As demonstrated above, the results can be found using the continuous variation model and the assumed modes method.

Take, for example, variable forces equal in both segments and given by an exponential function: $P_1(x) = P_2(x) = e^{-[(x/L)^2]}$. Then $F(\xi) = e^{-\xi^2}$ (refer to Eqs. (1.20) and (1.21)) and $f_1 = f_2 = e^{-\xi^2}$ in Eq. (1.26).

The frequency response functions given by the forced motion and assumed mode approaches, respectively, are seen in Fig. 1.12.

In the forced motion plot, the FRF points are represented via a trend line. Very good agreement for the first frequency is seen.

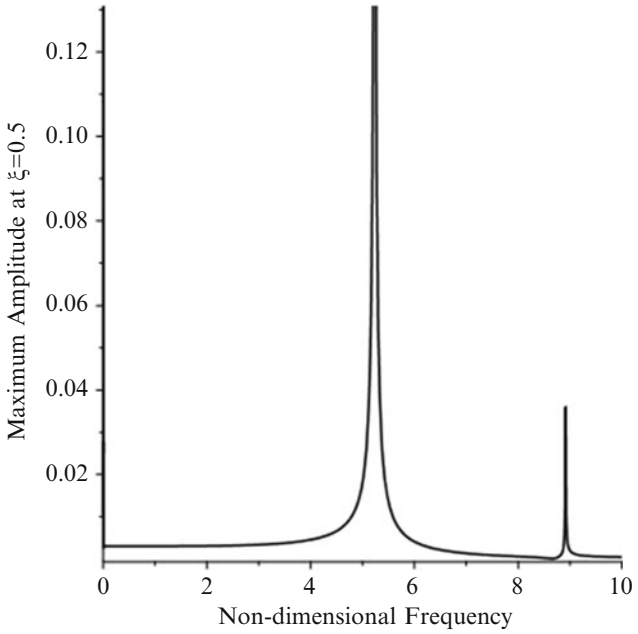

Fig. 1.13 FRF for non-homogeneous beam mid-point—Fixed/Fixed

1.5.2 Fixed-Fixed Boundary Conditions

For the fixed-fixed case ($\alpha = 1$), the determinant of [A] in Eq. (1.18) leads to the following values for the first two non-dimensional natural frequencies: $\lambda_1 = 5.2329$ and $\lambda_2 = 8.9156$. (The parameters γ_r, E_r, A_r, ρ_r, and Q_0 are the same as above.)

For this case the non-dimensional version of Eq. (1.13) is:

$$R_1(\xi) = b_1 \cosh(\lambda\xi) + b_2 \sinh(\lambda\xi) + b_3 \cos(\lambda\xi) + b_4 \sin(\lambda_1\xi) - \frac{Q_0}{\lambda^4} \tag{1.33}$$

Setting $\xi = 0.50$ and using b_1 and b_2 from Eq. (1.18), amplitudes can be calculated for different values of the frequency λ. The frequency response function spanning the first two natural frequencies for the mid-point of the beam is shown in Fig. 1.13.

Next only the numerical methods that led to consistent results in the previous example are used to obtain frequencies and FRFs for this case, i.e., the forced motion and assumed modes approaches.

The forced motion produces these resonance frequencies: $\lambda = 5.25$ and $\lambda = 8.90$. Monitoring amplitudes for the response at the center of the beam (Eq. (1.21)) leads to the numerical FRF shown in Fig. 1.14.

The figure shows an overlap of the numerical results and the results from the analytical approach, Eq. (1.33). As in the previous example good agreement is obtained.

For the assumed modes method, in this case, the first polynomial is chosen to satisfy the fixed boundary conditions at the ends. It is given by (fixed-fixed non-dimensional homogeneous beam static deflection under distributed load):

$$\varphi_1(x) = s_1\left(4x^3 - 6x^2 + 2x\right) \tag{1.34}$$

The constant s_1 satisfies Eq. (1.30).

Utilizing six polynomials, the resulting frequencies are $\lambda = 5.27$ and $\lambda = 8.95$. Following the procedure given above and using the non-dimensional time $\tau = 100$, monitoring amplitudes at $\xi = 0.5$ leads to the results shown in Fig. 1.15. Good agreement is also seen here.

Lastly, the spatial force with exponential variation is considered. Results are given in Fig. 1.16 for this case.

Good agreement for frequencies is seen while the assumed modes approach predicts somewhat higher amplitudes.

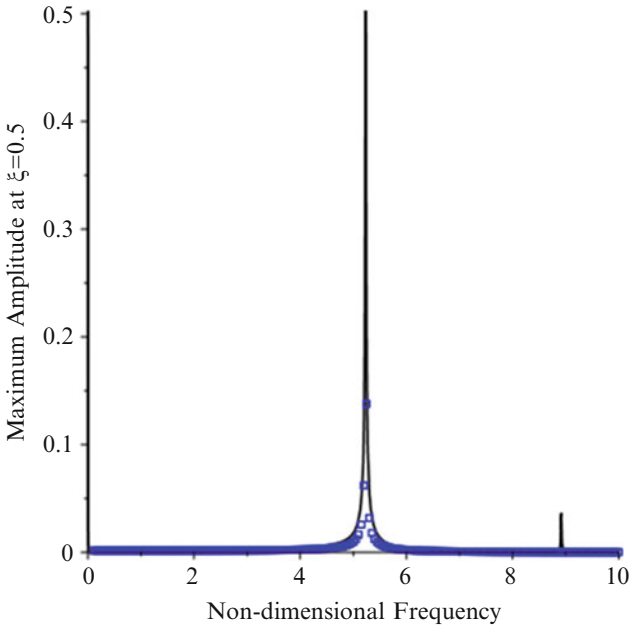

Fig. 1.14 Results comparison—numerical and analytical approaches (ODE)—Fixed/Fixed

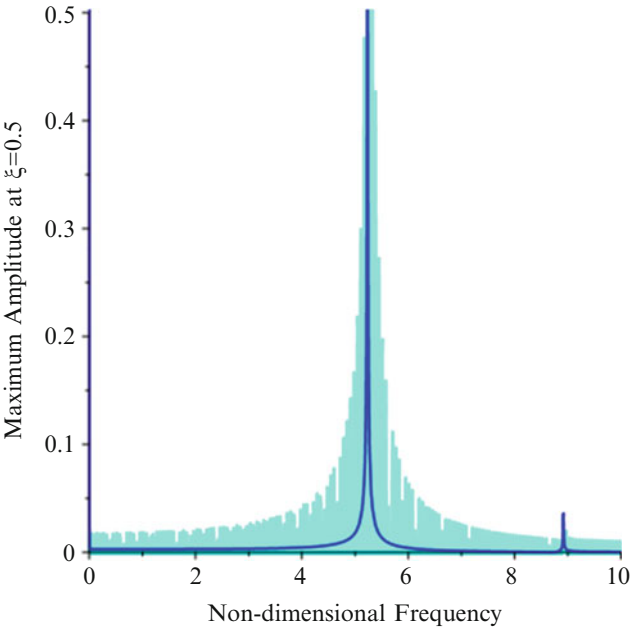

Fig. 1.15 Results comparison—assumed modes six polynomials and analytical approaches—Fixed/Fixed

1.6 Conclusions

Replacing discrete property variations with continuously varying ones, in conjunction with numerical solutions, has been shown to lead to good results for resonant frequencies and FRFs of layered beams subject to harmonic excitation.

Both resonance monitoring of forced motion solutions of the resulting single ordinary differential equation and an assumed modes approach produced good results toward this objective. MAPLE® software was utilized and it has been shown to lead to accurate solutions via the two approaches, based on a comparison to analytical results for a specific case.

Two sets of boundary conditions were studied. Namely, fixed-free and fixed-fixed for a uniform two-cell beam made of aluminum and silicon-carbide.

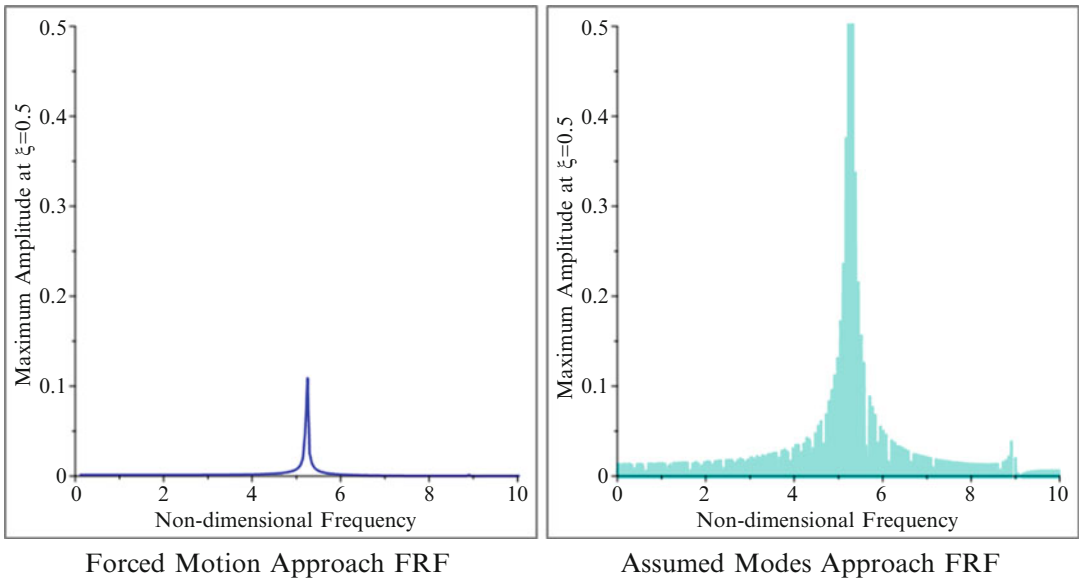

Fig. 1.16 FRF for varying spatial functions—Fixed/Fixed

Very good agreement was observed for both cases, with some variation on the amplitudes for the FRFs. For improved accuracy it is conjectured that using more polynomials in the assumed mode approach will produce better agreement.

References

1. Mazzei, A.J., Scott, R.A.: Natural frequencies of layered beams using a continuous variation model. In: Wicks, A. (ed.) Shock & Vibration, Aircraft/Aerospace, and Energy Harvesting, Volume 9: Proceedings of the 33rd IMAC, a Conference and Exposition on Structural Dynamics, 2015, pp. 187–200. Cham, Springer International Publishing (2015)
2. Cekus, D.: Use of Lagrange multiplier formalism to solve transverse vibrations problem of stepped beams according to timoshenko theory. Sci. Res. Inst. Math. Comput. Sci. **2**(10), 49–56 (2011)
3. Jang, S.K., Bert, C.W.: Free vibration of stepped beams: exact and numerical solutions. J. Sound Vib. **130**(2), 342–346 (1989)
4. Bert, C.W., Newberry, A.L.: Improved finite element analysis of beam vibration. J. Sound Vib. **105**, 179–183 (1986)
5. Lee, E.H., Yang, W.H.: On waves in composite materials with periodic structure. SIAM J. Appl. Math. **25**(3), 492–499 (1973)
6. Hussein, M.I., Hulbert, G.M., Scott, R.A.: Dispersive elastodynamics of 1d banded materials and structures: analysis. J. Sound Vib. **289**(4–5), 779–806 (2006)
7. Mazzei, A.J., Scott, R.A.: Vibrations of discretely layered structures using a continuous variation model. In: Allemang, R. (ed.) Topics in Modal Analysis Ii, Volume 8: Proceedings of the 32nd Imac, a Conference and Exposition on Structural Dynamics, 2014, pp. 385–396. Cham, Springer International Publishing (2014)
8. Kang, Y., Shen, Y., Zhang, W., Yang, J.: Stability region of floating intermediate support in a shaft system with multiple universal joints. J. Mech. Sci. Technol. **28**(7), 2733–2742 (2014)
9. Berezovski, A., Engelbrecht, J., Maugin, G.A.: Numerical Simulation of Waves and Fronts in Inhomogeneous Solids. World Scientific Publishing Co. Pte. Ltd., Singapore (2008)
10. Mazzei, A.J., Scott, R.A.: On the effects of non-homogeneous materials on the vibrations and static stability of tapered shafts. J. Vib. Control. **19**(5), 771–786 (2013)
11. Chiu, T.C., Erdogan, F.: One-dimensional wave propagation in a functionally graded elastic medium. J. Sound Vib. **222**(3), 453–487 (1999)
12. Chihara, T.S.: Introduction to Orthogonal Polynomials. Gordon and Breach, London (1978)
13. Bhat, R.B.: Transverse vibrations of a rotating uniform cantilever beam with tip mass as predicted by using beam characteristic orthogonal polynomials in the Rayleigh-Ritz method. J. Sound Vib. **105**(2), 199–210 (1986)

Chapter 2
A New Surrogate Modeling Method Associating Generalized Polynomial Chaos Expansion and Kriging for Mechanical Systems Subjected to Friction-Induced Vibration

E. Denimal, L. Nechak, J.-J. Sinou, and S. Nacivet

Abstract This study focuses on a hybrid surrogate modelling technique in order to predict parameter-dependent mode coupling instabilities for uncertain mechanical systems subjected to friction-induced vibration. For this purpose, the most common strategy consists in associating a Monte Carlo procedure and/or a scanning technique together with the Complex Eigenvalue Analysis (CEA). This numerical strategy is computationally too prohibitive, particularly in an industrial context such as in the brake systems. To overcome this drawback, a novel approach is proposed. It consists in the combination of the generalized polynomial chaos (GPC) together with the kriging based meta-models. The association of both methods gives rise to a hybrid meta-model allowing taking into account two sets of uncertain parameters in the prediction of mode coupling instabilities. Moreover, it permits avoiding the use of the prohibitive MC and scanning methods. Thereby, this study analyses the feasibility of the proposed meta-model and its potential to be an efficient predictor of squeal propensity under parameter uncertainty.

Keywords Friction-induced vibrations • Kriging • Generalized polynomial chaos • Uncertainty • Meta-modelling

2.1 Introduction

Numerous studies have been proposed the last decades for the prediction of friction-induced instabilities submitted to parameter uncertainties [1–4]. A suitable choice of the predictor depends on models considered for the uncertainty description. For example, the generalized polynomial chaos based predictor is preferred to the MC method when dealing with random uncertainties described by probability density functions [4] while methods based on Kriging are privileged when parameters are defined only by intervals [1–3]. However, in several cases, friction induced instabilities may be simultaneously submitted to random and interval parameters. Thus, it is necessary to develop hybrid predictors capable of taking into account of both uncertainties sets. So, the purpose of this paper is to present a new surrogate modeling method that associate the generalized polynomial Chaos and Kriging formalisms for the prediction of friction-induced instabilities when subjected to random and interval parameters. The Complex Eigenvalue analysis method associated with the Monte Carlo and/or Scanning methods commonly used is unfortunately prohibitive. Hence, the main aim is to propose a surrogate which offers a suitable compromise between the accuracy of predictions and the computation time. The method developed here lies in the superposition of the two methods to namely the generalized polynomial chaos and the Kriging meta-models. The first purpose is to assess the feasibility of the proposed meta-model. A mechanical system with four degrees of freedom is then considered. Otherwise, another objective of this study is to study the impact of the input law on the stability of the system under study.

E. Denimal (✉) • L. Nechak
Laboratoire de Tribologie et Dynamique des Systèmes, UMR CNRS 5513, Ecole Centrale de Lyon, 36 avenue Guy de Collongue, 69134 Ecully Cedex, France
e-mail: enora.denimal@doctorant.ec-lyon.fr

J.-J. Sinou
Laboratoire de Tribologie et Dynamique des Systèmes, UMR CNRS 5513, Ecole Centrale de Lyon, 36 avenue Guy de Collongue, 69134 Ecully Cedex, France

Institut Universitaire de France, 75005 Paris, France

S. Nacivet
PSA Peugeot Citroën, Centre technique de La Garenne Colombes, 18 rue des Fauvelles, 92250 La Garenne Colombes, France

N. Dervilis (ed.), *Special Topics in Structural Dynamics, Volume 6*, Conference Proceedings of the Society for Experimental Mechanics Series, DOI 10.1007/978-3-319-53841-9_2

2.2 System Under Study

2.2.1 Description of the System

A minimal system of four-degrees-of-freedom is studied and displayed on Fig. 2.1. This phenomenological model is based on the well-known two-degree-of-freedom model proposed by Hulten [5, 6]. It is used in [7] to point out the role of the damping and the destabilization paradox. The system under study is an extension to investigate the case of multi-instabilities. The model consists of two masses m_1 and m_2 linearly coupled and held against moving bands disposed as in Fig. 2.1. Contact between masses and bands are modeled by plates supported by spring and damping. The Coulomb's law with a constant friction coefficient μ is used. A more developed description of the system can be found in [2].

By noting $\mathbf{M}$, $\mathbf{C}$ and $\mathbf{K}$ the mass, damping and stiffness matrix respectively and $\ddot{\mathbf{X}}$, $\dot{\mathbf{X}}$ and $\mathbf{X}$ the acceleration, velocity and displacement vectors respectively, the equation of motion is given by:

$$\mathbf{M}\ddot{\mathbf{X}} + \mathbf{C}\dot{\mathbf{X}} + \mathbf{K}\mathbf{X} = \mathbf{0} \tag{2.1}$$

2.2.2 The Complex Eigenvalue Analysis to Predict the Stability of the System

Due to the high computation cost of non-linear transient and stationary responses of the system, methods based on the CEA are often used in order to predict the instabilities of the system in a given frequency range, even if this method can lead to an under- or over-estimation of the unstable modes [8].

The CEA is based on the numerical analysis of the system eigenvalues. Assuming a solution of the form $\mathbf{X}(t) = \mathbf{\Phi} e^{\lambda t}$ where $\boldsymbol{\lambda}$ is a complex eigenvalue of the system and $\mathbf{\Phi}$ the associated eigenvector, the equation of motion becomes:

$$\left(\boldsymbol{\lambda}^2\mathbf{M} + \boldsymbol{\lambda}\mathbf{C} + \mathbf{K}\right)\mathbf{\Phi} = \mathbf{0} \tag{2.2}$$

So the eigenvalue analysis can be performed by solving the characteristic equation:

$$\det\left(\boldsymbol{\lambda}^2\mathbf{M} + \boldsymbol{\lambda}\mathbf{C} + \mathbf{K}\right) = 0 \tag{2.3}$$

According to the Lyapunov theory, the asymptotic stability of the system is given by the sign of the real part of eigenvalues. If at least one eigenvalue has a positive real part, the system is unstable. The corresponding imaginary part is the pulsation of the associated unstable mode.

The set of parameters for the mechanical model under study is given in Table 2.1. Eigenvalues obtained with the CEA by increasing the constant friction coefficient μ from 0 to 1 are presented Fig. 2.2. Three mode-coupling phenomena are

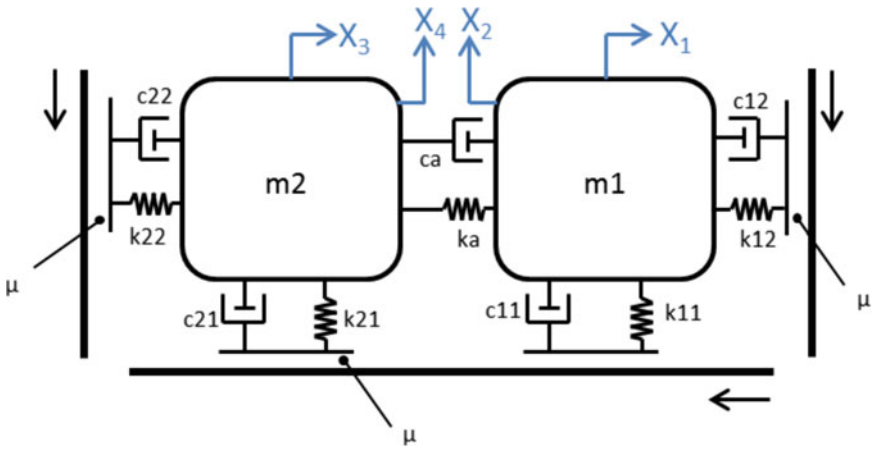

Fig. 2.1 Mechanical system

Table 2.1 Set of considered parameters

Parameters	M1 (kg)	M2 (kg)	K11 (N/m)	K12 (N/m)	K21 (N/m)	K22 (N/m)	Ka (N/m)	C11 (N.s/m)	C12 (N.s/m)	C21 (N.s/m)	C22 (N.s/m)	Ca (N.s/m)
Value	1	1	3000	6000	1000	3000	1000	1	1	1	1	1

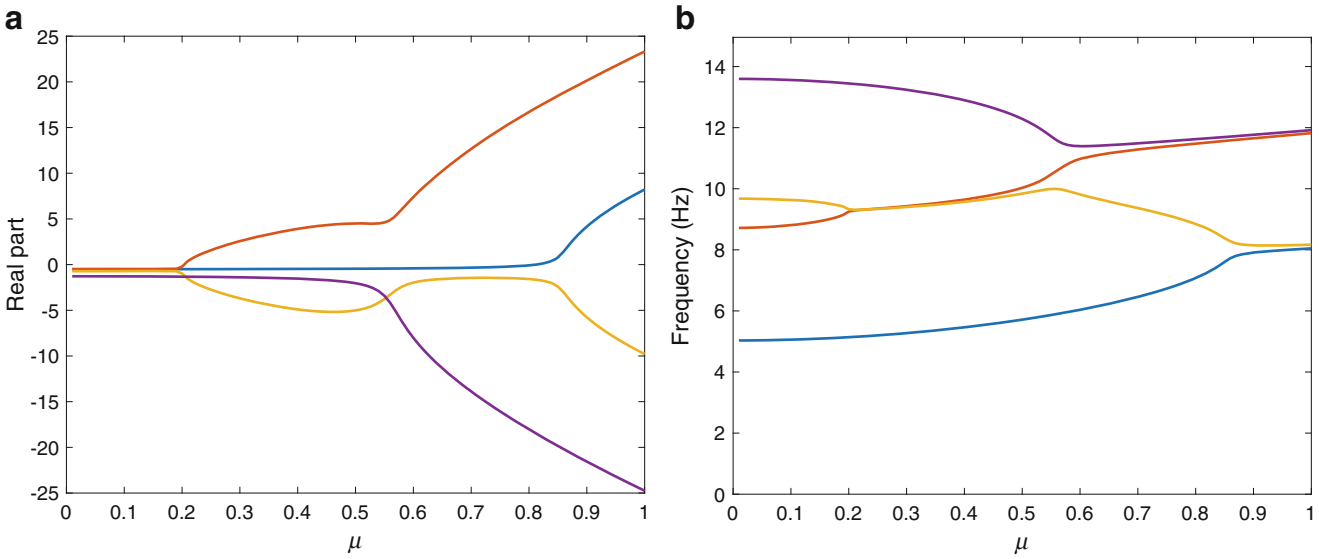

Fig. 2.2 Evolution of real (**a**) and imaginary (**b**) parts of eigenvalues versus the friction coefficient **μ**

observed. The first one appears when $\mu = 0.20$ with the frequency of the unstable mode equal to 9.25 Hz. The other coalescences are detected for $\mu \geq 0.5$ and $\mu \geq 0.81$. Modes are involved in several successive coupling coalescences, a crossing phenomenon between two modes is observed for $\mu = 0.55$.

2.3 Hybrid Surrogate Modeling Method

As mentioned in the introduction, the construction of a hybrid surrogate model is required for the predicting of friction induced instabilities when these depend on two sets of uncertain parameters (random parameters described by their probability density functions and interval parameters). The GPC expansion combined with the Kriging meta-model proposed in recent studies [1–4] for the prediction of friction-induced instabilities subjected to parameter uncertainties, are proposed in this framework. The main idea consists of exploiting a limited number of simulations (CEA solutions) to build the response surfaces of the system's eigenvalues. The taking into account of probabilistic and interval parameters, results in the expression of the stochastic modes of the GPC expansions by kriging functions. Brief descriptions of the two formalisms are given below.

2.3.1 Kriging

The main idea from the kriging theory [9–11] is based on the possibility to estimate a response surface just with a small number of simulations at points generated, randomly or pseudo-randomly, from the design space. Hence, any parameter-dependent eigenvalue $\lambda(\mathbf{p})$ ($\mathbf{p}$ being a vector parameter) can be approximated by a meta-model constructed from a regression defining the average behavior of the function and the stochastic process $Z(\mathbf{p})$ defining its dispersion.

$$\lambda(\mathbf{p}) = \sum_{i=1}^{m} \beta_i f_i(\mathbf{p}) + Z(\mathbf{p}) \tag{2.4}$$

where the first terms is a linear combination of m polynomial functions weighted by regression parameters β_i. $Z(.)$ is a zero-mean random process characterized by a special correlation function which estimates the similarity of two points in the design space, [9–11]. The regression β_i and correlation parameters characterize the kriging meta-model. In this study, they are calculated by using the DACE toolbox [9].

2.3.2 Generalized Polynomial Chaos

The generalized polynomial chaos (GPC) formalism the possibility to approximate the random parameter-dependent eigenvalue $\lambda(\boldsymbol{\xi})$ by a convergent, in the L^2 sense, expansion onto a polynomial basis which is orthogonal with respect to the probability measures associated to the random parameter vector $\boldsymbol{\xi}$, [12, 13].

$$\lambda(\boldsymbol{\xi}) \cong \sum_{i=0}^{d} a_i \psi_i(\boldsymbol{\xi}) \tag{2.5}$$

Coefficients a_i are the unknown deterministic coefficients and ψ_i the multivariate polynomial basis. Coefficients a_i can be computed with non-intrusive techniques as the regression or the non-intrusive spectral projection method [14].

2.3.3 Association of Kriging and Generalized Polynomial Chaos Expansion

Based on the both approximations presented previously, a system eigenvalue depending on random and interval parameters can be approximated by the following double expansion:

$$\lambda(\mathbf{p}, \boldsymbol{\xi}) \cong \sum_{j=0}^{d} \left(\sum_{i=1}^{m} \beta_i f_i(\mathbf{p}) + Z(\mathbf{p}) \right) \psi_j(\boldsymbol{\xi}) \tag{2.6}$$

The main task is then to compute GPC coefficients $a_j$that, as they are functions in the vector parameter p, are approximated by kriging functions. Two experimental plans are constructed: the first one concerns the probabilistic parameters while the second concerns the interval parameters. The first plan is used to determine a small number of GPC expansions by using the regression technic [14] while the second plan is used to construct the surface response of the GPC coefficients $(a_j)_{j \in [0, P-1]}$ by the kriging meta-model.

2.4 Application

To assess the proposed hybrid meta-model, the approximating of the eigenvalues depending on the random friction coefficient μ and the two interval stiffnesses parameters k_{11} and k_{22} is realized. The friction coefficient is assumed to follow a Beta distribution, when the two stiffnesses are supposed to be within two known intervals given by 10% around their mean values. Reference results obtained from performing the CEA associated with a scanning method is presented in [2]. As the friction coefficient is governed by a beta-probability density function, the Jacobi polynomial basis is used to propagate and quantify the corresponding uncertainty [13]. A 10th order Jacobi polynomial expansion is considered. The associated coefficients depending on k_{11} and k_{22} are approximated by a kriging function which is constructed by considering a first order regression functions and a cubic correlation function [9]. A μ-experience plan defined by 14 samples (zeros of the 14th order Jacobi polynomial) with a (k_{11}, k_{22})-LHS plan (Latin hypercube sampling) with 50 samples of the couple (k_{11}, k_{22}), define 700 CEA solutions required for the calculation of the hybrid meta-model. Otherwise, to observe the influence of the probability density function on the prediction results, different density functions are considered as indicated in Table 2.2.

Figure 2.3 displays response surfaces of the three first chaos coefficients and the last one corresponding to the real part of the first eigenvalue of the system under study. Results obtained by kriging (in black) are compared to those computed with the regression technique in blue. Points of the design space used to build the kriging surrogate model are represented in red. It can be observed that the kriging meta-mode gives suitable approximations of polynomial chaos coefficients.

Table 2.2 Parameters of beta laws

Parameters	α	β
Law Beta 1	5	5
Law Beta 2	2	8
Law Beta 3	8	2

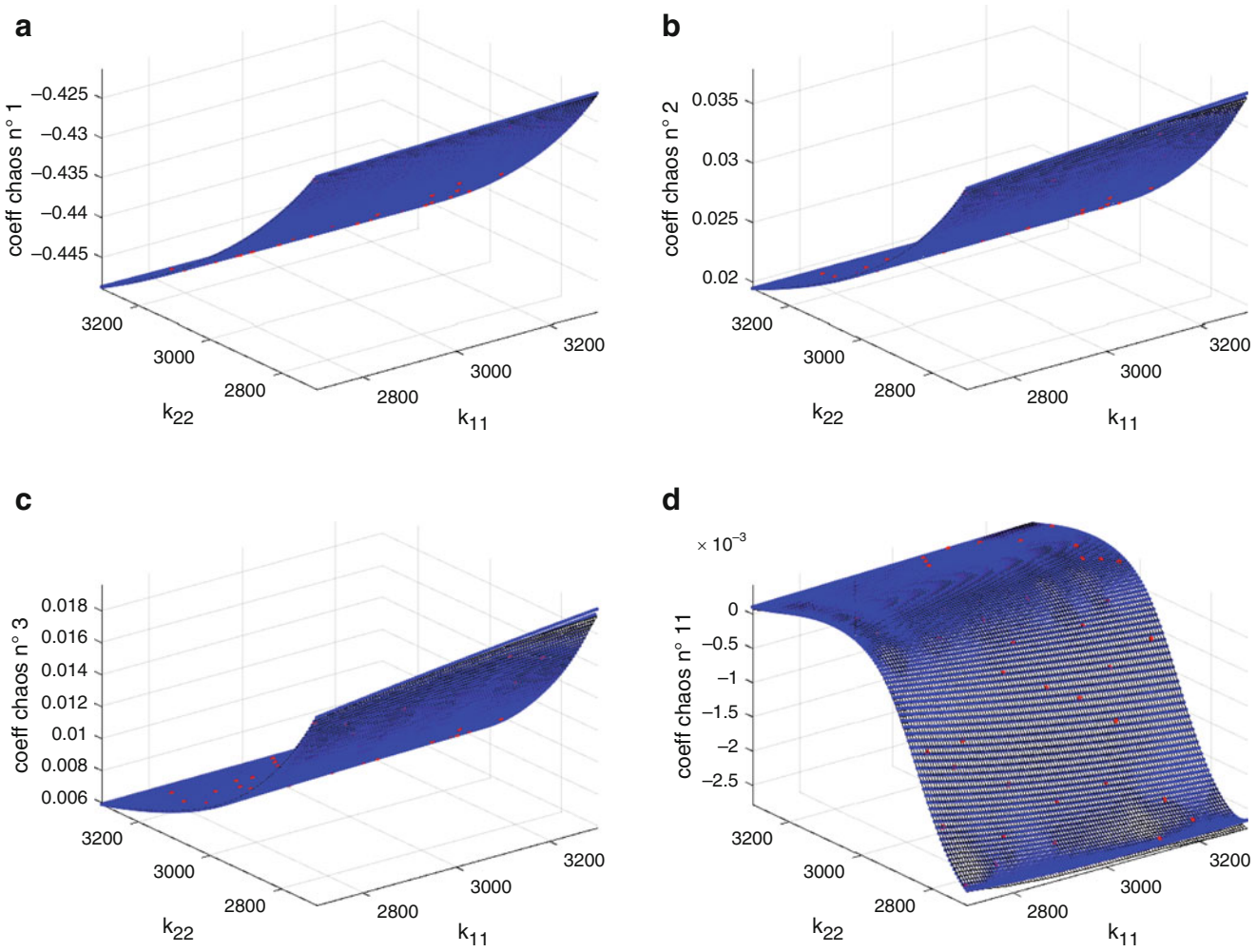

Fig. 2.3 First (**a**), second (**b**), third (**c**) and last (**d**) Polynomial Chaos coefficients: Kriging results (*blue*), experimental design (*red*) and deterministic results (*black*)

The resulting hybrid meta-model is considered to predict friction-induced instabilities. Moreover, to analyze the effect of the density function governing the friction coefficient on the predicted friction-induced instabilities, three beta-distributions with different parameters (Table 2.2) are considered. The parameters α and β are chosen in such a manner to have different repartitions for the friction coefficient. The first couple $\alpha = 5$ and $\beta = 5$ gives rise to a symmetric law centered on 0.5 while the other couples define repartitions with mirror effect.

The hybrid meta-model predictions corresponding to friction coefficient governed by a beta distribution of parameters $\alpha = 5$ and $\beta = 5$ are plotted in Fig. 2.4b. The associated reference, shown in Fig. 2.4a, is obtained by associating the MC and scanning methods with the CEA. The total number of CEA solutions required for the reference was equal to $25 * 10^7$. With only 700 CEA solutions, the calculated hybrid meta-model has allowed accurate repartitions of the real and imaginary parts of the unstable modes. Moreover, the almost-sure unstable character of the system is also well predicted by the hybrid meta-model. Otherwise, it can be observed, from Fig. 2.4b, c, d that the stability properties are strongly impacted by the probability density function governing the friction coefficient. Indeed, the real and imaginary parts of unstable modes obtained with the

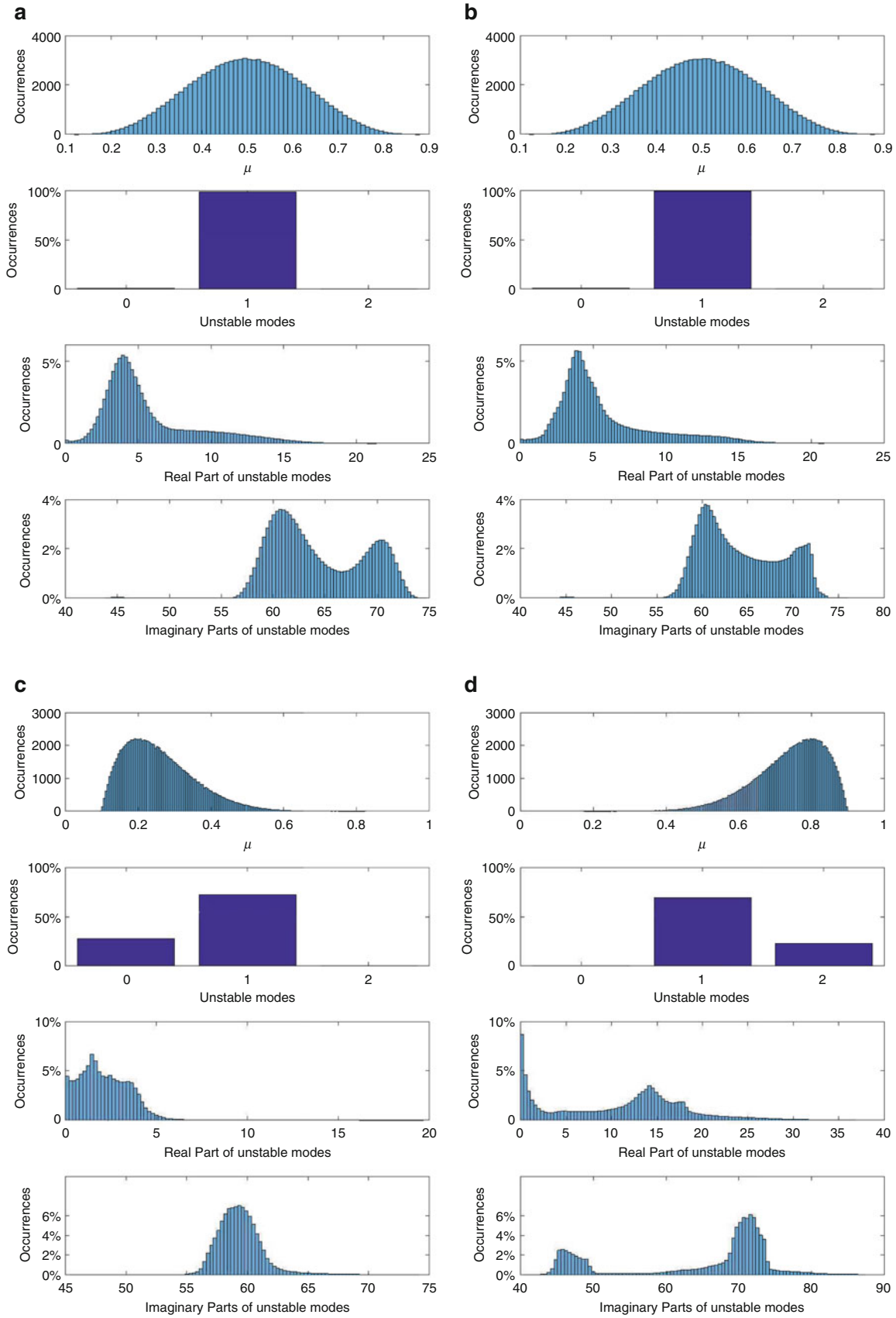

Fig. 2.4 Results of simulation using different Beta laws: (from *top* to *bottom*) the histograms of the random parameter $\boldsymbol{\mu}$, histograms of stable/unstable occurrences, histograms of unstable frequencies, histograms of unstable real parts—Case of a CEA computation for a $\text{Beta}_{5,5}$ law (**a**), of using the hybrid surrogate model for a $\text{Beta}_{5,5}$ law (**b**), a $\text{Beta}_{2,8}$ law (**c**) and a $\text{Beta}_{8,2}$ law (**d**)

beta law 3 are spread over larger intervals than the two other laws. For example, by considering frequencies, the $\text{Beta}_{2,8}$ distribution points out a peak at 58 rad/s while the $\text{Beta}_{5,5}$ distribution reveals two peaks at 62 rad/s and 72 rad/s and $\text{Beta}_{8,2}$ presents two peaks around 48 rad/s and 72 rad/s corresponding to the frequencies of the two unstable modes. Otherwise, the impact of the friction law on the stability analysis is non-negligible. Indeed, when for the first Beta law the system is stable 30% of the time, it is almost-surely unstable for the other cases. All these results point out the high sensitivity of the results of the stability analysis of mechanical systems subjected to friction induced vibration toward the probability density functions governing system parameters. These are needed to be accurately identified.

2.5 Conclusion

This study presents a new hybrid meta-model dedicated to the prediction of friction-induced instabilities. The proposed predictor is constructed from the associating of the general polynomial chaos expansion together with the kriging meta-model. Its main interest is related to its capacity to take into account of uncertain parameter defined by different models. The feasibility of the proposed hybrid surrogate model has been shown while its efficiency has been shown to be promising for applications involving squeal prediction under uncertainty. Otherwise, the taking into account of the uncertainty related to the probability density functions describing random parameters, in the stability analysis is carried out.

References

1. Nechak, L., Gillot, F., Besset, S., Sinou, J.-J.: Sensitivity analysis and Kriging based models for robust stability analysis of brake systems. Mech. Res. Commun. **69**, 136–145 (2015)
2. Denimal, E., Nechak, L., Sinou, J.-J., Nacivet, S.: Kriging surrogate models for predicting the complex eigenvalues of mechanical systems subjected to friction-induced vibration. Shock. Vib. **2016**, 1–22 (2016)
3. Nobari, A., Ouyang, H., Bannister, P.: Uncertainty quantification of squeal instability via surrogate modelling. Mech. Syst. Signal Process. **60**, 887–908 (2015)
4. Sarrouy, E., Dessombz, O., Sinou, J.-J.: Piecewise polynomial chaos expansion with application to brake squeal of a linear brake system. J. Sound Vib. **332**, 577–594 (2013)
5. Hulten, J.: Friction phenomena related to drum brake squeal instabilities. In: ASME Design Eng. Tech. Conf. 16th Biennal Conf; Mech. Vib. & Noise (1997)
6. Hulten, J.: Brake Squeal—A Self-Exciting Mechanism with Constant Friction. Technical Report, SAE Technical Paper (1993)
7. Sinou, J.-J., Jezequel, L.: Mode coupling instability in friction-induces vibrations and its dependency on system parameters including damping. Eur. J. Mech. A Solids. **27**, 106–122 (2007)
8. Sinou, J.-J.: Transient non-linear dynamic analysis of automotive disc brake squeal—on the need to consider both stability and non-linear analysis. Mech. Res. Commun. **37**(1), 96–105 (2010)
9. Lophaven, S., Nielsen, H., Sondergaard, J.: Dace—A Matlab Kriging Toolbox. Technical Report, Technical University of Denmark (2002)
10. Kleijnen, J.: Kriging metamodeling in simulation: a review. Eur. J. Oper. Res. **192**, 707–716 (2009)
11. Sacks, J., Welch, W., Mitchell, T., Wynn, H.: Design and analysis of computer experiments. Stat. Sci. **4**(4), 409–423 (1989)
12. Wiener, N.: The homogeneous chaos. Am. J. Math. **60**(4), 897 (1938)
13. Xiu, D., Karniadakis, G.: Modeling uncertainty in flow simulations via generalized polynomial chaos. J. Comput. Phys. **187**(1), 137–167 (2003)
14. Sudret, B.: Global sensitivity analysis using polynomial chaos expansions. Reliab. Eng. Syst. Saf. **93**, 964–979 (2008)

Chapter 3
Multi-Objective Parametric Optimization of an Equilibrator Mechanism

Ergin Kurtulmus

Abstract In order to eliminate the moment unbalance of rotary systems, a certain type of equilibrator mechanism which is able to perfectly balance is utilized. It includes helical spring(s), a pulley and a cable attached to a certain hinge point on the rotary body. Actual implementations of the mechanism may not allow realization of the conditions for perfect balancing. Then, the problem is transformed into a multi objective constrained optimization, which includes multiple parameters and multiple objectives like minimizing the residual moment unbalance, minimizing the diameter and the length of the spring(s), maximizing the spring fatigue life as well necessity to satisfy some geometrical layout constraints and operational constraints on the springs. The system has been modeled in a quasi-static manner and optimized parametrically around the regions of operation. Pareto optimal fronts have been determined and the optimized parameters have been used as design parameters for realization of the actual system. The design of the mechanism has been algorithmically automated based on the requirements and constraints.

Keywords Moment unbalance • Nonlinear systems • Optimization • Pareto optimality • Pareto fronts

3.1 Introduction

Moment unbalance is a major engineering issue in civil and especially military applications. It is mainly due to the fact that the location of the center of mass (CM) of a rotating system is not on the axis of rotation. This excess moment needs to be eliminated for many practical purposes such as to decrease the load on the actuation system or to increase the overall control system performance [1]. The concept is briefly illustrated in Fig. 3.1 below.

The amount of moment unbalance for the state described in Fig. 3.1 is given simply by

$$|M_{unb}| = m_{unb} g CM_x \tag{3.1}$$

where, m_{unb} is the total mass of the rotary system, g is the gravitational acceleration and CM_x is the x-coordinate of the CM. When the rotary structure is rotated or elevated around the axis of rotation by α in the counter clockwise direction, the CM changes its location accordingly and the Eq. (3.1) takes the form

$$|M_{unb}| = m_{unb} g r \cos(\lambda + \alpha) \tag{3.2}$$

where

$$\begin{aligned} r &= \sqrt{{CM_x}^2 + {CM_y}^2} \\ \lambda &= a\tan 2\left(CM_y, CM_x\right) \end{aligned} \tag{3.3}$$

and where CM_y is the y-coordinate of the CM. One way to perfectly balance this system is utilize an equilibrator mechanism where a spring loaded cable is attached to the rotor at the hinge point and supported at a pivot point. The concept is discussed in [2].

E. Kurtulmus (✉)
FNSS Savunma Sistemleri A.Ş., 06830 Ankara, Turkey
e-mail: erginkurtulmus@gmail.com

N. Dervilis (ed.), *Special Topics in Structural Dynamics, Volume 6*, Conference Proceedings
of the Society for Experimental Mechanics Series, DOI 10.1007/978-3-319-53841-9_3

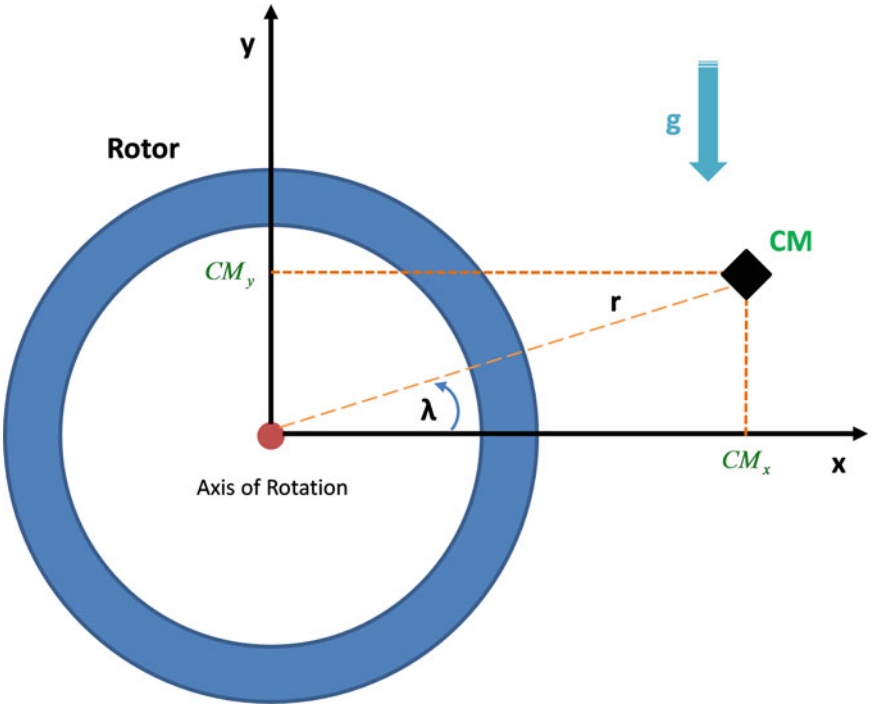

Fig. 3.1 Moment unbalance of a generic rotary structure at $\alpha = 0$

3.2 Modelling of the System

3.2.1 Equilibrator System Components

The major system components of the equilibrator mechanism are as follows;

- Compression Springs contained in housing
- Pivot point (usually it is a pulley in actual applications)
- Hinge Point (mechanically attached to the rotary structure)
- Cable for transmission of the equilibrator force

These components are schematically illustrated in Fig. 3.2 below

Basically, the cable loaded by the springs is wrapped around a pulley which is located at a fixed pivot point. The springs are housed in a container which is also fixed to the ground. The force induced on the cable by the spring is transmitted through the hinge point which is mechanically fixed to rotor structure. The force applied at the hinge point creates a moment in the counterclockwise direction and balances the moment created by CM of the rotary structure, which acts in the clockwise direction.

3.2.2 System Variables

The system described in Fig. 3.2 is schematized geometrically and kinematically in Fig. 3.3.

The variables depicted in Fig. 3.3 above can be briefly described as follows:

λ: The angle between the position vector of the CM of rotary mass and x-axis in counter clockwise (CCW) direction
α: Angle of elevation of the rotatory system measured from its initial configuration (0°) in CCW direction
θ: Orientation of the position vector of the CM measured from the x-axis in CCW direction at α
γ: The angle between the position vector of the CM and the position vector of the Hinge Point (H)
β: The angle between the position vector of the Hinge Point (H) and the position vector of the Pivot Point (P) in CCW direction

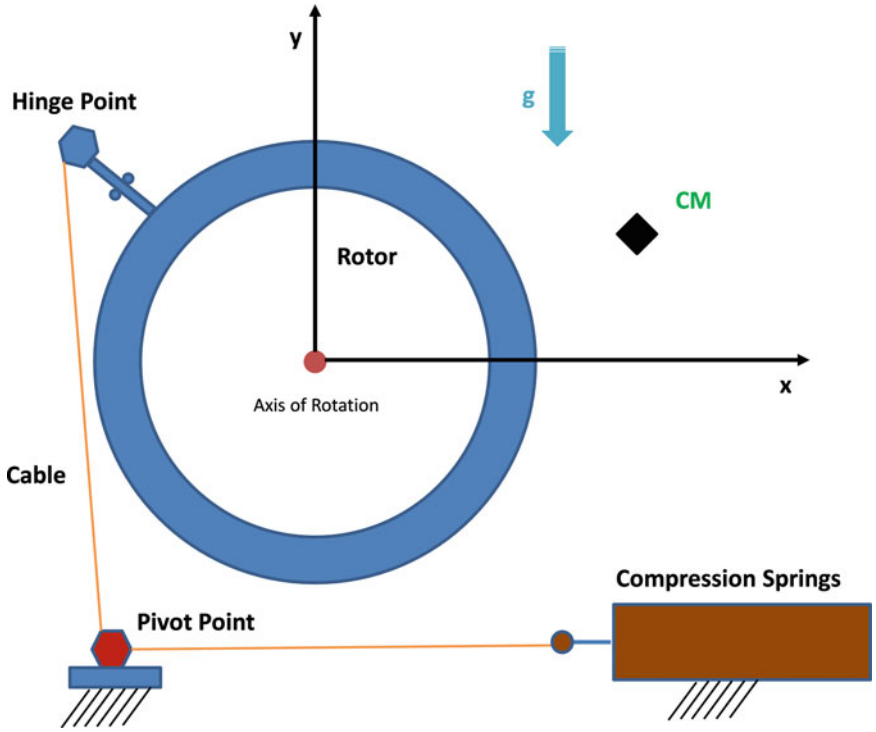

Fig. 3.2 Schematic illustration of equilibrator mechanism

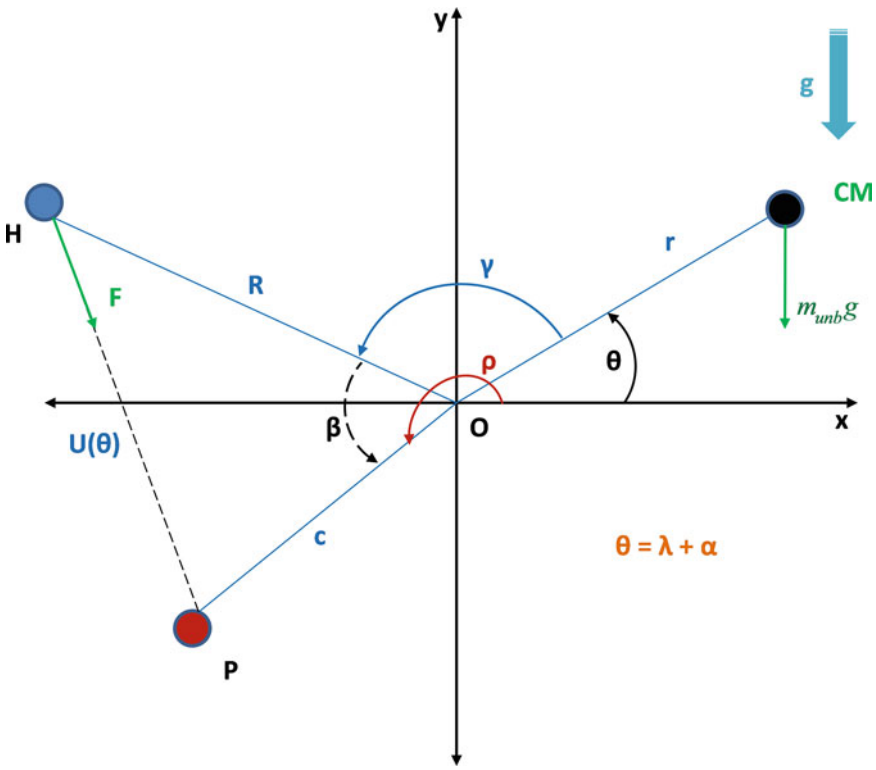

Fig. 3.3 Kinematic and geometric variables of the system

r: The magnitude of the position vector of CM and it is defined in Eq. (3.3)
R: The magnitude of the position vector of Hinge Point (H)
c: The magnitude of the position vector of Pivot Point (P)
U(θ): The distance between the point H to the point P as a function of θ
F: The magnitude of the force applied by the equilibrator cable to the rotary structure at the Hinge Point (H) in the direction of the vector **HP**

The variables which define the overall layout of the equilibrator mechanism above can be classified into the design parameters, the system parameters, the independent variables and the dependent variables. From mechanical point of view, the rotary system is assumed to be free to attain any elevation angle between some defined limits, i.e., $\alpha \in [\alpha_{min}, \alpha_{max}]$. This automatically makes α the independent variable. Since the m_{unb}, r and λ are the properties of the rotary system to be balanced, they are considered to be the system parameters. Observing Figs. 3.2 and 3.3, it is seen that the parameters **γ**, β, R, c are properties of the equilibrator mechanism layout yet to be designed. Thus, they are considered to be the design parameters. Since U(**θ**) is the distance between the points H and P, and the F is defined by the mechanism layout and the springs, they are the dependent variables of the system.

A typical compression spring and its housing depicted in Fig. 3.2 is also a part of the system and its detailed illustration is given in Fig. 3.4 below.

In this system, the spring force F is applied to the compression spring contained in the housing by a retainer at one end, while the other end of the spring is supported and fixed. Here, due to some space limitations, the spring housing is constrained by the maximum allowable length L_{alw} and maximum allowable diameter D_{alw}. On the other hand, the spring itself has its own parameters and properties which must be taken into account during the design of the overall system.

Parameters related with spring and force F applied to the spring is depicted in Fig. 3.5 below

Spring parameters, its properties and their relation to each other in terms of strength, performance and mechanical behavior are explained and can be found in [3]. The ones taken into consideration and related with our system are explained briefly in this study as follows. The spring stiffness or the spring rate k is defined as

$$k = \frac{d^4 G}{8D^3 n_a} \tag{3.4}$$

where d is wire diameter, D is the mean diameter, G is the shear modulus of the spring material and n_a is the active number of coils and for the squared and ground compression springs is given by

$$n_a = n_t - 2 \tag{3.5}$$

and n_t is the total number coils in the spring. The solid length of the spring L_s is given as

$$L_s = (n_t - 0.75)\, d \tag{3.6}$$

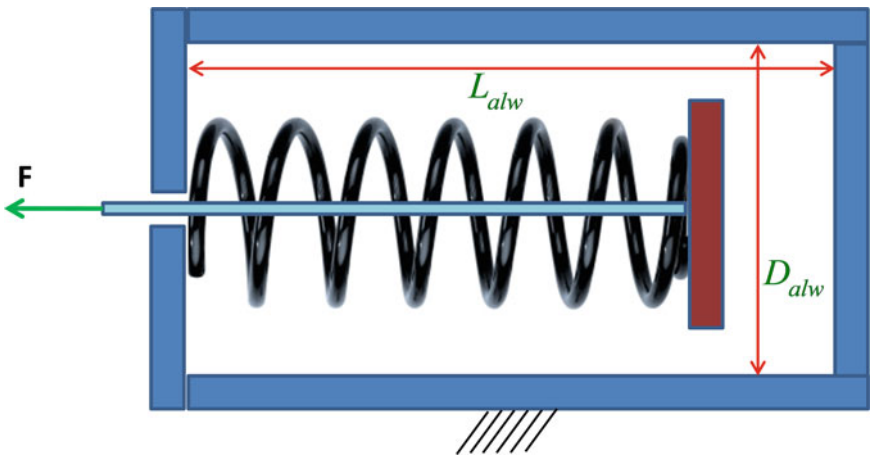

Fig. 3.4 Compression spring, its housing and spring force representation

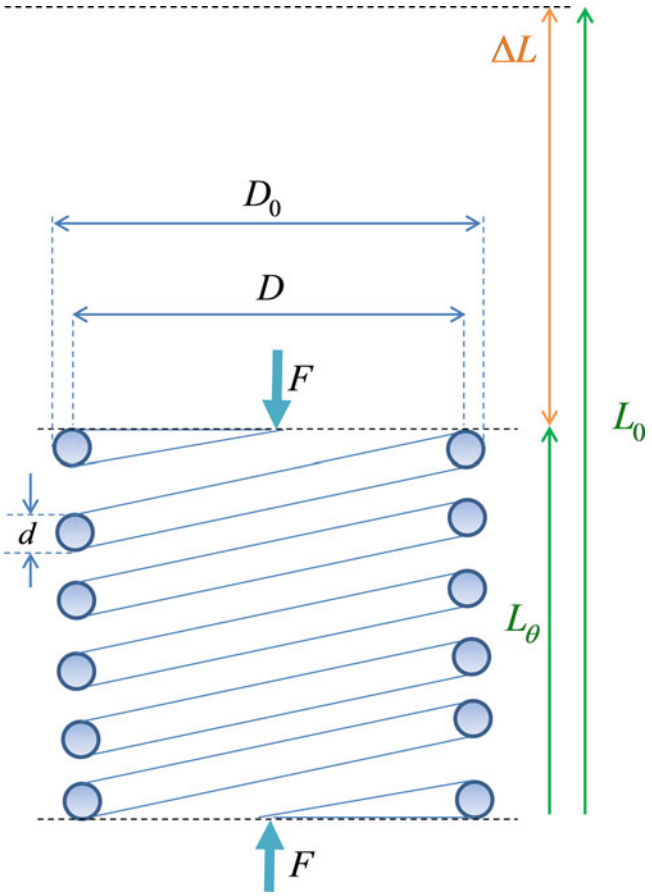

Fig. 3.5 Spring parameters and the spring force F

The critical shear stress in the spring is given by

$$\tau = K_w \frac{8FD}{\pi d^3} \tag{3.7}$$

where K_w is the Wahl factor and is given by

$$K_w = \frac{4C-1}{4C-4} + \frac{0.615}{C} \tag{3.8}$$

and C is the spring index and given by

$$C = \frac{D}{d} \tag{3.9}$$

For squared and ground steel springs, free length must satisfy the following relation in order avoid buckling [3]

$$L_0 \leq 5.26D \tag{3.10}$$

The maximum allowable torsional yield stress S_{sy} is given in [3, 4]as a widely accepted and conservative relation

$$S_{sy} = \tau_{alw} = 0.56S_{ut} \tag{3.11}$$

where S_{ut} is the ultimate tensile strength of the material. Also the first fundamental frequency of the spring is [3]

$$\omega = \frac{1}{2}\sqrt{\frac{k}{m_s}} \tag{3.12}$$

where m_s is the mass of the spring and is given by

$$m_s = \frac{\pi^2 d^2 D n_a \rho}{4} \tag{3.13}$$

where ρ is the density of the spring material.

3.2.3 Balance Equations of the System

Observing Figs. 3.2 and 3.3, the static balance equation of the overall system is

$$\overrightarrow{M}_{eq} + \overrightarrow{M}_{unb} = 0 \tag{3.14}$$

where $\overrightarrow{M}_{eq}$ is the moment vector created by the equilibrator force F around the axis of rotation and $\overrightarrow{M}_{unb}$ is the moment vector created by the CM and they are given as

$$\overrightarrow{M}_{eq} = \left(R\cos(\theta+\gamma)\,\hat{i} + R\sin(\theta+\gamma)\hat{j}\right) \otimes \overrightarrow{F} \tag{3.15}$$

and

$$M_{unb} = \left(r\cos(\theta)\,\hat{i} + r\sin(\theta)\hat{j}\right) \otimes \left(-m_{unb}g\hat{j}\right) = -m_{unb}gr\cos(\theta)\,\hat{k} \tag{3.16}$$

If we let $\overrightarrow{f}$ be the vector pointing from the point H to point P, then it is given by

$$\overrightarrow{f} = \left[(c\cos(\theta+\gamma+\beta) - R\cos(\theta+\gamma))\,\hat{i} + (c\sin(\theta+\gamma+\beta) - R\sin(\theta+\gamma))\hat{j}\right] \tag{3.17}$$

The magnitude of $\overrightarrow{f}$, which equals U(θ), is given by

$$\left|\overrightarrow{f}\right| = U(\theta) = \left[[c\cos(\theta+\gamma+\beta) - R\cos(\theta+\gamma)]^2 + [c\sin(\theta+\gamma+\beta) - R\sin(\theta+\gamma)]^2\right]^{1/2} \tag{3.18}$$

Then the spring force $\overrightarrow{F}$ with magnitude F is given by

$$\overrightarrow{F} = \frac{F\left[[c\cos(\theta+\gamma+\beta) - R\cos(\theta+\gamma)]\,\hat{i} + [c\sin(\theta+\gamma+\beta) - R\sin(\theta+\gamma)]\hat{j}\right]}{\left|\overrightarrow{f}\right|} \tag{3.19}$$

Then $\overrightarrow{M}_{eq}$ becomes

$$\overrightarrow{M}_{eq} = \left[R\cos(\theta+\gamma)\,\hat{i} + R\sin(\theta+\gamma)\hat{j}\right] \otimes \frac{F\left[[c\cos(\theta+\gamma+\beta) - R\cos(\theta+\gamma)]\,\hat{i} + [c\sin(\theta+\gamma+\beta) - R\sin(\theta+\gamma)]\hat{j}\right]}{\left|\overrightarrow{f}\right|} \tag{3.20}$$

After carrying out the cross product multiplication we obtain

$$\overrightarrow{M}_{eq} = \frac{cFR\left[\sin\left(\theta+\gamma+\beta\right)\cos\left(\theta+\gamma\right)-\cos\left(\theta+\gamma+\beta\right)\sin\left(\theta+\gamma\right)\right]\hat{k}}{\left|\overrightarrow{f}\right|} \tag{3.21}$$

Since the nominator of Eq. (3.21) is a trigonometric identity, we obtain

$$\overrightarrow{M}_{eq} = \frac{cF\left(\theta\right)R\sin\left(\beta\right)}{\left|\overrightarrow{f}\right|}\hat{k} \tag{3.22}$$

The overall moment balance equation becomes

$$\overrightarrow{M}_{res} = \overrightarrow{M}_{eq} + \overrightarrow{M}_{unb} = \frac{cF\left(\theta\right)R\sin\left(\beta\right)}{\left|\overrightarrow{f}\right|}\hat{k} - m_{unb}gr\cos\left(\theta\right)\hat{k} = \left[\frac{cF\left(\theta\right)R\sin\left(\beta\right)}{\left|\overrightarrow{f}\right|} - m_{unb}gr\cos\left(\theta\right)\right]\hat{k} = 0 \tag{3.23}$$

where $\overrightarrow{M}_{res}$ is the residual moment. In order for this equation to hold independent of θ, the relation sin(β) = cos(θ) must hold. This means

$$\theta + \beta = 90^{\circ} \tag{3.24}$$

which is the same result obtained in [2].

If Eq. (3.24) holds, it implies

$$F\left(\beta,\gamma\right) = \frac{m_{unb}gr}{Rc}\left|\overrightarrow{f}\right| = \frac{m_{unb}gr}{Rc}U\left(\beta,\gamma\right) \tag{3.25}$$

Since

$$F\left(\beta_2,\gamma_2\right) - F\left(\beta_1,\gamma_1\right) = \frac{m_{unb}gr}{Rc}\left[U\left(\beta_2,\gamma_2\right) - U\left(\beta_1,\gamma_1\right)\right] = k_s\Delta L\left(\beta\right) \tag{3.26}$$

The Eq. (3.26) implies that in order for the equilibrator system to perfectly balance, the stiffness of the spring k must satisfy the equation

$$k = \frac{m_{unb}gr}{Rc} \tag{3.27}$$

If Eqs. (3.24) and (3.27) are satisfied then the system is perfectly balanced. However, in actual implementations there may be constraints which prevent the designer from satisfying these equations. In these cases, an optimization process must be employed in order to minimize $\overrightarrow{M}_{res}$ and at the same time, some other possible objective functions while satisfying the system constraints.

3.3 Optimization of the System

Equations (3.24) and (3.27) cannot be satisfied at all times in actual systems due to some geometrical constraints in the layout depicted in Fig. 3.3 or due to some other constraints related with the spring parameters. For this reason, the problem should be stated quantitatively as an optimization problem.

3.3.1 Constraints and Objective Function of the Optimization Problem

Equation (3.24) can be satisfied is the sum of system parameter λ and the design parameter β is made 90° since

$$\lambda + \beta = 90^0 \rightarrow \theta + \beta = 90^0 \forall \alpha \tag{3.28}$$

However, depending on the value of λ, β may not attain the value 90°−λ. On the other hand, the maximum total length of the spring or springs employed in the housing cannot exceed L_{alw} or the outer diameter D_0 of the spring should be lower than D_{alw}. Also the factor of safety at solid length should be higher than 1.2 [3]. The spring(s) ideally should operate on some portion of its available stroke for the validity of assumption of linear behavior. Also there can be some constraints on the layout design parameters $\boldsymbol{\gamma}$, β, R, c. The overall constraints on the system can be expressed as

$$\begin{aligned}
&1) L_{\max} \leq L_{alw} \\
&2) D_O \leq D_{alw} \\
&3) \tfrac{1}{8} F_s \leq F \leq \tfrac{7}{8} F_s \\
&4) \gamma \in [\gamma_{\min}, \gamma_{\max}] \\
&5) \beta \in [\beta_{\min}, \beta_{\max}] \\
&6) R \in [R_{\min}, R_{\max}] \\
&7) c \in [c_{\min}, c_{\max}] \\
&8) L_{\min} \geq 0.02 n_a (D + d) + L_s \\
&9) L_0 \leq 5.26 D
\end{aligned} \tag{3.29}$$

where eighth constraint it is due to [5]. There are many approaches in the literature to estimate the fatigue life of a spring. In this study, we use a parametric life estimation formula as expressed in [6]

$$Life = e^{\left[\frac{1}{y} \ln\left(\frac{K_E}{K_C}\right)\right]} \tag{3.30}$$

where

$$\begin{aligned}
K_E &= \frac{K_U (K_{S2} - K_{S1})}{2K_U - (K_{S2} + K_{S1})} \\
K_{S1} &= \frac{\tau_{\min}}{S_{ut}} \\
K_{S2} &= \frac{\tau_{\max}}{S_{ut}}
\end{aligned} \tag{3.31}$$

It is evident that, the total system is composed two subsystems interacting with each other via the force F. The first one is the equilibration mechanism layout which is governed by Eqs. (3.18) and (3.23). The second is the compression spring(s) whose internal state is governed by Eqs. (3.4)–(3.12). Also, since for α > 0, $U(\theta) < U(\lambda)$and $L(\lambda) < L(\theta)$, we know that the spring force F(θ) is

$$F(\theta) = F(\lambda) + [U(\theta) - U(\lambda)] k \tag{3.32}$$

and at the same time

$$F(\theta) = F(\lambda) + [L(\lambda) - L(\theta)] k \tag{3.33}$$

which means the two subsystems are coupled through the relation

$$L(\theta) = -U(\theta) + L(\lambda) + U(\lambda) = -U(\theta) + \left(L_0 - \frac{F(\lambda)}{k}\right) + U(\lambda) \tag{3.34}$$

It is natural to require $\overrightarrow{M}_{res}$ to be zero at zero elevation angle $\alpha = 0$, which means that $\theta = \lambda$. Then solving for F(λ) in Eq. (3.23), we obtain

$$F(\lambda) = \frac{m_{unb} g r \cos(\lambda)}{cR \sin(\beta)} U(\lambda) \tag{3.35}$$

Also we know that,

$$L_0 = L_{\max} + \frac{F(\theta_{\max})}{k} \tag{3.36}$$

where $L_{\max} = L(\theta_{\max})$. Substituting the Eq. (3.35) into the Eq. (3.32), and then substituting the Eq. (3.32) into the Eq. (3.36) yields

$$L_0 = L_{\max} + \frac{F(\lambda)}{k} + U(\theta_{\max}) - U(\lambda) \tag{3.37}$$

Substituting the Eq. (3.37) into the Eq. (3.34) yields,

$$L(\theta) = -U(\theta) + L_{\max} + U(\theta_{\max}) \tag{3.38}$$

where U(θ) was given by Eq. (3.18). The Eq. (3.38) is actually expected and it could directly be derived from the Eqs. (3.32) and (3.33). Thus, if the design parameters for the layout **γ**, **β**, **R, c** and the design parameters of the spring **D, n_t, L_{max}** along with the coupler design parameter **k** are selected, then the rest of the variables in the system are completely defined. The two subsystems are interacting with each other through the force F and hence the spring constant k.

Moreover, the total system state defined in the design parameter $x = [R, \gamma, \beta, c, k, D, n_t, L_{\max}] \in \mathbb{R}^8$ for $\theta \in [\theta_{\min}, \theta_{\max}]$ shall should be optimized according to some performance measure(s) which is related with both the layout and the spring, while obeying the constraints. We define the performance measure related with the layout as

$$J_1 = RMS\left(\overrightarrow{M}_{res}\right) = \sqrt{\frac{1}{\theta_{\max} - \theta_{\min}} \int_{\theta_{\min}}^{\theta_{\max}} \left[\frac{cF(\theta) R \sin(\beta)}{U(\theta)} - m_{unb} g r \cos(\theta)\right]^2 d\theta} \tag{3.39}$$

One ideally would desire to minimize J_1, since it is root mean square of the residual moments over the operational range $\theta_{\min} \le \theta \le \theta_{\max}$ of the system. On the other hand, the performance measure related with the spring is

$$J_2 = -a_1 \ln(Life) - a_2 \omega + a_3 n_s \tag{3.40}$$

where a_n's are the weighting coefficients and n_s is the load factor (reciprocal of safety factor) at the solid length L_s and it is defined by

$$n_s = \frac{K_w 8 F_s D}{\pi d^3 S_{sy}} \tag{3.41}$$

Then J_2 becomes

$$J_2 = -a_1 e^{\left[\frac{1}{y} \ln\left(\frac{K_E}{K_C}\right)\right]} - a_2 \frac{d}{2\pi n_a D^2} \sqrt{\frac{G}{2\rho}} + a_3 \frac{\pi d^3 S_{sy}}{K_w 8 F_s D} \tag{3.42}$$

One ideally would desire to minimize J_2 in order to maximize the operational life, the natural frequency and the static safety factor of the spring. The natural frequency of a spring should be as high as possible in order to avoid resonance with the operational frequency of the applied force F. If Eq. (3.42) is observed, it is obvious that there should already be some trade-offs in selection of design parameters in order to maximize J_2.

Thus the overall optimization problem can described as follows

$$\begin{aligned} &\textit{minimize } \langle J = b_1 J_1 + b_2 J_2 \rangle \\ &\textit{subject to } \langle \textit{constra}\text{ints given by inequalities (29)} \rangle \\ &\textit{for } \theta_{\min} \leq \theta \leq \theta_{\max} \end{aligned} \tag{3.43}$$

where b_n's are the weighting coefficients.

3.3.2 Solution Approach

Solution to the problem defined by (3.43) has been implemented in Python programming language. First, the system has been mathematically modeled and has been optimized by the SLSQP (Sequential Least Square Programming) routine [7]. The solution approach to the problem has been schematized in Fig. 3.6 below.

As shown Fig. 3.6, the optimal solution is being searched in the search space (state space) defined by $x = [R, \gamma, \beta, c, k, D, n_t, L_{\max}] \in \mathbb{R}^8$ for $\theta \in [\theta_{\min}, \theta_{\max}]$. The state x is optimized according to the measure defined in (3.43) and the successful termination of the optimization algorithm yields the optimal state $x^* = [R^*, \gamma^*, \beta^*, c^*, k^*, D^*, n_t{}^*, L_{\max}{}^*]$.

The selection of the weighting coefficients a_1, a_2, a_3, b_1 and b_2 is somewhat dependent on the specific application and may be subjective to some extent.

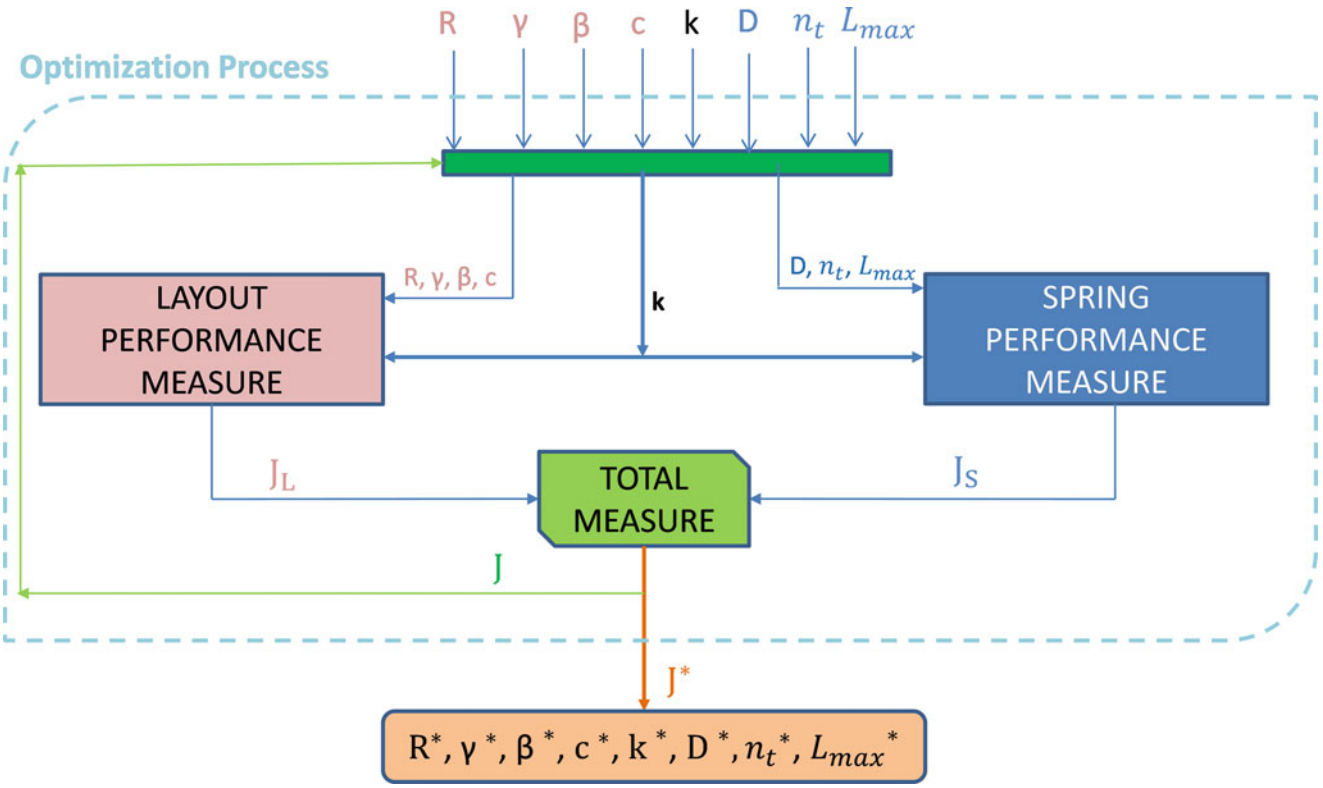

Fig. 3.6 Diagram of the implemented optimization procedure

3.4 Optimal Solution and Results

Since the problem described by (3.43) is a multiobjective constrained optimization problem, a trade-off must be made between J_1 and J_2. As in any other multiobjective optimization, it is vital to determine the pareto optimal front of the system. Pareto optimality is an important concept in engineering and science. A state is pareto optimal if there is no other state which decreases (in the case of minimization) one of the relevant measurues (J_2 and $-J_1$ in our case) without increasing at least one of the rest. The set of all points which are pareto optimal is called the pareto front [8]. In this study, the pareto front(s) are determined for the specific system variables and weighting coefficients, then optimimum solutions have been obtained for two extreme operating conditions.

3.4.1 System Parameters and the Constraints for a Specific Case

The rotary system has $\mathbf{m_{unb} = 350\ kg}$, with $\mathbf{CM_x = 180\ mm}$ and $\mathbf{CM_y = 5\ mm}$, which makes $\boldsymbol{\lambda = 1.591°}$. The rotary system is assumed to elevate in the range $-10^{\circ} \leq \alpha \leq 45^{\circ}$. Limits of the search space are given in Table 3.1 below.

The material properties (chrome silicon steel) of the spring are assumed to be G = 80,000 MPa, S_{ut} = 1875 MPa, ρ = 7800 kg/m^3. The spring wire material is assumed to be hot coiled, shot peened and set removed while the spring is squared and ground. The coefficients for the given material conditions are given in Table 3.2 below [6].

By considering the specific requirements of our implementation of the equilibrator mechanism, the weighting coefficients of the total system measure J are determined by trial and error and are given in Table 3.3.

The values in Table 3.3 are subjective and may acquire different values depending on the preferences and priorities.

3.4.2 Pareto Optimal Solutions and Pareto Fronts

Before proceeding to the optimal solution(s) it is quite beneficial to obtain the pareto fronts of the system in order to grasp the solution space in $x = [R, \gamma, \beta, c, k, D, n_t, L_{\max}] \in \mathbb{R}^8$ for $\theta \in [\theta_{\min}, \theta_{\max}]$in a qualitative manner. In order to obtain the pareto fronts, Monte Carlo simulations have been performed by randomly sampling states $x = [R, \gamma, \beta, c, k, D, n_t, L_{\max}]$ from the regions defined in Table 3.1, except for the design variable β.

Four independent Monte Carlo simulations have been performed where design variable β is restricted to four different regions for the each simulation. These four regions are given in Table 3.4 below.

The results of the simulations are given in Figs. 3.7, 3.8, 3.9, and 3.10 below

Table 3.1 Limits of the search space for optimization

	R (mm)	γ (Deg)	β (Deg)	c (mm)	k (N/m)	D (mm)	n_t	L_{max}
Range	[300, 360]	[90, 210]	[40, 95]	[350, 550]	[3000, 5000]	[45, 71.5]	[23, 43]	[450, 635]

Table 3.2 Values used for the inequality constraints

	K_U	y	K_C
Value	0.74	−0.13	1.808

Table 3.3 Weighting coefficients of the total system measure J

	a_1	a_2	a_3	b_1	b_2
Value	0.04	0.10	45	15.5	80

Table 3.4 Selected regions for β

	β (Region-1)	β (Region-2)	β (Region-3)	β (Region-4)
Range	[85°, 95°]	[70°, 80°]	[55°, 65°]	[40°, 50°]

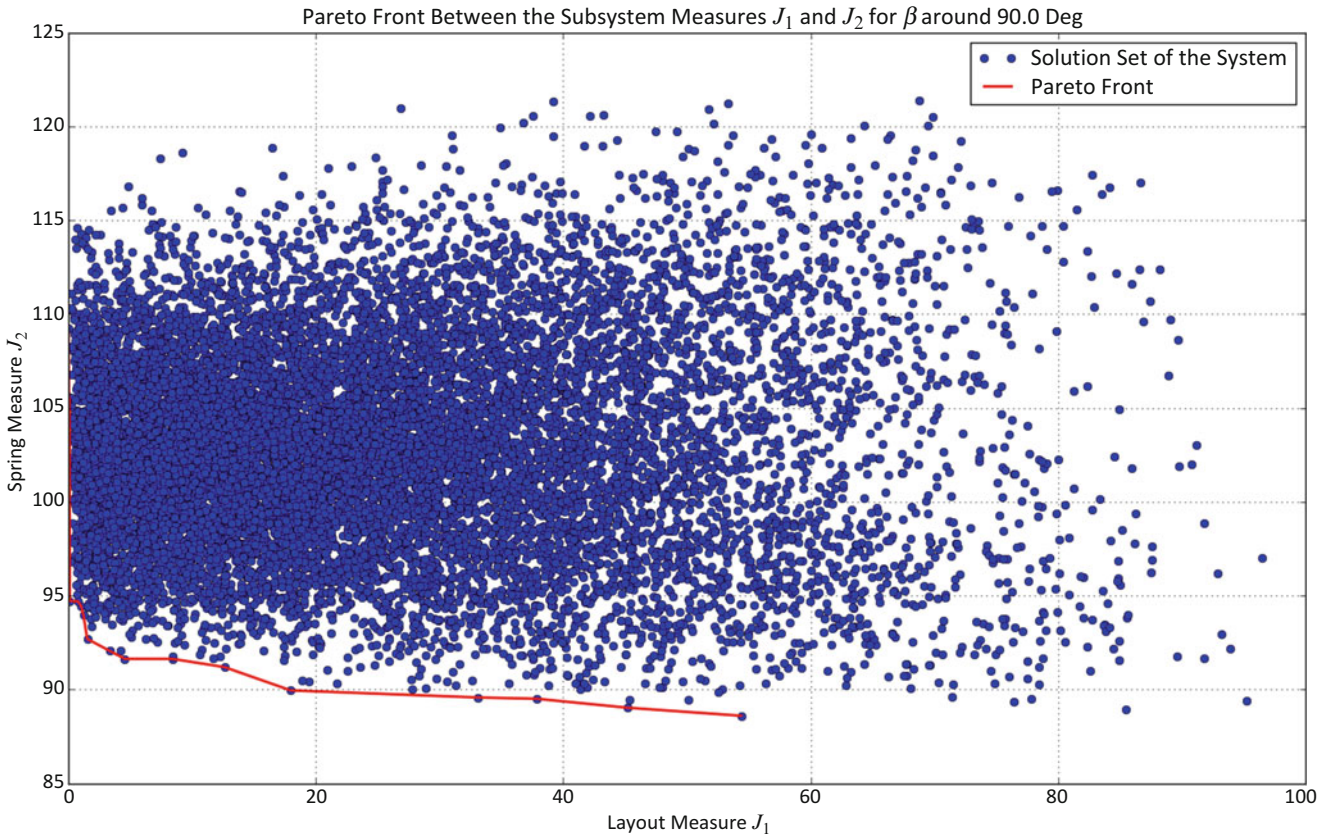

Fig. 3.7 Pareto front for the region-1

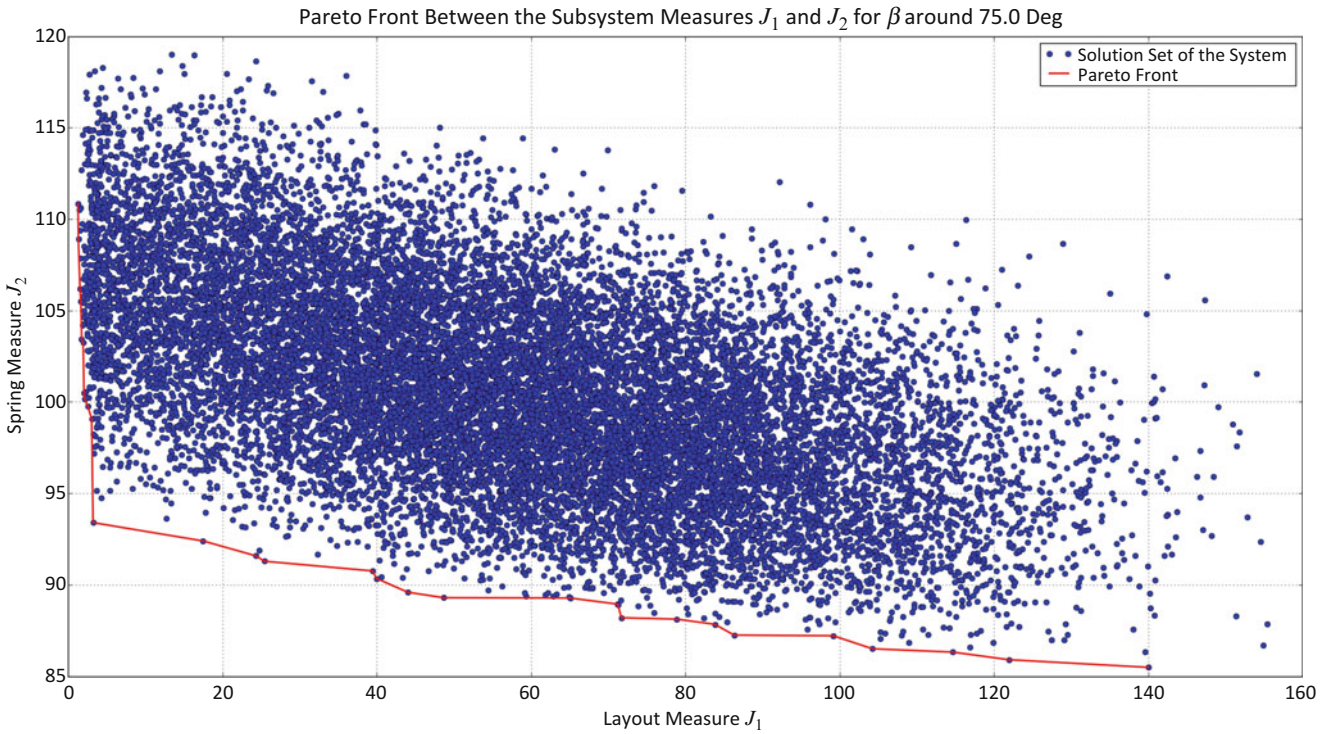

Fig. 3.8 Pareto front for the region-2

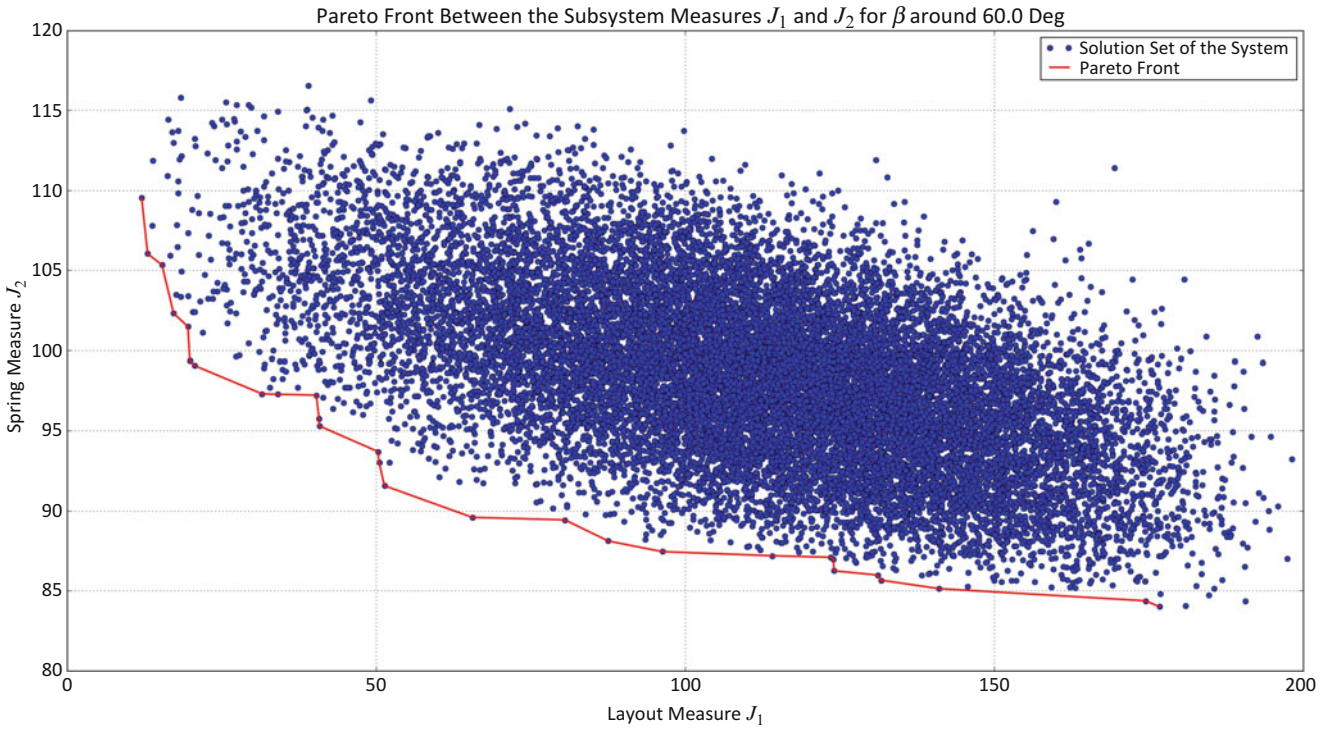

Fig. 3.9 Pareto front for the region-3

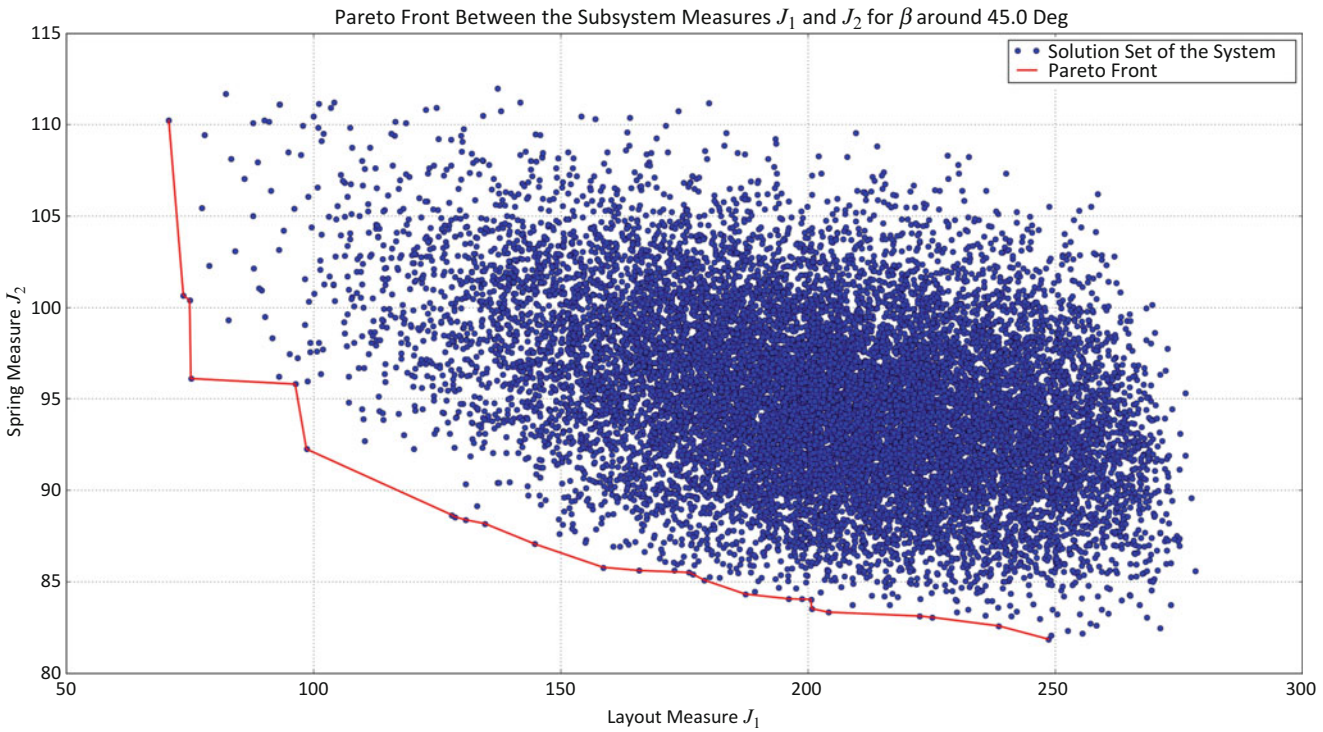

Fig. 3.10 Pareto front for the region-4

The blue dots in the figures Figs. 3.7, 3.8, 3.9, and 3.10 above represent the J_1 and J_2 values for a given state randomly sampled from the search space given Table 3.1. Pareto optimality, in our case, is between J_1 and J_2 and the red curves on the plots represent the pareto front. We know that, since $\boldsymbol{\lambda} = 1.59°$, when β is around 90°, the perfect equilibration condition dictated by the Eq. (3.28) is achievable. This result is confirmed by the solution set and the pareto front depicted in Fig. 3.7 above. We observe that, when β is around 90°, the layout measure J_1 is approaching to zero which means perfect equilibration. However, when we gradually decrease β, it becomes harder to achieve a good moment balance. In any case, depending on the constraints on β and the value of λ (system specific), any optimal solution should lie on the pareto curve.

3.4.3 Optimal Solution

Using the parameters given in Tables 3.1, 3.2, and 3.3, and by following the process depicted in Fig. 3.6, the optimal solution x^* is obtained as $x^* = [R^*, \gamma^*, \beta^*, c^*, k^*, D^*, n_t{}^*, L_{\max}{}^*]$ = **[341.99, 145.36, 88.41, 350.0, 5163.42, 71.5, 34.43, 635]** for the region-1. The corresponding values of $\mathbf{J_1}$ **and** $\mathbf{J_2}$ **are** $\mathbf{5 \times 10^{-6}}$ **and 92.39** respectively. The relevant spring and layout characteristics are shown in Figs. 3.11 and 3.12 below. It is evident that, the equilibration is perfect and the optimization solution is on the red curve in Fig. 3.7, as expected. It is simply because β^* is satisfying the Eq. (3.28) and k^* is satisfying the Eq. (3.27).

If we assume now, that we are constrained to operate in the region-4, the optimal solution becomes $x^* = [R^*, \gamma^*, \beta^*, c^*, k^*, D^*, n_t{}^*, L_{\max}{}^*]$ = **[313.43, 145.66, 50.00, 350.0, 3982.09, 71.5, 34.43, 635]**. The values of $\mathbf{J_1}$ **and** $\mathbf{J_2}$ **are 50.42 and 99.31** respectively. The relevant spring and layout characteristics are shown in Figs. 3.13 and 3.14 below. This situation now is drastically different from the previous case, since the equilibration is not perfect anymore. However, the optimal solution is still on the red curve in Fig. 3.10, as expected. It should be noted that, of the constraints listed in Eq. (3.29), the ninth one was, which is related with the buckling condition, the most difficult to satisfy. This necessitated using three springs connected in series in the equilibrator housing. Thus, it made possible shorter spring free length L_0. This modification simply resulted in springs with $k = 3k^*$, $n_t = n_t^*/3$ and $L_0 = L_0^*$ which is clearly visible in Figs. 3.11 and 3.13 below. However this modification does not cause any violation of the constraints since this has been taken into account in the optimization procedure.

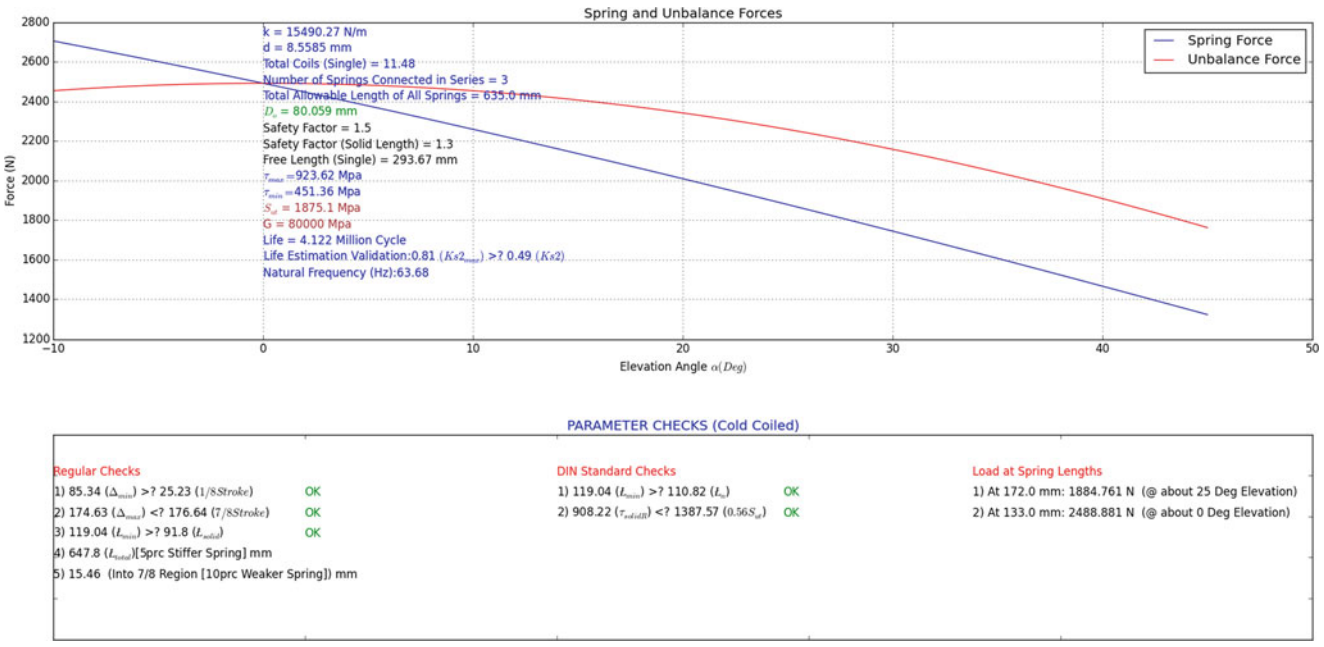

Fig. 3.11 Spring characteristics for optimization in the region-1

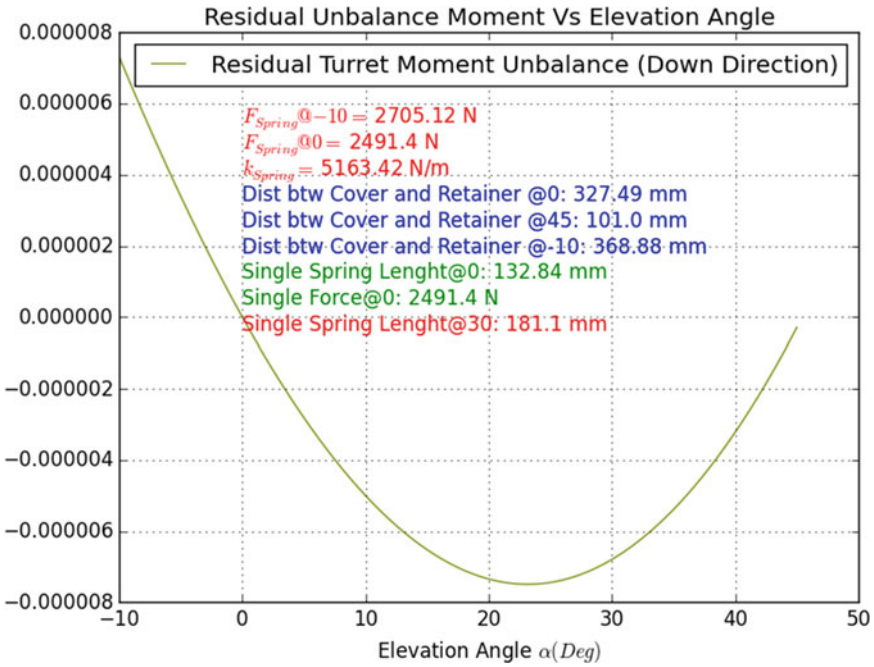

Fig. 3.12 Layout characteristics for optimization in the region-1

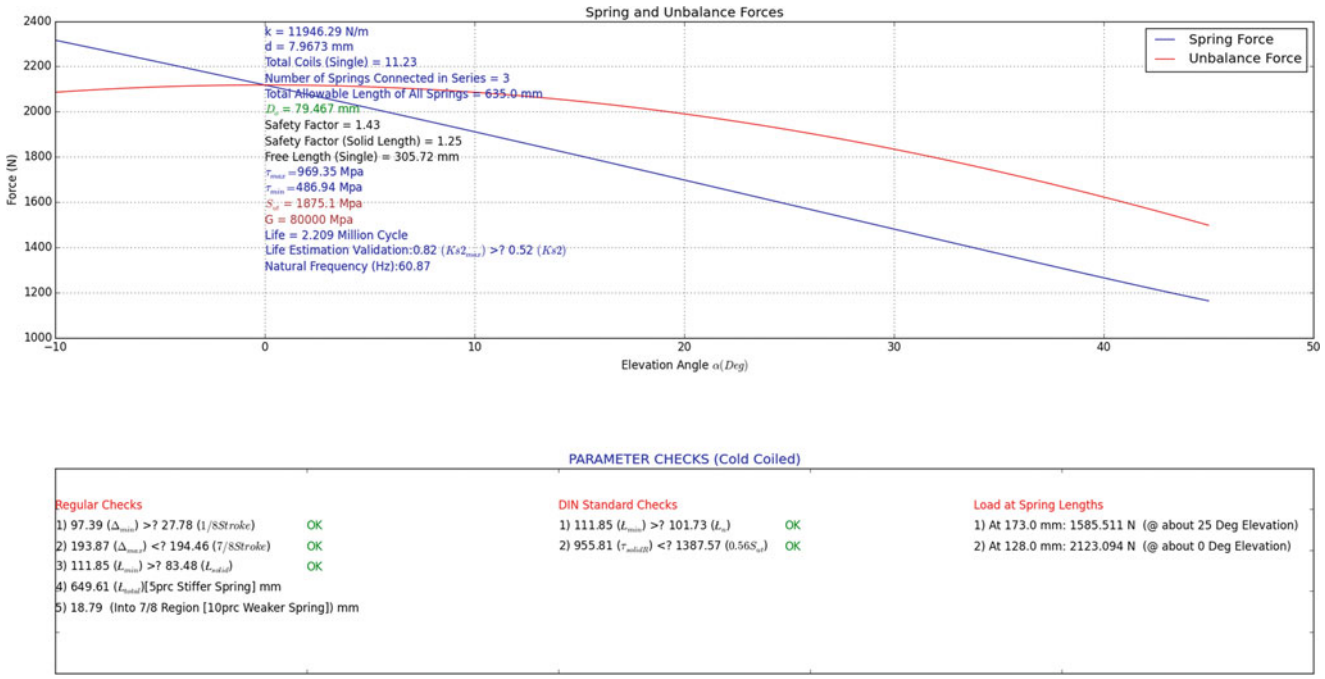

Fig. 3.13 Spring characteristics for optimization in the region-4

3.5 Conclusion

In this study, an equilibrator mechanism which is able to perfectly balance a rotary system has been mathematically modeled. The system is composed of two subsystems which are coupled to each other through the spring force which is acting on both of them. If some conditions are satisfied it is theoretically possible to attain the perfect balance for the system. However, in real world applications it may not be possible to satisfy these conditions at all times. What is more, there are different, independent and conflicting performance measures related with these two subsystems. Often times, there must be a trade-

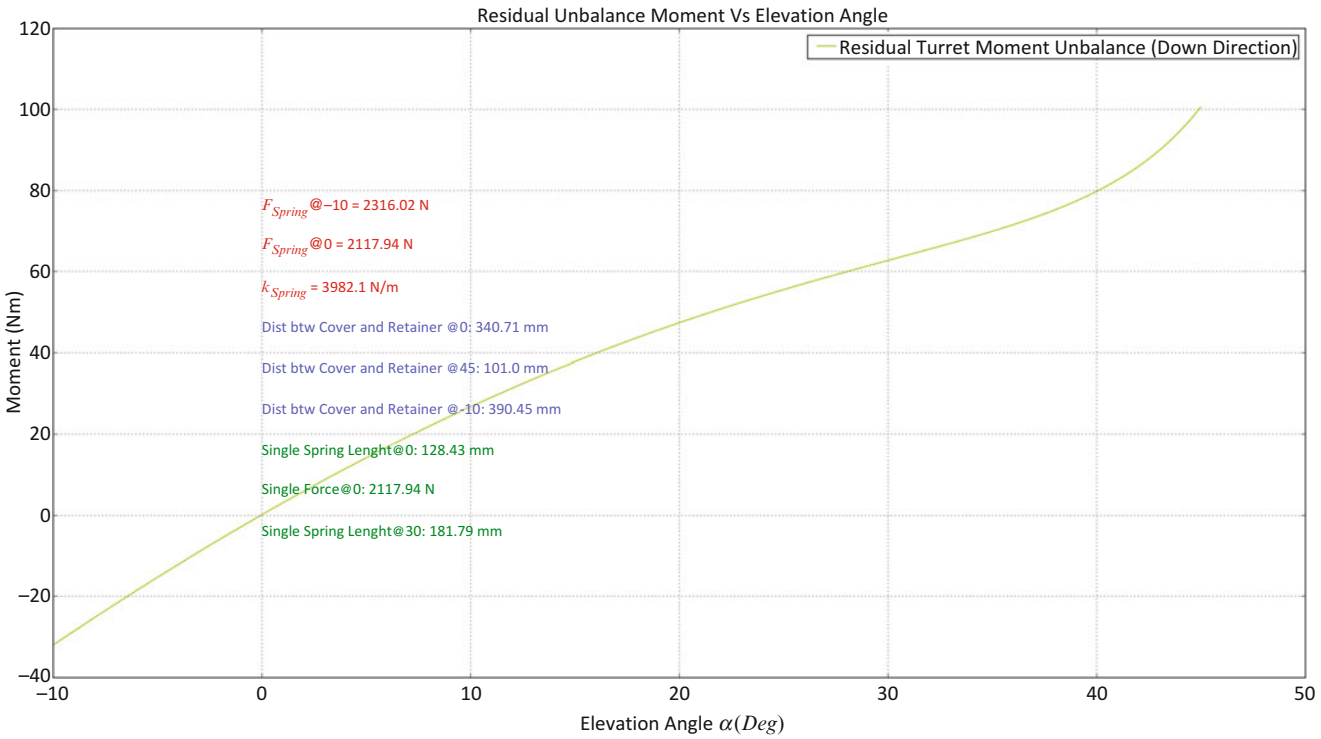

Fig. 3.14 Layout characteristics for optimization in the region-4

off analysis between the conflicting measures. Concepts of pareto optimality and pareto fronts are beneficial in terms of exploring the search space of the design parameters in quantitative manner. On that account, the problem has been converted to a multi objective constrained optimization problem. The pareto states and the pareto fronts of the system have been identified for different regions of operation by using Monte Carlo simulations. Then, the optimization problem has been solved in two extreme operating regions. Stark differences between these two extremes have been observed in terms of the subsystem measures J_1 and J_2. As expected, it has been confirmed that the optimized states of the system lies on the pareto front curves for the relevant regions operation. A systematic and algorithmic method has been developed and implemented for the optimized design of an equilibrator system. As a further study, dynamical effects can be taken into consideration when the elevation is performed with a significant amount of acceleration.

References

1. Kurtulmus, E., Arikan, S.: Cam geometry generation and optimization for torsion bar systems. In: Nonlinear Dynamics, vol. 1, pp. 459–471. Springer International Publishing (2016)
2. Engineering Design Handbook Equilibrators. US Army Materiel Command, Washington, DC (1970)
3. Budynas, R., Nisbett, J.: Shigley's Mechanical Engineering Design, 8th edn. McGraw-Hill, New York (2006)
4. Solecki, R., Conant, R.J.: Advanced Mechanics of Materials. Oxford University Press (2003)
5. DIN, E. 13906-1. Cylindrical helical spring made from round wire and bars-Calculation and design Part, 1
6. Spring Design Manual, 2nd edn. Society of Automotive Engineers, Warrendale (1996)
7. Python Scipy v0.13.0 [Online]. Available: https://docs.scipy.org/doc/scipy-0.13.0/reference/generated/scipy.optimize.fmin_slsqp.html
8. Miettinen, K.: Nonlinear Multiobjective Optimization. Springer Science (2012)

Chapter 4
Development of a Numerical Model for Dynamic Analysis of a Built-Up Structure by a Two-Step FEM-Test Correlation Approach

Vignesh Jayakumar and Jay Kim

Abstract A finite element method (FEM) model of a lightly damped built-up structure was developed based on a two-step approach. The approach utilizes the fact that damping changes natural frequencies very little but the resonance amplitudes significantly. In the first step, stiffness property of the model is refined by correlating natural frequencies obtained from test and FEM model while neglecting the effect of damping. In the second step, damping properties are identified by matching the resonance amplitudes of the system obtained from the FEM model with those obtained from measurement. As a demonstration, the approach was applied first to a simple cantilevered beam structure, then a simplified vane assembly structure clamped into a fixture. The two-step approach was applied to the vane assembly in the free-free configuration, then the assembly clamped in a cantilever form. It was shown that the proper boundary condition of the FEM model can be identified by adjusting the contact stiffness at the clamped edge. Various different damping models were adopted to identify the damping property of the model. It was shown that different models lead to slightly different forced responses of the system. Typical applications and limitations of the correlated model are discussed with some practical examples.

Keywords Damping modeling • FEM-Test correlation • Boundary condition modeling • Spatial distribution of damping • Modeling of composite structure

Abbreviations

FRF	Frequency Response Function
MAC	Modal Assurance Criterion
MIMO	Multiple Input Multiple Output

4.1 Introduction

Finite Element Analysis (FEA) can save development cost and time of a mechanical system by enabling numerical prototyping if an accurate model can be built. In structural applications, accurate modeling entails capturing accurately the mass, stiffness and damping characteristics of the system through steps of model updating. Model updating is an essential part of this process and numerous methods are found in literature [1]. Modeling errors usually lead to significant errors in simulation results as a consequence [2]. One of the most difficult parts in building a FE model is in accurately capturing the boundary conditions in many cases. One example of such a case is modeling a vane segment in its assembled state on a compressor casing. Vane segments are inserted into slots provided on the compressor casing. Figure 4.1 [3] highlights a cross-sectional view of the stator assemblies used in compressors. [4] provides a comprehensive description of strategies currently adopted for design and simulation of such systems. Stress analysis and fatigue life studies are downstream analysis tasks that will heavily depend on correct development of a FE model. Considerable testing effort and expense can be saved if a relatively accurate FEA model is available. Such a model will also provide accurate feedback to design team at a very early stage in development.

The purpose of this study is to establish a procedure to develop an accurate FEA model of a built-up structure mounted in a clamped condition, specifically a vane segment in the stator assemblies in a compressor or other turbo machines.

V. Jayakumar (✉) • J. Kim
Department of Mechanical and Materials Engineering, University of Cincinnati, Cincinnati, OH 45221-0072, USA
e-mail: jayakuvh@mail.uc.edu

N. Dervilis (ed.), *Special Topics in Structural Dynamics, Volume 6*, Conference Proceedings
of the Society for Experimental Mechanics Series, DOI 10.1007/978-3-319-53841-9_4

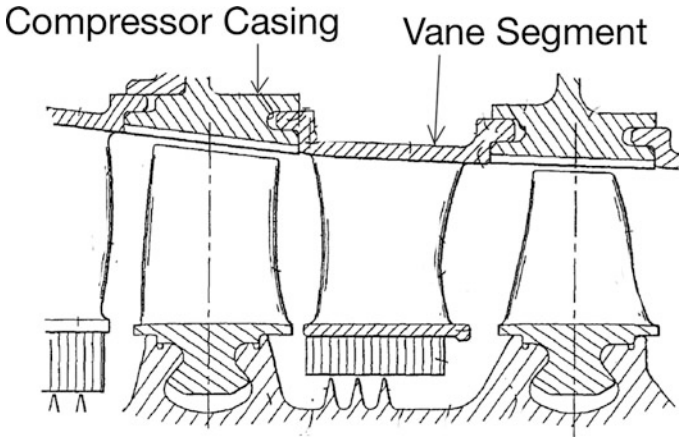

Fig. 4.1 Vane assembly in compressors—cross section view [3]

For this purpose, a built-up structure that resembles a vane segment with a much simpler geometry was designed and built. The proposed procedure to build the FE model of the vane assemblies installed is carried out in two phases. First the numerical model is updated for stiffness characteristics while ignoring the damping in the system. The natural frequencies of the simulation model are matched with the frequencies of the test model based on the fact that the effect of the damping on the natural frequencies of lightly damped structure is negligible. In the second stage, the damping parameters of the simulation model are identified by matching the response amplitudes at the resonant frequencies. The proposed methodology is highlighted as a flow chart in Fig. 4.2. The method is demonstrated by implementation on two different structures. The stiffness modeling approach employed to capture accurately the boundary conditions is demonstrated using a simple aluminum beam structure that's fixed at one end. Subsequently the method is implemented on a more complex system that resembles a vane segment. The built up structure is a simplified vane segment that is correlated for boundary stiffness first before modeling damping into the system.

4.2 FE-Test Correlation Approach

4.2.1 Free-Free Correlation

FEM-Test correlation activity for the built up structure starts with correlating a free-free model to the test results. This can be achieved through geometry correlation, mass correlation and elasticity correlation. Geometry correlation can be obtained by ensuring that the solid model being used in the FE analysis accurately represents the physical model being tested. Once this is achieved the density of the material is varied to ensure that the mass of the physical model and the simulation model match. Once this has been achieved, the Young's modulus of the system material is varied until the natural frequencies from testing and simulation can be matched in the frequency range of interest. In addition, the model may have to be further revised to reflect the effects of welds, nuts and bolts etc. in the structure if any. This part of the approach is fairly well studied and documented already. It helps to calibrate the mass, and material stiffness of the FE model being developed and has been shown to be capable of predicting variations in system characteristics due to small mass or stiffness additions to the system [5]. However, this approach alone is not sufficient when it comes to being able to account for the boundary conditions of the system when in a clamped state.

4.2.2 Clamped Condition Correlation

The condition of the clamped boundary of an assembled structure is always difficulty to model in FEM analysis. As a demonstration of the proposed approach, a simple cantilever aluminum beam is considered. The dimension of the beam is (0.35 m long, 0.03 m wide and 0.003 m thick). Figure 4.5 shows the beam in test. Table 4.1 compares the natural frequencies

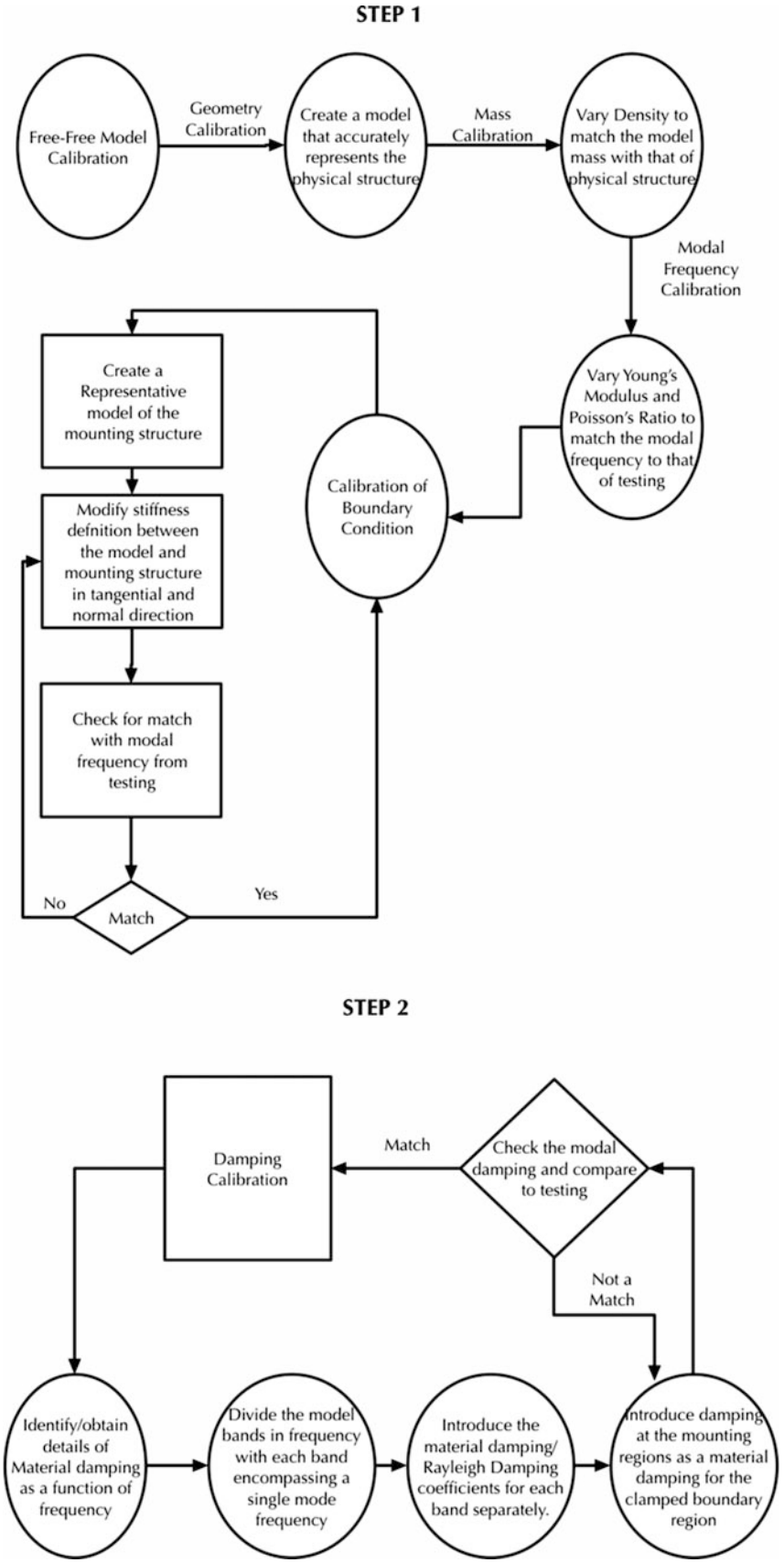

Fig. 4.2 Flow diagram of the two-step approach for development of FE model

Table 4.1 Comparison of fixed-free boundary condition and adjusted stiffness boundary condition in simulation

Mode number	Measured frequency (Hz)	Mode description	Frequency (Hz)—FE results with fixed free condition	Percentage difference (%) of FE from experimental
1	18.08	First bending transverse	22.204	22.81
2	103.43	First bending sideways	218.98	113
3	114.99	Second bending transverse	139.11	21.0
4	320.82	Third bending transverse	389.71	21.47
5	412.96	First torsion	463.85	12.32

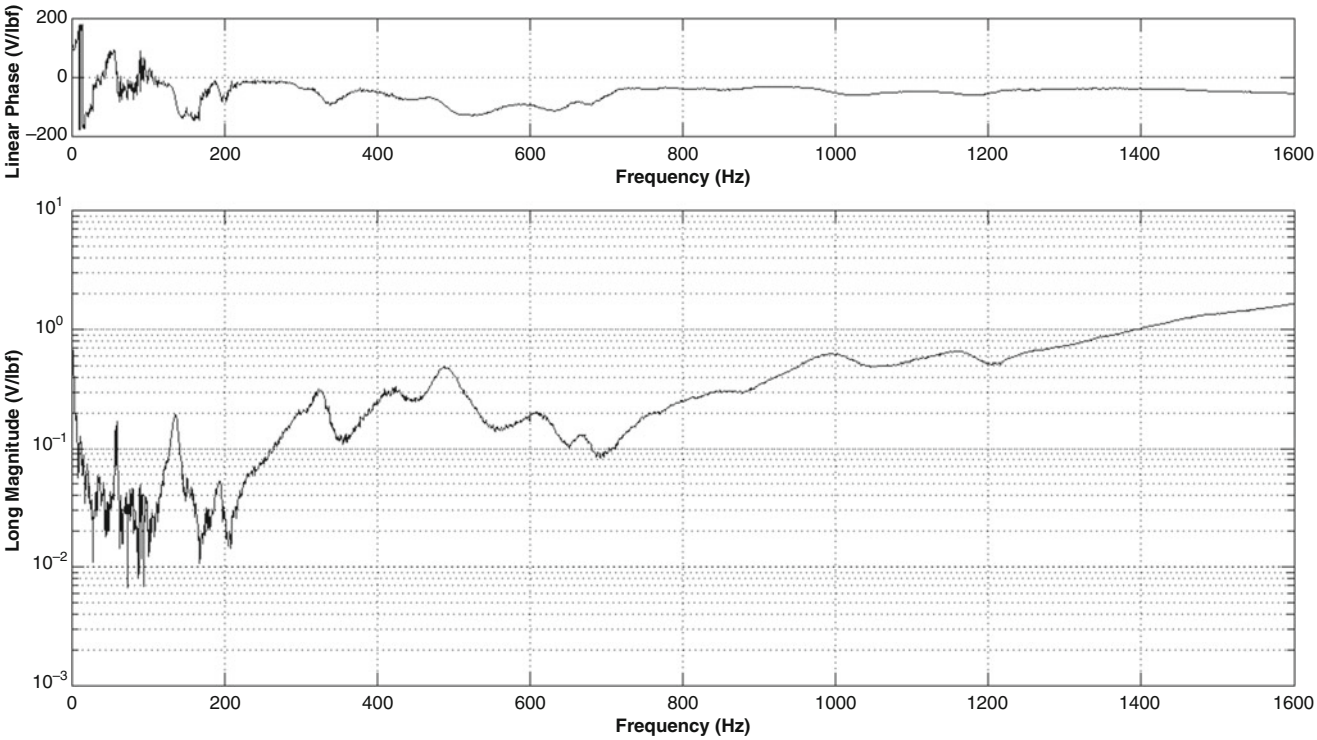

Fig. 4.3 Measured FRF between a point on the beam and a point on the mounting structure

and modes obtained from the FE model and test. No rotation or displacement was allowed at the boundary of the FEA model, that is a fully clamped condition.

It is seen that the difference between calculated and measured natural frequencies becomes lower at high frequency modes, which is expected, as the effect of boundary condition is less significant in higher mode. As the cross section of the beam has a small aspect ratio, the beam mode vibrating sideways is fairly low (103.43 Hz measured, 218.98 Hz calculated). A very large error in this mode indicates the clamping effect on the sideways bending of the beam is looser than that in vertical modes.

Figure 4.3 shows a driving point frequency response function (FRF) measured on the mounting structure. The mounting structure is seen to have several modes of its own in the range of interest, indicating that the clamping does not provide a true clamped condition.

Representation of clamped boundary condition has been studied by many investigators [6]. Also there have been several attempts to capture the stiffness characteristics of such boundary conditions via testing and correlation to reduced DOF mathematical models [7–9]. In this study a clamped boundary condition is described by the contact stiffness. Figure 4.4 shows the boundary definition between two structures in contact as defined in ANSYS. The contact stiffness between the two surfaces can be defined in the tangential and normal directions. This boundary stiffness can be adjusted to improve the match between the measured and calculated natural frequencies. Table 4.2 compares natural frequencies of the modes of the simulation model and test for the same cases shown in Table 4.1 when further adjustment was implemented using the contact stiffness. Frequencies are now in much better agreement.

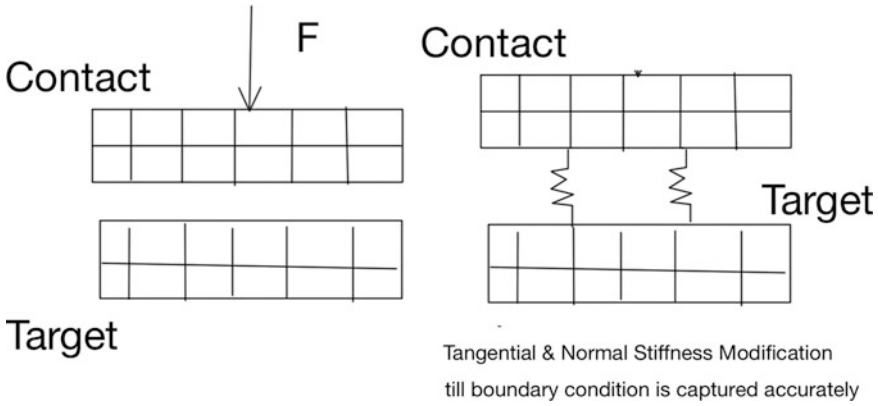

Fig. 4.4 Stiffness definition between contacts surfaces in ANSYS

Table 4.2 Comparison of modal testing estimates to FE modal estimates with an adjusted stiffness boundary condition in simulation

Measured frequency (Hz)	Frequency (Hz) from FEM with adjusted boundary stiffness	Percentage difference (%)	Mode description
18.08	18.063	0.09	Bending 1 transverse
103.43	109.02	5.40	Bending 1 sideways
114.99	117.14	1.87	Bending 2 transverse
320.82	335.14	4.46	Bending 3 transverse
412.96	445.35	7.84	Torsion 1

4.2.3 Damping Modeling

In lightly damped structures, damping affects little on natural frequencies, but significantly on the amplitudes of the resonances. Various approaches have been studied to make more accurate description of damping over the years [10, 11]. Most commercial FEA software offer a few options to model damping including viscous damping, Rayleigh proportional damping, structural damping as documented in [12]. These damping models are developed to describe not the underlying physics of the damping but the effect of the damping. Another difficulty in damping modeling comes from the fact that the signature of the damping is much smaller than that of the mass or stiffness.

4.3 Modeling of a Cantilever Beam

4.3.1 Measurement Setup

A small aluminum beam (350 mm × 30 mm × 3 mm) is shown in Fig. 4.5. The test setup includes a clamping structure used to clamp down the aluminum beam. 15 mm of one edge of the beam is inserted into the clamping structure and clamped down. The clamp is adjusted to two different levels of tightening and modal test are carried out to figure out the effect of the boundary clamping condition on the system characteristics. MIMO measurements were carried out using two accelerometers (nominal calibration values of 100 mV/g) and a small impact hammer (nominal calibration value of 5 mV/lbf). To avoid the high frequency overload issues, data was captured up to 4000 Hz by capturing data for 2 s. An average of three measurements was used to average out noise and to arrive at the FRF estimates corresponding to each point of impact.

4.3.2 Free-Free Correlation

The free-free tests were carried out first to estimate the modal frequency and correlate the FEM model. Table 4.3 shows the comparison of the Free-Free correlation study for the simple cantilevered beam. The mode shapes were observed to be the same as those obtained from testing.

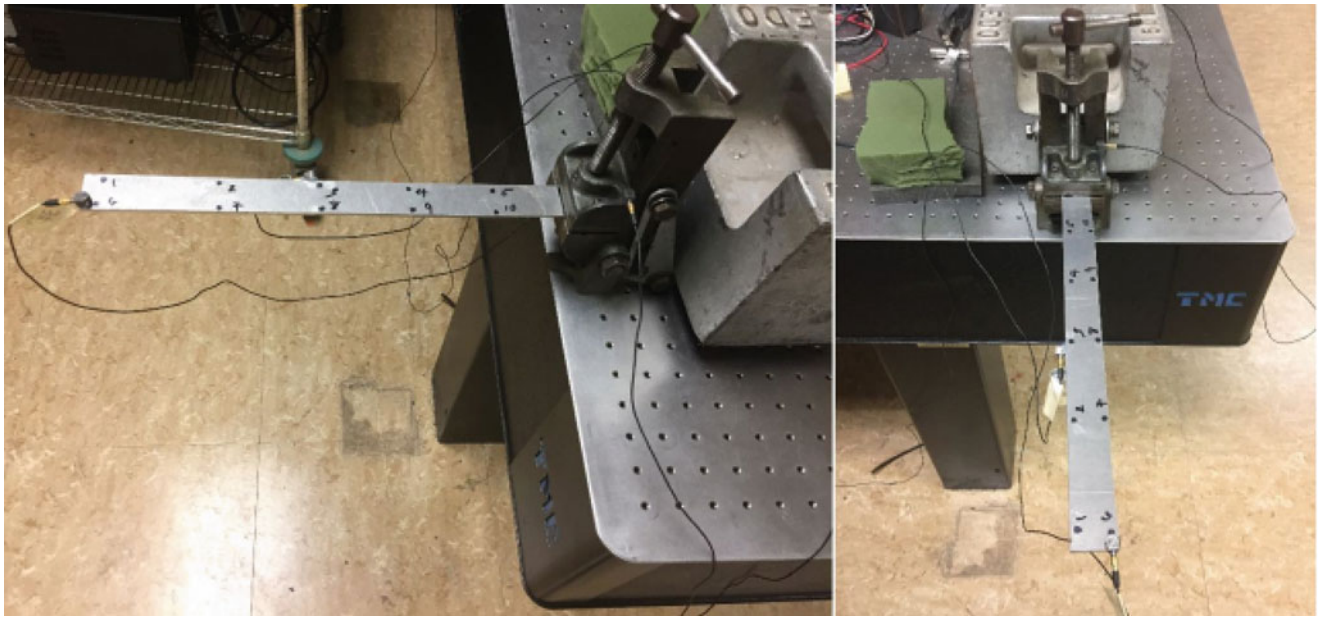

Fig. 4.5 Cantilever beam test setup

Table 4.3 Free-free modal frequency comparison between testing and simulation

	Measurement	FEM with free-free boundary		
Mode number	Frequency (Hz)	Frequency (Hz)	Percentage difference (%)	Mode description
1	126.81	128.54	1.37	1st bending
2	361.90	354.74	1.98	2nd bending
3	691.08	696.62	0.80	3rd bending
4	822.27	869.57	5.75	1st torsion
5	1144.10	1153.8	0.85	4th bending

Table 4.4 Cantilever beam modal frequency comparison between testing and simulation

Clamped boundary case #1			Clamped boundary case #2			
Measurement frequency (Hz)	FEM frequency (Hz)	Percentage difference (%)	Measured frequency (Hz)	FEM frequency (Hz)	Percentage difference (%)	Mode description
18.08	18.063	0.09	19.72	20.527	4.11	Bending 1 transverse
103.43	109.02	5.40	124.76	128.88	3.30	Bending 2 transverse
114.99	117.14	1.87	176.82	170.03	3.84	Bending 1 sideways
320.82	335.14	4.46	356.75	361.67	1.38	Bending 3 transverse
412.96	445.35	7.84	433.87	452.6	4.32	Torsion 1

4.3.3 Identification of Boundary Condition of the Clamped Beam

4.3.3.1 Boundary Stiffness

With the correlated free-free FE model, the boundary condition was identified. The test results from the two different clamping conditions studied are presented in Table 4.4. Then the stiffness of the contact elements at the clamped region was modified in an iterative manner to find the proper value of the contact stiffness. Table 4.4 compares natural frequencies obtained from the calibrated FE model and test, which shows very good agreements, within 5% for most modes within the frequency range of interest.

Table 4.5 Acoustic Modal results vs. Modal results with accelerometers for cantilever beam structure (free-free test) (same aluminum material used for building the simplified vane structure)

Acoustic		Accelerometer	
Frequency (Hz)	Modal damping (%)	Frequency (Hz)	Modal damping (%)
1165.11	0.03	1122.46	0.65
1742.47	0.14	1666.51	0.72
1835.00	0.03	1854.00	5.01
2435.65	0.06	2350.24	0.95
2743.54	0.07	2462.29	1.54

- Case 1 - Damping only at root (Material Damping) (Damping in the dark zone in the root of the beam)
- Case 2 - Damping over entire beam(Material Damping) (Damping in the dark zone and the white zone of the beam)
- Case 3 - Damping at the mounting structure (Material Damping) (Damping only in the hatched region)
- Case 4 - Damping as structural damping
- Case 5 - Damping as modal damping

Fig. 4.6 Approaches to include damping in the FEA model

4.3.3.2 Damping

The damping for the free-free structure was estimated to be very low. As the beam is fairly lightly damped even in the clamped condition, a non-contact acoustic modal testing was used [13] in addition to the conventional accelerometer testing. The results from the acoustic testing and a conventional modal test using accelerometers are compared in Table 4.5. Modal frequencies checked for damping estimates in this study start from higher modes because of difficulties in getting a good noise free measurement with microphones for lower frequency ranges. A force-expo window was used in the measurement to ensure a quick ring down and subsequently the damping estimates obtained were corrected for the use of the window.

It was determined that the damping of the cantilever beam can be modeled in five different ways after carefully studying available options in ANSYS. The different approaches are explained in Fig. 4.6. However, the challenge of modeling damping starts with the ability to accurately estimate damping from measurements. The measurements with accelerometers were seen to lead to inaccurate and high damping estimates and the acoustic modal measurements could not be used to obtain good noise free damping estimates in the frequency range of interest. However, once accurate damping estimates are obtained the damping correlation can be easily carried out in a piecewise manner in the frequency domain.

4.4 Modeling of the Simplified Vane Structure

4.4.1 Measurement Setup

Figure 4.7a shows the simplified vane assembly used in this study. The structure was made in parts using aluminum sheets with precise aluminum welding used to join the parts together. The structure was tested in free-free condition by placing it on foam material. The clamped condition for the vane structure was achieved by placing an edge between two heavy steel plates and clamping the two edges using C-clamps,

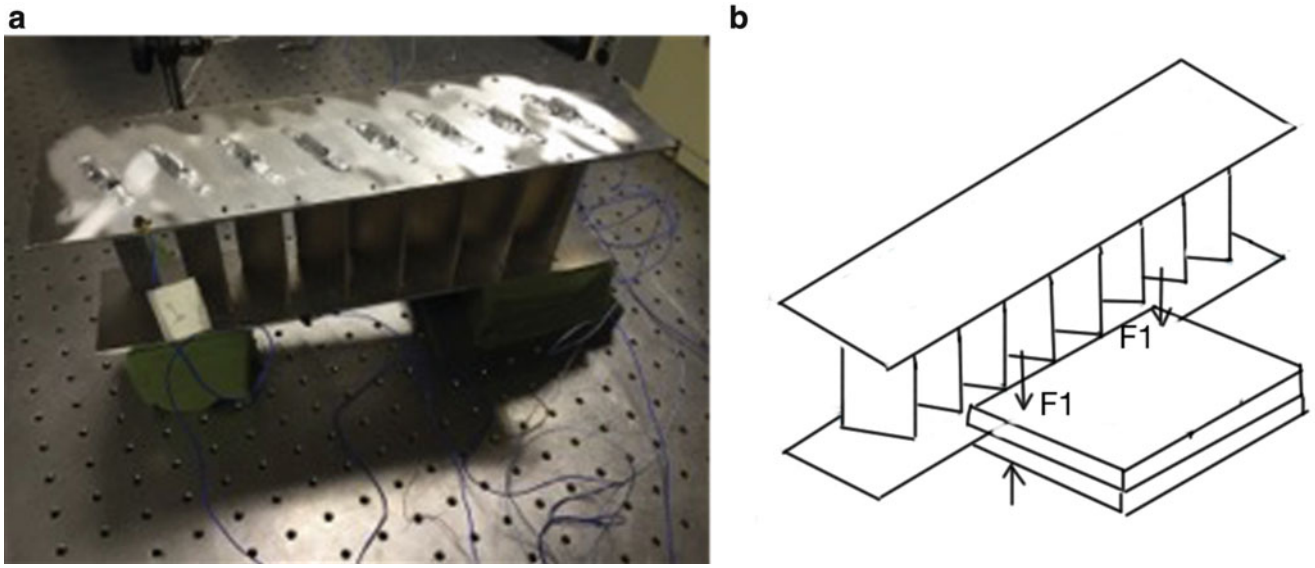

Fig. 4.7 (**a**) Simplified vane segment in free-free condition. (**b**) Simplified vane segment in clamped condition

Table 4.6 Modal frequency comparison for free-free testing and simulation

Mode number	Experimental frequency (Hz)	Simulation frequency (Hz)	Percentage difference (%)
1	192.32	196.67	2.26
2	318.42	314.67	1.18
3	340.37	337.69	0.79
4	535.35	526.39	1.67
5	710.25	695.40	2.09
6	810.50	796.61	1.71

Testing of the structure was carried out using impact hammers and small single axis accelerometers. A sampling frequency of 4000 Hz was used with 8000 Frequency lines. Force-expo window was used to ensure the signal died out in the time interval for which system was being observed. The very lightly damped aluminum structure provides a lot of ring down and care needs to be taken to avoid any issues of low signals, high frequency overload etc. and ensure a clean set of FRF measurements [14]. The lightly damped small built up structure also meant that the accelerometers and the cables contributed significantly to the damping estimations.

4.4.2 Free-Free Test and Correlation

Table 4.6 highlights the results after model correlation using the following approach for a simplified vane structure. Figure 4.8 shows the mode shapes obtained and Fig. 4.9 compares the FRF from the test and the simulation for a particular driving point on the structure.

Fairly good correlation is seen between the FE model and the test results in terms of stiffness characteristics. The experimental result includes the additional damping that the accelerometer and the cabling introduce into the system while the simulation results will not include these effects. The mode shapes were visually compared and confirmed to be similar for the two cases.

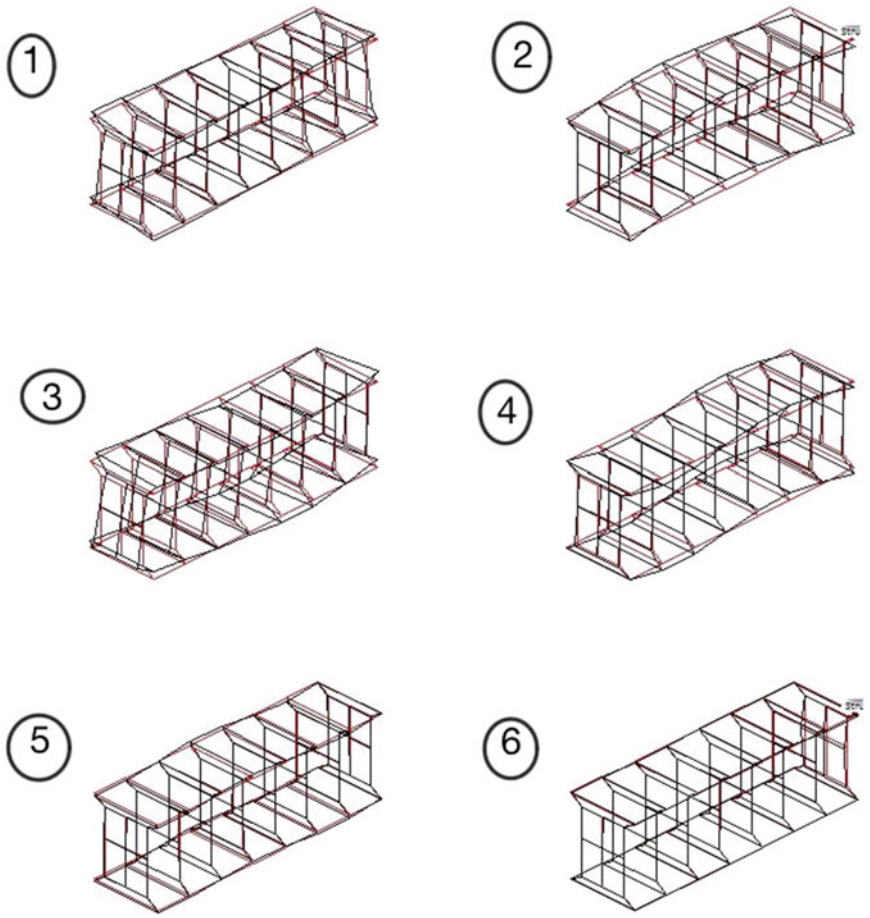

Fig. 4.8 Mode shapes

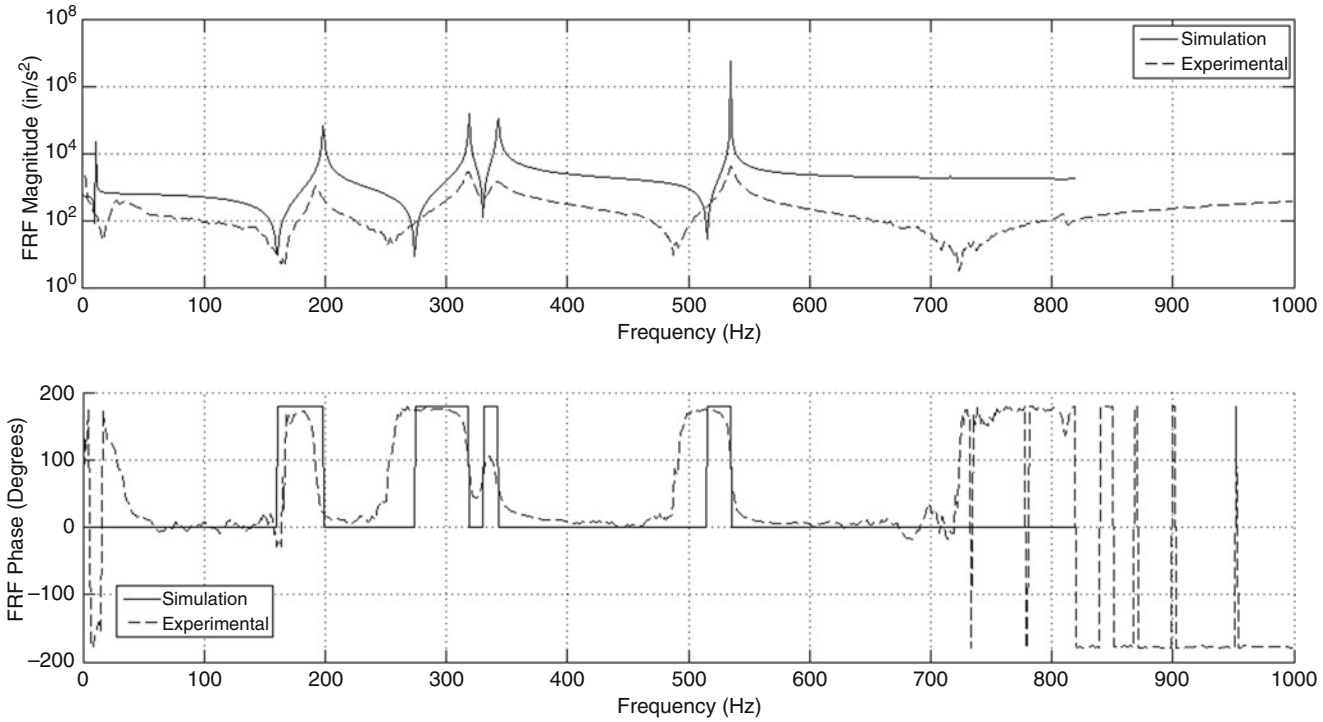

Fig. 4.9 FRF comparison between test and simulation

Table 4.7 Modal frequency comparison for clamped testing and simulation

Mode number	Frequency (Hz)—Experimental	Frequency (Hz)—FE results	Percentage difference (%)
1	72.2579	72.892	0.88
2	118.8553	124.44	4.70
3	193.7234	202.21	4.38
4	293.609	309.71	5.48
5	415.5217	433.98	4.44
6	682.9975	712.77	4.36

Fig. 4.10 Cross MAC for clamped condition

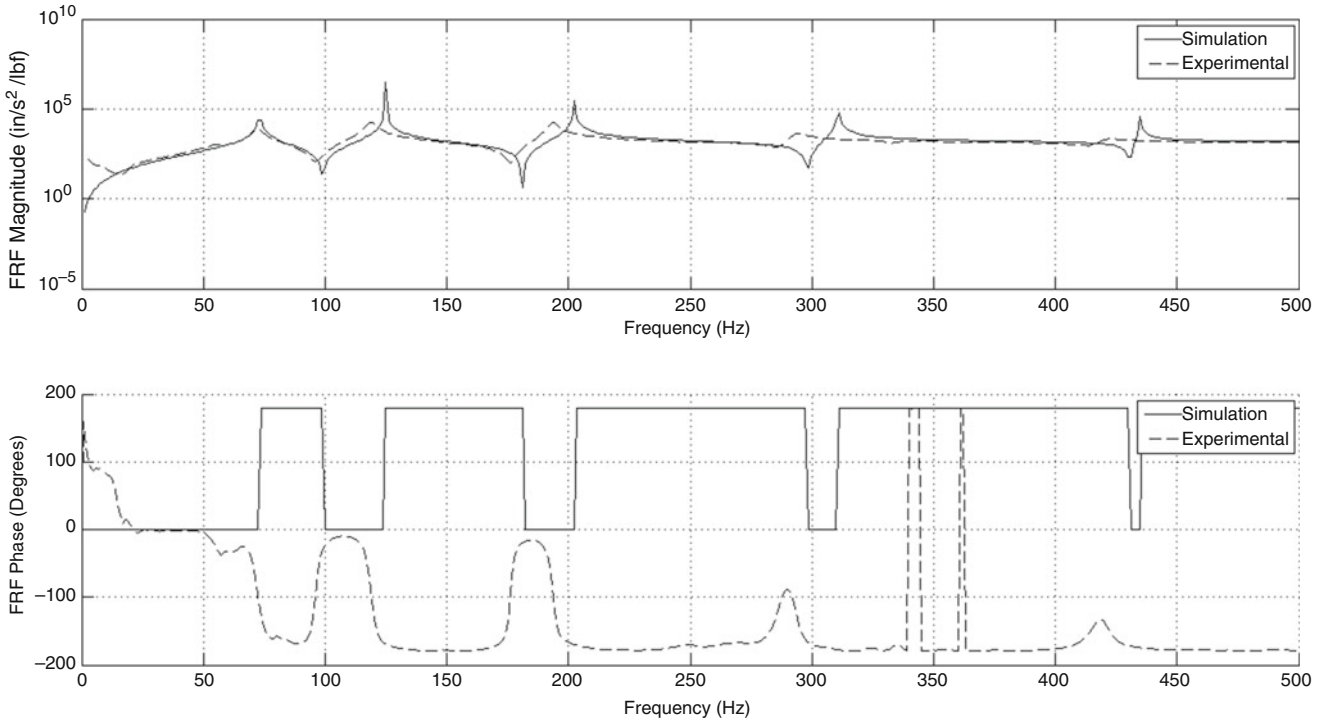

Fig. 4.11 FRF comparison between test and simulation for clamped condition

4.4.3 Boundary Condition Correlation

Table 4.7 highlights the results after model correlation using for the simplified vane structure in clamped condition. The stiffness at the boundary region was varied iteratively to arrive at the appropriate boundary conditions Fig. 4.10 shows a comparison of the cross Modal Assurance Criteria (MAC) results between the test and simulation results for the mode vectors. The MAC diagram shows high numbers above 0.9 along the diagonal and very low numbers for the off-diagonal terms indicating that the mode shapes from testing and simulation match up fairly well. Figure 4.11 compares the FRF from the test and the simulation for a particular driving point on the structure. As can be seen from the figure, the results match very well and indicate that the FE model is able to replicate the physical system characteristics well.

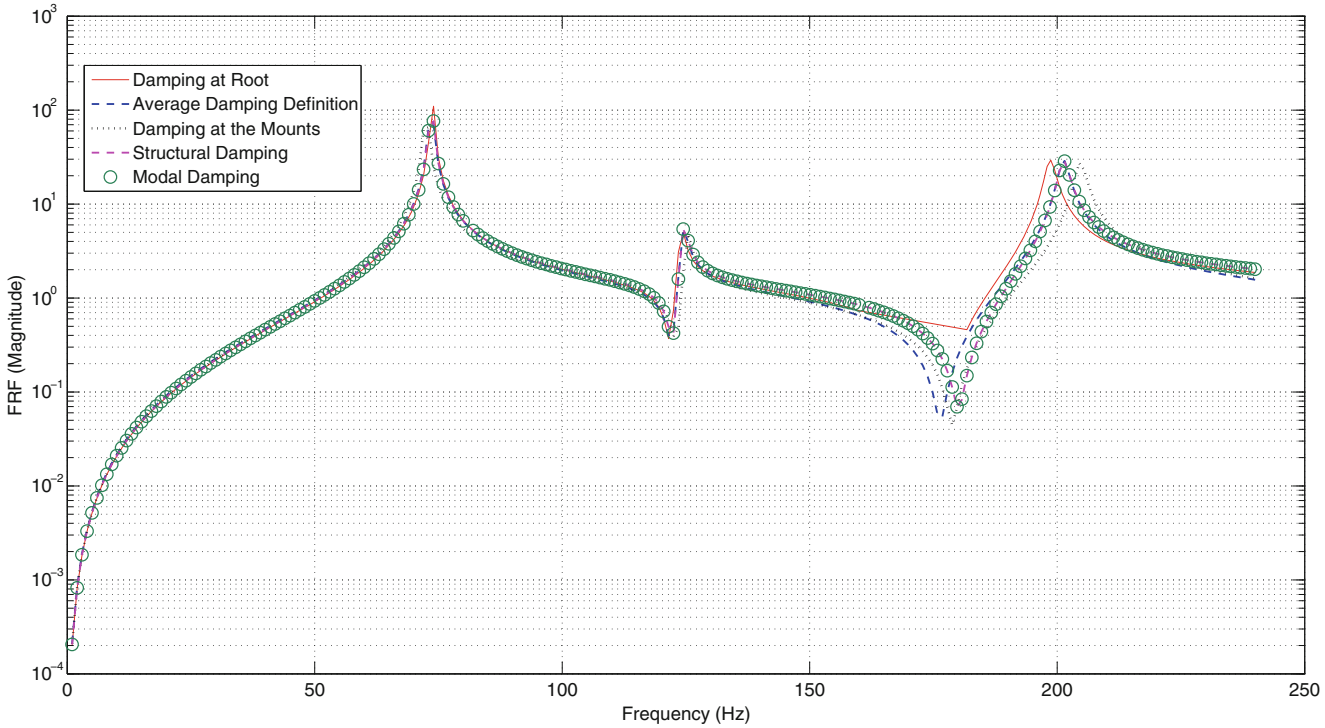

Fig. 4.12 FRF comparison between different damping modeling approaches for simplified vane in clamped condition

4.4.4 Damping Modeling

The damping modeling faces the same challenges of making a good damping estimate as discussed for the simple cantilevered beam case. The same five different damping modeling approaches are adopted in the case of the built up structure too. The comparison of the FRF's obtained from simulation with the different damping modeling approaches is presented in Fig. 4.12. The different modeling approaches were used to check on the influence of spatial distribution of damping on the system characteristics. The approach was implemented in a piecewise manner in the frequency domain. As can be seen from the results, spatial damping distribution has very small influence on the system dynamics. However, depending on the method of damping definition used small differences in the peak response amplitudes as well as small modal frequency shifts are observed.

4.5 Conclusion

The two-step approach to developing an accurate numerical FEA model of a structure with a clamped boundary is studied. In the first step, stiffness property of the FEA model is identified by comparing the measured and calculated natural frequencies. With the model that has refined stiffness properties, damping model is identified in the second step by comparing the peaks at the resonances of the modes in the range of frequency of interest. Accurate estimation of damping was observed to be a challenge for the correct implementation of this step in the modeling approach. The approach was applied to a simple cantilever beam for demonstration, and then applied to a realistic structure with a clamped boundary. It has been shown that the approach has good potential to obtain an accurate FEA model of a structure with a hard-to-model boundary condition such as a clamped boundary.

Obviously the accurate updating of the FE model depends on ability to make good measurements. In addition it is important to keep an eye on the condition number of the system matrices generated in ANSYS via this modeling approach to ensure that the stiffness characteristics are not being heavily modified to ill condition the resultant stiffness matrix in the FE model. It is not a practical approach to try to produce a model that can correlate system characteristics across all frequency ranges, especially damping properties. A more practical option is to identify damping in a piecewise manner, mode-by-mode for example. Forced response analysis using such a model can be implemented in the frequency domain in separate frequency bands with a different damping model for each band.

References

1. Mottershead, J.E., Friswell, M.I.: Model updating in structural dynamics: a survey. J. Sound Vib. **167**(2), 347–375 (1993)
2. Ewins, D.J., Imregun, M.: On the reliability of computational dynamic response prediction capabilities (DYNAS). J. Soc. Environ. Eng. **27**(116), 3–13 (1988)
3. Abgrall, O., Cloarec, Y.: Assembly of Sectorized fixed stators for a turbo machine compressor. United States Patent 7,946,811, 24 May 2011
4. Amoo, L.M.: On the design and structural analysis of jet engine fan blade structures. Prog. Aerosp. Sci. **60**, 1–11 (2013)
5. Pasha, H.G., Kohli, K., Allemang, R.J., Phillips, A.W., Brown, D.L.: Structural dynamics model calibration and validation of a rectangular steel plate structure. Conference Proceedings of the Society for Experimental Mechanics Series, vol. 3, pp. 351–362 (2015)
6. Baqersad, J, Niezrecki, C, Avitabile, P: Effects of boundary conditions on the structural dynamics of wind turbine blades—Part 1: Flapwise modes. Conference Proceedings of the Society for Experimental Mechanics Series, vol. 1, pp. 355–368 (2014)
7. Ahmadian, H., Mottershead, J.E.: Boundary condition identification by solving characteristic equation. J. Sound Vib. **247**(5), 755–763 (2001)
8. Waters, T.P., Brennan, M.J., Sasananan, S.: Identifying the foundation stiffness of a partially embedded post from vibration measurements. J. Sound Vib. **274**, 137–161 (2004)
9. Pabst, U., Hagedorn, P.: Identification of boundary conditions as a part of model correction. J. Sound Vib. **182**(4), 565–575 (1995)
10. Lee, J.H., Kim, J.: Identification of damping matrices from measured frequency response functions. J. Sound Vib. **240**(3), 545–565 (2001)
11. Adhikari, S., Wodehouse, J.: Identification of damping: Part 1—Viscous damping. J. Sound Vib. **243**(1), 43–61 (2001)
12. Pasha, H.G., Allemang, R.J., Phillips, A.W.: Techniques for synthesizing FRF's from analytical models. Conference Proceedings of the Society for Experimental Mechanics Series, vol. 6, pp. 73–79
13. Elwali, W., Satakopan, H., Shauche, V.: Modal parameter estimation using acoustic modal analysis. Conference Proceedings of the Society for Experimental Mechanics Series, vol. 3, pp. 22–33 (2011)
14. Brown, D.L., Allemang, R.J., Phillips, A.W.: Forty years of use and abuse of impact testing: a practical guide to making good FRF measurements. Conference Proceedings of the Society for Experimental Mechanics Series, vol. 8, pp. 221–241 (2015)

Chapter 5
Testing Methods for Verification of a Mounted Accelerometer Frequency Response

Marine Dumont, David Kuntz, and Thomas Petzsche

Abstract The mounted resonance frequency of an accelerometer is a key parameter to ensure a sensor's performance, its functional state, and how well the sensor has been mounted. The mounted resonance frequency leads directly to the frequency response limitation of a sensor, and how sensor sensitivity will change according to the frequency range of interest.

The mounted resonance frequency can become a quite important property, and provides hints on the mounting conditions of a sensor and related issues. Some things that could be identified are, the accelerometer is loose from the mounting surface, the sensor's mass is too high in relation to the mass of the structure, or the mounting method lacks in stiffness. Under these various cross conditions, different resonance modes are theoretically expected from the solution of the equation of motion.

The way to measure and specify such a parameter can be challenging. It is important to understand in which conditions this value has been determined when comparing one sensor to another, from one mounting method to another, from the sensor mass to unit under test mass ratio, or from a sensor's initial state to its response after several test cycles.

In this paper we will provide you with an overview of the different procedures to perform such a resonance frequency test. We will then provide you with an understanding on a response if the measurement is performed on a free sensor hanging in the air, on a sensor mounted on a heavy structure, and with other intermediate mounting configurations.

We will discuss different results obtained if the resonance frequency determination is performed using a shaker and performing a frequency sweep, using the pencil break test technique (similar to ASTM E976-84) or inverse piezoelectric excitation. We will then provide a rule of thumb on how to derive from those measurements an approximation of the sensor frequency response, if the damping properties of the sensor are known.

Keywords Accelerometer • Vibration • Resonance • Frequency • Mounting

5.1 Introduction

The Mounted Resonance Frequency (MRF) and the damping ratio are usually given in acceleration datasheets among the other sensor specifications where an ideal, very stiff, mounting configuration is used. The resonant frequency of a sensor leads directly to the frequency response limitation of that sensor, and how sensor sensitivity will change according to the frequency range of interest.

Knowing the sensor MRF can provide a wide range of valuable information to the user. First of all, it will ensure a sensor's performance, as well as its functional state.

A sensor's resonance frequency can also indicate the quality of the mounting itself. For example, a deviation of the MRF toward the lower values would indicate a softer mounting to the structure. This would then allow the user detect a panel of issues such as an imperfect plane between sensor and mounting surface, mounting surface not smooth enough, scratches or foreign bodies in the interface layer, cracks in the mounting studs or base.

A deviation of the MRF toward the higher values could on the other hand provide information that the sensor mounting is getting loose, or that the sensor's mass is too heavy for the weight of the structure under test. It also may mean that the MRF is splitting into two.

Thomas Petzsche: In honor and gratitude to Prof. Dr. Günther Schmidt, Halle/Saale, Germany to his 95 birthday.

M. Dumont • D. Kuntz (✉)
Kistler Instrument Corporation, 75 John Glenn Drive Amherst, New York, NY, 14228, USA
e-mail: david.kuntz@kistler.com

T. Petzsche
Kistler Instrumente GmbH, 71063, Sindelfingen, Germany

N. Dervilis (ed.), *Special Topics in Structural Dynamics, Volume 6*, Conference Proceedings
of the Society for Experimental Mechanics Series, DOI 10.1007/978-3-319-53841-9_5

Under the various conditions we just mentioned, one can expect different resonance modes. Those can be derived from the solution of the equation of motion under different boundary conditions.

The way to measure and specify such a parameter can be challenging. It will be very important to understand in which conditions this value has been determined, such as, when comparisons are being made from one sensor to another, from one mounting method to another, from the sensor to unit under test mass relationship, or from a sensor's initial state to its response after several test cycles.

All tests described in the following paper have been done with charge output accelerometers in order to be able to use the inverse piezoelectric effect to drive the seismic system and excite it.

The following methods will be used to determine the MRF:

(1) Measuring the electric impedance with a Vector Signal Analyzer and determine resonances,
(2) Usage of the pencil break test technique according to ASTM E976-84 [1] or ISO5347-14 [2],
(3) Resonance excitation using the inverse piezoelectric effect by a Dirac voltage pulse excitation with a white noise excitation. The inverse piezoelectric exciting methods can also be used to investigate a free suspended sensor.
(4) Performing a frequency sweep with a shaker according to the ISO5347-22 [3] which is the most commonly used method

The suitable methods will be introduced and their results compared with each other.

Last but not least, a summary will be provided on how to derive from those measurements an approximation of the sensor's frequency response.

5.2 Seismic Sensor (Accelerometer) Vibration Mode Considerations

In order to get a basic understanding, we will be starting with theoretical considerations. Let us consider a mounted and non-mounted accelerometer and determine the natural frequency.

The spring constant k of a single spring mass system is:

$$k = \frac{F}{-\Delta x} = -\frac{E \bullet A}{l} \tag{5.1}$$

With an applied force $\boldsymbol{F}$ and a spring displacement $\Delta \boldsymbol{x}$ according to Hook's Law and with the elastic modulus $\boldsymbol{E}$, the cross section $\boldsymbol{A}$ and the length $\boldsymbol{l}$ of the spring.

Considering a simple balance between potential and kinetic energy [4], the angular frequency ω for the one dimensional spring mass system will then be given by:

$$\omega = \sqrt{\frac{k}{m}} = \sqrt{\frac{E \bullet A}{l \bullet m}} \tag{5.2}$$

In the case of a free suspended two masses spring system also called a non-fixed two mass spring system, such as shown in Fig. 5.1, a one dimensional, linear vibration can be excited. In this case both end with mass $\boldsymbol{m_1}$ and $\boldsymbol{m_2}$ will move compared to each other after releasing them. Before initiation of the vibration, the conservation of momentum was at zero. As no momentum is acting externally, the Law of the conservation of momentum can be applied: $\sum m \bullet \dot{x} = const$. Therefore we get:

$$m_1 \bullet \dot{x}_1 - m_2 \bullet \dot{x}_2 = 0 \text{ and hence } m_1 \bullet \dot{x}_1 = m_2 \bullet \dot{x}_2 \tag{5.3}$$

During the extension of the spring, one part of the spring called the nodal point of vibration, will not be displaced. From the geometrical observation of Fig. 5.1 we will compute:

$$\frac{x_1}{x_2} = \frac{l_1}{l_2} \tag{5.4}$$

By differentiation of the displacement $\boldsymbol{x}$ and Eq. (5.3) we will get

$$\frac{\dot{x}_1}{\dot{x}_2} = \frac{l_1}{l_2} = \frac{m_2}{m_1} \tag{5.5}$$

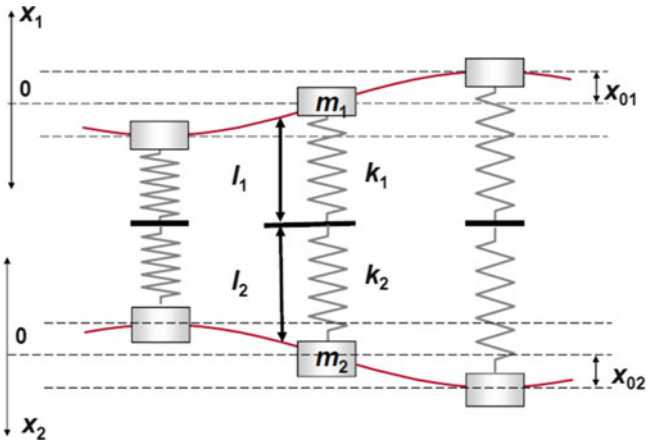

Fig. 5.1 Non-fixed two mass spring system

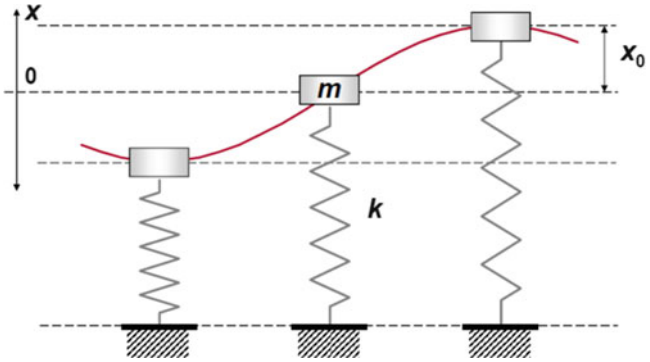

Fig. 5.2 Fixed one mass spring system

The nodal point divides the spring into two parts where the length is inversely proportional to the corresponding masses. The nodal point is situated closer to the vibrating system having the higher mass.

As the nodal point is steady (still) we can consider it as two partial systems with angular frequencies

$$\omega_{01} = \sqrt{\frac{k}{m_1}} = \sqrt{\frac{E \bullet A}{l_1 \bullet m_1}} \text{ and } \omega_{02} = \sqrt{\frac{k}{m_2}} = \sqrt{\frac{E \bullet A}{l_2 \bullet m_2}} \tag{5.6}$$

$\boldsymbol{k}$ is the spring constant formed out of the two spring constants $\boldsymbol{k}_1$ and $\boldsymbol{k}_2$ in series.

From Eq. (5.5) we then determine:

$$\omega_{01} = \omega_{02} = \omega_0 \tag{5.7}$$

Both masses vibrate mutually to each other with the same frequency. If we take $l_1 = l_2 \bullet m_2/m_1$ into the equation $l = l_1 + l_2$ and introduce $\boldsymbol{l_2}$ into Eq. (5.6) for ω_{02}, then we get for the angular frequency of this system

$$\omega_0 = \sqrt{k \bullet \left(\frac{1}{m_1} + \frac{1}{m_2}\right)} \tag{5.8}$$

In theory, a free accelerometer suspended in the air and not mounted can be considered a non-fixed two mass system.

Applying the limit condition for $m_2 \to \infty$ in Eq. (5.8) of the non-fixed two mass spring, we get the natural frequency for the fixed one mass spring system given in Eq. (5.2) and illustrated in Fig. 5.2.

Only one natural frequency is possible for these two non-fixed masses coupled with a spring models. In theory, two natural frequencies are possible, but the first one is always zero. This allows the computation of the natural frequency similar to the

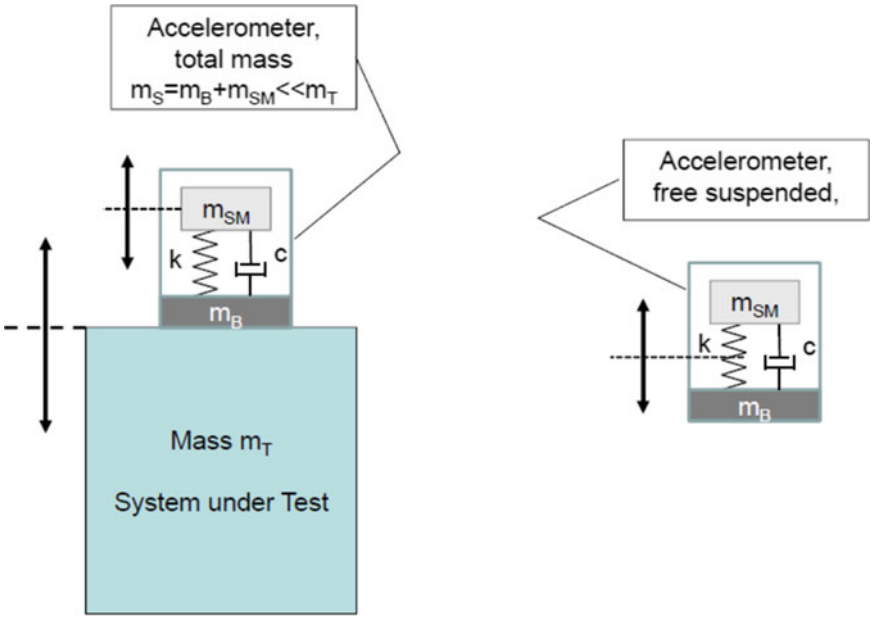

Fig. 5.3 Accelerometer under mounted and loose boundary conditions—*Left*: Case 1: Typical Vibration Testing configuration, Accelerometer mass $m_S = m_B + m_{SM}$, Mass system under test $m_T >> m_S$. *Right*: Sensor free suspended in air, Accelerometer mass $m_S = m_B + m_{SM}$

fixed one mass spring system. A more complex and accurate mathematical deviation of the two non-fixed masses model can be achieved by solving the differential equation system in [5]. Here a more basic understanding was preferred to prevent complex calculations.

Similar to what we just did, we can differentiate an accelerometer under two different boundary conditions:

Case 1: The accelerometer is mounted to a system of very large mass $\boldsymbol{m_T}$ compared to the sensor mass $\boldsymbol{m_S = m_B + m_{SM}}$ (with $\boldsymbol{m_B}$—sensors mass w/o seismic mass; $\boldsymbol{m_{SM}}$—mass of seismic mass). One can find this case when a sensor is mounted to a heavy test structure in vibration. In a first step, it can be represented by a simple spring mass system similar to the fixed one mass spring system. The natural frequency is given by Eq. (5.2) and Fig. 5.2.

Case 2: The accelerometer is free hanging with no attachment point. The vibration occurs in a mode of two masses $\boldsymbol{m_1}$ and $\boldsymbol{m_2}$ with a spring $\boldsymbol{k}$ in the middle. This would be similar to a simple non-fixed two mass spring system, such as Fig. 5.1 and Eq. (5.8) where the natural frequency would be higher than in Case 1. Figure 5.3 is providing a representation of both cases.

The natural frequency in the mounted state f_m from Case 1 is given by:

$$f_m = \frac{1}{2\pi}\sqrt{\frac{k}{m_{SM}}} \tag{5.9}$$

In Case 2 where the sensor is free suspended in the air, the natural frequency f_s becomes:

$$fs = \frac{1}{2\pi}\sqrt{k\left(\frac{1}{m_B}+\frac{1}{m_{SM}}\right)}. \tag{5.10}$$

With $\boldsymbol{k}$ the spring constant of the transducer piezoelectric element. In those Eqs. (5.9) and (5.10), the mass of piezoelectric elements and its fixing tools has been neglected.

Based on these two boundary conditions we will investigate in the following paragraphs, using different excitation methods the resonances of two different types of charge output piezoelectric accelerometers. Charge output accelerometers have been used here to allow also an excitation of the sensor seismic mass using the inverse piezoelectric effect thanks to an alternating voltage applied to the capacitance of the sensor.

5.3 Accelerometer Resonance Test Methods

Per standard definitions, the resonance frequency is achieved at the lowest frequency where the sensor reaches its maximum sensitivity while excited with an external vibration [1, 2, 6]. In the literature we can find different methods to determine the accelerometer resonance frequency, e.g. in [7]. We could use, in a first step, an undamped spring-mass system fixed on one side to a large mass structure. The natural frequency f_0 can be given by:

$$f_0 = \frac{1}{2 \bullet \pi} \sqrt{\frac{k}{m}} \tag{5.11}$$

Here we have to know the piezoelectric element stiffness constant k and the mass of the seismic mass m.

As most accelerometers used nowadays are shear mode transducers, the spring mechanism of the seismic system is a shear mode vibration. We could then express the spring constant using a shear modulus, the thickness and the cross area of the element and compute the natural frequencies from the material and sensor. Unfortunately all this information is not known to us. Therefore we chose to use the inverse piezoelectric effect of a charge type accelerometer to excite the seismic system into vibrations and investigate the resonances of the excited modes. Many different modes are to be expected as the piezoelectric effect is very morphic. We can then expect with an alternating voltage to the electrodes to excite the shear, thickness, lateral and longitudinal vibration mode, as well as their higher harmonics, and the case and cover resonances of the housing as well.

In a first test we will investigate the resonances for the two charge type piezo-ceramic shear accelerometers type 8203A50 and 8202A10, inversely excited between 10 and 80 kHz using a Hewlett Packard Vector Signal Analyzer HP89410A. Some of the key sensor specifications are provided in Table 5.1.

With this method we are connecting the accelerometer capacitance (for a piezoelectric charge only) in series with a resistor of 100 Ω to a variable frequency oscillator (illustrated in Fig. 5.4). An electronic voltmeter connected across the resistor measures the accelerometer impedance variations over the frequency range excited. In case of resonance, the impedance

Table 5.1 8203A50 and 8202A10 sensor specifications

	8203A50	8202A10
Minimal mounted resonance frequency belong to data sheet	24 kHz	45 kHz
Sensitivity at 100 Hz	50 pC/g	10 pC/g
Principle	Ceramic shear	
Capacitance	1400 pF	500 pF
Total sensor mass m_1	44.5 g	14.5 g
Total mass of seismic element	13.06 g	2.335
Total mass of sensor m_1 without mass of PE element m_{PE} and mass of seismic mass m_2	30.62 g	11.813 g

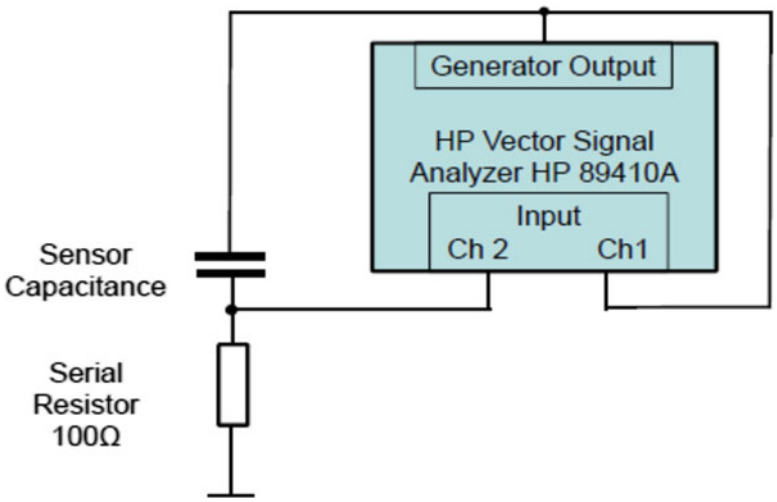

Fig. 5.4 Inverse piezoelectric resonance excitation of an accelerometer using Vector Analyzer Technology

Table 5.2 Hanging and mounted resonances for sensors type 8203A50 and 8202A10 (It means: $1/m = 1/m_1 + 1/m_2$; $m_1 = m_S - (m_{PE} + m_2)$; where it is: m – reduced mass; m_1 – mass sensor – (mass of seismic mass m_2 + mass of PE element of seismic m_{PE}) mass of the piezoelectric element and its fixing m_{PE})

Sensor type	Mass of seismic mass m_2 (g)	Total Mass of sensor m_S (g)	Total Mass of sensor m_s–(mass of seis. mass m_2 and mass of PE element) m_1 (g)	Reduced mass m (g)	Measured res. freq., hanging $f_{res,\ loose}$ (Hz)	Calculated spring const. k (N/m)	Calculated mounted res. freq. $f_{res,\ mount}$ (Hz)	Measured mounted res. freq., $f_{res,\ mount}$ (Hz)	
								1st mode	2nd mode
8203A50	13.06	44.5	30.62	9.155	26,316	**250,287,758**	22,033	**23,850**	26,842
8202A10	2.335	14.5	11.81	1.949	50,350	**195,112,505**	46,007	38,421	**46,666**

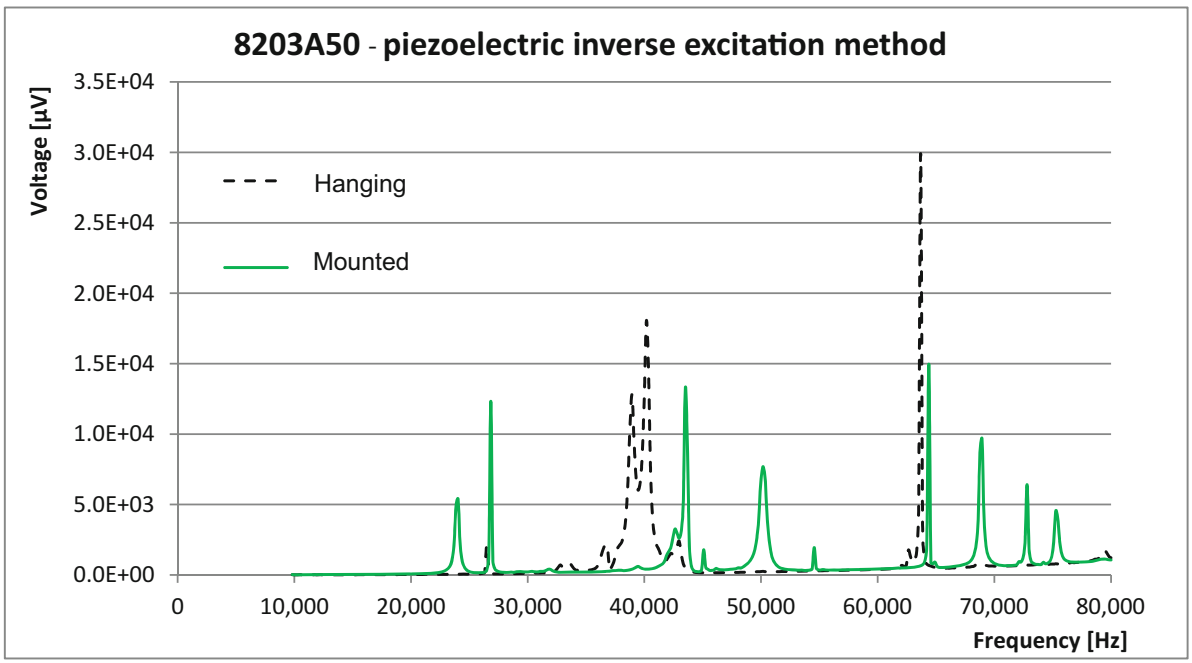

Fig. 5.5 8203A50 resonance modes in both hanging and mounted configurations using the piezoelectric inverse excitation method

decreases and most of the oscillator voltage is applied over the resistor. A more typical method would be to use a Vector Signal Analyzer HP 89410A (DC to 10 MHz). It allows the measurement of the transfer characteristic between input and output signals.

An average of 50 samples has been made. The sensors have been excited with an effective sinusoidal voltage of 2 V rms in the frequency range of 10–80 kHz. The sensors have been investigated in a case of a free mounting condition and in a mounted state on top of a 50 mm steel cube. Both resonance frequencies have been measured with the Vector Signal Analyzer. The spring constant k can be determined using Eq. (5.10) in case of the hanging sensor. Thanks to this calculated spring constant, the mounted resonance frequency can be determined using Eq. (5.9).

Table 5.2 summarizes our findings.

In case of both the 8203A500 and 8202A10, it shows a fairly good correlation between computed and measured resonances. For the lowest measured resonance frequency a good correlation has been found for the type 8203A50 sensor. For the 8202A10 a correlation is evident for the second resonance mode; the first mode at 38.4 kHz, being of a much lower amplitude as Fig. 5.6 shows.

Figures 5.5 and 5.6 are showing all the resonance modes of the hanging and mounted cases for both sensors. As mentioned earlier, the multiple resonances are most likely caused by the other resonance modes, induced by the piezoelectric inverse excitation method.

The third method used is a pencil break test, where the sensor is mounted to a steel cube of 25.4 mm cube, such as shown in Fig. 5.7. Such a break generates a very short, nearly Dirac pulse to the sensor and excites the resonance of its seismic element. The steel cube must have a polished surface and the sensor must be mounted using a coupling agent such as grease.

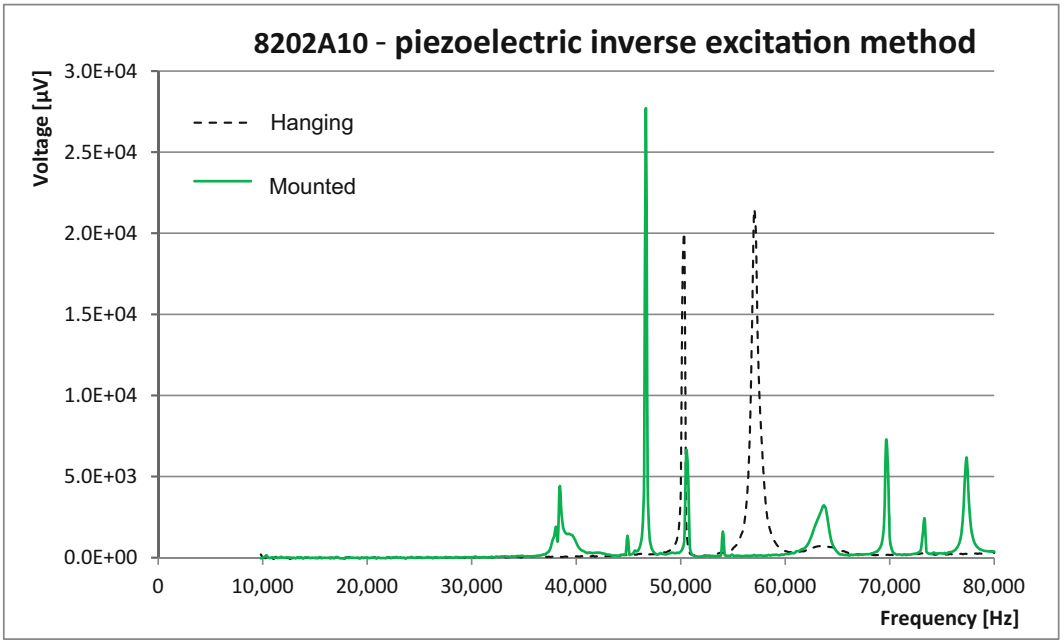

Fig. 5.6 8202A10 resonance modes in both hanging and mounted configurations using the piezoelectric inverse excitation method

Fig. 5.7 Pencil lead break, or impact with a steel ball on a steel cube of 25.4 mm^3 (The pencil is using a cushion tube at the tip to prevent multiple impacts, similar to the HSU-Nielson source for acoustic emission testing)

This technique is described in technical standards, such as "Resonance frequency testing of undamped accelerometers on a steel block" in ISO5347-14 [2] or in the Instrumentation Society of America Recommended Practices ISA-RP37.2-1982 (R1995) Guide for Specification and Tests for Piezoelectric Acceleration Transducers for Aerospace Testing [8]. This method is mainly applicable only for an undamped sensor with a mass lower than 30 g. In our investigations the sensor has been mounted on a steel block of 28 × 28 × 28 mm with a mass of 180 g. The cube should be made from tungsten with a much higher density or hardened steel. In our case the cubes resonance might be limited to 50 kHz.

A new method ISO16063-32 "Methods for the calibration of vibration and shock transducers – Part 32: Resonance testing – Testing the frequency and the phase response of accelerometer by means of shock excitation" [6] has just been released in 2016 by ISO, which should replace the older ISO 5347-14 standard. In this case the cube is replaced with a hardened steel ball. A smaller steel ball drops via a guide tube to this against the larger ball creating a very short directed shock pulse to the sensor under test.

In our test the transient signal from the sensor was recorded with a sufficient high sampling rate in the time domain and transferred in the frequency domain by means of an FFT-transformation. From here we could identify the MRF of the unit under test. We used an FFT with a frequency bandwidth of 80 kHz and 25600 lines with a time capture of 320 ms. The window function used was an exponential one, as the signal is expected to be strong at the beginning. The sampling interval was 4.8 µs (Figs. 5.8 and 5.9).

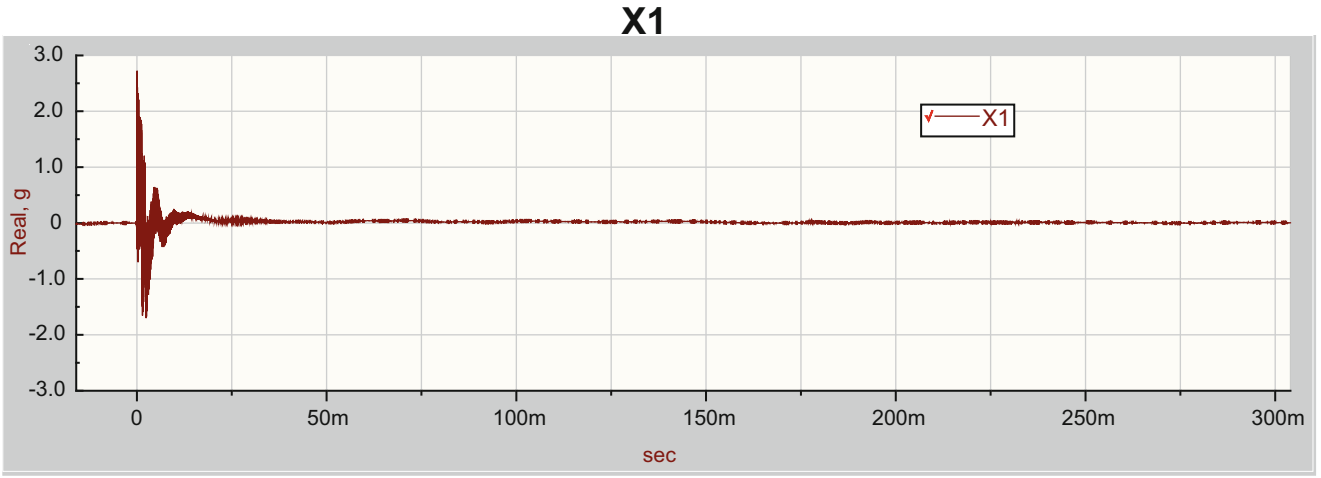

Fig. 5.8 Time domain signal of the pencil lead break test for the sensor 8203A50. The signal decay is observed after 25 ms time frame

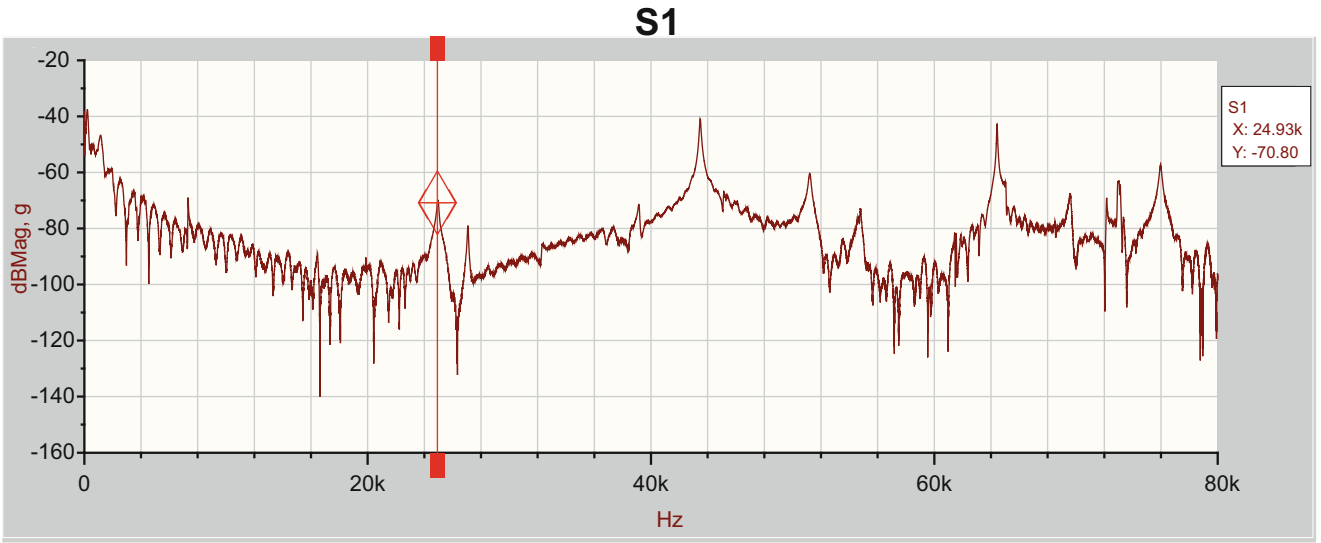

Fig. 5.9 FFT auto power spectrum from the signal in Fig. 5.8 for the sensor 8203A50

Sensors resonances at:

1	2	3	4	5	6	7	8	9
24.93 kHz	27.09 kHz	43.49 kHz	51.17 kHz	54.79 kHz	64.46 kHz	69.55 kHz	73.01 kHz	75.94 kHz

Our fourth test method used an FFT analyzer with the capability to measure transfer characteristics. In this case, two methods can be used with the inverse excitation of mechanical vibrations in the seismic system with the inverse piezoelectric effect to the sensing element. It can be done either with a short excitation pulse, or with a sufficient high frequency white noise excitation continuous for a defined duration. Averaging over 40 times can reduce noise tremendously. This method can be used for both hanging, and mounted accelerometers (Figs. 5.10 and 5.11). The results are similar to the previous ones, and are documented in Figs. 5.13 and 5.14.

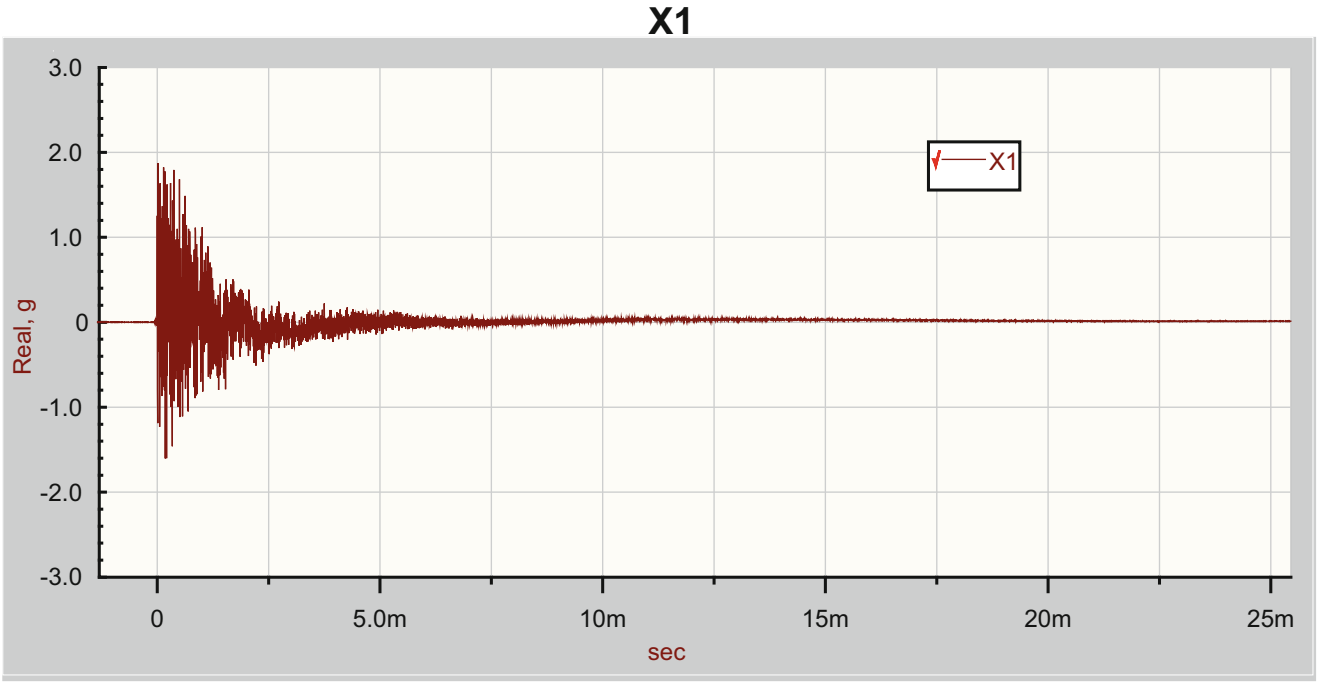

Fig. 5.10 Time domain signal of the pencil lead break test for the sensor 8202A10. The signal decay is observed after 50 ms time frame

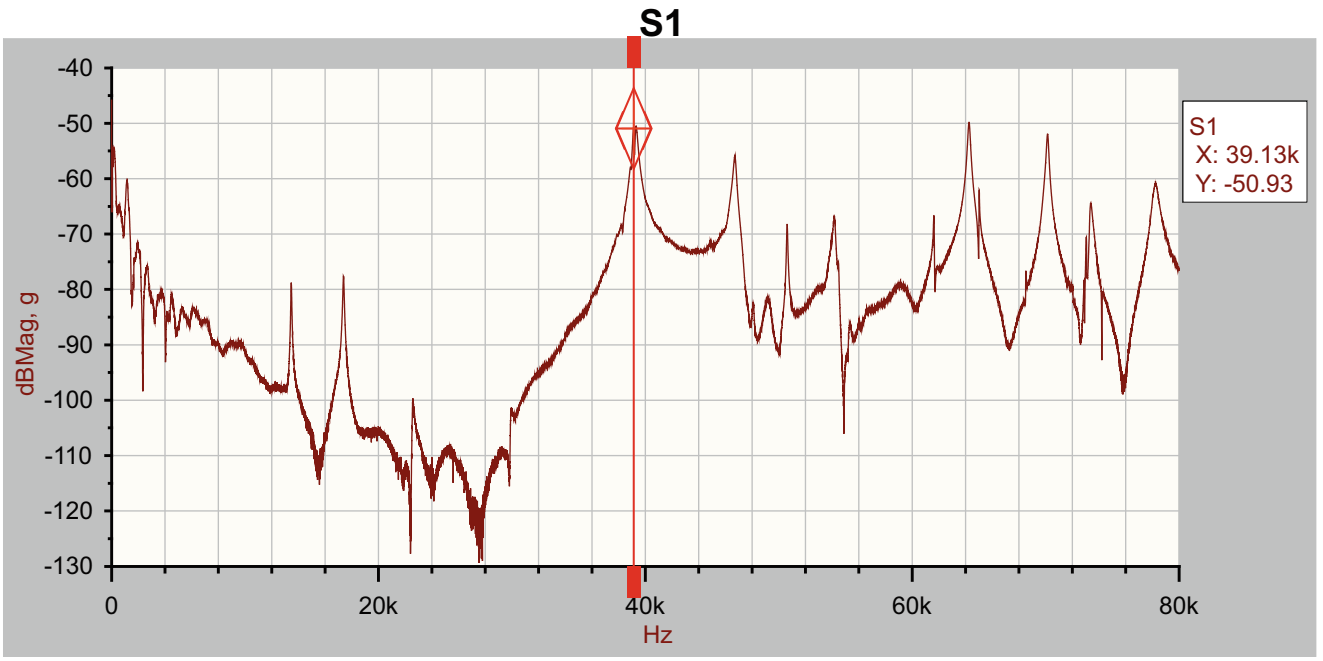

Fig. 5.11 FFT auto power spectrum from the signal in Fig. 5.8 for the sensor 8202A10

Sensor resonances at:

1	2	3	4	5	6	7	8	9
39.13 kHz	46.70 kHz	50.62 kHz	54.16 kHz	61.62 kHz	64.23 kHz	70.11 kHz	73.37 kHz	78.21 kHz

Our fifth method was to use a swept sine test on a shaker in the high frequency zone between 10 and 60 kHz. In this case, the high frequency shaker Spektra SE-09 has been used due to the sufficiently high resonance frequency of >70 kHz of the reference grade standard embedded in the shaker. The test has to take into account up to 40 dB or more resonance amplification of the maximum resonance range of the sensor. At least 40 points/Decade must be taken (more would be better), to get the resonances precisely avoiding the "picket fence" effect for high mechanical quality resonances (typical for low damping seismic systems). This method is described in ISO 5347-22:1993, Methods for the calibration of vibration and shock pick-ups—Part 22: Accelerometer Resonance Testing—General methods, confirmed 2002 and it is one of the most common in use [3]. If a suitable shaker is available, this method can be applied to undamped and damped sensors in a wide frequency range from 50 Hz to 200 kHz (Table 5.3). Results are shown in Fig. 5.12a, b.

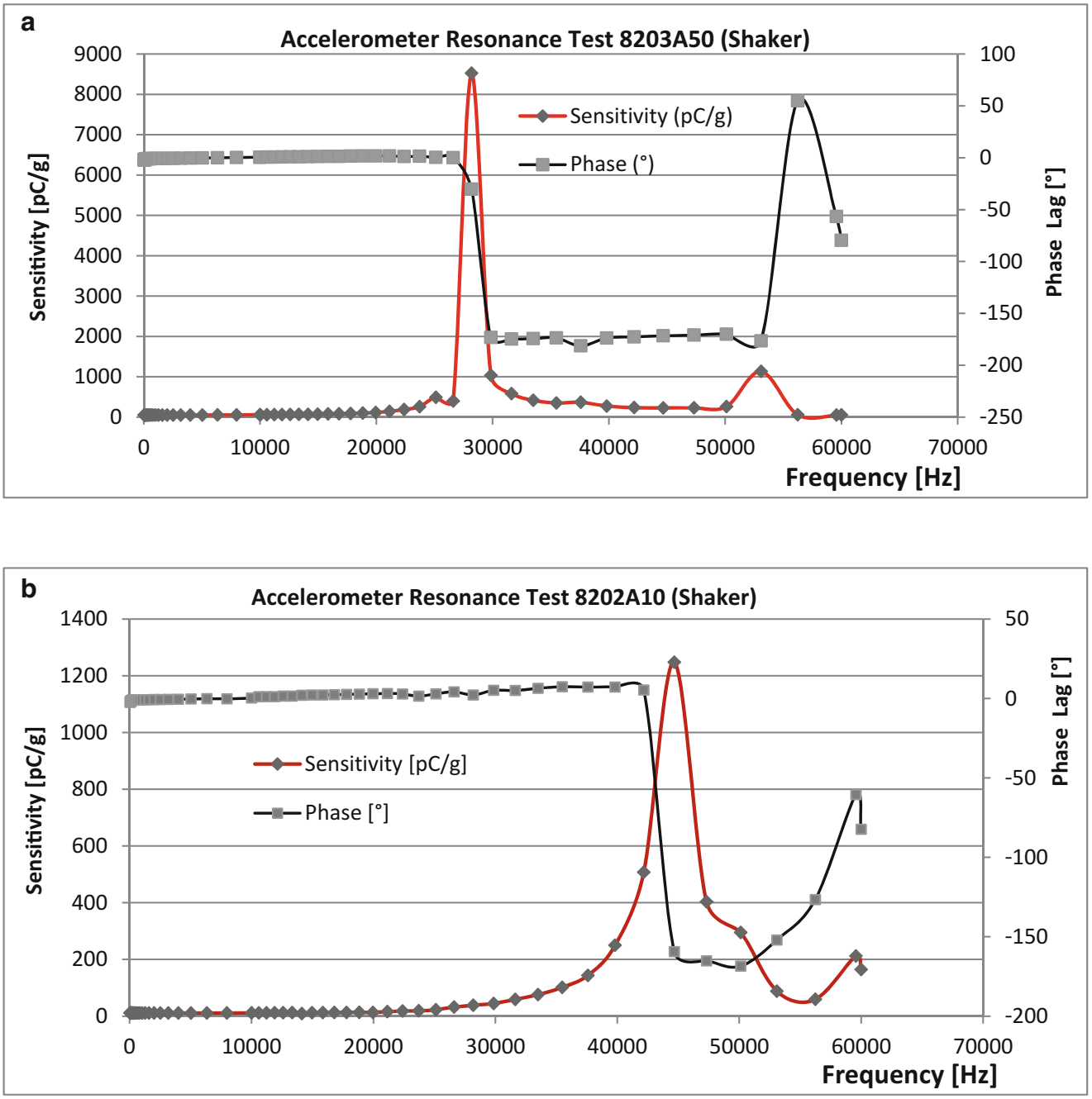

Fig. 5.12 (**a**) Shaker resonance test—sensitivity and phase shift (40 points/Decade) for sensor type 8203A50. Resonances at 25.12 kHz (weak), 28.18 kHz and 53.09 kHz. (**b**) Shaker resonance test—sensitivity and phase shift (40 points/Decade) for sensor type 8202A10. Resonances at 44.67, 59.57 kHz

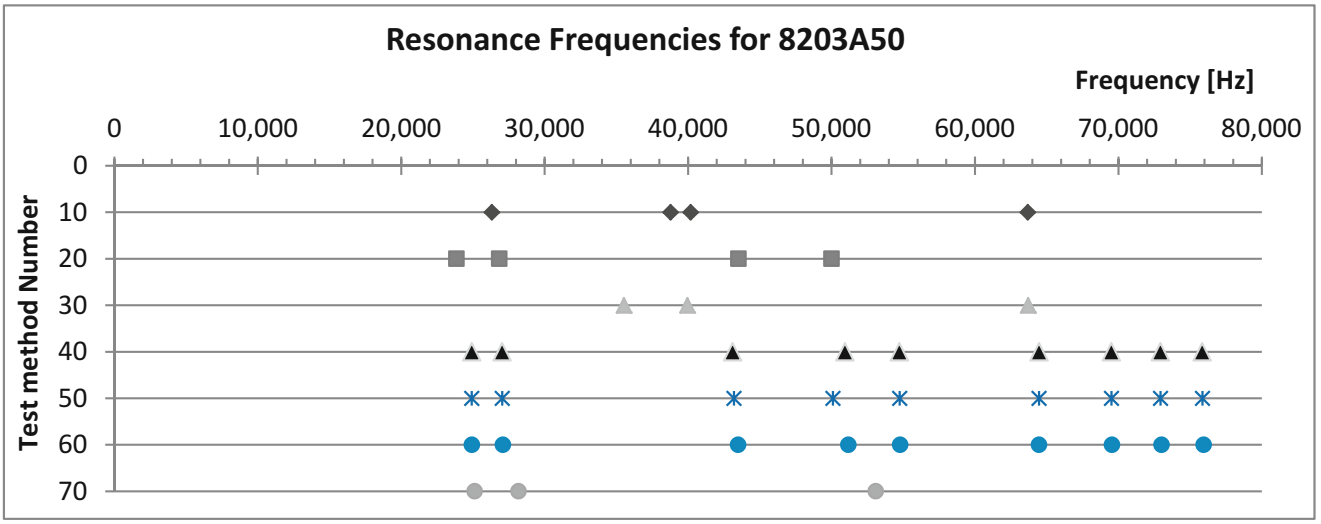

Fig. 5.13 8203A50 MRF summary for all the different test methods described (see corresponding test method number in Table 5.3)

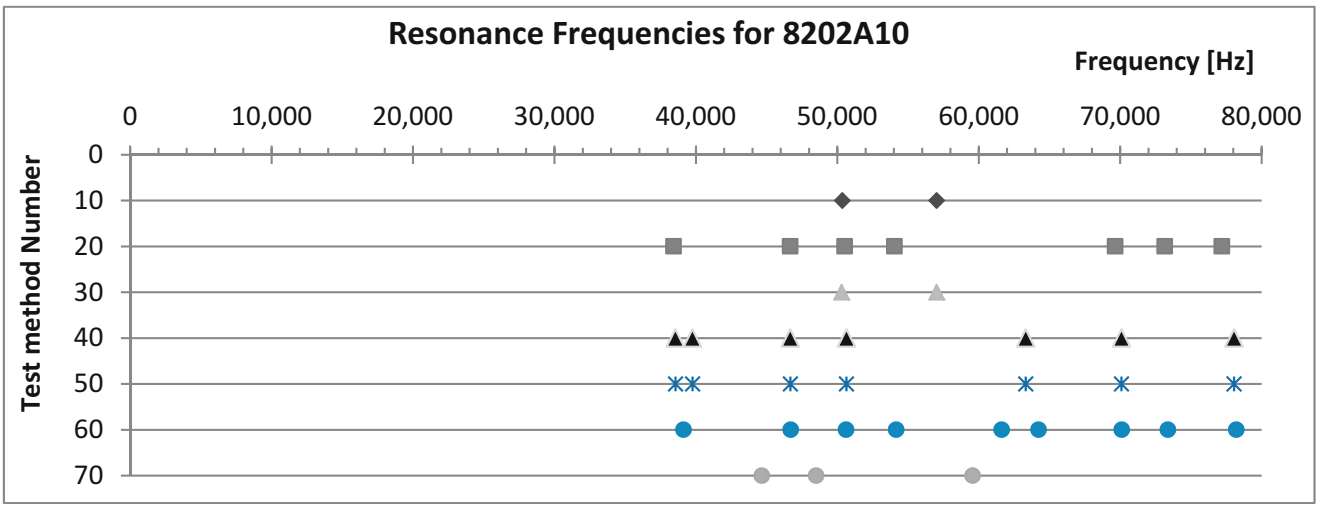

Fig. 5.14 8202A10 MRF summary for all the different test methods described (see corresponding test method number in Table 5.3

Table 5.3 Test method ref. for Figs. 5.13 and 5.14

Test method No.	Sensor	Test description	No.	Sensor	Test description
10	Loose	Vector signal analyzer	50	Mount.	Random noise test, transfer fct.
20	Mount.	Vector signal analyzer	60	Mount.	HSU-Nielson test (pencil lead), transfer fct.
30	Loose	Single electrical pulse, transfer fct.	70	Mount.	Shaker test, sinusoidal excitation
40	Mount.	Single electrical pulse, transfer fct.			

Figures 5.13 and 5.14 are summarizing the results of mounted or hanging resonance frequencies in one chart. There is a strong correlation of the main resonance modes of all these methods with just a few exceptions. To identify certain resonances and determine their modes will become quite difficult, as it needs a detailed knowledge on the design and the piezoelectric material, as well as its piezoelectric coefficient matrix. The lowest and highest resonances of the free hanging sensor is always much higher than the mounted one, and is in agreement with our calculations. To be accurate, the swept sine method would need a much higher point/decade density than we could use here; it explains why some of the resonances were missed with this technique. It could also be that the shaker armature was too lightweight and did cause a resonance shift to higher values. A test with a heavier armature could help identify this. It would need further investigation.

5.4 What Do We See in Our Daily Routine?

The typical frequency responses apply under the marginal condition that the mass of the accelerometer is small compared to the mass of the structure under test, or, for large homogeneous structures, that the mass of the accelerometer is small compared to the partial mass in the vicinity of the transducer mounting area. For cases in which this rule does not apply, Fig. 5.15 specifies a qualitative frequency response trend.

Two marginal cases can be distinguished with different natural frequency of an accelerometer, which also corresponds to the two boundary conditions in Fig. 5.3. At the beginning we considered the fixed one mass spring system in Eq. (5.9) and the non-fixed two mass spring system with Eq. (5.10).

Case 1 in Fig. 5.15 represents the first one: The transducer is mounted on a heavy (inertial) structure by contrast with the transducer mass. This is what is implied when the resonance frequency is specified in the data sheet as "mounted". It actually is much lower than the natural frequency in the second case.

Here the transducer is not mounted and it is hanging free. In this case, the seismic mass of the transducing element alone vibrates against the transducer casing, which leads to a much higher natural frequency. The other two cases 3 and 4 are between the marginal cases 1 and 2. In case 3 the transducer is mounted to a structure but with a loose assembly, a soft part in between the layers, or a soft mounting method. Here we may see a pre-resonance created by the entire sensor mass to the spring constant formed by the stiffness of the mounting and an additional higher resonance caused by the looseness itself. Theoretically we have here the case of a fixed two spring, and two mass system.

In the last case 4, the sensor is mounted to a lightweight structure compared to the sensor mass. Here the resonance may shift to higher values as we are shifting more to the non-fixed two mass spring system case. Here might also be one of the reasons for the differences in high frequency calibration on shakers with different masses of the moving elements, or the mass loading effect for back-to-back reference grade standards, beside other effects [9].

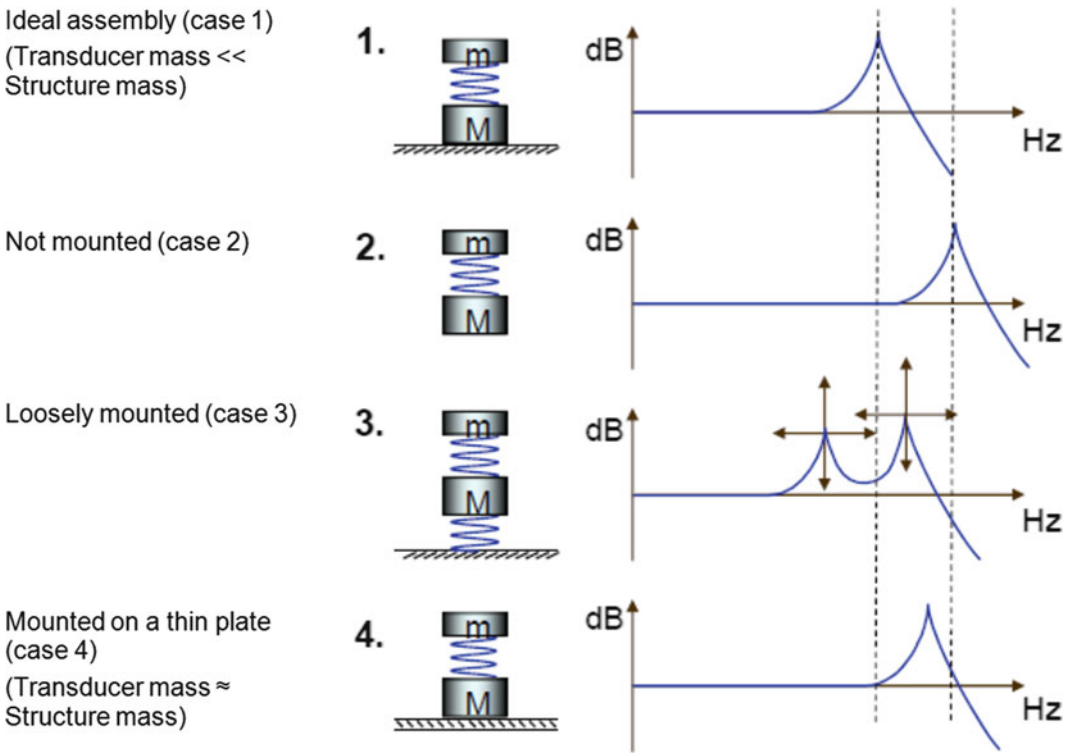

Fig. 5.15 Influence of the mounting conditions on the frequency response

5.5 The Parameter Supported Frequency Response Function in the IEEE 1451.4 TEDS

During the last decade a new method has been established to recombine the frequency response of an accelerometer just with a few parameters, saved in the memory of a transducer. The MRF is one of those parameters. It has been established in the IEEE 1451.4 standard as "Transducer Electronic Data Sheet" [10]. The model equation for the sensitivity's in dependence of frequency $\boldsymbol{f}$ is:

$$s(f,T) = I_C(Sign) \bullet s_{ref} \bullet \left[1 + b \bullet \left(T - T_{ref}\right)\right] \bullet \frac{\frac{j\bullet f}{f_{HP}} \bullet \left(\frac{j\bullet f}{f_{Ref}}\right)^{\frac{a}{\ln(10)}}}{\left(1 + \frac{j\bullet f}{f_{HP}}\right) \bullet \left(1 + \frac{j\bullet f}{f_{LP}}\right) \bullet \left[1 + \left(\frac{j\bullet f}{f_{Res}}\right)^2 + \frac{j\bullet f}{Q\bullet f_{Res}}\right]} \bullet \tag{5.12}$$

with the parameters:

$\hat{\boldsymbol{I}}_c$	Sensitivity direction
Sign	Polarity
$\boldsymbol{s}_{ref}$	Reference sensitivity ("box value")
$\boldsymbol{b}$	Temperature coefficient
$\boldsymbol{T}$	Temperature
$\boldsymbol{T}_{ref}$	Reference temperature
$\boldsymbol{f}$	Frequency
$\boldsymbol{f}_{HP}$	High-pass cut off frequency
$\boldsymbol{f}_{LP}$	Low-pass cut off frequency
$\boldsymbol{f}_{res}$	(mounted) resonance frequency
$\boldsymbol{f}_{ref}$	Reference frequency
$\boldsymbol{Q}$	Mechanical quality factor
$\boldsymbol{a}$	Amplitude slope/decade

These parameters are part of the extended "template 25". The mathematical model equation contains for the frequency response the following parameters: the resonance frequency $\boldsymbol{f_{res}}$, the mechanical quality $\boldsymbol{Q}$, a high pass-$\boldsymbol{f_{HP}}$ and a low pass filter frequency $\boldsymbol{f_{TP}}$, the sensitivity direction sign "**sign**" and a slope/decade $\boldsymbol{a}$ for the specified frequency range of the sensor. The sensitivity reference value is given as $\boldsymbol{s_{Ref}}$ refer to a reference frequency, in most cases written to the sensor box as "box value".

This allows the recombination of the sensitivity frequency response by computation of a few parameters by Eq. (5.12).

This method allows in a FFT-analyzer the extension of the frequency range of the accelerometer into the resonance area by correction of the measured FFT with the transducer frequency response as long as no overload occurs within a wider measurement uncertainty in respect to the amplitude of the signal. Here the mounted resonance frequency must be known precisely; otherwise substantial mistakes will be made.

5.6 Conclusions from the MRF

A known MRF of a mounted accelerometer provides a wide base of knowledge to the user, such as:

a. The estimated frequency response of the sensor, if an estimated value for the damping coefficient is known. As an approach the sensitivity deviated by approx. ± 5 for 20% of the MRF with a nearly undamped sensor (like a piezoelectric one) or 50% for optimal damped one with a damping coefficient $\boldsymbol{c} = 0.7$. This results out of the theoretical model of the seismic transducer as a basic model for the vibration sensor [7, 11]
b. If a MRF can be measured, it indicates basically a sensor performance and operating state in a first approach.
c. If the sensor is de-coupled from its test structure (e.g. glue gets too hot) the MRF will increase substantially. It will increase on lightweight structures in respect to the sensor mass, if mounting is loose or similar circumstances. Partially a second MRF may occur.

d. MRF will decrease if the sensor is soft mounted. This can be caused by the mounting method itself (see [12]). The accelerometer is not parallel to the mounting surface, a rougher mounting surface than specified is used, scratches or foreign bodies in the interface layer exist, mounting stud has cracks or similar.

Further considerations not made here, are:

a. High cross axis sensitivities of the accelerometer can be caused by strong and short duration lateral shocks. This affects the alignment of the seismic system for the sensor. As the MRF in the lateral direction is in most cases half a decade lower, it will create a contribution by the high sensitivity in the lateral MRF range to the nominal direction in case the accelerometer is exposed to strong lateral movements. In most cases it is the most frequent reason of damaging accelerometers. Just a swept sine calibration over the entire range can bring this to attention.
b. The mounting conditions affect the MRF very strongly. The softer the stiffness of mounting, the lower will become the MRF, and tighter will become the usable frequency range for a dedicated deviation of the sensitivity. This was already presented during last year IMAC's conference 2016 in [12].

Acknowledgement I like to thank Dr. Martin Diestelhorst, Martin-Luther-University Halle-Wittenberg, Institute of Physics, Germany cordially for the possibility to take data with the Vector Analyzer Method.

References

1. ANSI S2.2-1959, Chap.: 2.13: American Standard Method for the Calibration of Shock and Vibration Pickups
2. ISO5347-14 (1993): Methods for the calibration of vibration and shock pick-ups – Part 32: Resonance frequency testing of undamped accelerometers on a steel block
3. ISO 5347-22:1993, Methods for the calibration of vibration and shock pick-ups – Part 22: Accelerometer Resonance Testing – General methods, confirmed 2002
4. Karl Klotter: Technische Schwingungslehre, 1. Band: Einfache Schwinger, Teil A: Lineare Schwingungen; Springer Verlage Berlin, Heidelberg, New York 1981, 3. Auflage; Chap. 3.17 Elastische Schwinger, p. 119
5. Peter Zeller (ed.): Handbuch Fahrzeugakustik: Grundlagen, Auslegung, Berechnung, Versuch; Vieweg-Teubner Verlag; Springer Fachmedien Wiesbaden (2012); [see Chapter 3.1.]
6. ISO 16063-32: Methods for the calibration of vibration and shock transducers – Part 32: Resonance testing – Testing the frequency and the phase response of accelerometer by means of shock excitation (This std. replaces (5) (2016))
7. Endevco: Shock and Vibration Measurement Technology, Handbook; 1988, San Juan Capistrano (in English); ENDEVCO: Handbuch der Schock- und Vibrationsmesstechnik, 1992 , Heidelberg (in German)
8. ISA–RP37.2–1982(R1995): Guide for the Specifications and Tests for Piezoelectric Acceleration Transducers for Aerospace Testing
9. Bruns, T., Link, A., Täubner, A.: The influence of different vibration exciter systems on high frequency primary calibration of single-ended accelerometers: II. Metrologia. **49**, 27–31 (2012)
10. IEEE 1451.4 Standard on "Transducer Electronic Data Sheet", published as "A Smart Transducer Interface for Sensors and Actuators - Mixed-Mode Communication Protocols and Transducer Electronic Data Sheet (TEDS) Formats" by the IEEE.org
11. Handbuch der Mess- und Automatisierungstechnik in der Produktion, Der.: H.-J. Gevatter, U. Grünhaupt: Chapter 4: Beschleunigung, Th. Petzsche u. H. Müller; Springer Verlag, 2006 (in German)
12. Acceleration Measurement Optimization: Mounting Considerations and Sensor Mass Effect: Andy Cook, Marine Dumont–XXXIV. Int. Modal Analysis Conference, IMAC 2016

Chapter 6
Experimental Evaluation and Statistical Analysis of Synchronous Averaging

V. Camerini, G. Coppotelli, and S. Bendisch

Abstract Time synchronous averaging for the extraction of periodic waveforms is a rather common processing method for rotating machinery diagnosis. By synchronizing the signal to the rotational angle of the component of interest (e.g. by using a tachometer reference signal), it is possible to perform the averaging in the angular domain, thus obtaining an angle-synchronous signal. Such an operation usually requires a resampling procedure. In this paper, the operations of averaging in time and angular domain are thoroughly discussed, referring to the main measurement and computational errors affecting the extracted waveform. The effects of uncertainty in the pulse arrival times of the reference signal on the synchronous averaging method are studied. Jittering of the reference signal affects the quality of the synchronous averaging process resulting in an attenuation of the extracted synchronous signal components, especially in the high frequency band. A theoretical analysis of the linkage between jitter model and attenuation is performed and an analytical model is proposed. The agreement of the analytical model with numerical simulations is first shown, and then an experimental case study involving the early detection of bearing damage is examined. The results are discussed in the framework of the cyclostationary signal theory.

Keywords Jitter • Error analysis • Synchronous average • Cyclostationarity

6.1 Introduction

Rotating machinery vibration signals have been recently modeled as cyclostationary processes [1–5]. Cyclostationarity is a property characterizing stochastic processes whose statistics vary periodically with respect to some variable. Due to this generality, cyclostationarity property is particularly fit to describe rotating machinery signals [6]. Formally, a first order time-cyclostationary signal (CS1) is such that its expected value $m_X(t)$ is periodic with some period T [6], i.e.:

$$m_X(t) \triangleq E[x(t)] = m_X(t+T) \tag{6.1}$$

Where $E[\bullet]$ is the ensemble average operator. More generally, a nth order cyclostationary signal (CSn) has periodic nth order moments. Among CSn signals, the class of CS1 and CS2 are particularly important in machinery diagnostic. Specifically, the CS1 part of the signal carries in fact important information about gears and shafts health, e.g. it is strongly correlated with unbalance of the shafts and with the teeth-meshing process of gears [6]. The second order cyclostationary part carries instead information about potential bearing faults [4]. Rotating machinery signals contains multiple periodicities (i.e. they are composed of different CS components of different period T, associated to components rotating at different speeds). They are then classified as poly-cyclostationary (PC) processes [6]. According to [6], this means that the set of their statistical Fourier coefficients is the combination of the statistical Fourier coefficients of all the basic cyclostationary signals composing the poly-cyclostationary signal. Thus, in a PC signal there exist more CS components with different fundamental periods. Without loss of generality, the extraction of the periodic mean (CS1 component) of a given period T from a cyclostationary

V. Camerini (✉)
Airbus Helicopters, Industriestraße 4, Donauwörth, Germany

Department of Mechanical and Aerospace Engineering, University of Rome La Sapienza, Via Eudossiana 18, Roma, Italy
e-mail: valerio.camerini@uniroma1.it

G. Coppotelli
Department of Mechanical and Aerospace Engineering, University of Rome La Sapienza, Via Eudossiana 18, Roma, Italy

S. Bendisch
Airbus Helicopters, Industriestraße 4, Donauwörth, Germany

N. Dervilis (ed.), *Special Topics in Structural Dynamics, Volume 6*, Conference Proceedings
of the Society for Experimental Mechanics Series, DOI 10.1007/978-3-319-53841-9_6

signal is considered in this paper, avoiding the distinction between the different classes of cyclostationary processes. An accurate estimation of the CS1 component of a signal is key to the diagnostics procedure of rotating machinery for two reasons. First, its important role in gears and shafts diagnostic as mentioned, and secondly, subtracting the periodic mean from the signal allows for directly analyzing the pure CS2 part, correlated with, e.g., bearing faults (for a more detailed definition of pure cyclostationarity at order n, see [6]). The operator $P[x(t)]$ was introduced in [6] as the operator which extracts the periodic part of a signal. Assuming cycloergodicity of the signal and since for a CS1 signal the periodic part coincides with its expected value, the ensemble average of Eq. (6.1) can be replaced by the operator P: Such an operator can be given either in terms of infinite cycle average or in terms of a Fourier series. Here we report it in the form of infinite cycle average, addressing the reader to [6] for further details about its equivalent Fourier series representation. Hence, from the above definition:

$$P\left[x(t)\right] = \lim_{N\to\infty} \frac{1}{2N+1} \sum_{i=-N}^{N} x\left(t + iT\right) \tag{6.2}$$

Equation (6.2) is of practical relevance since it states the equivalence of cycle averaging with ensemble averaging for cycloergodic signals [6]. Such an equivalence enables the estimation of the periodic mean $m_X(t)$ from a single realization of the process of interest. In a way, this presents analogies with the power spectral density (PSD) estimation through segment averaging: the property of cycloergodicity for CS signals is in fact the equivalent of the ergodicity property for stationary signals. Since any measurement process results in a finite-length signal, $m_X(t)$ needs in practice to be estimated from a finite set of cycles. Different estimators of $m_X(t)$ where proposed in literature. Following [6], we refer to those estimators as first order cyclostationary tools. Two situations of interest can be distinguished. In one case, the fundamental cycle of the CS signal is known a priori, e.g. from the knowledge of the kinematic relations in a machine. In the other, such basic cycle is unknown and one must resort to blind estimators. Generally, blind filters performance is negatively affected by signal to noise ratio. Moreover, those filters require a proper parameter tuning which may not be trivial in every case. When the cycle of the signal is known, a popular estimator of $m_X(t)$ is the synchronous average (SA) operator, which is better known as Time Synchronous Average (TSA) due to its original formulation in time domain. TSA is basically approximating Eq. (6.2) using a finite number of averages N. Rotating machinery signals are better described as periodic in the angular domain defined by the reference shaft rotation angle (i.e. they are angle-cyclostationary rather than time-cyclostationary). Therefore, they are better analyzed in the angle-domain, where the cyclostationary property is preserved. The description of a signal in the angular domain is typically achieved through computed order tracking [7], which consists of resampling the time signal at constant-angle increments based on the information from a tachometric signal. The tachometer device provides a certain number of tacho pulses per revolution of a reference shaft, which can be used as a reference for resampling the signal at constant angular increments. Once the resampled signal is obtained as a function of the reference shaft angle θ, the periodic mean $m_X(\theta)$ can be estimated given the fundamental cycle Θ. In absence of a tachometric reference signal, the tacho pulse instants may still be estimated directly from the vibration signal under some conditions (e.g. small speed fluctuations), as in [12, 13]. Practically, the tacho pulses time of arrival suffers in any case from a random jitter error which arises mostly from the measurement process in the case of pulses obtained from a tachometric signal, and from estimation errors in the case of pulses obtained from the vibration signal. In this paper, a comprehensive analysis of the effect the random jitter error on the synchronous averaging procedure is performed. First, the synchronous averaging procedure is briefly introduced, then a model for SA in presence of a general random jitter error affecting tacho pulses arrival time is proposed. Errors in amplitude and phase of the recovered signal are derived. The special case of a uniform distribution of the jitter error is discussed. Analytical results are compared to numerical simulations. Finally, an application of synchronous averaging aimed at removing the CS1 part from a signal measured on a helicopter gearbox is presented with considerations regarding the effects of the jittering error.

6.2 Theoretical Background

6.2.1 Synchronous Averaging

The basic idea of synchronous averaging is illustrated in Fig. 6.1. It consists of averaging data values separated by exact periods. All the components in the signal which are not synchronous with the fundamental period get attenuated in the process. In the limit of an infinite number of averages, the purely synchronous, periodic part of the signal is extracted (see Eq. 6.2). As introduced, under the assumption of cycloergodicity, SA is indeed a practical estimation of the periodic mean of a CS signal [6], that is its first order cyclostationary part of cycle equal to the fundamental period used for averaging. The

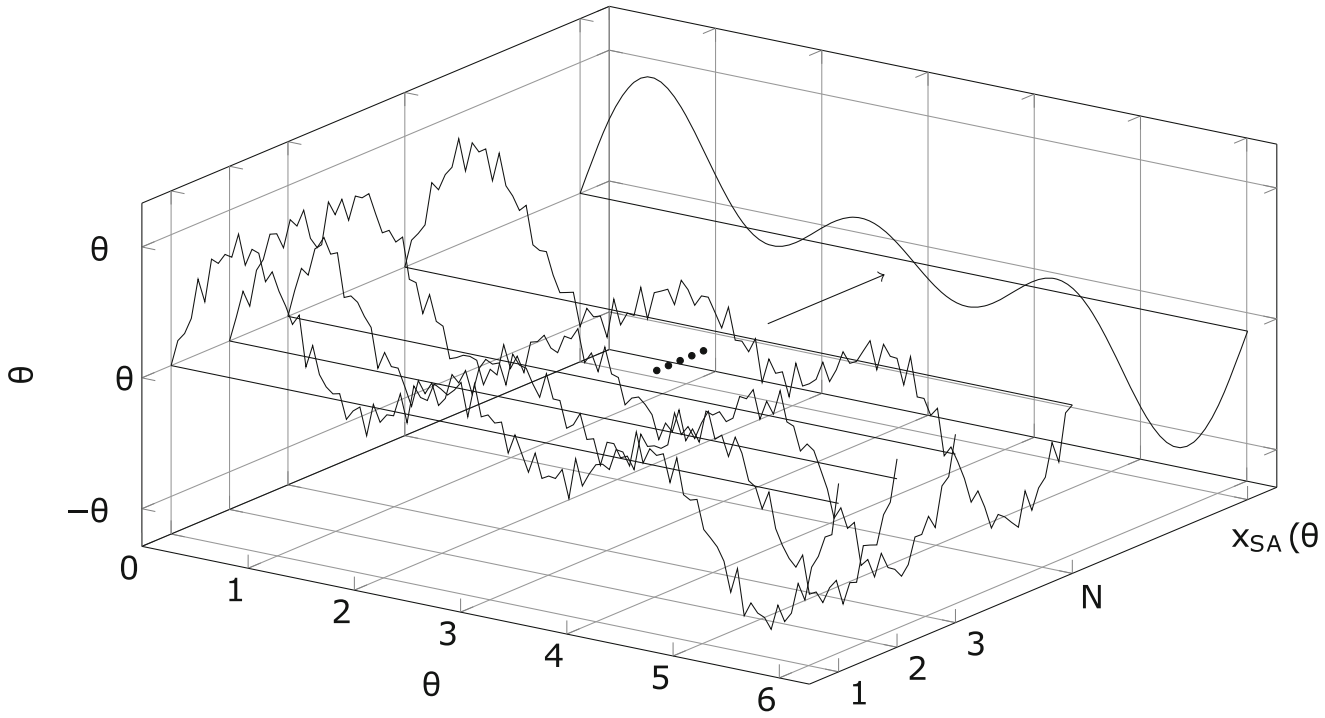

Fig. 6.1 Synchronous averaging procedure in angular domain

equation for SA of a signal of fundamental cycle Θ reads then in angle domain:

$$SA_{\Theta}\left[x\left(\theta\right)\right] = \frac{1}{N}\sum\nolimits_{i=0}^{N-1} x\left(\theta + i\Theta\right) \tag{6.3}$$

Synchronous averaging is thus equivalent to applying a comb filter to the signal, which extract the multiples of the reference harmonic. The number of averages controls the bandwidth of the lobes, the amount of noise rejection and the position of the notches of the filter. In fact, by Fourier transforming to the order domain γ (i.e. the angular-counterpart of the frequency domain normalized by the fundamental cycle of the signal), the SA reads:

$$\mathcal{F}_{\theta\to\gamma}\left\{SA_{\Theta}\left[x\left(\theta\right)\right]\right\} = X\left(\gamma\right)\sum\nolimits_{i=0}^{N} e^{j2\pi i\gamma} = X\left(\gamma\right)H_{SA}\left(\gamma\right) \tag{6.4}$$

Where the symbol j indicates the imaginary unit and $X(\gamma)$ is the order domain representation of $x(\theta)$. Here the quantity $H_{SA}(\gamma)$ acts as a transfer function which filters the angle-domain signal. It is easy to check that such a transfer function has unitary gain when the order variable gamma takes integer values. Developing the summation in Eq. (6.4) one has:

$$H_{SA}\left(\gamma\right) = \frac{\sin\left(\pi\gamma N\right)}{N\sin\left(\pi\gamma\right)} e^{j\pi\gamma(N-1)} \tag{6.5}$$

Figure 6.2 shows the gain of the transfer function of Eq. (6.5) on a linear scale, taking $N = 20$. The depicted comb filters out the signal which is not synchronous with the reference order. It can be shown that the stationary noise is attenuated by a factor $1/\sqrt{N}$ [6]. From Eq. (6.5), the parameter N controls the selectivity of the filter and the attenuation of the non-synchronous components. Moreover, the position of the notches depends on the number of averages as well. Hence, if a strong periodic component of a cycle which is not multiple of the basic cycle of interest is present in the signal, it can be completely cancelled from the response if it is possible to select a number of averages such that a notch gets located in correspondence of the frequency of such component. Since the averaging procedure results in a signal representing one cycle of interest, the maximum resolution of the transform in the order domain will be that of one order. Therefore, the residual non-synchronous components will leak into the bins representing the response at a given integer order. Further details on the interpretation of synchronous averaging as a comb filter are given in [11].

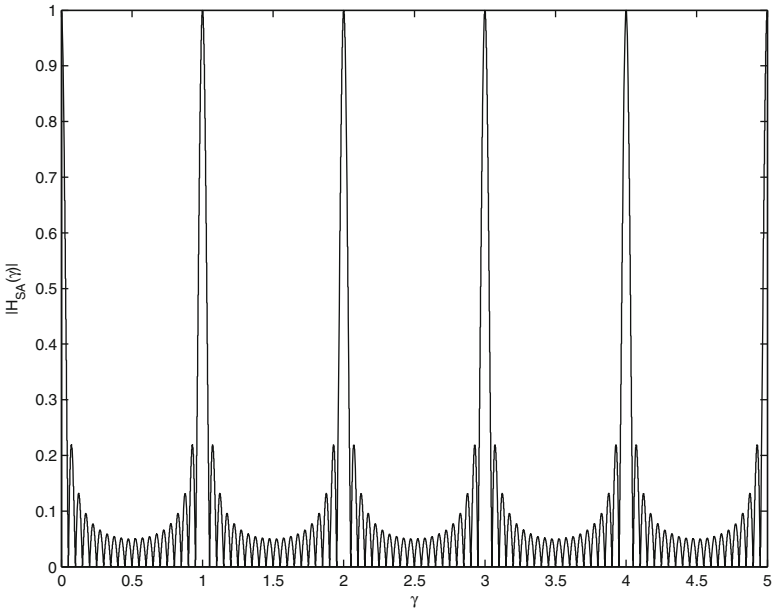

Fig. 6.2 Synchronous averaging in shaft order domain, gain of the transfer function for N = 20

6.2.2 Jittering Error Model

As already introduced, SA is typically performed using the pulse arrival times from a tachometer device to detect the beginning and end of each signal cycle. If the pulse arrival times are not exact, we expect some errors in the obtained averaged signal. A first model for the jittering error due to uncertainty in the pulse arrival times was given in [12], with the aim of discussing the effects of phase estimation errors in the automatic tacho-less synchronous averaging procedure that they propose, extending the work in [13]. The authors present the following model for the *i*-th rotation period of a signal considering a random jitter estimation error ε_i of the tacho pulse instant at rotation *i*:

$$x_i(t) = s\left(t - \epsilon_i\right) + b(t) \tag{6.6}$$

Where *s(t)* is the deterministic part of the signal periodic with the period of interest and *b(t)* the random and non-synchronous sources. After an infinite number of averages, i.e. in the case of ideal synchronous averaging of Eq. (6.2), the extracted signal reads accordingly:

$$m_x(t) = E\left[x_i(t)\right] = E\left[s\left(t - \epsilon_i\right)\right] \tag{6.7}$$

Then, assuming commutativity of the Fourier transform with expectancy and considering that $m_x(t)$ is a periodic signal, its frequency representation reads:

$$M_x(f) = E\left[S(f)e^{-j2\pi f\epsilon_i}\right] = S(f)E\left[e^{-j2\pi f\epsilon_i}\right] \tag{6.8}$$

Which, introducing the probability density function (p.d.f.) of the random jitter variable ε_i and naming it $p(\varepsilon_i)$, can be written as:

$$M_x(f) = S(f)\Phi(f) \tag{6.9}$$

With $\Phi(f)$ denoting the Fourier transform of $p(\varepsilon_i)$, acting as a low-pass filter on the SA spectrum. Clearly, the narrower is the probability density function of the random jitter error, the higher is the cut-off frequency of the low-pass filter (in the limit of zero jitter we may think of the p.d.f. as a Dirac delta distribution, which has unit Fourier transform and results therefore in no attenuation of the periodic signal at any order). This simple model has two main limitations. On one side, the effect of a finite number of averages is not discussed. On the other hand, we point out that the model is equivalent to summing cycles of the signal with a random phase delay ε_i. Indeed, one should notice that the effect of the random jitter

on the cyclic average is subtler. In fact, the jitter on the recovered tacho pulses arrival time affects both the phase and the frequency of the signal corresponding to the i-th cycle. For major understanding, the time-domain notation is used, for the notions of frequency domain and time-averaging are more easily understood than their angle-domain counterparts. However, the discussion and the derived results hold equally in the angular domain. To derive a general model which better represents the effects of the jitter, we consider the generic harmonic component at frequency f of the signal of interest. The i-th tracked cycle is determined using the reference tacho-pulses at times $[iT + \varepsilon_i, (i + 1)T + \varepsilon_{i+1}]$. The corresponding vibration signal is resampled to a constant number of samples N_p. Assuming constant speed[1] of the tracked shaft, the times corresponding to the re-sampling points can be determined by piecewise linear interpolation of each interval without introducing signal distortion. The values of the vibration signal are then obtained using higher-order interpolation (e.g. spline interpolation) with care of not introducing aliasing in the resampled signal. A thorough discussion of the effect of resampling on the vibration signal in the context of order tracking is given in [14]. Here we are not interested in analyzing this effect and we assume that the recovered signal is not attenuated nor aliased from the interpolation filter (i.e. ideal interpolation with a proper number of resampling points is performed). Thus, N segments of length N_p are obtained and can then be averaged resulting in the synchronous average estimation. This procedure is equivalent, taking the limit of the continuous signal case (i.e. in the limit of sampling period going to zero), to mapping each detected cycle to the interval *[0,T]* and then averaging in order to obtain the synchronous average signal. By representing *x(t)* in the Fourier domain as the sum of infinite complex sinusoids, the generic unit-amplitude component of frequency f^* and phase φ^* undergoing the SA process of fundamental cycle T is then mapped to the considered interval according to:

$$x_i(t) = e^{j2\pi\left((f^*+f_i)t+\frac{\phi^*}{2\pi}+\epsilon_i f^*+iTf^*\right)} \tag{6.10}$$

Where the i-th pulse defines the beginning of the i-th cycle and ε_i is the jitter error on the i-th pulse arrival time, and f_i is the deviation from f^* which appears in the estimated i-th cycle due to the difference in the estimated duration $(i + 1)T + \epsilon_{(i+1)} - (iT + \epsilon_i)$ and the actual duration of the cycle T. It is given as:

$$f_i = \frac{f^*}{T}\left(\epsilon_{i+1} - \epsilon_i\right) \tag{6.11}$$

The synchronous average reads then:

$$X_{SA}(t) = \frac{1}{N}\sum\nolimits_{i=1}^{N} x_i(t) = \frac{1}{N}\sum\nolimits_{i=1}^{N} e^{j2\pi\left((f^*+f_i)t+\frac{\phi^*}{2\pi}+\epsilon_i f^*+(i-1)Tf^*\right)} \tag{6.12}$$

One may recognize that setting the jitter error to zero in Eq. (6.12), it reduces to an expression that represents a periodic component of frequency f multiplied by an attenuation factor and undergoing a phase shift depending solely on the number of averages and the product Tf^*. Specifically, when such product is an integer, meaning that f^* is a multiple of the fundamental period, the attenuation factor is identically one for any value of N and no phase shift takes place. Conversely, when the product is non-integer, the component is not synchronous with the fundamental period and gets attenuated according to the transfer function of the SA from Eq. (6.5). In fact, the sum in Eq. (6.12) can be viewed as a sum of phasors of frequency f^* in the complex plane: when Tf^* is not integer, each one will add with its own phase. The notches in the filter description of Eq. (6.5) are then located at those frequencies (orders in Eq. 6.5) corresponding to phasors that sum to zero in the complex plane. Taking the Fourier transform of Eq. (6.12) and using a rectangular window limiting the signal to the interval *[0, T]* gives the frequency representation of the extracted periodic-mean signal as:

$$X_{SA}(f) = e^{j\phi^*}\delta\left(f - f^*\right) * \frac{1}{N}\sum\nolimits_{i=1}^{N} D\left(f - f_i\right) e^{j2\pi(\epsilon_i f^*+iTf^*)} \tag{6.13}$$

Where $\delta(f)$ is the Dirac delta function and $D(f)$ is the Fourier transform of the rectangular window shifted to the interval *[0, T]*:

$$D(f) = T\frac{\sin\left(\pi fT\right)}{\pi fT}e^{-j\pi fT} \tag{6.14}$$

[1]We consider here a constant speed shaft as to have constant fundamental period T, enabling to confuse the angle-cyclostationarity with the time-cyclostationarity. When analyzing the signal in angular domain, we indeed have a constant fundamental angular period Θ.

Equation (6.13) expresses the frequency representation of the synchronous average as the convolution of the spectral line of frequency f^* and phase Φ^* with a function of the number of averages and of the jitter random variables which we will refer to as the SA kernel.[2] Again, when the jitter is null, Eq. (6.13) boils down to the product of the two terms:

$$X_{SA}(f) = D\left(f - f^*\right) \frac{1}{N} \sum_{i=0}^{N-1} e^{j2\pi(Tf^*)} \tag{6.15}$$

The interpretation of Eq. (6.15) is still that of a filter attenuating non-synchronous components. However, keeping into account the finite duration of the signal has introduced a convolution of the spectral line located at f^* with the transform of the causal rectangular window of duration T, i.e. $D(f)$. The discrete representation in the frequency domain can be derived by sampling the continuous representation according to the sampling frequency. Note that since the duration of the considered record is T, the actual transform of $x_{SA}(t)$ can resolve only components which have a separation equal or greater than the inverse of the fundamental period T, which is enough, since ideally we aim to extract the periodic part of the signal synchronous to the period T. Such a periodic part can always be represented as a Fourier series of harmonic components spaced apart by $1/T$. The residual disturbance will affect the extracted signal frequency representation by leaking energy into the bins representing the actual periodic signal. Moving to the case of jittered time-pulses, we see from Eq. (6.13) that, the synchronous averaged signal representing the cyclic average of the component of the signal of frequency f^*, is represented in frequency domain as the sum of N harmonic components distributed around the actual component frequency f^* with the distribution of the random variable f_i and different phase shift depending on the random phase error introduced through ε_i. Each frequency line is then weighted according to the convolution with the transform of the rectangular window. To better clarify, consider the transform of the f^* component of the vibration signal estimated for the i-th cycle:

$$X_i(f) = e^{j\phi^*} \delta\left(f - f^* - f_i\right) e^{j2\pi(\epsilon_i f^* + iTf^*)} * D(f) \tag{6.16}$$

Equation (6.16) shows that in mapping the vibration signal sampled from the interval $[iT + \varepsilon_i, (i+1)T + \varepsilon_{i+1}]$ to the interval $[0, T]$ we introduce both an error in the phase of the signal equivalent to $2\pi\epsilon_i f^*$ and a frequency shift equal to f_i. Note that the extent of the errors is consistently depending on the frequency of the considered component and will be higher for the high-frequency components of the signal. Here the attenuation factor depending on the product Tf^* gets coupled with the random jittering effect. Another important observation concerns the choice of the rectangular window. It is well known that the rectangular window is the best choice in terms of achieving separation between harmonic components, although it generates broadband leakage. Since our resolution is limited to one period, choosing another window would result in excessive mixing of adjacent synchronous components of the signal. Furthermore, in the ideal case of zero jittering, the extracted periodic components in the DFT which are synchronous with the period T of the considered cycle will not suffer from scalloping loss and will not mutually affect each other thanks to the position of the nulls of the window. The aim of the next section is to establish the magnitude and phase errors on the generic harmonic component of the synchronous averaged signal due to the random jittering variables ε_i.

6.2.3 Jittering Error Analysis

The model from Eq. (6.16) is suitable for analyzing the effect of jittering variables on the reconstructed extracted periodic mean through the SA estimator. By making use of Euler's identity, from Eq. (6.16) we give the absolute value of the synchronous averaged unit amplitude component f^* as:

$$|X_{SA}(f)| = \sqrt{\left(\frac{1}{N}\sum_i \cos(k_i)\, sinc(\tau_i)\, T\right)^2 + \left(\frac{1}{N}\sum_i \sin(k_i)\, sinc(\tau_i)\, T\right)^2} \tag{6.17}$$

With:

$$k_i = 2\pi\left(f^*\epsilon_i + iTf^*\right) - \tau_i \tag{6.18}$$

$$\tau_i = \left(f - f^* - f_i\right)\pi T \tag{6.19}$$

[2] We make use of the sifting property of the delta function: $f(x) * \delta(x-a) = f(x-a)$.

$$sinc(x) = \frac{\sin(x)}{x} \tag{6.20}$$

Similarly, the phase reads:

$$\phi_{SA}(f) = \phi^* + \phi_r \tag{6.21}$$

Where:

$$\phi_r = \tan^{-1} \frac{\frac{1}{N}\sum_i \sin(k_i)\, sinc(\tau_i)\, T}{\frac{1}{N}\sum_i \cos(k_i)\, sinc(\tau_i)\, T} \tag{6.22}$$

To derive statistics on the amplitude and phase errors of depending on the frequency of the considered component and on the jittering variables, it is necessary to assign a probability density function to the random variables. In this work, the following assumptions are made:

1. The jitter variables ε_i are independent, identically distributed (i.i.d.);
2. The jitter variables are uniformly distributed as $U_{[-\Delta/2,\, \Delta/2]}$.

While the exact distribution of the jitter error is unknown, it will be shown in Sect. 6.3 that assuming a uniform distribution has practical relevance for some configurations of the acquisition system. We observe that both the statistics are made up from the sum of N functions of random variables, each one depending on two i.i.d. random variables ε_i, ε_{i+1}. We denote g_{1i} and g_{2i} the i-th functions of the random variables ε_i, ε_{i+1} which appear respectively inside the summations in the denominator and the numerator of Eq. (6.22) and introduce the index $k = \{1,2\}$. The dependency of g_{ki} on the random variables and the frequency is omitted for easiness of notation. Given the assumptions, we now compute the distribution for the absolute value. The two squared terms under root in Eq. (6.17) are both in the form of the average of a series of random variables. Two distinct cases arise: when analyzing a synchronous component, the product Tf^* is an integer and, owing to the periodicity of the trigonometric functions, it can be neglected from the equation. For asynchronous components, the product is not an integer and therefore cannot be neglected. In such a case, it is difficult to derive appropriate statistics for the solution. However, we can still expect that the asynchronous terms will be attenuated in a similar way as in absence of jittering, though the case of the phases summing up to zero will become extremely unlikely, and seemingly the frequency of each component will undergo slight fluctuations per each revolution. Consequently, we cannot expect any equivalent of the zeros of the transfer function of Eq. (6.5). In fact, to zero out with certainty a component f^*, the SA kernel shall be certainly zero for some value of f^*, which is impossible due to the presence of the random variables. Conversely, if we focus on the synchronous components, that is the part of the signal that we are interested in extracting, then the processes g_{ki} fulfil mixing conditions[3] such that the central limit theorem holds for N large enough:

$$\sqrt{N}\,(\boldsymbol{g} - E[\boldsymbol{g_i}]) \rightarrow N_2(0, \boldsymbol{\Sigma_i}) \tag{6.23}$$

Where:

$$\boldsymbol{g} = \left[\frac{1}{N}\sum_i g_{1i}, \frac{1}{N}\sum_i g_{2i}\right]^T = [g_1, g_2]^T \tag{6.24}$$

N_2 denotes the multivariate normal distribution with two degrees of freedom and $\boldsymbol{\Sigma}$ the associated covariance matrix (to not be confounded with the number of averages N). Given the independence of the random variables (i.e. $p_{X,Y}(x,y) = p_X(x)p_Y(y)$ when $p(\bullet)$ denotes a probability density function), and saving from the notation the dependency of $\boldsymbol{g}$ on all the deterministic variables, the expected value of $\boldsymbol{g}$ is given as:

$$E[g_{ki}] = \frac{1}{\Delta^2}\int_{-\frac{\Delta}{2}}^{\frac{\Delta}{2}}\int_{-\frac{\Delta}{2}}^{\frac{\Delta}{2}} \boldsymbol{g_{ki}}(\boldsymbol{x},\boldsymbol{y})\, dxdy;\, k = \{1,2\} \tag{6.25}$$

[3]Here it is sufficient to observe that g_{ki}, g_{kj} are mutually independent for every $|i\text{-}j| > 1$.

In the following, we consider the solution for the frequency line $f = f^*$ as to simplify the computations. Moreover, we set $f^* = 1$ and recognize that the dependency of the attenuation and phase shift can be incorporated without loss of generality in the jitter statistics. Specifically, linear relationship hold for the transformation of uniform random variables. Similarly, we consider the unitary period $T = 1$. Under the mentioned conditions, the integrals from Eq. (6.25) read:

$$E\left[g_{1i}\right] = \frac{1}{\Delta^2}\int_{-\frac{\Delta}{2}}^{\frac{\Delta}{2}}\int_{-\frac{\Delta}{2}}^{\frac{\Delta}{2}} \cos\left(\pi\left(x+y\right)\right) sinc\left(\pi\left(x-y\right)\right) dxdy \tag{6.26}$$

$$E\left[g_{2i}\right] = \frac{1}{\Delta^2}\int_{-\frac{\Delta}{2}}^{\frac{\Delta}{2}}\int_{-\frac{\Delta}{2}}^{\frac{\Delta}{2}} \sin\left(\pi\left(x+y\right)\right) sinc\left(\pi\left(x-y\right)\right) dxdy \tag{6.27}$$

The closed form solution of the second (Eq. 6.27) integral is identically zero, whereas for the first (Eq. 6.26) integral it takes the following expression:

$$E\left[g_{1i}\right] = \frac{1}{4\nu^2}\left(-4\gamma\cos\left(\nu\right) + 4\cos\nu Ci\left(2\nu\right) - 4\cos\left(\nu\right)\ln\left(2\nu\right) + 4\sin\left(\nu\right) Si\left(2\nu\right)\right) \tag{6.28}$$

Where *Ci(x)* and *Si(x)* are the cosine and sine integral functions and $\nu = \pi\Delta$. Considering that the random variables take small values bounded in the region $[-\Delta;\Delta]\times[-\Delta;\Delta]$, we propose to approximate the integrals by expanding the sine cardinal function in power series and truncating the expansion to the second-order. Hence, Eq. (6.26) becomes:

$$E\left[g_{1i}\right] = \frac{1}{\Delta^2}\int_{-\frac{\Delta}{2}}^{\frac{\Delta}{2}}\int_{-\frac{\Delta}{2}}^{\frac{\Delta}{2}} \cos\left(\pi\left(x+y\right)\right)\left(1 - \frac{\pi^2x^2}{6} - \frac{\pi^2y^2}{6} + \frac{\pi^2}{3}xy + q\left(x,y\right)\right) dxdy \tag{6.29}$$

Using trigonometric identities for *cos(x + y)*, considering the extremes of integration and observing that *cos(x)* is a bounded function, it is possible to show that the residual *q(x,y)* integrates to a small error in the considered region. Therefore, we give the following approximation for the expected value:

$$E\left[g_{1i}\right] \approx -\frac{\pi^2\left(\frac{\Delta}{2}\right)^2 + 2\cos\left(\pi\Delta\right) - 2}{3\pi^2\left(\frac{\Delta}{2}\right)^2} \tag{6.30}$$

With similar reasoning, we derive approximate expressions for the terms of the covariance matrix as:

$$\sigma_{1i}^2 \approx \frac{\pi^2\left(\frac{\Delta}{2}\right)^2\left(-32\pi^4\left(\frac{\Delta}{2}\right)^4 + 120\pi^2\left(\frac{\Delta}{2}\right)^2 - 21\cos\left(2\pi\Delta\right) + 21\right) - 32\left(\pi^2\left(\frac{\Delta}{2}\right)^2 + 2\cos\left(\pi\Delta\right) - 2\right)^2}{\frac{288\pi^4\Delta^4}{16}} \tag{6.31}$$

$$\sigma_{2i}^2 \approx -\frac{32\pi^4\left(\frac{\Delta}{2}\right)^4 - 168\pi^2\left(\frac{\Delta}{2}\right)^2 - 21\cos\left(2\pi\Delta\right) + 21}{\frac{288\pi^4\Delta^4}{16}} \tag{6.32}$$

$$\sigma_{12i}^2 \approx 0 \tag{6.33}$$

Where Eq. (6.31) is the variance of g_{1i}, Eq. (6.32) the variance of g_{2i} and Eq. (6.33) the covariance. Next, considering the distribution of the absolute value, we have:

$$\left|X_{SA}\left(f^*\right)\right|^2 = \boldsymbol{g}^T\mathbf{I}\boldsymbol{g} \tag{6.34}$$

The random vector $\boldsymbol{g}$ is distributed as $N_2(\mathrm{E}[\boldsymbol{g_i}], \boldsymbol{\Sigma})$ according to Eq. (6.23), where the terms in $\boldsymbol{\Sigma}$ are given from Eqs. (6.31, 6.32, 6.33, 6.34) and the quantity in Eq. (6.34) is a quadratic form of normal variables. Such distributions are widely studied in literature [9]. As for this work, the probability density function was approximated using the moment-based method as proposed in [9]. The procedure can be summarized as follows[4]:

[4]The general expression for a quadratic form in the multivariate normal variable $\mathbf{X}$ is $\mathrm{Q}(\mathbf{X}) = \mathbf{X}^{\mathrm{T}}\mathbf{A}\mathbf{X}$. In the considered case $\mathbf{A} \equiv \mathbf{I}$ and since $\mathbf{S} > 0$, its eigenvalues are always positive. For the more general case, refer to [9].

1. Determine the eigenvalues λ_k and the matrix of the normalized eigenvectors $\mathbf{\Lambda}$ of $\mathbf{\Sigma}$;
2. Compute $\mathbf{\Sigma}^{-1/2} = \mathbf{\Lambda}\ \mathrm{diag}(\lambda_k{}^{-1/2})\ \mathbf{\Lambda}^{\mathrm{T}}$;
3. Compute $\boldsymbol{b} = \lambda^x\ \mathbf{\Sigma}^{-1/2}\mathrm{E}[\boldsymbol{g}]$;
4. Consider the transformed quadratic form $\mathrm{Q}_1 = \mathbf{W_1}^{\mathbf{T}}\mathbf{A_1}\mathbf{W_1}$ where the random normal variables have now identity covariance matrix and mean $\boldsymbol{b}$, and $\mathbf{A_1}$ is defined as $\mathrm{diag}(\lambda_k)$;
5. Compute the cumulants and moments of Q_1 respectively as:

$$k(s) = 2^{s-1}s!\left(\frac{tr(\boldsymbol{A}_1)^2}{s} + \boldsymbol{b}^T\boldsymbol{A}_1^s\boldsymbol{b}\right) \tag{6.35}$$

$$\mu(h) = \sum_{i=0}^{h-1}\frac{(h-1)!}{(h-1-i)!i!}k\,(h-i)\,\mu(i) \tag{6.36}$$

6. With $Z = X/\beta$ and X gamma-type random variable, use Laguerre polynomials to approximate the p.d.f. as:

$$f(x) = \frac{x^{\nu}e^{-\frac{x}{\beta}}}{\beta^{\nu+1}}\sum_{j=0}^{d}\delta_j^{\nu}L_j^{\nu}\left(\frac{x}{\beta}\right) \tag{6.37}$$

Where:

$$\delta_j^{\nu} = \sum_{k=0}^{j}\frac{(-1)^k j!\mu_Z\,(j-k)}{k!\,(j-k)!\Gamma\,(\nu+j-k+1)} \tag{6.38}$$

$$L_j^{\nu}(x) = \sum_{k=0}^{i}d_{i,k}^{\nu}x^k \tag{6.39}$$

$$d_{i,k}^{\nu} = \frac{(-1)^{i-k}\Gamma\,(i+\nu+1)}{(i-k)!k!\Gamma\,(\nu+k+1)} \tag{6.40}$$

$$\beta = \frac{\mu_X(2)}{\mu_X(1)} - \mu_X(1) \tag{6.41}$$

$$\nu = \frac{\mu_X^2(1)}{\mu_X(2) - \mu_X^2(1)} - 1 \tag{6.42}$$

7. Finally, the distribution function evaluated at $c > 0$ is obtained by integration of Eq. (6.37) as:

$$F_X(c) = \int_0^c f_X(x)dx \tag{6.43}$$

Equations (6.37) and (6.43) give an approximation to the probability density function and to the cumulative distribution function of the squared absolute value $|X_{SA}(f)|^2$. Since $|X_{SA}(f)| = \sqrt{|X_{SA}(f)|^2}$ and the square root is an invertible and monotonically increasing function of the positive argument when negative solutions are not allowed, it also holds for the c.d.f.:

$$F_{|X_{SA}(f)|}(y) = P\left(|X_{SA}(f)|^2 \leq y^2\right) \tag{6.44}$$

Similarly, we have for the distribution of the phase:

$$R = \frac{\frac{1}{N}\sum_i \sin\,(k_i)\,sinc\,(\tau_i)}{\frac{1}{N}\sum_i \cos\,(k_i)\,sinc\,(\tau_i)} = \frac{z}{w} \tag{6.45}$$

Which for the same previous arguments can be approximated for large N with the ratio distribution of two normal variables z, w. For such a distribution, the analytical probability density function and cumulative distribution function are known [15]. Considering uncorrelated variables as from Eq. (6.33), we define as in [15]:

$$b = \frac{\mu_w}{\sigma_w}; a = \frac{\mu_z}{\sigma_z}; r = \frac{\sigma_w}{\sigma_z} \tag{6.46}$$

With μ_z, μ_w, σ_z, σ_w being respectively expected value and standard deviation of normal variables z, w. According to [15], for $a < 2.5$ and $b > 8$, R is well approximated from a normal distribution such that:

$$R \sim N\left(\mu_R, \sigma_R\right) \tag{6.47}$$

Where:

$$\mu_R = \frac{a}{(1.01b - 0.2713)\, r} \tag{6.48}$$

$$\sigma_R^2 = \frac{\left(\frac{a^2+1}{b^2+0.108b-3.795} - \mu_R^2\right)}{r^2} \tag{6.49}$$

In the case under study, a is always zero since μ_z is always zero as from Eq. (6.27). Furthermore, μ_w/σ_w from Eqs. (6.30) and (6.31) is of the order of magnitude of hundreds for typical values of Δ. Therefore, the normal approximation to R generally holds and again, using the same argument as from Eq. (6.44), we can derive the approximated distribution of ϕ_i given the approximated distribution of R.

6.3 Results

6.3.1 Numerical Validation of the Jitter Analysis

We present here the main results of the study in terms of quantification of the tacho signal jittering effects. The jitter variables are modelled as a centered uniform distribution in the interval $[-\Delta/2, \Delta/2]$. Such a choice is motivated if we think of the prevalent error in pulse arrival time being due to the discretization of the keyphasor signal used in the tacho device for the pulse time of arrival determination. Figure 6.3 (similarly to [7] shows a keyphasor signal sampled with a sampling frequency f_{KP}. The rate of sampling f_{KP} at which the keyphasor is sampled determines the resolution of the keyphasor pulse arrival times. A pulse will be detected when, e.g., the rising edge of the signal surpass a threshold. We model the uncertainty due to such resolution as a uniform random variable, hence we assume $\Delta = 1/f_{KP}$ in the distribution of the jitter variables. Such an assumption is reasonable when the main uncertainty is coming from the discretization of the keyphasor signal. In order to validate the statistical analysis of Sect. 6.2.3, the results in terms of statistical moments and distributions are compared to numerical simulations drawn from the proposed model in a Montecarlo-fashion. The remainder of the section is organized as follows: first, the expected value and variance computed for g_{ki} are validated against numerical simulation. Then, the Laguerre-expansion approximation to the distribution of the absolute value is compared to the numerically simulated distribution. The same comparison is finally made for the phase error distribution. All the simulations are run in MATLAB® environment.

6.3.1.1 Expected Value and Variance of the Functions g_{ki}

The free parameters used in the simulation and in the analytical expressions are given in Table 6.1. The high value for the number of revolutions N is fed to the simulation to obtain an estimate of the expected value and the variance of the simulated quantity. Figure 6.4 shows the analytical mean value in closed form and approximated through Eq. (6.30) as compared with the outcome of numerical simulations from the model. In the upper part of the plot it can be seen that the mean values (exact, approximated, simulated) of g_{1i} are virtually superposed. Concerning the expected value of g_{2i}, the scattering of the simulated values around the predicted value is increasingly higher with increased variance of the function (see Fig. 6.5), suggesting that the zero-mean mismatch is mostly related to an insufficient number of averages. Figure 6.5 shows the estimations of the

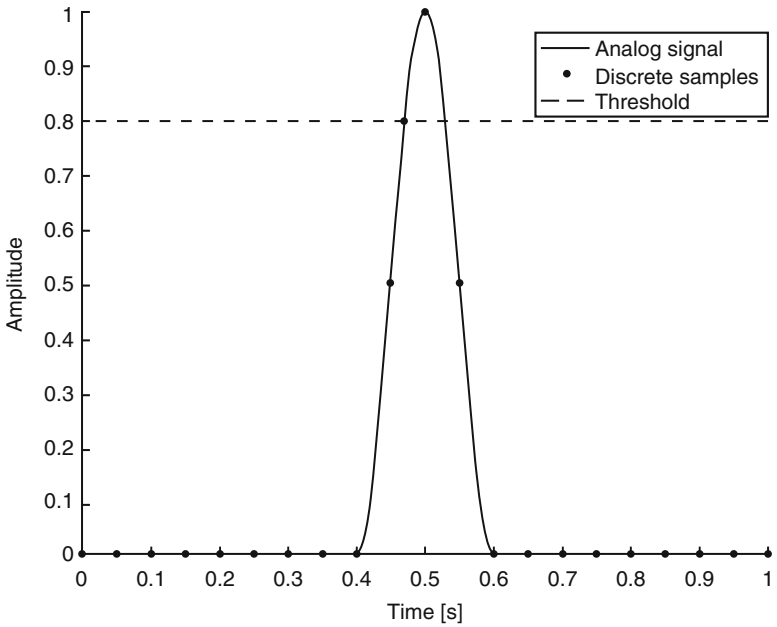

Fig. 6.3 Example of discrete sampling of an analog keyphasor signal

Table 6.1 parameters used for analytical expected value and variance validation

Parameter	Value
N	1,000,000
T	1
f*	1

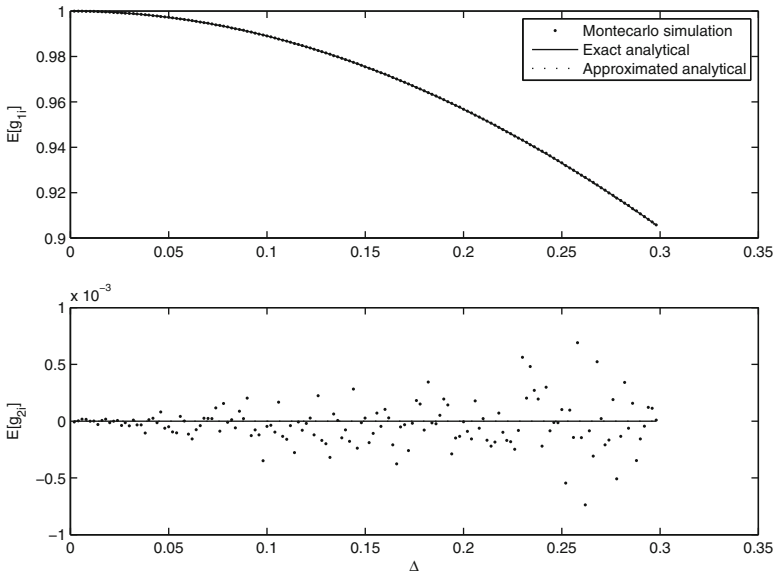

Fig. 6.4 Mean values, comparison of analytical expressions and numerical simulations varying jitter entity. Upper plot: g_{1i} expectancy. Lower plot: g_{2i} expectancy

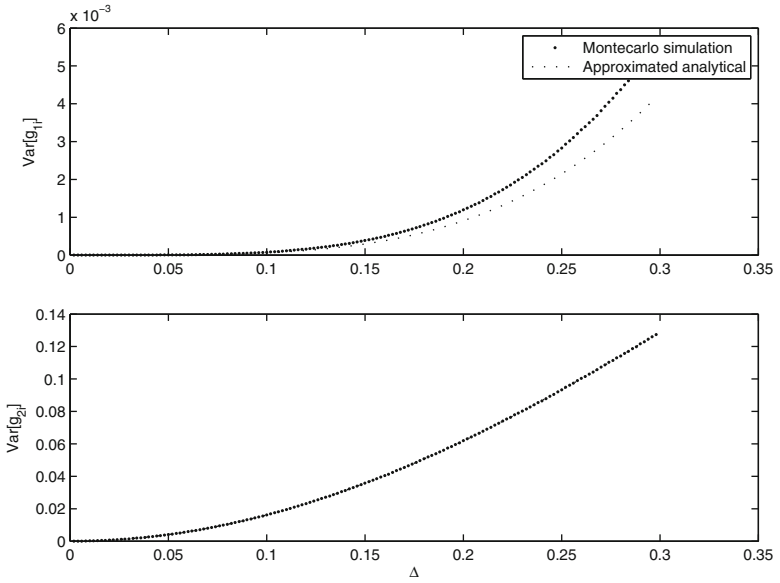

Fig. 6.5 Variance values, comparison of analytical expressions and numerical simulations varying jitter entity. *Upper plot*: g_{1i} variance. *Lower plot*: g_{2i} variance

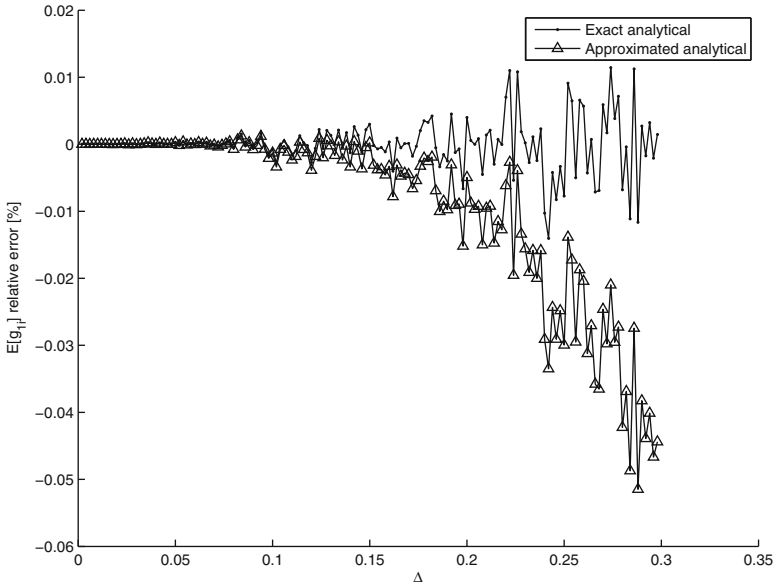

Fig. 6.6 Mean values for g_{1i}, comparison of analytical expressions and numerical simulations varying jitter entity. Relative error in percentage points between simulation (reference) and analytical solutions

variance respectively for g_{1i} and g_{2i}. It can be seen that the second-order approximation for the variance of g1i is increasingly worse with increasing entity of the jitter Δ. This is consistent with the hypothesis done in the truncated expansion and suggest to add more terms for improving the analytical approximation in the high error region. Figures 6.6 and 6.7 provide a zoom on the accuracy of the approximations for the expectance of g_{1i} and the variance of g_{2i}, that could not be seen clearly in the previous figures. The values are reported in terms of relative error and show for Fig. 6.6 consistently decreasing accuracy for the approximated solution as the jitter entity grows, and oscillating precision of the analytical solution which can be explained as for the case of the expectancy of g_{2i} in Fig. 6.4. Figure 6.7 shows consistently increasing (though relatively small) approximation error still attributable to the neglected terms in the power series expansion. Note that the parameter controlling the extent of the jitter, Δ can be interpreted in terms of relative importance of the uncertainty with respect to the considered frequency component's period as already explained in the theoretical part.

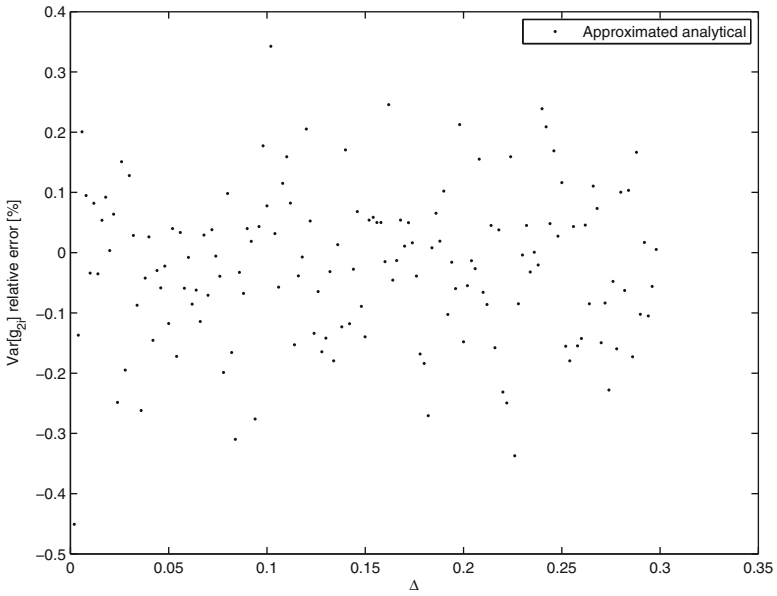

Fig. 6.7 Variance values for g_{2i}, comparison of analytical expressions and numerical simulations varying jitter entity. Relative error in percentage points between simulation (reference) and analytical solutions

Table 6.2 Parameters used for simulating the distribution of the absolute value

Parameter	Value
Number of iterations	100,000
N	200
T	1
f*	1
Δ	1e-4*2000

6.3.1.2 Approximation of the Absolute Value Distribution

Although extensive simulations were performed to validate the model, for the sake of brevity here only one comparison is reported. The used parameters are reported in Table 6.2. From the developed model, it is known that the distribution of the squared absolute value will be affected by the number of revolutions averaged. The more revolutions will be averaged, the less will be the variance. Seemingly, it is expected to have higher attenuation and higher variance when the jitter is of a higher entity. For the analyzed case, the number of averages N was set to a typical value used in helicopter vibration diagnostic systems. The value of the jitter parameter is approximatively one that could have for the first harmonic of the gearmesh frequency (i.e. one prominent harmonic in geared transmission typical signature, computed as shaft rotational speed times number of teeth of a connected gear) when sampling with $f_{KP} = 10$ kHz. Figure 6.8 shows the predicted probability density function using $d = 20$ terms in the expansion, compared to the simulated one for the squared absolute value. Seemingly, Fig. 6.9 shows a comparison between the estimated distribution of the variable R in and the simulated one for the same set of parameters. Fair agreement between prediction and simulations is observed. It can be concluded that the analytical approximations offer a viable way of predicting the attenuation and phase errors due to the jittering error in pulse arrival times according to the proposed model. Note that since the jitter effects are proportional to frequency, an attenuation of around 10% is reached for the 2 kHz harmonic only by considering the uncertainty due to the sampling of the keyphasor signal. Moreover, the values present themselves a certain variability. The approximated analytical and simulated expected value and variance for the considered simulation are given in Table 6.3.

6.3.2 Experimental Case Study

In this section, a short example on SA application is presented. The case study involves the detection of a bearing fault artificially introduced in a helicopter's gearbox. The test took place in the context of a short experimental campaign aimed

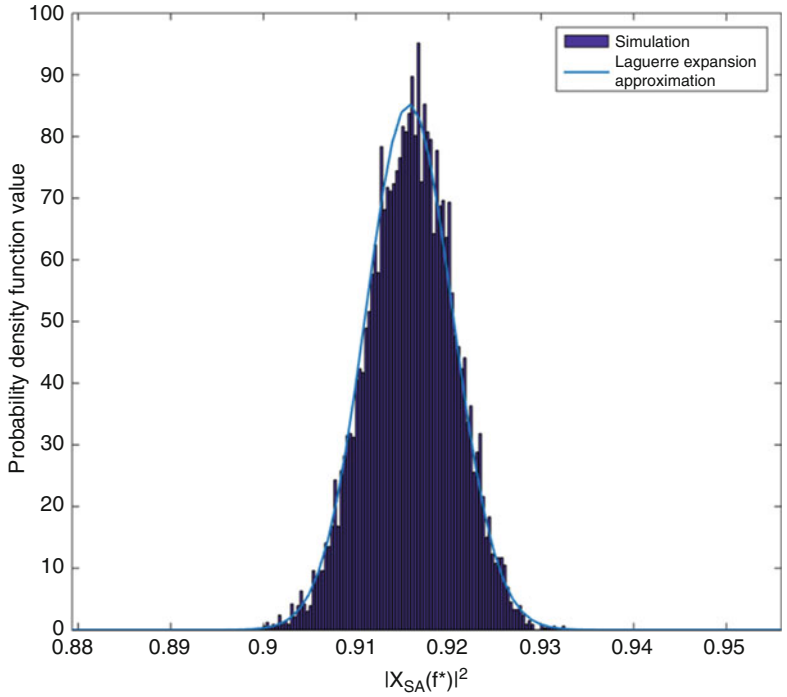

Fig. 6.8 Approximated p.d.f. of the squared absolute value computed through Laguerre expansion (*continuous line*), and the simulated distribution (histogram)

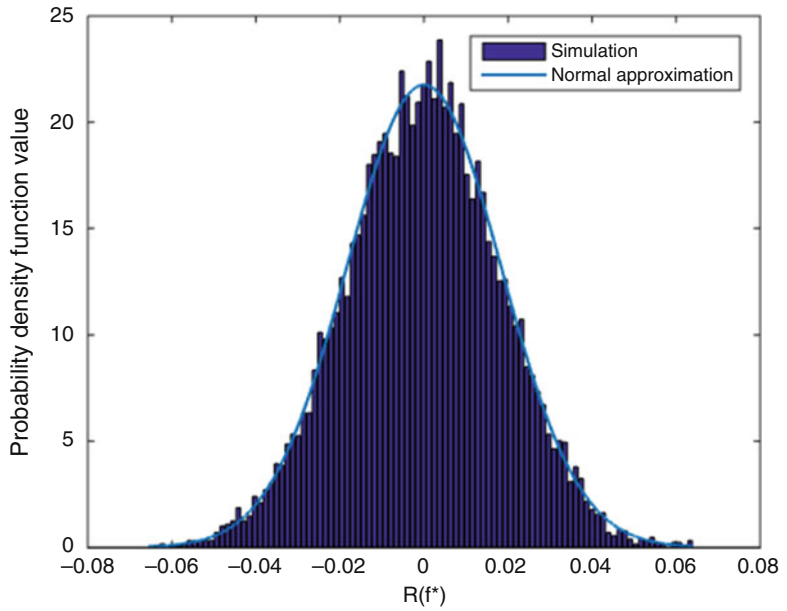

Fig. 6.9 Approximated p.d.f. of the random variable *R* computed through Normal approximation (*continuous line*), and the simulated distribution (histogram)

to assessing the capabilities of state-of-the-art algorithms in detecting various kinds of faults. Vibration data acquired with systems compliant with those that can be installed on board of a helicopter were used. Vibration signals were recorded from accelerometers located at seven specific locations on the main gearbox case. Moreover, a tachometric signal was recorder as a reference for performing synchronous averaging, digitalized with the same sampling rate of the vibration signals. Based on the kinematic relationships of the gearbox, the reference can be used for performing SA signal extraction for each shaft via interpolation. The considered test consisted of disassembling a ball bearing component and damaging three of the ball

Table 6.3 Simulated and approximate analytic expected value and variance for the random variables $|X_{SA}(f)|^2$ and R

Value	Simulation	Analytic
$E[\|X_{SA}\|^2]$	0.9159	0.9158
$Var[\|X_{SA}\|^2]$	2.21e-05	2.19e-05
$E[R]$	−13.5e-05	0
$Var[R]$	33.6e-05	33.6e-05

Table 6.4 Characteristic frequencies of the considered bearing

f_o [Hz]	f_i [Hz]	f_b [Hz]	f_c [Hz]
508.9	691.2	221.8	42.4

elements by scratching the surface. The characteristic defect frequencies of the considered ball bearing assembly are given in Table 6.4, referring to the nominal shaft speed of 100 Hz. The defect frequencies f_o, f_i, f_b, f_c are respectively the outer race defect frequency, the inner race defect frequency, the ball spin defect frequency and the cage defect frequency. Those defect frequencies are computed from the simplified kinematic relations of the bearing and correspond to the expected frequencies of impulses emitted from a damaged bearing when periodically striking a localized defect. The periodic impacts excite the high-frequency resonances of the component and can therefore be better detected when demodulating the signal around resonances. Further details can be found in the literature [4]. A comprehensive discussion about the signature of localized defects in bearings is given in [16]. In the context of this work, we focus on the diagnosis using the popular squared envelope spectrum[5] (SES) of the signal. The SES of a discrete signal x can be computed as [8]:

$$SES_x = \left| DFT\left\{ x_f[n]^2 \right\} \right|^2 \tag{6.50}$$

Where DFT denotes discrete Fourier transform and x_f is the filtered analytic signal through some filter f aimed to enhance some properties of x_f. A common filtering operation is, e.g., that of band-pass filtering the signal in a narrow region in which the impulsive content of the signal due to the damage is revealed. The reason for the successful performance of SES is thoroughly discussed in [4]. In fact, it is shown in [4] that the SES of the signal coincides with the integrated cyclic spectral density (CSD) when the random part of the signal is dominating. Moreover, conditions for the equivalence of the SES with the integrated cyclic coherence (ICC) are derived in [10]. The power of such a cyclostationary framework is in defining strong theoretical basis for the analysis of the CS2 part of a signal, including the derivation of proper statistical tests. In general, in order for the SES to perform optimally according to [10], a whitening of the signal should be performed before the analytic transformation. When the periodic components to be removed are known, such a whitening can be efficiently performed using the SA procedure. In this section, it is first shown that performing SA removal for signal pre-whitening effectively improves the diagnostic capability in the studied case. Once the importance of SA is proved on the experimental case, data from the same campaign is used in order to discuss the effect of jittering in SA extraction according to the results presented in Sect. 6.3.1.

Figure 6.10 shows the squared envelope spectrum of a faulty acquisition from the closest sensor to the faulty bearing. No band-pass filtering is performed and no whitening as well. Each vibration record in this analysis is 2 s long and the vibration signal is acquired with 93,750 Hz sampling frequency. The signal is analyzed in the angular domain synchronously with rotations of the shaft connected to the bearings of interest. Frequencies are expressed in orders of the fundamental shaft frequency (100 Hz in the considered case) and amplitudes are normalized to maximum value. It is readily clear that the harmonic content of the signal due to multiple CS components is completely hiding the fault signature. The dominant periodic components appear at integer multiples of the reference shaft. Hence, a first strategy for enhancing our envelope can be to separate the periodic mean with the period of the shaft from the rest of the signal. Using the SA procedure and 100 averages, we compute the periodic mean and remove it from the signal. Then, we show the squared envelope spectrum after this gross pre-whitening step in Fig. 6.11. As it can be seen, most of the important periodic components that were masking the fault signature are removed, and the harmonics of the ball pass frequency (red squares) modulated from the cage frequency (blue squares) are now readily visible. Here the whitening was successful thanks to a precise extraction and removal of the SA part from the signal. Clearly, this would not be the case otherwise. It has been shown how extracting the periodic mean from a signal can improve the diagnosis using the tool of SA. The discussion of other techniques is out of the scope of the paper, and the case was presented as a support to the importance of extracting correctly the SA from a signal, even when CS2-based diagnosis is concerned. According to the model proposed for the jittering error, the random error introduced on the unitary

[5]Note that the SES quantity is a squared-amplitude spectrum (signal-units^2) and not a power spectrum.

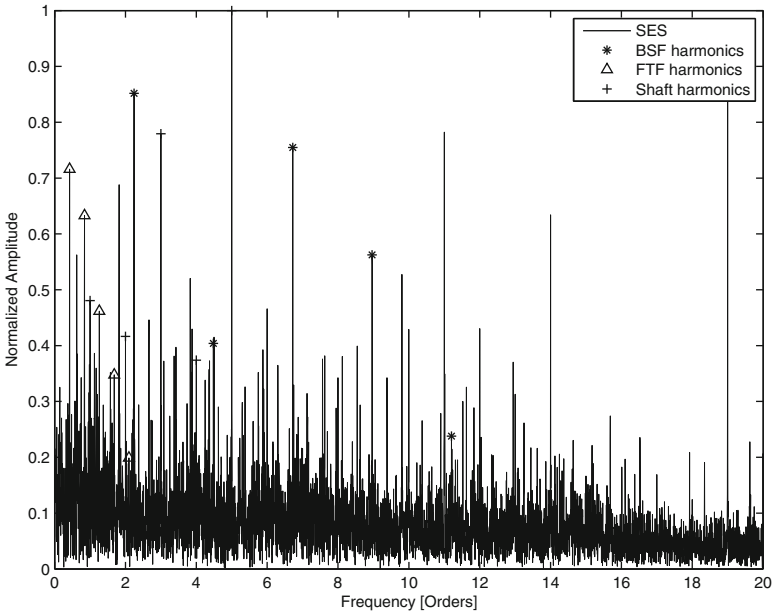

Fig. 6.10 Squared envelope spectrum in order domain, raw signal, faulty bearing. *Blue triangles*: harmonics of the cage frequency (FTF); *red stars*: harmonics of the ball spin frequency (BSF); *green crosses*: harmonics of the input drive shaft

Table 6.5 Comparison of jittering effects as predicted and as obtained using experimental data (ratio between SA harmonic amplitude computed using high-precision tacho signal and SA harmonic amplitude computed using lower precision tacho signal)

Harmonic	Predicted ratio	Measured ratio
GMF×1	0.993	0.990
GMF×2	0.971	0.967

frequency synchronous component due to the jitter would be such that $\Delta = 1/f_s = 1/93750$s. Computing the attenuation for the modulus of the first gearmesh frequency related to the pinion connected to the reference shaft, which is $f = 1900$ Hz, we obtain in average (based on Eq. 6.35) square root of the first cumulant) a value of about 0.9991/1. According to the analytical prediction, therefore, the SA should be able of recovering almost correctly such harmonic. Since no reference is available, it is complicated to verify directly the model. However, a tachometer signal sampled with $f_{s2} = 23{,}438$ Hz is available, hence we can validate our predictions based on the ratio between the amplitude of the harmonics of the SA signal obtained using the higher-precision tacho and the amplitude of the harmonics of the SA signal obtained using the lower-precision tacho. Still, available data for comparison is limited. However, it provides a first validation of the observations proposed in the paper. Table 6.5 reports the predicted and experimental attenuation ratios (amplitude of harmonic computed using low precision tacho divided by amplitude of harmonic computed using the higher precision tacho) obtained from the analysis of eight vibration records in healthy gearbox conditions and stable operating conditions. Attenuation ratios are computed for the first two gearmesh harmonics, since they have high signal to noise ratio. Although the values match quite well showing a remarkable ability of the model in explaining the difference in amplitude of the SA harmonics, further validation is required before confirming the capability of the model of well-predicting the jitter effects on experimental data. In particular, the design of a specific experiment would solve the issue. It can be of some interest to put an effort in actually characterizing the distribution of jittering errors and eventually validating the analysis proposed in this paper.

6.4 Concluding Remarks

In this paper a novel model for the random jittering error of the synchronization signal on the synchronous averaging procedure was introduced. A statistical analysis was performed to assess the distortion introduced by the error on the absolute

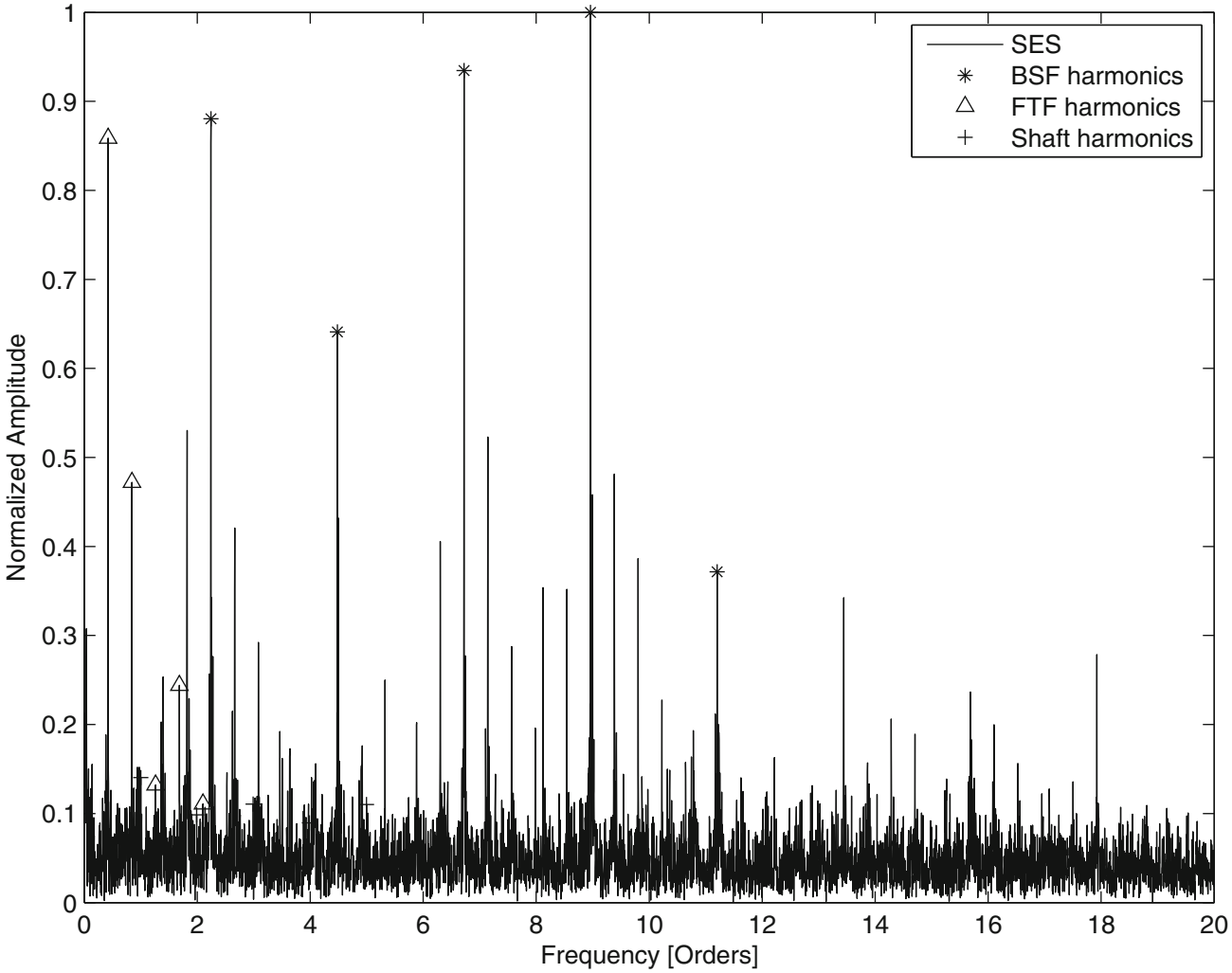

Fig. 6.11 Squared envelope spectrum in order domain, input drive shaft harmonics removed through SA. *Blue triangles*: harmonics of the cage frequency (FTF); *red stars*: harmonics of the ball spin frequency (BSF); *green crosses*: harmonics of the input drive shaft

value and the phase of the synchronous components in the signal, considering the dependency on the number of averages and on the entity of the jitter error. The analysis considered uniform jitter variables, though the model lends itself to the introduction of any other random model for the jitter times. An analytical approximation was derived for the attenuation and the phase shift. Numerical simulations showed adequate performance of the analytical approximation model in predicting the distortion of the generic synchronous harmonic, validating the study. The proposed expressions provide a mean for quantifying the severity of random jitter effects and, therefore, help in defining design criteria for vibration diagnostics systems. The results were derived considering a single sinusoid. However, the model is general and allow to consider any harmonic. The leakage interaction between different synchronous components can be considered by solving the equations for $f \neq f^*$, though for multiple harmonics the mixing might be complex. An important remark is that the given general model for the synchronous averaging gives ground for extending the analysis to different cases of interest, e.g. it can be adapted for studying the uncertainty in tacholess synchronous averaging procedures. As for the analytic approximations, it is recognized that a better estimation of the variance of the function g_{1i} is required for high error values, hence adding additional terms to the proposed second-order expansion is recommended. Finally, an experimental case study was presented to show the relevance of jitter effects in a practical diagnosis case where it is necessary to remove parasitic harmonics from the signal to detect the signature of a faulty gearbox bearing. In the considered case, relatively high precision in the tacho pulse times was available, hence the attenuation factor for most of the important harmonics (specifically, the first and second harmonics of the gearmesh frequency) was not relevant. By making use of two different reference signals, it was shown a good agreement between predicted and experimentally observed attenuation of the synchronous components due to jittering. In the considered

case, the jittering effect was fairly neglectable in terms of affecting the ability of separating the deterministic part and the random part of the signal. Hence, the deterioration of the SA did not affect negatively the diagnostic capability. The modelled (and successively observed) attenuation effect due to the jitter might be important for less precise tacho signals than the one available for this experimental analysis. On one side, the attenuation of some frequency components might distort the residual signal in a region of interest; on the other, the variance in the estimated magnitudes of harmonics of interest may lead to some scattering in the results when analyzing the CS1 part of the signal. It is therefore recommended to keep into account the importance of acquiring a precise synchronization signal when designing a monitoring system.

References

1. Capdessus, C., et al.: Cyclostationary processes: application in gear faults early diagnosis. Mech. Syst. Signal Process. **14**(3), 371–385 (2000)
2. Bouillaut, L., Sidahmed, M.: Cyclostationary approach and bilinear approach: comparison, applications to early diagnosis for helicopter gearbox and classification method based on HOCS. Mech. Syst. Signal Process. **15**(5), 923–943 (2001)
3. McCormick, A.C., Nandi, A.C.: Cyclostationarity in rotating machine vibrations. Mech. Syst. Signal Process. **12**(2), 225–242 (1998)
4. Randall, R.B., Antoni, J., Chobsaard, S.: The relationship between spectral correlation and envelope analysis for cyclostationary machine signals, application to ball bearing diagnostics. Mech. Syst. Syst. Process. **15**(5), 945–962 (2001)
5. Antoni, J., Daniere, J., Guillet, F.: Effective vibration analysis of IC engines using cyclostationarity. Part I: a methodology for condition monitoring. J. Sound Vib. **257**(5), 815–837 (2002)
6. Antoni, J., et al.: Cyclostationary modelling of rotating machine vibration signals. Mech. Syst. Signal Process. **18**(2), 1285–1384 (2004)
7. Fyfe, K.R., Munck, E.D.S.: Analysis of computed order tracking. Mech. Syst. Signal Process. **11**(2), 187–205 (1997)
8. Borghesani, P., et al.: Testing second order cyclostationarity in the squared envelope spectrum of non-white vibration signals. Mech. Syst. Signal Process. **40**, 38–55 (2013)
9. Ha, H., Provost, S.B.: An accurate approximation to the distribution of a linear combination of non-central chi-squared random variables. REVSTAT Stat. J. **11**(3), 231–254 (2013)
10. Antoni, J.: Cyclic spectral analysis of rolling-element bearing signals: Facts and fictions. J. Sound Vib. **304**, 497–529 (2007)
11. Braun, S.: The synchronous (time domain) average revisited. Mech. Syst. Signal Process. **25**(4), 1087–1102 (2011)
12. Combet, F., Gelman, L.: An automated methodology for performing time synchronous averaging of a gearbox signal without speed sensor. Mech. Syst. Signal Process. **21**, 2590–2606 (2007)
13. Bonnardot, F., El Badaoui, M., Randall, R.B., Dani'ere, J., Guillet, F.: Use of the acceleration signal of a gearbox in order to perform angular resampling (with limited speed fluctuation). Mech. Syst. Sig. Process. **19**, 766–785 (2005)
14. McFadden, P.D.: Interpolation techniques for the time domain averaging of vibration data with application to helicopter gearbox monitoring, DSTO Area Propulsion Technical Memorandum 437
15. Marsaglia, G.: Ratios of normal variables. J. Stat. Softw. **16**(4), (2006)
16. Randall, R.B., Antoni, J.: Rolling element bearing diagnostics—A tutorial. Mech. Syst. Signal Process. **25**(2), 485–520 (2011)

Chapter 7
Optimization of a Zigzag Shaped Energy Harvester for Wireless Sensing Applications

Brittany C. Essink, Robert B. Owen, and Daniel J. Inman

Abstract Research involving energy harvesters to power systems are often carried out in a laboratory setting where vibration excitations are created using shakers. These excitations can be tuned to the natural frequency of the harvester to achieve the highest power output possible for the harvester design. Adapting these designs for use in real world applications introduces many additional layers of complexity. These added complications come in various forms including different input vibration and acceleration profiles, sensor energy requirements, and space constraints. Existing optimization for application-based research is limited to one set of constraints and cannot be applied to different cases.

This optimization is based around the use of a zigzag shaped device that is capable of achieving low natural frequencies in a compact design space. Piezoelectric materials bonded to the zigzag substrate are used to harvest energy from vibration excitations. The research in this paper presents an optimization for a zigzag shaped energy harvester based on varying input parameters in the design space to provide the optimum design for each application scenario. Optimization of this harvester creates the start of a design guide software that can be quickly used to implement sensor networks subject to a wide range of operating conditions typical of varied applications.

Keywords Energy harvesting • Vibration excitation • Zigzag structures • Optimization • Design guide

7.1 Introduction

Energy harvesting devices have attracted high amounts of interest in literature, wireless sensing applications, and structural health monitoring. Many of these devices are designed to have a resonant frequency that matches the natural frequency of the excitation, however, if the harvester resonant frequency and excitation frequency deviate, energy harvesting capabilities are extremely reduced. For this reason, it is difficult to have a simple harvester design that can be easily adapted for different excitation frequency applications. While tuning methods have been investigated in order to accommodate changing natural frequencies during operation [1–3], this research seeks to create a design guide capable of creating an optimized harvester specific to each input excitation without the added complexity to fabrication and operation that additional tuning methods incorporate.

Traditional cantilever beam designs encounter the issue of an increase in fundamental frequency with a decrease in beam length. Designing a cantilever device to have specific fundamental natural frequencies for harvesting can become infeasible due to space restrictions or impossible due to material constraints. Using a zigzag shaped harvester design as seen in Reference [4] overcomes the impracticalities of the traditional design by achieving a higher tip deflection which allows a wider range of achievable natural fundamental frequencies.

The optimized device presented in this paper is based on data collected from pumping stations at Stennis Space Center, however other excitation frequencies could easily be used as inputs. This design attempts to achieve the maximum harvested voltage within the constraints imposed by geometry and desired excitation frequency. This optimization code creates the start of a design guide software that can be used for a wide variety of input excitations and geometric constraints.

B.C. Essink (✉) • D.J. Inman
Department of Aerospace Engineering, University of Michigan, François-Xavier Bagnoud Building, 1320 Beal Ave, Ann Arbor, MI 48105, USA
e-mail: essinkb@umich.edu

R.B. Owen
Extreme Diagnostics, 2525 Arapahoe Ave, Bldg. E4 #262, Boulder, CO 80302, USA

N. Dervilis (ed.), *Special Topics in Structural Dynamics, Volume 6*, Conference Proceedings of the Society for Experimental Mechanics Series, DOI 10.1007/978-3-319-53841-9_7

7.2 Methodology

The design for this harvester is based on the initial zigzag harvester from Reference [4]. A prototype zigzag harvester was modeled and fabricated in Reference [5] and provides the basis for this optimization. The analytical model was verified using the experimental prototype data and has been extended to include optimization based on a desired fundamental frequency. A photograph of the harvester prototype is shown in Fig. 7.1. Additional information on the design and fabrication of the harvester can be found in [5].

To find the frequency objective for the harvester optimization, acceleration data was collected for four different pumping station locations at Stennis Space Center. Figure 7.2 shows the pumping station with accelerometer locations and Fig. 7.3 shows a closer view of the pump for two of the accelerometers. Accelerometers 2 and 4 were placed directly on the pumps while accelerometer 1 was located on a valve near the liquid nitrogen tanks, and accelerometer 3 was placed on the oil pump line for the pump motor.

From this acceleration data, the power spectral density of the signals was calculated to find the frequency content of the signals. This data was used to determine the frequency areas of interest for the harvester design. Figure 7.4 contains the power spectral data while Fig. 7.5 shows a zoomed in view for all four accelerometers at the primary frequency of interest.

Using this frequency criteria, a multivariable constrained design optimization was conducted using MATLAB. The objective of the optimization was to obtain the maximum voltage from the harvester constrained to the frequency of interest which was 358.47 Hz. For this optimization, the number of beams was limited between 1 and 10, the length of the beams was limited between 2 and 5 cm, and the width of the beams was constrained to be between 5 and 13 mm. The desired natural frequency was set as an equality constraint and the optimization routine attempted to maximize the harvester voltage while meeting the frequency criteria. Acceleration for the optimization was held constant at 13 m/s^2. Due to the linear response of this optimization, varying the acceleration changes the optimal RMS voltage value, but the geometric design remains constant.

7.3 Results

Figure 7.6a shows that the optimization routine was able to find solutions for the objective function for a design with the number of beams less than or equal to 3. As the number of beams increases, the natural frequency drops lower meaning that the desired natural frequency is not achievable within the provided constraints for higher numbers of beams. Figure 7.6b, c show the variation of the length and width of the design as the number of beams changes. Figure 7.6d shows that the optimal number of beams for achieving this frequency while satisfying the objective function is three beams. The optimal length and width of the design are 2.73 cm and 7.55 mm respectively.

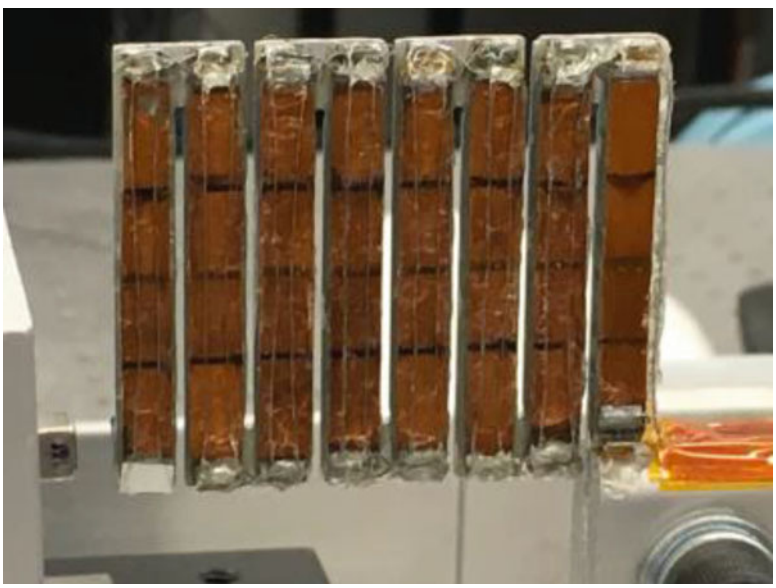

Fig. 7.1 Prototype zigzag harvester

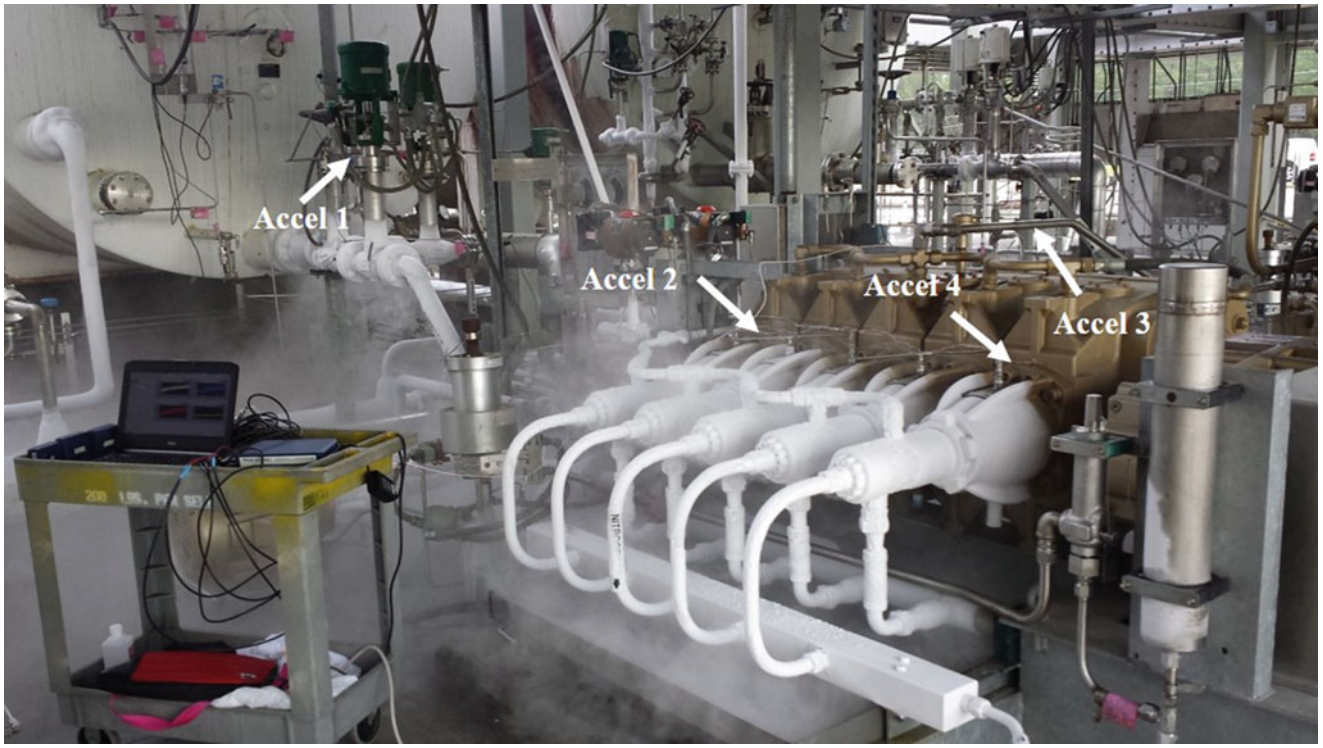

Fig. 7.2 Accelerometer locations on pumping station

Fig. 7.3 Close-up view of accelerometers 2 and 4

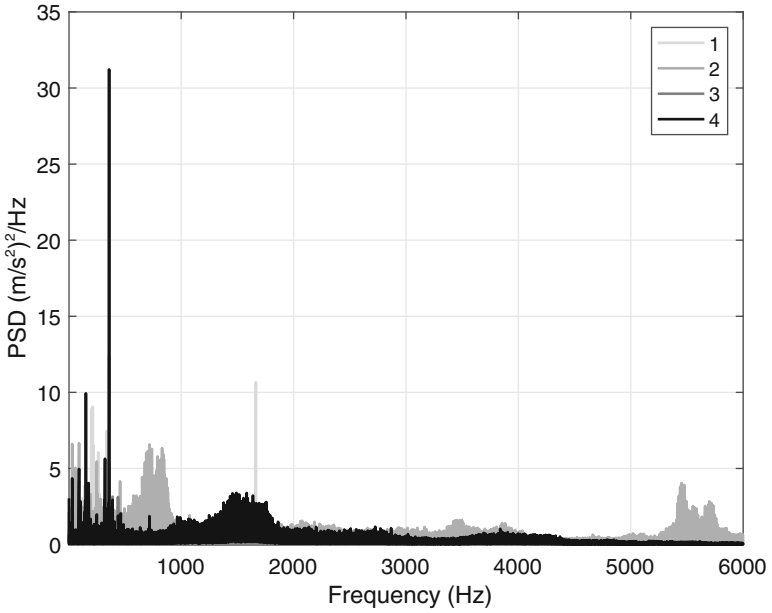

Fig. 7.4 PSD of pumping station data

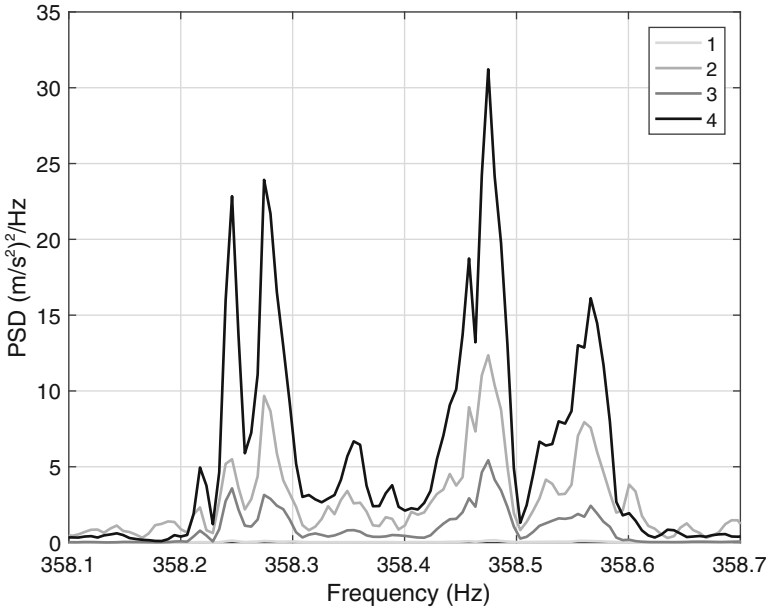

Fig. 7.5 PSD zoomed in on frequency of interest

Additions to this design guide can be made by including the effects of a repelling tip magnet in order to introduce nonlinearities and harvest over a broadband frequency range. Further extensions could also include varied excitation inputs such as multiple frequency excitations as well as constraints on volume, mass, or required power values.

Acknowledgements This work was supported by a Phase II NASA STTR titled “Compact Energy Conversion Module” awarded to Extreme Diagnostics, Inc.

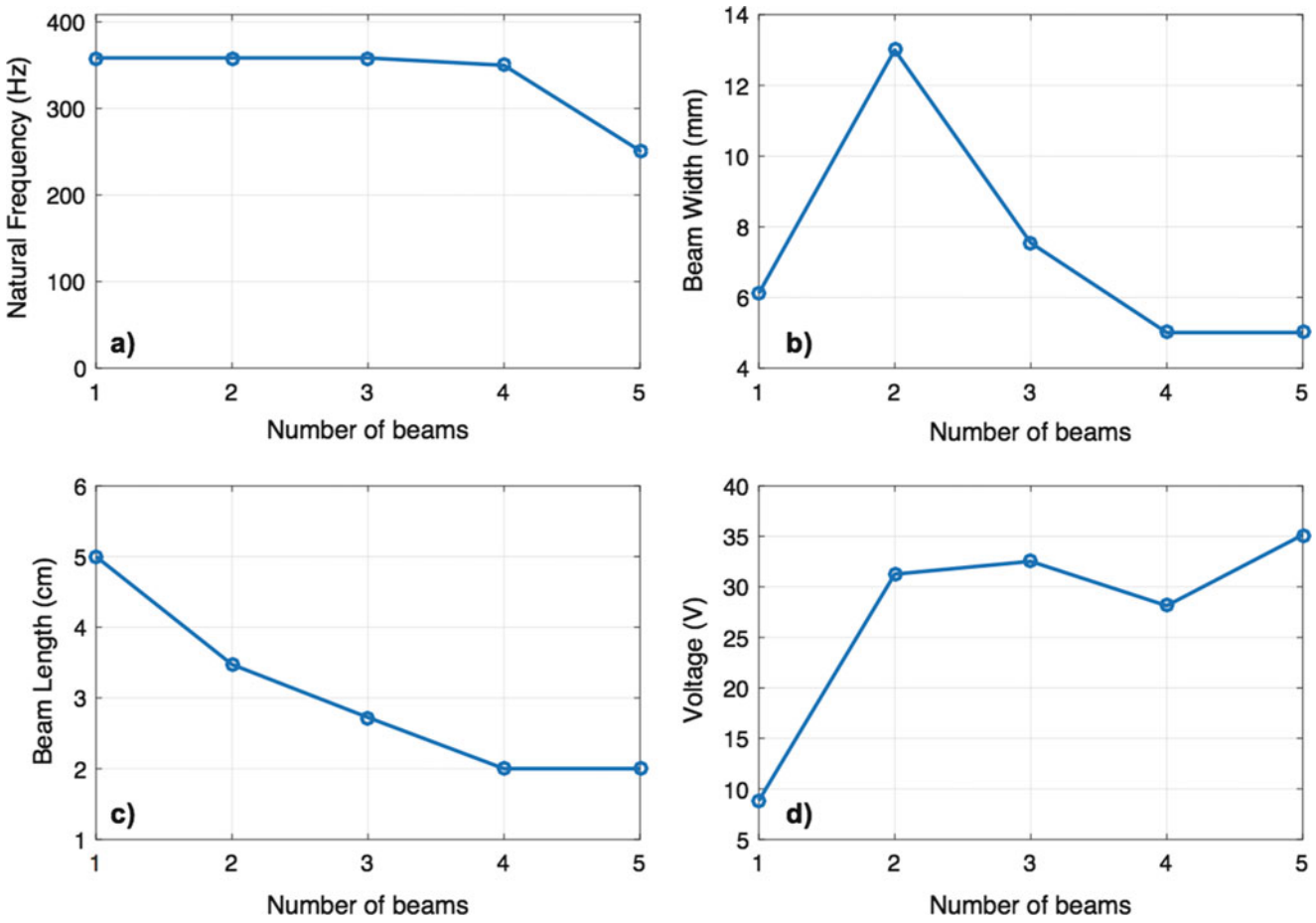

Fig. 7.6 Design optimization results

References

1. Roundy, S., Zhang, Y.: Toward self-tuning adaptive vibration-based microgenerators. In: Proceedings of SPIE 5649, Smart Structures, Devices, and Systems II, 9 March 2005
2. Challa, V.R., Prasad, M.G., Shi, Y., Fisher, F.T.: A vibration energy harvesting device with bidirectional resonance frequency tunability. Smart Mater. Struct. **17**, 015035 (2008)
3. Zhu, D., Tudor, M.J., Beeby, S.P.: Strategies for increasing the operating frequency range of vibration energy harvesters: a review. Meas. Sci. Technol. **21**, 022001 (2009)
4. Karami, M.A., Inman, D.J., Vibration Analysis of the Zigzag Micro-Structure for Energy Harvesting. SPIE Smart Structures and Materials + Nondestructive Evaluation and Health Monitoring, International Society for Optics and Photonics (2009)
5. Essink, B.C., Hobeck, J.D., Owen, R.B., Inman, D.J., Magnetoelastic Energy Harvester for Structural Health Monitoring Applications. SPIE Smart Structures and Materials + Nondestructive Evaluation and Health Monitoring, International Society for Optics and Photonics (2015)

Chapter 8
Fuzzy Finite Element Model Updating Using Metaheuristic Optimization Algorithms

I. Boulkaibet, T. Marwala, M. I. Friswell, H. H. Khodaparast, and S. Adhikari

Abstract In this paper, a non-probabilistic method based on fuzzy logic is used to update finite element models (FEMs). Model updating techniques use the measured data to improve the accuracy of numerical models of structures. However, the measured data are contaminated with experimental noise and the models are inaccurate due to randomness in the parameters. This kind of aleatory uncertainty is irreducible, and may decrease the accuracy of the finite element model updating process. However, uncertainty quantification methods can be used to identify the uncertainty in the updating parameters. In this paper, the uncertainties associated with the modal parameters are defined as fuzzy membership functions, while the model updating procedure is defined as an optimization problem at each α-cut level. To determine the membership functions of the updated parameters, an objective function is defined and minimized using two metaheuristic optimization algorithms: ant colony optimization (ACO) and particle swarm optimization (PSO). A structural example is used to investigate the accuracy of the fuzzy model updating strategy using the PSO and ACO algorithms. Furthermore, the results obtained by the fuzzy finite element model updating are compared with the Bayesian model updating results.

Keywords Finite Element Model updating • Fuzzy logic • Fuzzy membership function • Ant colony optimization • Particle swarm optimization • Bayesian

8.1 Introduction

In many engineering areas, the finite element model (FEM) [1–3] is considered as one of the most practical numerical tools that can be used to obtain approximate solutions for real systems. Unfortunately, the accuracy of the models obtained by the FEMs degrades with the complexity of the modeled system. Furthermore, certain model parameters are uncertain and the variability of these parameters may reduce the accuracy of the FEM. Usually, the obtained finite element model is improved by correcting certain uncertain model parameters to reduce the error between the numerical model and the measured data. This process is known as "model updating" [4, 5]. Generally, there are two main approaches to perform a finite element model updating (FEMU): direct methods in which the FEM output is directly equated to the measured data [4]. In the second class, which is the class of the iterative approaches, an optimization procedure is performed to minimize the differences between the measured output and FEM output. In this optimization procedure, several unknown parameters are selected and corrected according to a preselected objective function [4].

In reality, the presence of uncertainties is inevitable in the modeling process as well as the experimental studies. These uncertainties can result from the mathematical simplifications that have been assumed during the modeling procedure (e.g., the variability of material-properties or mechanical joints). Furthermore, the experimental noises may contaminate the measured data (e.g., the accuracy of the equipment, such as the sensors, used to conduct an experimental study). These uncertainties may have a significant influence on the modeling process as well as the updating procedure. To obtain reliable models, the uncertainty quantification methods can be implemented to update FEMs [6].

Several uncertainty quantification methods have been used in FEMU such as: Bayesian method, perturbation methods and methods based on fuzzy sets [6, 7]. Generally, the uncertainty quantification methods are divided into two main classes: probabilistic and possibilistic (non-probabilistic) methods [6]. In the probabilistic methods, the uncertain parameters are

I. Boulkaibet (✉) • T. Marwala
Electrical and Electronic Engineering Department, University of Johannesburg,
PO, Box 524, Auckland Park 2006, South Africa
e-mail: ilyes@aims.ac.za

M.I. Friswell • H.H. Khodaparast • S. Adhikari
College of Engineering, Swansea University Bay Campus, Crymlyn Burrows, Swansea SA1 8EN, UK

N. Dervilis (ed.), *Special Topics in Structural Dynamics, Volume 6*, Conference Proceedings
of the Society for Experimental Mechanics Series, DOI 10.1007/978-3-319-53841-9_8

defined as random variables where the variability of each parameter is described by a probability density function (PDF). Both the Bayesian and the perturbation methods belong to the probabilistic class [6–10]. In the case that the density functions of the uncertain parameters are unknown (or their forms are unspecified), the possibilistic methods can be used to quantify the uncertainties associated with the structures. In this case, the variability of the uncertain parameters is described in a non-probabilistic way, e.g., intervals, membership functions . . . etc. The most recognized possibilistic methods are: the interval and the fuzzy logic methods. In the interval method, the uncertain parameters vary within intervals where each parameter is constrained by lower and upper bounds [6, 11, 12]. The interval finite element model updating concentrates on finding the minimal and maximal bounds of the unknown parameters. Khodaparast et al. [13] used the interval method to define the uncertainties associated with the measurements while a Kriging Meta model was employed to update the bounds of the unknown parameters. Describing uncertainties as fuzzy sets was first introduced by Zadeh [14]. In fuzzy finite element model updating (FFEMU) [6, 15–17], the fuzzy membership functions are used to define the uncertainties associated with the measured outputs (instead of probability density function) while the membership functions of the uncertain parameters are obtained by applying the interval finite element model updating at different membership function levels. Moens and Vandepitte [15] applied FFEMU to compute the uncertain frequency response functions of damped structures. Fuzzy sets were also used by Erdogan and Bakir [18] to represent the irreducible uncertainties caused by the measurement noise in the modal parameters while the membership functions of the uncertain parameters were obtained by minimizing an objective function using a genetic algorithm.

In this paper, a fuzzy finite element model updating approach based on metaheuristic optimization algorithms is discussed and used to quantify the uncertainty associated with the modal parameters. First, the FFEMU procedure is discussed in Sect. 8.2 where the irreducible uncertainties are defined as fuzzy membership functions while the α-cut methodology is used to simplify the computing process by transferring the fuzzy calculations into a series of interval calculations. The objective function, which is defined by the upper and lower bounds of the numerical model and the measured data, is also presented in Sect. 8.2 along with the interval natural frequencies and mode shapes of the numerical model. In Sect. 8.3, the ant colony optimization (ACO) algorithm is discussed where this algorithm is used to compute the upper and lower bounds of the intervals at each α-cut. In Sect. 8.4, the FFEMU based on ACO algorithm was investigated by updating a structure. The accuracy of the proposed FFEMU-ACO algorithm is highlighted by comparing its results with the results obtained by the FFEMU based on a PSO and Bayesian results. Section 8.5 concludes the paper.

8.2 Fuzzy Finite Element Model Updating

Instead of using the probability density functions to represent the irreducible uncertainty, the fuzzy finite element model updating method defines the uncertainty as a membership function. In general, the objective of the FEEMU method is to estimate the membership functions of the updated quantities given the membership functions of the measured outputs [6, 19]. This can be done by transferring the fuzzy arithmetic to a series of interval calculations. In this section, a brief introduction on fuzzy sets is given where the main idea of the α-cut technique will be presented. Next, the objective function used in this paper is defined in Sect. 8.2.2, and since the interval technique is used to compute the membership functions, the bounds of the numerical eigenvalues are computed in the last subsection.

8.2.1 Introduction to Fuzzy Sets

Since the first introduction of the concepts of fuzzy logic in 1965 [14], the fuzzy methodology has been very attractive in many engineering areas such as: control systems and system identification. Unlike the standard set theory that separates between the members of the set and the non-members, a fuzzy set $\widetilde{A}$ uses the degree of membership, which is measured by the membership function $\mu_{\widetilde{A}}(x)$, to express the degree to which a member x belongs to the fuzzy set $\widetilde{A}$. A fuzzy set can be described as follows [18, 20]:

$$\widetilde{A} = \left\{ \left(x, \mu_{\widetilde{A}}(x) \right) \mid x \in X, \mu_{\widetilde{A}}(x) \in \left[0, 1 \right] \right\} \tag{8.1}$$

As described in Eq. (8.1), $\mu_{\tilde{A}}(x) = 1$ indicates that x is a member of the fuzzy set $\tilde{A}$, while $\mu_{\tilde{A}}(x) = 0$ indicates that x does not belong to the set $\tilde{A}$. When $0 < \mu_{\tilde{A}}(x) < 1$, the element x belongs to the fuzzy set $\tilde{A}$ with certain degree $\mu_{\tilde{A}}(x)$. There are an infinite number of possible shapes in which a membership function can be defined, however the most frequent shapes are: trapezoidal, triangular and Gaussian shape. In this paper, the triangular form will be used to describe a membership function $\mu_{\tilde{A}}(x)$ such that:

$$\mu_{\tilde{A}}(x) = \begin{cases} 0, & x \leq a, \\ \frac{x-a}{b-a}, & a < x \leq b, \\ \frac{c-x}{c-b}, & b < x \leq c, \\ 0, & c < x. \end{cases} \tag{8.2}$$

Usually, problems with fuzzy variables can be analyzed using the α-cut technique. In this technique, a membership function $\mu_{\tilde{A}}(x)$ of the member x is divided into a series of sublevels. At each α-sublevel, the interval $\tilde{A}_\alpha = [\underline{x}, \bar{x}]$ is obtained where $\underline{x}$ and $\bar{x}$ are the upper and the lower bounds of the interval $\tilde{A}_\alpha$. The α-cut of the fuzzy set $\tilde{A}$ can also be described as follows:

$$\tilde{A}_\alpha = \left\{ x \in X, \mu_{\tilde{A}}(x) \geq \alpha \right\} \tag{8.3}$$

In general, the problem of FFEMU can also be regarded as a propagation of a m-dimensional vector of fuzzy inputs $\tilde{\boldsymbol{x}}$, where the main idea is to attain the membership functions of the a d-dimensional vector of fuzzy outputs $\tilde{\boldsymbol{y}}$ when the membership functions of the input quantities $\tilde{\boldsymbol{x}}$ were given. The mathematical equation that describes this problem is given by: $\tilde{\boldsymbol{y}} = \boldsymbol{f}\left(\tilde{\boldsymbol{x}}\right)$. Unfortunately, due to the complexity of this fuzzy problem, it cannot be numerically implemented [21]. The easiest way is to transfer the problem into an equivalent problem that can be solved as an interval analysis at different α-cuts [22]. Thus, the fuzzy uncertainty propagation is then expressed as the application of a series of interval analysis at a number of α-sublevels. There are two main strategies to evaluate fuzzy uncertainty propagation: interval algebra based approaches and global optimization based approach [21]. In the first approach, fuzzy variable is treated as an interval variable for each α-cut while the standard interval arithmetic will be used for the propagation procedure. In the second approach, which is the approach adopted in this paper, two optimization problems are solved for each α-sublevel. In this approach, the first optimization procedure is defined so that the minimum value of the output vector is obtained while the maximum value of the output vector is obtained from the second optimization procedure. Combining the results obtained by these two optimization problems for all α-sublevels, the membership functions of the output quantities are attained. The optimization problem at each α-level is described as follows:

$$\begin{cases} \bar{\boldsymbol{y}}_{\boldsymbol{\alpha}} = \underset{\boldsymbol{x}_\alpha \in \boldsymbol{x}_\alpha^I}{\max} \boldsymbol{f}\left(\boldsymbol{x}_{\boldsymbol{\alpha}}\right) \\ \underline{\boldsymbol{y}}_{\boldsymbol{\alpha}} = \underset{\boldsymbol{x}_\alpha \in \boldsymbol{x}_\alpha^I}{\min} \boldsymbol{f}\left(\boldsymbol{x}_{\boldsymbol{\alpha}}\right) \end{cases}, \alpha = \alpha^k, k = 1, \ldots, m \tag{8.4}$$

where $\bar{\boldsymbol{y}}_{\boldsymbol{\alpha}}$ and $\underline{\boldsymbol{y}}_{\boldsymbol{\alpha}}$ are the upper and lower bounds of the output vector, respectively. $\boldsymbol{x}_{\boldsymbol{\alpha}}^{\boldsymbol{I}}$ is the interval variable (defined earlier as $\tilde{A}_\alpha$). The optimization problem defined in Eq. (8.4) can be simplified to optimize a simple objective function. In the next subsection, the objective function will be described in details.

8.2.2 The Objective Function

In this paper, the FFEMU approach is defined as a global optimization based approach where an objective function is defined by a difference between the experimental and the numerical modal parameters. The objective function can be reformed to include both lower and upper bounds of the numerical and experimental modal parameters as described in Eq. (8.5) [18, 20]:

$$f\left(\boldsymbol{\theta}^I\right) = f\left(\overline{\boldsymbol{\theta}}, \underline{\boldsymbol{\theta}}\right) = \underline{\boldsymbol{e}}^{\boldsymbol{T}} \boldsymbol{W}_{\boldsymbol{l}} \boldsymbol{e} + \bar{\boldsymbol{e}}^{\boldsymbol{T}} \boldsymbol{W}_{\boldsymbol{u}} \bar{\boldsymbol{e}} \tag{8.5}$$

where $\overline{\boldsymbol{\theta}}$ and $\underline{\boldsymbol{\theta}}$ are the lower and upper bounds of the interval updating parameters $\boldsymbol{\theta}^I$, respectively. $\boldsymbol{W_l}$ and $\boldsymbol{W_u}$ are the weighting matrices for the upper and lower parts of the objective function, respectively. $\underline{\boldsymbol{e}}$ represents the lower error where $\underline{\boldsymbol{e}} = \begin{bmatrix} \underline{\boldsymbol{e}}_f \\ \underline{\boldsymbol{e}}_{\boldsymbol{\phi}} \end{bmatrix}$, $\underline{\boldsymbol{e}}_f = \left[\frac{\underline{\lambda}_1^m - \underline{\lambda}_1}{\underline{\lambda}_1^m}, \ldots, \frac{\underline{\lambda}_n^m - \underline{\lambda}_n}{\underline{\lambda}_n^m}\right]^T$ and $\underline{\boldsymbol{e}}_{\boldsymbol{\phi}} = \left[\frac{\left\|\underline{\phi}_1^m - \underline{\beta}_1 \underline{\phi}_1\right\|}{\left\|\underline{\phi}_1^m\right\|}, \ldots, \frac{\left\|\underline{\phi}_n^m - \underline{\beta}_n \underline{\phi}_n\right\|}{\left\|\underline{\phi}_n^m\right\|}\right]^T$. $\underline{\lambda}_j^m$ and $\underline{\lambda}_j$ are the j-th lower bounds of the measured and the analytical eigenvalues, respectively. $\underline{\phi}_j^m$ and $\underline{\phi}_j$ are the j-th lower bounds of the measured and the analytical eigenvectors, respectively. $\underline{\beta}_j$ is a normalizing constant given by $\underline{\beta}_j = \frac{\left(\underline{\phi}_j^m\right)^T \underline{\phi}_j}{\left\|\underline{\phi}_j\right\|^2}$. In the same way, the error of the upper part of the objective function is given by $\overline{\boldsymbol{e}} = \begin{bmatrix} \overline{\boldsymbol{e}}_f \\ \overline{\boldsymbol{e}}_{\boldsymbol{\phi}} \end{bmatrix}$, $\overline{\boldsymbol{e}}_f = \left[\frac{\overline{\lambda}_1^m - \overline{\lambda}_1}{\overline{\lambda}_1^m}, \ldots, \frac{\overline{\lambda}_n^m - \overline{\lambda}_n}{\overline{\lambda}_n^m}\right]^T$ and $\overline{\boldsymbol{e}}_{\boldsymbol{\phi}} = \left[\frac{\left\|\overline{\phi}_1^m - \overline{\beta}_1 \overline{\phi}_1\right\|}{\left\|\overline{\phi}_1^m\right\|}, \ldots, \frac{\left\|\overline{\phi}_n^m - \overline{\beta}_n \overline{\phi}_n\right\|}{\left\|\overline{\phi}_n^m\right\|}\right]^T$. The upper bounds of j-th measured and the analytical eigenvalues are given by $\overline{\lambda}_j^m$ and $\overline{\lambda}_j$, respectively. $\overline{\phi}_j$ and $\overline{\phi}_j^m$ are the j-th upper bounds of the analytical and measured eigenvectors, respectively. Again, the normalizing constant $\overline{\beta}_j$ of the j-th upper eigenvector is defined by $\overline{\beta}_j = \frac{\left(\overline{\phi}_j^m\right)^T \overline{\phi}_j}{\left\|\overline{\phi}_j\right\|^2}$. The optimization procedure defined by Eq. (8.5) is completed by adding two constraints to the problem. First, the updating parameter vector is bounded by the maximum and minimum values ($\boldsymbol{\theta}_{max}$ and $\boldsymbol{\theta}_{min}$) to keep the searching process within a limited region (which eventually limits the number of iterations). These maximum and minimum values help keeping the updating parameters physically realistic. Furthermore, to obtain convex membership functions, another constraints are included where the lower bounds $\underline{\boldsymbol{\theta}}^{k+1}$ of the updating parameters at $(k+1)$-th α-sublevel should be smaller than the previous $\underline{\boldsymbol{\theta}}^k$ that corresponds (k)-th α-sublevel. On the other hand, upper bounds $\overline{\boldsymbol{\theta}}^{k+1}$ of the updating parameters at $(k+1)$-th α-sublevel must be larger than the previous $\overline{\boldsymbol{\theta}}^k$ that corresponds (k)-th α-sublevel. Then, the new constraints are given in Eq. (8.6):

$$\begin{cases} \overline{\boldsymbol{\theta}}^k \leq \overline{\boldsymbol{\theta}}^{k+1} \leq \boldsymbol{\theta}_{max} \\ \boldsymbol{\theta}_{min} \leq \underline{\boldsymbol{\theta}}^{k+1} \leq \underline{\boldsymbol{\theta}}^k \end{cases}, \alpha = \alpha^k, k = 1, \ldots, m \tag{8.6}$$

It is clear that at the first α-sublevel ($\alpha^1 = 1$), which corresponds to $\mu_{\underset{\sim}{A}}(\theta_j) = 1, j = 1, \ldots, d$, a simple deterministic optimisation is performed to obtain the center of membership functions. In the next subsection, the analytical bounds of the eigenvalues and eigenvectors are computed.

8.2.3 The Bounds of the Numerical Eigenvalues

As shown in Eq. (8.5), the interval modal parameters of the numerical model are required in order to perform the optimization procedure. Generally, the eigenvalues behave monotonically during the variation of the updating parameters if the eigenvalues are linear functions of the mass and stiffness matrices. In this case, the bounds of the eigenvalues and the eigenvectors are given by Eqs. (8.7) and (8.8):

$$\overline{\boldsymbol{K}}\,\overline{\boldsymbol{\phi}}_j = \overline{\lambda}_j \underline{\boldsymbol{M}} \overline{\boldsymbol{\phi}}_j \tag{8.7}$$

$$\underline{\boldsymbol{K}}\,\underline{\boldsymbol{\phi}}_j = \underline{\lambda}_j \overline{\boldsymbol{M}} \underline{\boldsymbol{\phi}}_j \tag{8.8}$$

More details about the computing procedure can be found in [23].

8.2.4 The ACO Algorithm for Continuous Domain

In this paper, the metaheuristic optimization techniques are selected to perform the FFEMU. These optimization algorithms belong to the class of the population based algorithms (swarm intelligence). Generally, the metaheuristic optimization algorithms are accurate and produce reliable results. Unfortunately, some of these algorithms are computationally expensive due to the large population sizes involved in order to obtain accurate results. In this study, the ACO algorithm [24, 25] is

employed since it requires less population (ants) size due to its ability to adjust to small (or large) search spaces. The results obtained by the ACO algorithm are highlighted by comparing its results with the PSO algorithm [26, 27, 28] results. The PSO algorithm was first introduced by Kennedy and Eberhart [26] where this algorithm was inspired from the behavior of flocks of birds (particles) in nature. In the standard PSO algorithm, particles (or individuals) represent potential solutions to an optimization problem where each particle is composed of three vectors: its position in the search space**,** the best position that has been found by the individual (or particle) and the velocity of the individual. Further details about the PSO algorithm can be found in [26, 27, 28].

Recently, the application of the ACO algorithm has increased in many engineering areas. This algorithm was inspired by the colonies of ants, and has been frequently used to solve both continuous and discrete optimization problems. In this section, the ACO for continuous optimization problems (sometimes called $\text{ACO}_{\mathbb{R}}$), which is proposed by Socha and Dorigo [24], is discussed in detail. In this algorithm, the probability density function (PDF) is used in the decision making process where a set of solutions (called a solution archive) is usually sampled and used to obtain the probability density function. First, the solution archive is initialized by randomly generating Q solutions. Next, P new solutions are generated and added to the previous Q solutions so that the solution archive size becomes $Q + P$. Then, these solutions are sorted according to an objective function and the best Q solutions are stored in the solution archive. This procedure is called archive update where the solution archive matrix is represented in Eq. (8.9).

$$\boldsymbol{T} = \begin{bmatrix} \check{x}_1^1 & \check{x}_1^2 & \cdots & \check{x}_1^i & \cdots & \check{x}_1^d \\ \check{x}_2^1 & \check{x}_2^d & \cdots & \check{x}_2^d & \cdots & \check{x}_2^d \\ \vdots & \vdots & \cdots & \vdots & \cdots & \vdots \\ \check{x}_j^1 & \check{x}_j^2 & \cdots & \check{x}_j^i & \cdots & \check{x}_j^d \\ \vdots & \vdots & \cdots & \vdots & \cdots & \vdots \\ \check{x}_Q^1 & \check{x}_Q^2 & \cdots & \check{x}_Q^i & \cdots & \check{x}_Q^d \end{bmatrix} \tag{8.9}$$

where d represents the number of solution components or the size of the updating parameters, Q is the number of solutions stored in the archive while $\check{x}_j^i$ represents the i-th solution component (or the i-th updating parameter) of j-th solution. As indicated by Eq. (8.9), each row in the matrix $\boldsymbol{T}$ corresponds to a possible solution and the value of the objective function provides the value of each solution. The probabilistic solution construction procedure is one of the important procedures in the ACO algorithm. In this procedure, a multimodal one-dimensional probability density function based on a Gaussian kernel is employed to generate (or construct) solutions. This Gaussian kernel function consists of the weighted sum of several Gaussian functions g_j^i where i is the coordinate index (or the solution component) and j is the solution index. The Gaussian kernel for the coordinate i is given by:

$$G^i(x) = \sum_{j=1}^{Q} w_j g_j^i(x) = \sum_{j=1}^{Q} w_j \frac{1}{\sigma_j^i \sqrt{2\pi}} e^{-\frac{\left(x-\mu_j^i\right)^2}{2\sigma_j^{i\,2}}} \tag{8.10}$$

Note that: $j \in \{1, \ldots, Q\}$ and $i \in \{1, \ldots, d\}$. The quantity w_j represents the weight with the ranking of solution j in the archive, $rank(j)$. The weight is also calculated according to a Gaussian function:

$$w_j = \frac{1}{qQ\sqrt{2\pi}} e^{-\frac{(rank(j)-1)^2}{2q^2Q^2}} \tag{8.11}$$

where q is a constant with a small value. In the solution construction process, each ant uses a probabilistic quantity defined in Eq. (8.12) to select one of the solutions in the archive according to its corresponding weight.

$$p_j = \frac{w_j}{\sum_{i=1}^{Q} w_i} \tag{8.12}$$

Then, the new component $\check{x}_j^i$ is obtained by sampling around the selected component using a Gaussian PDF where the mean value $\mu_j^i = \check{x}_j^i$, and σ_j^i is defined by:

$$\sigma_j^i = \xi \sum_{r=1}^{Q} \frac{\left|\check{x}_r^i - \check{x}_j^i\right|}{Q-1} \tag{8.13}$$

σ_j^i represents the average distance between the *i-th* component of the solution $\check{x}_j$ and the *i*-th component of the other solutions in the archive matrix while ξ is a constant. The constant ξ has a similar effect to that of the pheromone evaporation rate in ACO for discrete optimization [25]. After each solution construction, the pheromone update is performed by adding the new P constructed solutions to the solution archive matrix $\boldsymbol{T}$, then only the best Q solutions are kept in the archive solution. The ACO algorithm will be used to minimize the objective function described in Eq. (8.5).

8.3 Numerical Illustrations

In this subsection, a five-DOF linear system shown in Fig. 8.1 is updated by correcting a vector of 5 unknown parameters $\boldsymbol{\theta} = \{\theta_1, \theta_2, \theta_3, \theta_4, \theta_5\}$. The system consists of five masses and ten springs where the deterministic parameters of the system are: $m_1 = m_2 = 27$ kg, $m_3 = 71$ kg, $m_4 = 53$ kg, $m_5 = 29$ kg, $k_3 = 3200$ N/m, $k_5 = 1840$ N/m, $k_7 = 2200$ N/m, $k_9 = 2800$ N/m and $k_{10} = 2000$ N/m. The parameters: k_1, k_2, k_4, k_6 and k_8 are the uncertain parameters where their uncertainties are defined as fuzzy membership functions. First, the simulated measured data were generated using the true values of the uncertain parameters. These simulated measurements will be used to update the fuzzy membership functions of the input parameters using the proposed FFEMU based ACO algorithm. The results obtained by the FFEMU based ACO algorithm are compared with the results obtained by the FFEMU based PSO algorithm and the Metropolis-Hastings (M-H) algorithm.

In the FFEMU algorithms, ten α-cuts were used in the optimization procedure. The general bounds $\boldsymbol{\theta}_{max}$ and $\boldsymbol{\theta}_{min}$ are set to: $\{4600, 2500, 2370, 3300, 2650\}$ and $\{3400, 1900, 1700, 1900, 2150\}$, respectively. For the ACO algorithm, the value of Q is set to 10, $P = 20$, $q = 0.5$ and $\xi = 1$. Concerning the PSO algorithms, 80 particles were used for the optimization while the number of samples is set to $N_s = 10000$ for the M-H algorithm. The membership functions of the uncertain parameters obtained by the FFEMU based ACO and the FFEMU based PSO algorithms are shown in Figs. 8.2 and 8.3, respectively. The density functions obtained by the M-H algorithm are shown in Fig. 8.4.

As shown in Figs. 8.2 and 8.3, the membership functions obtained by the FFEMU based ACO algorithm have perfect triangular forms which are not the case with the membership functions obtained by the FFEMU based PSO algorithm. Moreover, the FFEMU based ACO algorithm does not require a large number of ants Q while the number of particles used

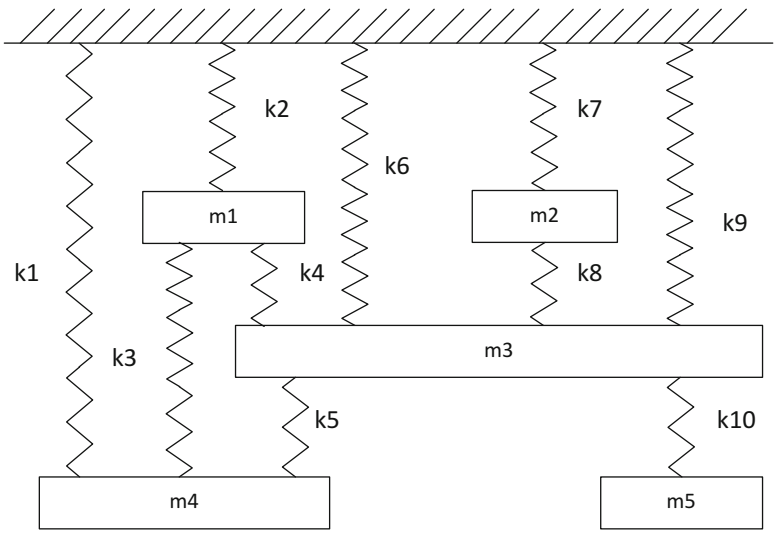

Fig. 8.1 Five degree of freedom mass-spring system

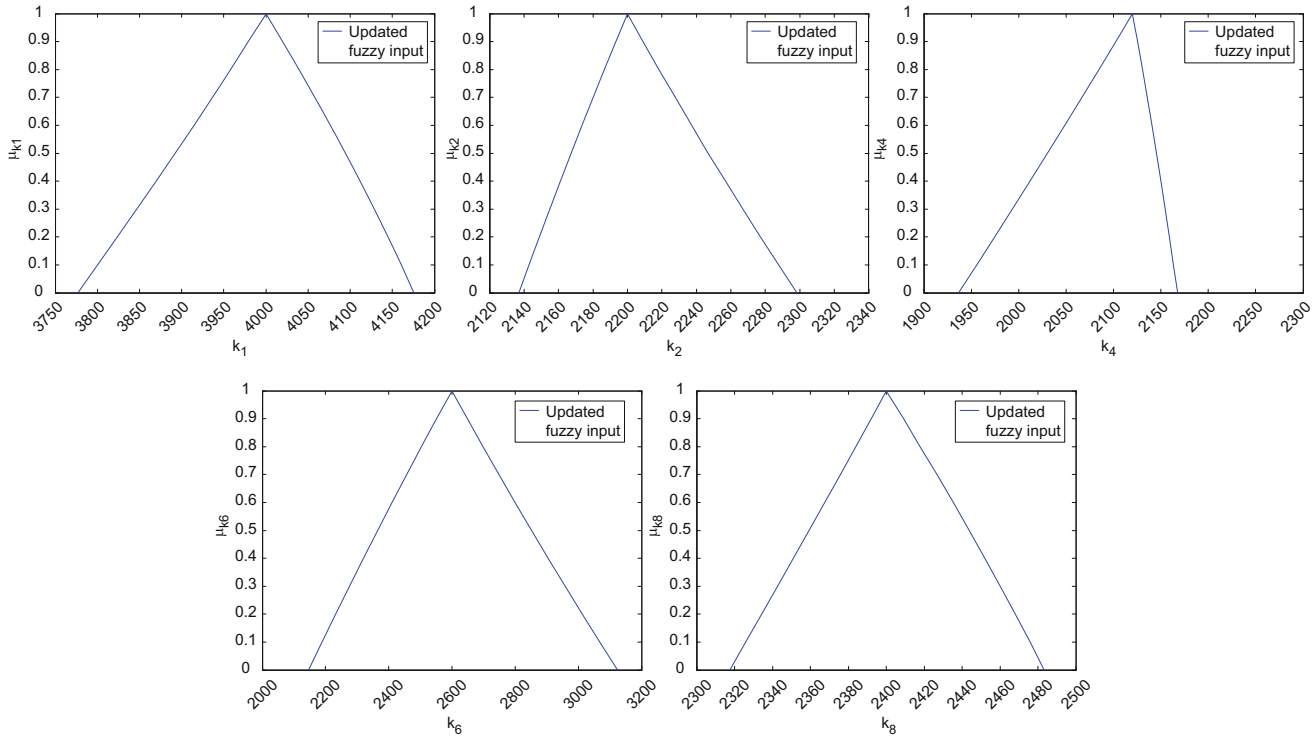

Fig. 8.2 The membership functions of the updating parameters obtained by the FFEMU base ACO algorithm

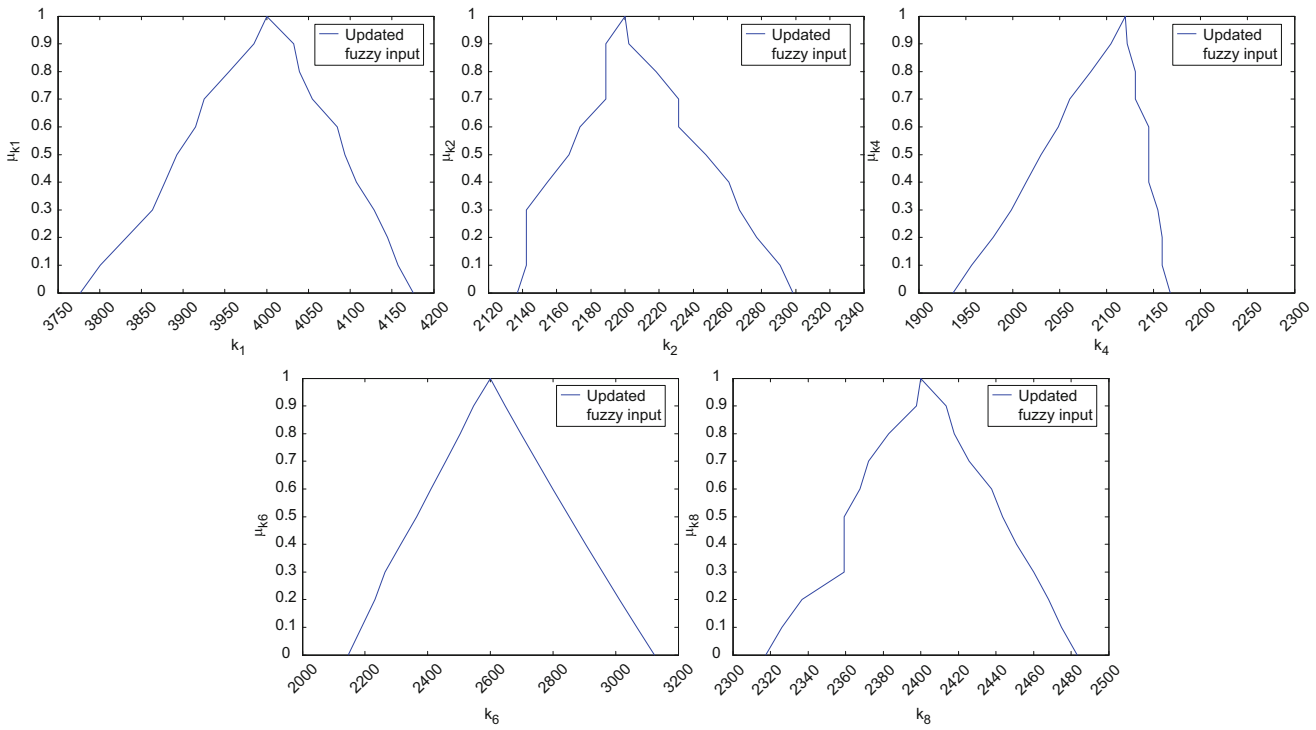

Fig. 8.3 The membership functions of the updating parameters obtained by the FFEMU base PSO algorithm

by FFEMU based PSO algorithm is 80 particles (the FFEMU based PSO algorithm gives poor membership forms when less than 80 particles are involved in the optimization). The reason that the FFEMU based ACO algorithm give better shapes with fewer ants is that the solution construction procedure is fully automated (see Eq. (8.13)) while the PSO algorithm uses

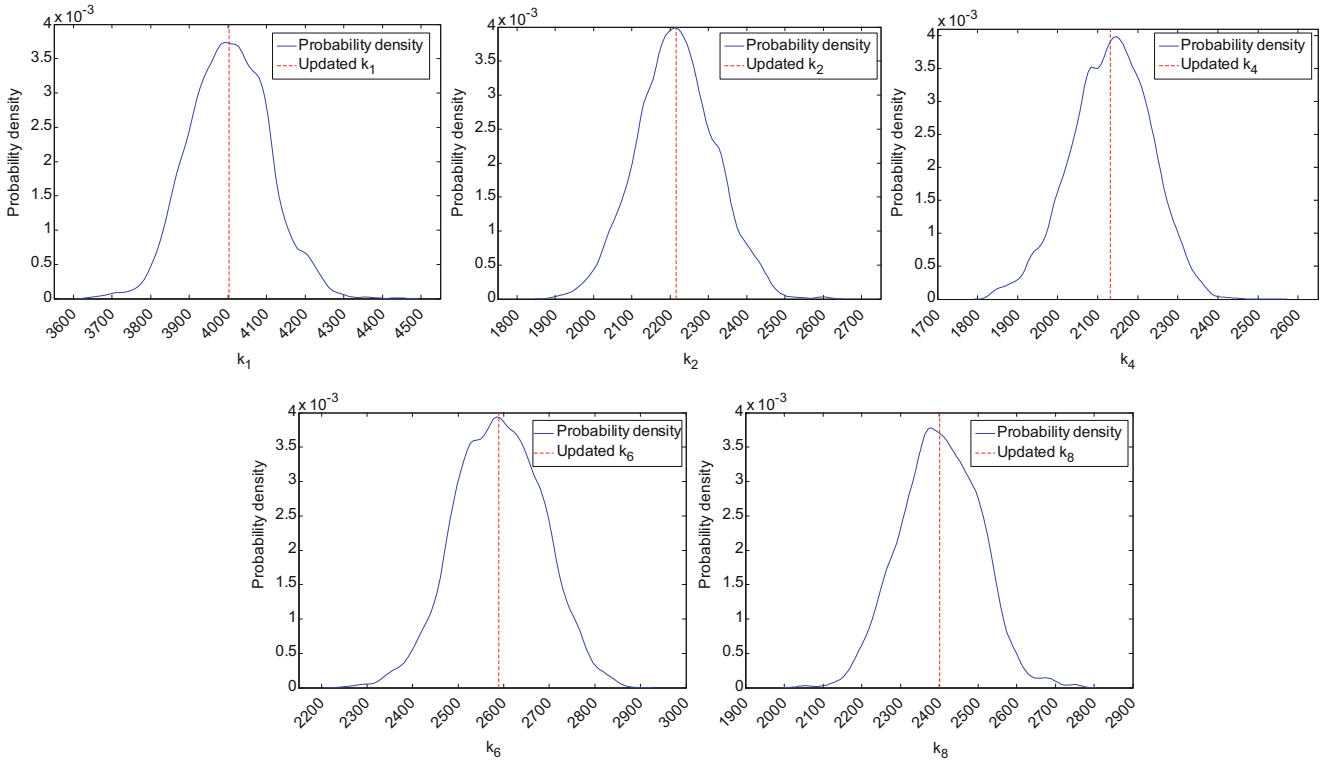

Fig. 8.4 The probability density functions of the updating parameters obtained by the M–H algorithm

Table 8.1 Initial, intervals and updated parameters when FFEMU and M–H algorithms are used to update the structure

	$\boldsymbol{\theta}_0$ vector initial	$\boldsymbol{\theta}$ vector, FFEMU-ACO method	$\boldsymbol{\theta}$ interval, FFEMU-ACO method	$\boldsymbol{\theta}$ vector, FFEMU-PSO method	$\boldsymbol{\theta}$ interval, FFEMU-PSO method	$\boldsymbol{\theta}$ vector, M-H method	$\frac{\sigma_i}{\theta_i}$ (%)
$k1$	4150	4000	[3776.4, 4175.6]	4000	[3776.4, 4175.6]	4002.6	2.55%
$k2$	2150	2200	[2137.0, 2298.3]	2200	[2137.0, 2298.3]	2215.5	4.61%
$k4$	2160	2120	[1936.6, 2167.6]	2120	[1936.6, 2167.6]	2132.0	4.63%
$k6$	2500	2600	[2146.7, 3123.9]	2600	[2146.7, 3123.9]	2589.3	3.66%
$k8$	2460	2400	[2317.4, 2483.4]	2400	[2317.4, 2483.4]	2401.7	4.24%

the velocity bounds to generate the new velocity of the particles (to generate new solutions). These bounds of the velocity are fixed and when the algorithm moves from one interval to the next, the search space will be reduced according to the constraints presented in Eq. (8.6). The new search space may require a different velocity bounds to obtain better results which is not true since the velocity bounds are already fixed. To overcome this weakness, a large number of particles are used to ensure good results or the velocity bounds are adjusted in every α-cut. The density functions presented in Fig. 8.4 show some similarity with the membership functions in term of variation range of the parameters.

The updating values of the uncertain parameters are presented in Table 8.1 along with their initial values, measured values and the updating bounds. In the case of M-H algorithm, the coefficients of variation (c.o.v) values are also presented. Table 8.1 shows that the updating parameters along with their bounds obtained by FFEMU based ACO and FFEMU based PSO algorithms are exactly the same. The results obtained by the M–H algorithm are slightly different which was expected since the PSO and ACO algorithms are more accurate than the Monte Carlo methods. The c.o.v values obtained by the M–H algorithm are relatively small (less than 5%) which indicates that the M–H algorithm has efficiently estimated the uncertain parameters.

Figs. 8.5 and 8.6 show the membership functions of the updated outputs for the FFEMU based ACO and FFEMU based PSO algorithms, respectively. The FFEMU based ACO algorithm gives an excellent match between fuzzy membership functions of the updated outputs and the measured outputs. Also, the membership functions obtained by the FFEMU based ACO are slightly better than those obtained by the FFEMU based PSO algorithm.

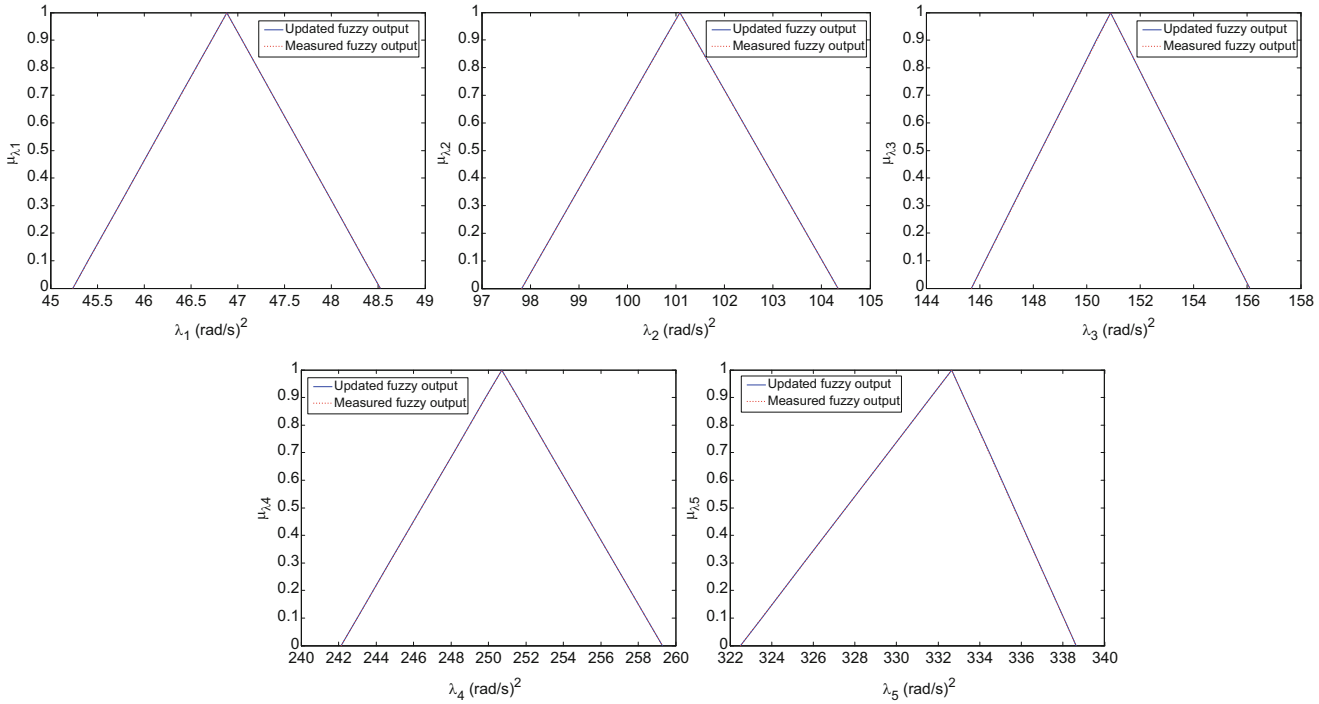

Fig. 8.5 The membership functions of the updating outputs obtained by the FFEMU base ACO algorithm

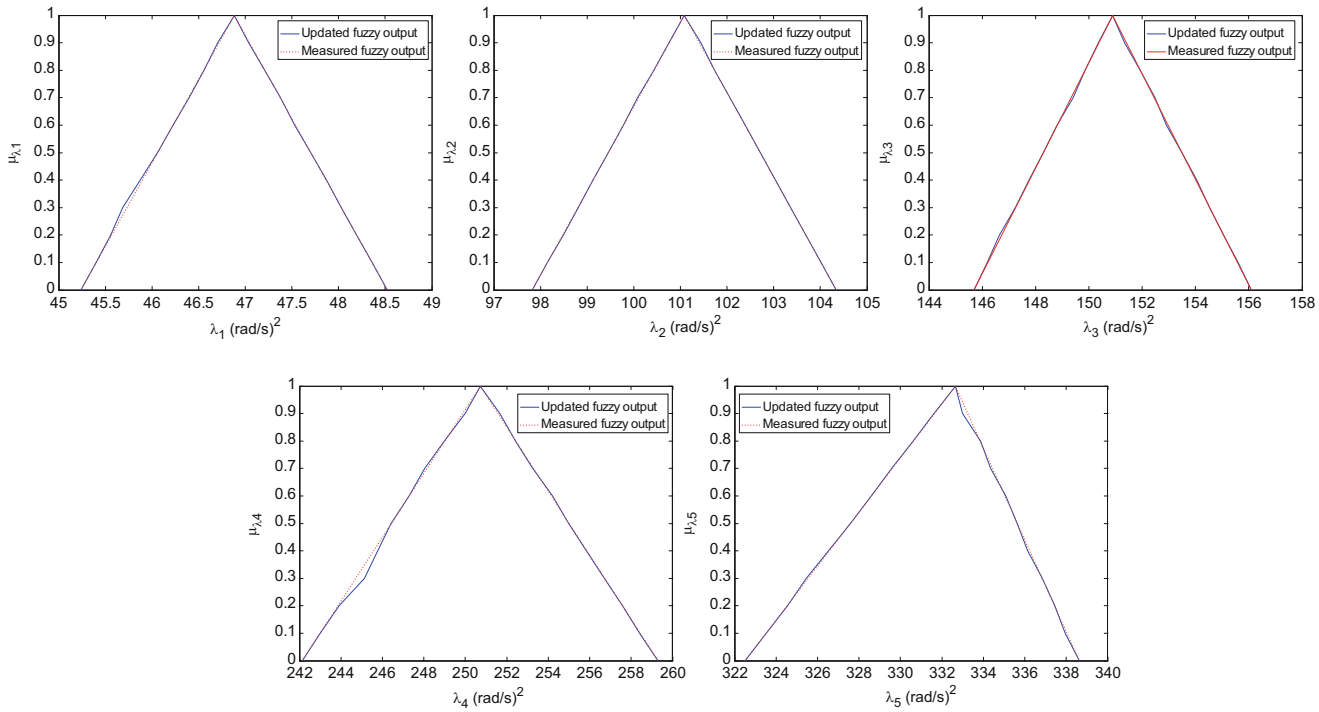

Fig. 8.6 The membership functions of the updating outputs obtained by the FFEMU base PSO algorithm

Table 8.2 shows the initial, updated eigenvalues and interval eigenvalues along with the absolute errors obtained by all methods. Again, the updating eigenvalues and their bounds obtained by both FFEMU based ACO and FFEMU based PSO algorithms are exactly the same. The M-H algorithm gives also good results in term of total error (0.17%) or c.o.v values (less than 2%).

Table 8.2 The eigenvalues, intervals and errors when FFEMU and M-H algorithms are used to update the structure

Mode	Measured eigenvalues (Hz)	Initial eigenvalues (Hz)	Error (%)	Eigenvalues FFEMU-ACO method (Hz)	Error (%)	Interval FFEMU-ACO method (Hz)	Eigenvalues FFEMU-PSO method (Hz)	Error (%)	Interval FFEMU-ACO method (Hz)	Eigenvalues M-H method (Hz)	Error (%)
1	46.88	46.50	1.99	46.88	0.00	[45.24, 48.52]	46.88	0.00	[45.24, 48.52]	46.90 (0.73%)	0.03
2	101.08	100.87	2.94	101.08	0.00	[97.82, 104.34]	101.08	0.00	[97.82, 104.34]	101.23 (1.17%)	0.15
3	150.89	148.52	2.93	150.89	0.00	[145.68, 156.10]	150.89	0.00	[145.68, 156.10]	151.36 (1.91%)	0.31
4	250.72	248.08	1.52	250.72	0.00	[242.13, 259.29]	250.72	0.00	[242.13, 259.29]	250.91 (1.48%)	0.08
5	332.66	333.89	3.02	332.66	0.00	[322.50, 338.64]	332.66	0.00	[322.50, 338.64]	333.57 (1.38%)	0.28
Total average error	–	–	*2.48*	–	*0.00*	–	–	*0.00*	–	–	*0.17*

8.4 Conclusion

In this paper, an FFEMU algorithm was implemented to identify the membership functions of the inputs. The FFEMU problem was formulated as an optimization problem where the ACO algorithm was employed to provide the membership functions of the inputs. To test this algorithm, a five-DOF mass-spring system was updated using the FFEMU based ACO algorithm. The results obtained were also compared with FFEMU based PSO and M–H algorithms results. The ACO algorithm was able to obtain very good results with few ants. In further work, more complex structures will be investigated and the fuzzy finite element model will be improved in term of computational cost and accuracy.

References

1. Bhatti, M.A.: Fundamental Finite Element Analysis and Applications: with Mathematica and Matlab Computations. Hoboken, New Jersey. Wiley (2005)
2. Onãte, E.: Structural analysis with the finite element method. Linear statics. In: Basis and Solids, vol. 1. Barcelona, Springer (2009)
3. Rao, S.S.: The Finite Element Method in Engineering, 4th edn. Elsevier Butterworth Heinemann, Burlington (2004)
4. Friswell, M.I., Mottershead, J.E.: Finite Element Model Updating in Structural Dynamics. Kluwer Academic Publishers (1995)
5. Marwala, T.: Finite Element Model Updating Using Computational Intelligence Techniques. Springer Verlag, London, UK (2010)
6. H.H. Khodaparast. Stochastic finite element model updating and its application in aeroelasticity. Ph.D. Thesis, Department of Civil Engineering, University of Liverpool, (2010).
7. Marwala, T., Boulkaibet, I., Adhikari, S.: Probabilistic Finite ElementModel Updating Using Bayesian Statistics: Applications to Aeronautical and Mechanical Engineering. Pondicherry, India, John Wiley & Sons (2016)
8. I. Boulkaibet, T. Marwala, M. I. Friswell, and S. Adhikari. An adaptive markov chain monte carlo method for bayesian finite element model updating. In Special Topics in Structural Dynamics, vol. 6, pp. 55–65. Springer International Publishing, 2016.
9. I. Boulkaibet, L. Mthembu, T. Marwala, M. I. Friswell and S. Adhikari. Finite Element Model Updating Using Hamiltonian Monte Carlo Techniques, Inverse Problems in Science and Engineering, 2016.
10. Boulkaibet, I., Mthembu, L., Marwala, T., Friswell, M.I., Adhikari, S.: finite element model updating using the shadow hybrid Monte Carlo technique. Mech. Syst. Signal Process. **52**, 115–132 (2015)
11. Moore, R.: Interval analysis. Prentice Hall, Englewood Cliffs (1966)
12. Moens, D., Vandepitte, D.: An interval finite element approach for the calculation of envelope frequency response functions. Int. J. Numer. Methods Eng. **61**, 2480–2507 (2004)
13. Khodaparast, H.H., Mottershead, J.E., Badcock, K.J.: Interval model updating with irreducible uncertainty using the Kriging predictor. Mech. Syst. Signal Process. **25**(4), 1204–1226 (2011)
14. Zadeh, L.A.: Fuzzy sets. Inf. Control. **8**(3), 338–353 (1965)
15. Moens, D., Vandepitte, D.: Recent advances in non-probabilistic approaches for non-deterministic dynamic finite element analysis. Arch. Comput. Methods Eng. **13**(3), 389–464 (2006)
16. Chen, L., Rao, S.S.: Fuzzy finite-element approach for the vibration analysis of imprecisely-defined systems. Finite Elem. Anal. Design. **27**(1), 69–83 (1997)
17. Moens, D., Vandepitte, D.: A fuzzy finite element procedure for the calculation of uncertain frequency response functions of damped structures: part 1 procedure. J. Sound Vib. **288**(3), 431–462 (2005)
18. Erdogan, Y.S., Bakir, P.G.: Inverse propagation of uncertainties in finite element model updating through use of fuzzy arithmetic. Eng. Appl. Artif. Intell. **26**(1), 357–367 (2013)

19. H.H. Khodaparast, Y. Govers, S. Adhikari, M. Link, M. I. Friswell, J. E. Mottershead, and J. Sienz. Fuzzy model updating and its application to the DLR AIRMOD test structure. Proceeding of ISMA 2014 including USD 2014, (2014).
20. Liu, Y., Duan, Z.: Fuzzy finite element model updating of bridges by considering the uncertainty of the measured modal parameters. Sci. China Technol. Sci. **55**(11), 3109–3117 (2012)
21. Adhikari, S., Khodaparast, H.H.: A spectral approach for fuzzy uncertainty propagation in finite element analysis. Fuzzy Sets Syst. **243**, 1–24 (2014)
22. Nguyen, H.T.: A note on the extension principle for fuzzy sets. J. Math. Anal. Appl. **64**(2), 369–380 (1978)
23. Qiu, Z., Hu, J., Yang, J., Lu, Q.: Exact bounds for the sensitivity analysis of structures with uncertain-but-bounded parameters. Appl. Math. Model. **32**(6), 1143–1157 (2008)
24. Socha, K., Blum, C.: An ant colony optimization algorithm for continuous optimization: application to feed-forward neural network training. Neural Comput. & Applic. **16**(3), 235–247 (2007)
25. I.C.J. Riadi. Cognitive Ant colony optimization: A new framework in swarm intelligence, Doctoral dissertation, University of Salford, (2014).
26. J. Kcnncdy, R.C. Eberhart, Particle swarm optimization, Proceedings of the IEEE International Joint Conference on Neural Networks, 4:1942–1948, (1995).
27. I. Boulkaibet, L. Mthembu, F. De Lima Neto and T. Marwala. Finite Element Model Updating Using Fish School Search Optimization Method, 1st BRICS & 11th CBIC Brazilian Congress on Computational Intelligence, Brazil, 2013.
28. Boulkaibet, I., Mthembu, L., De Lima Neto, F., Marwala, T.: Finite element model updating using fish school search and volitive particle swarm optimization. Integr. Computer-Aided Eng. **22**(4), 361–376 (2015)

Chapter 9
The Combination of Testing and 1D Modeling for Booming Noise Prediction in the Model Based System Testing Framework

Fábio Luis Marques dos Santos, Tristan Enault, Jan Deleener, Tom Van Houcke, and Herman Van der Auweraer

Abstract Nowadays, many of the proposed solutions to improve automotive vehicle efficiency, such as downsized engines and advanced torque lock-up strategies (for automatic transmissions), can lead to worse noise and vibration characteristics. A typical phenomenon that occurs in such situations is low-frequency booming noise, which happens because of the irregular torque vibrations that are transferred through the flexible driveline elements. This paper presents a combined test and 1D modelling approach used to analyze and predict driveline torsional oscillations and their effect on low frequency booming noise and vibration. In this context, Model Based System Testing (MBST) can be defined as the framework that combines physical testing and simulation with the objective of validating and improving the behavior of 1D multiphysical models. Tests are carried out to obtain insight in the dynamical system behavior, as well as to obtain specific component parameters. This data is then used to create and improve 1D models of the full vehicle driveline, and to predict booming noise characteristics.

Keywords Booming noise • Model based system testing • NVH • Multiphysics • Hybrid testing

9.1 Introduction

9.1.1 Vehicle Torsional Vibration

Recently, the ever pressing and growing demand for lower automotive vehicle emissions and higher fuel efficiency has led to the design of lightweight and other technology solutions to automotive vehicles [1], including the drivetrain. New powertrain technologies, such as start-stop systems [2], downsized engines [3], cylinder deactivation [4] and advanced torque lock-up strategies [5] are all examples of solutions that can be effective in reducing emissions, but that at the same time can generate undesired vibration issues, mostly propagated through the vehicle driveline. In this scenario, the advance of those technologies raises the importance of an in-depth understanding of torsional vibrations as they negatively impact comfort and are directly related to engine and driveline efficiency. The main consequences of these new technologies are:

- High torque oscillations: the torque generated by internal combustion engines is irregular, containing ripples due to combustion cycles. Reducing the number of cylinders has the consequence of increasing this torque irregularity.
- Lower engine speed: engine efficiency can be higher at lower rotational speeds, making it the tendency to operate engines at lower RPMs. However, these lower speed conditions can excite driveline torsional modes and suspension modes, leading to higher vibration levels.
- Lower torsional damping: in automatic transmissions, locking the clutch at lower RPMs can increase the transmission efficiency, with the drawback of having less torsional damping in lower rotational speeds.

Figure 9.1 summarizes these changes in the powertrain and how they affect the overall vibration levels. The first graph indicates how the lock-up condition happens before employing the more efficient methodologies, with the dashed line representing the RPM state in which the clutch is locked, and the peak is related to the driveline resonance. By using turbo

F.L.M. dos Santos (✉) • T. Enault • J. Deleener • T. Van Houcke
Siemens Industry Software NV, Interleuvenlaan 68, 3001 Leuven, Belgium
e-mail: fabio.m.santos@siemens.com

H. Van der Auweraer
Siemens Industry Software NV, Interleuvenlaan 68, 3001 Leuven, Belgium

Division PMA, KU Leuven (KUL), Celestijnenlaan 300B, 3001 Heverlee, Belgium

N. Dervilis (ed.), *Special Topics in Structural Dynamics, Volume 6*, Conference Proceedings of the Society for Experimental Mechanics Series, DOI 10.1007/978-3-319-53841-9_9

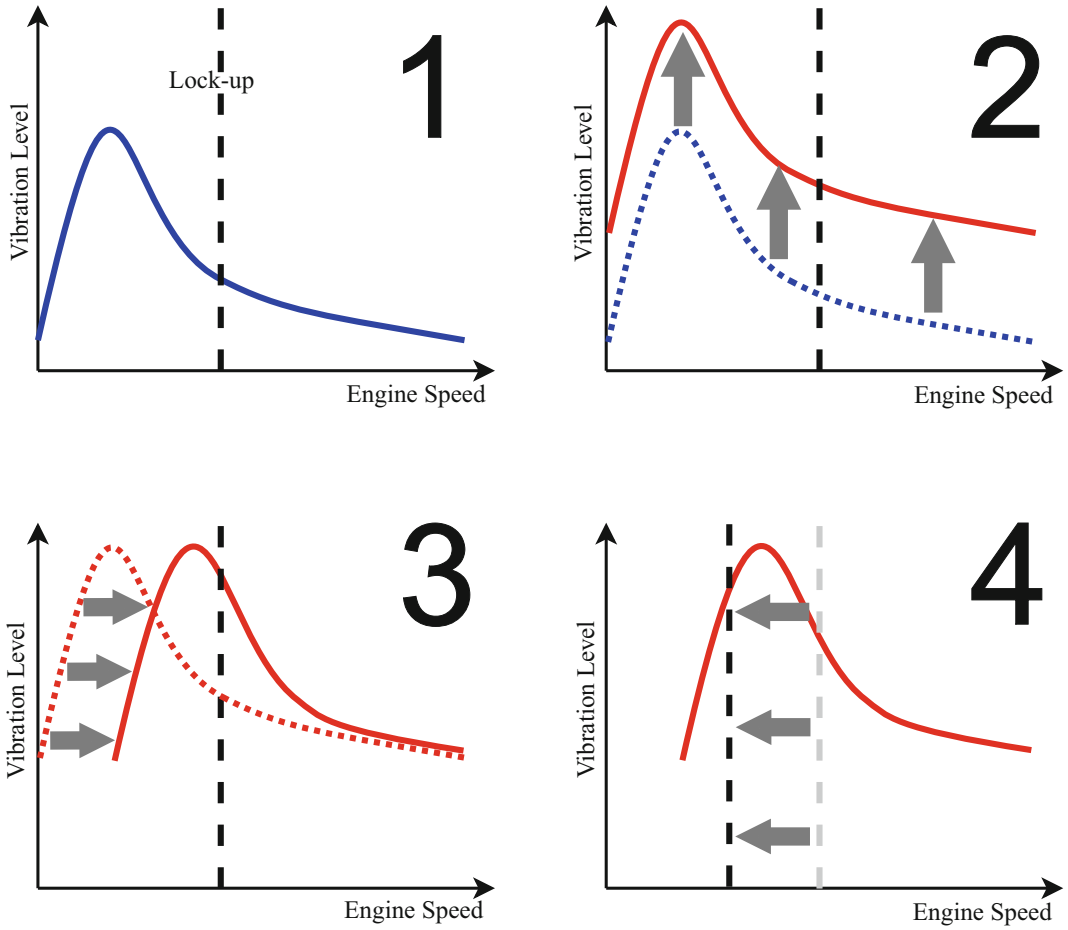

Fig. 9.1 Vehicle automatic transmission lock-up evolution: (1) Clutch lock-up without efficient technologies; (2) Increase of vibration levels due to turbocharged engines; (3) Shift of excitation peak due to reduced number of cylinders; (4) Use of lock-up at lower RPMs

charged engines with higher torque irregularities, the direct consequence is higher vibration levels, as shown in the second graph. Then, the use of a reduced number of cylinders leads to a shift in the excitation frequency, represented in the third graph. Finally, the clutch lock-up is carried out at lower rotational speeds to improve efficiency, as shown in the fourth graph. The consequences of these measures is the increased vibration level which is not damped by the torque converter, leading to undesired booming noise.

Vibration can propagate from the powertrain to the driver and passengers mainly in two ways: via the powertrain mounts and into the car body, or through the transmission and driveline into the suspension and then into the car body [6]. Figure 9.2 shows a scheme with the two vibration paths. In this context, vehicle boom can be defined as an undesirable low-frequency noise, which is induced by torsional vibrations propagated through the vehicle driveline (mainly transmission, propshaft and drive shaft) to the suspension [7]. The low frequency torsional vibrations can excite the differential and suspension natural frequencies, leading to amplified vibration.

9.1.2 Model Based System Testing

The use of testing for parameter identification and troubleshooting has been a common practice in the industry for a long time. In this context, experimental modal analysis (EMA) is a well known and established procedure in both academia [8] and industry [9]. It is widely accepted as a means of estimating and identifying the modal parameters of a system for structural dynamics and NVH applications. Modal analysis is commonly associated with the use of finite element simulation models for correlation [10] and updating [11] of parameters, with the purpose of improving the accuracy of the analysis, and even extend it beyond the common test boundaries. This practice is commonly used in automotive applications [12].

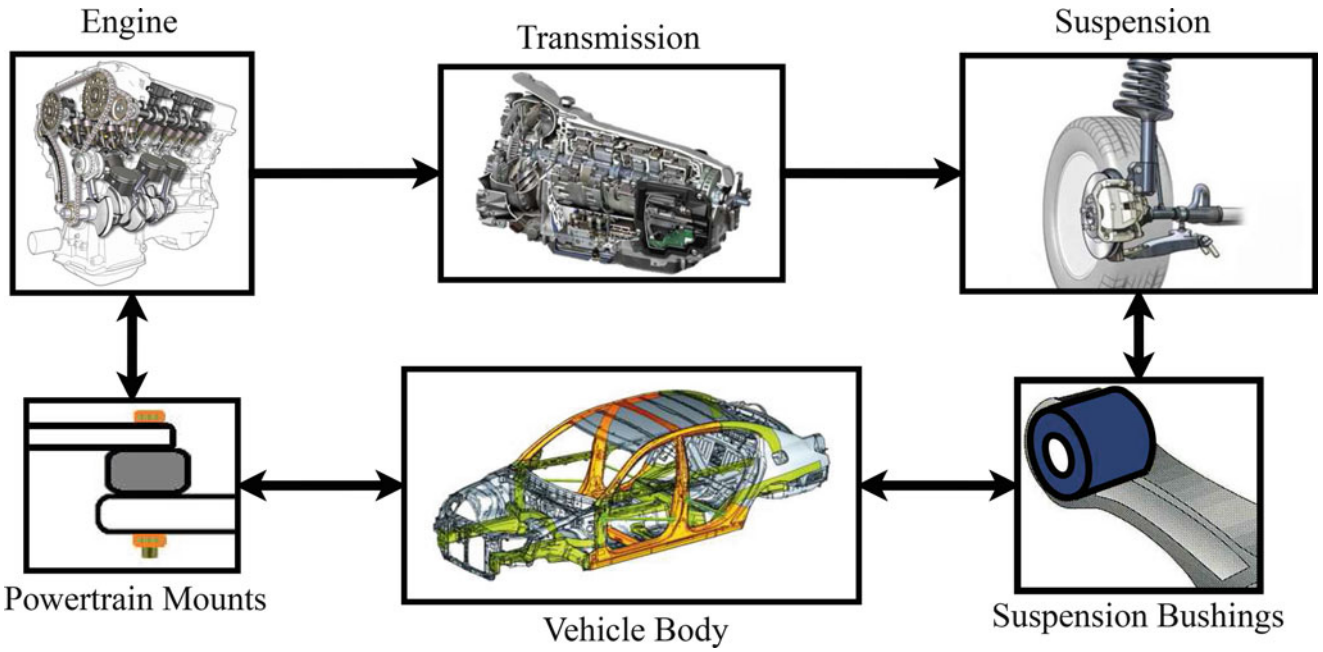

Fig. 9.2 Vibration generated by the powertrain and the two transmission paths

However, the growing need of more efficient methodologies for product development, combined with the increased use of mechatronic systems in automotive vehicles [13] has led to an evolution on the way testing, simulation and correlation is carried out. The experimental methodologies have gone beyond the boundaries of purely mechanical systems, with their applications expanded to other fields, such as electrical motor testing [14], electromechanical systems [15] and mechatronic applications [16]. Testing is also is no longer solely related to troubleshooting analysis, and the identified parameters can be used to estimate forces and loads [17, 18] acting on a system.

The challenges that arise with respect to physical testing are related to the growing complexity and multiphysical nature of these new systems and applications. In turn, this leads not only to new ways of carrying out the tests (and a more diverse type of measurement quantities), but also to new types of numerical models to be validated, such as multibody and 1D multiphysical simulation models. In this way, test data can be used on one hand to validate these models, and on the other hand for more complex and realistic interactions, combining these multiphysical models with experimental data into hybrid approaches, where a system can be tested in a system-in-the-loop (SyiL) configuration, where part of the system is physical, and part of it is simulated.

In this context, the Model Based System Testing (MBST) framework [19] was defined as the discipline combining physical testing and simulation models. Its main purpose is to study, identify, validate and improve the behavior of multiphysical and mechatronic systems. It expands the scope of testing beyond structural measurements and/or 3D simulation models, and also includes multiphysical systems and 1D simulation models. MBST can be divided into three categories: "Testing for Simulation", "Simulation for Testing" and "Testing with Simulation", with the first two being cases where test and simulation are decoupled, and in the latter, test and simulation are tightly coupled. The first category is an expansion of one of the main roles in modal analysis—obtaining test parameters to create and/or improve simulation models, but in this case also including multiphysics systems. It also includes the use test post-processing tools with simulation data. The "Simulation for Testing" category is related to the use of simulation models to improve or accelerate the testing process—this includes well known procedures, such as optimal sensor and excitation placement, but contains also more recent methodologies, such as virtual testing or human-in-the-loop interactions. Finally, the last category contains the cases in which test and simulation are tightly coupled. Such is the case with hardware-in-the-loop, system-in-the-loop, virtual sensing and hybrid testing, mostly involving real-time processing applications. Figure 9.3 shows the MBST tree diagram with all the categories.

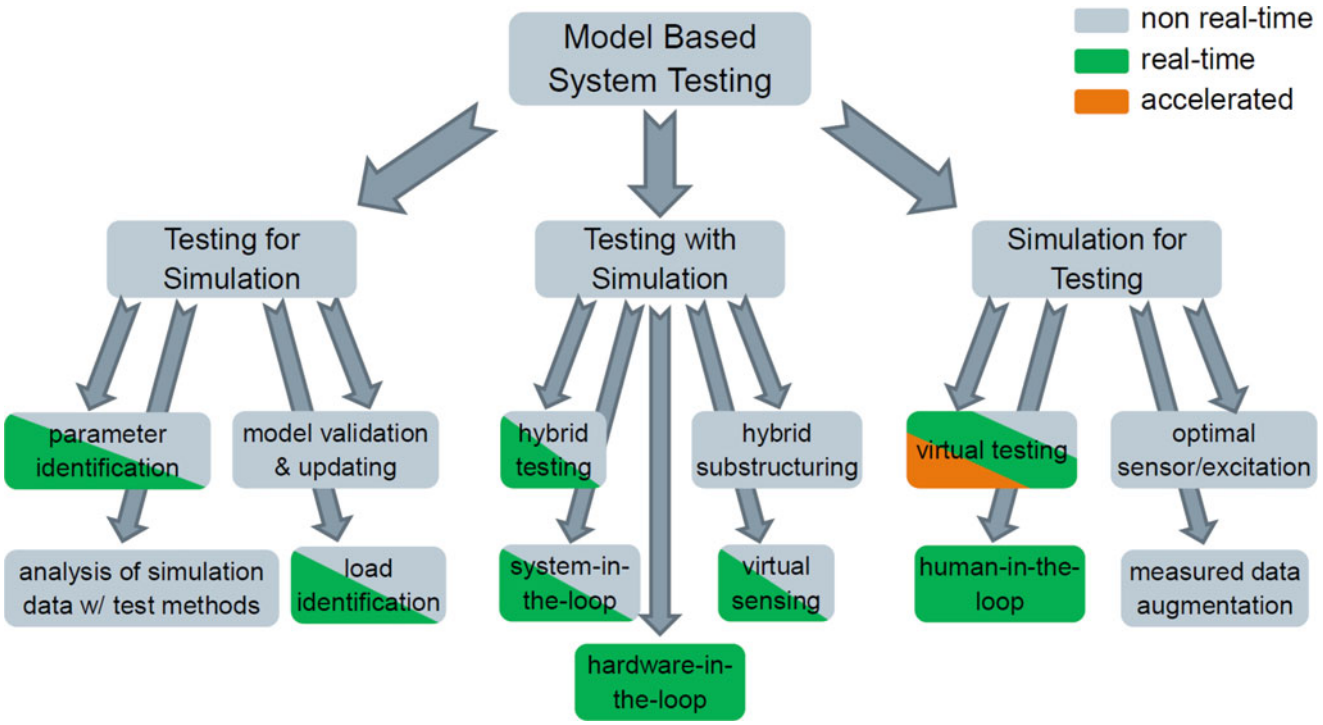

Fig. 9.3 Model based system testing application tree

9.2 MBST Applied to Driveline Boom

One of the traditional ways of carrying out NVH analysis in automotive vehicles is transfer path analysis (TPA). This technique is widely employed in the automotive industry, and is used to determine the overall contribution of different transmission paths towards defined targets, such as seat vibration or driver's ears. TPA is very efficient in determining the vibration paths and their contributions in higher frequencies, but can have limited accuracy in the lower frequency range. Moreover, due to the fact that booming noise arises from the interaction between rotational components and the vehicle suspension, it is hard to obtain realistic excitation (and measurements) when the vehicle is not in operational condition, which is one of the requirements of classical TPA approaches.

To overcome this limitation, an integrated approach is proposed, using 1D simulation tools combined with testing. In this way, test data is used to validate and improve 1D simulation models, which in turn can be used to analyze important system attributes. Figure 9.4 shows a diagram of the procedure and how it is carried out. Initially, static and component specific measurements are carried out for different components, to obtain their parameters used in simulation. This includes the geometry of parts and components, when necessary for the simulation, but also static stiffness and mass and inertia measurements. The modal analysis can be used to obtain the vibration modes of the suspension and related components. Then, operational measurements are also carried out, with the goal of understanding the interaction between the driveline components (engine, clutch, drivetrain, suspension, car body). These test parameters are used to model some components, and are also used to validate and correlate simulation with test results. There are two sets of results from the test and simulation parts. The testing can be used not only to obtain component parameters and validation data, but can also be used for troubleshooting, to verify root cause of possible problems. The analysis based on the simulation model can be used to predict changes in components, and how these will affect the overall behavior of the vehicle, with respect to the low-frequency NVH parameters.

The following sessions will show in detail how the test data can be used to generate the models, and how the driveline is modeled to predict booming noise.

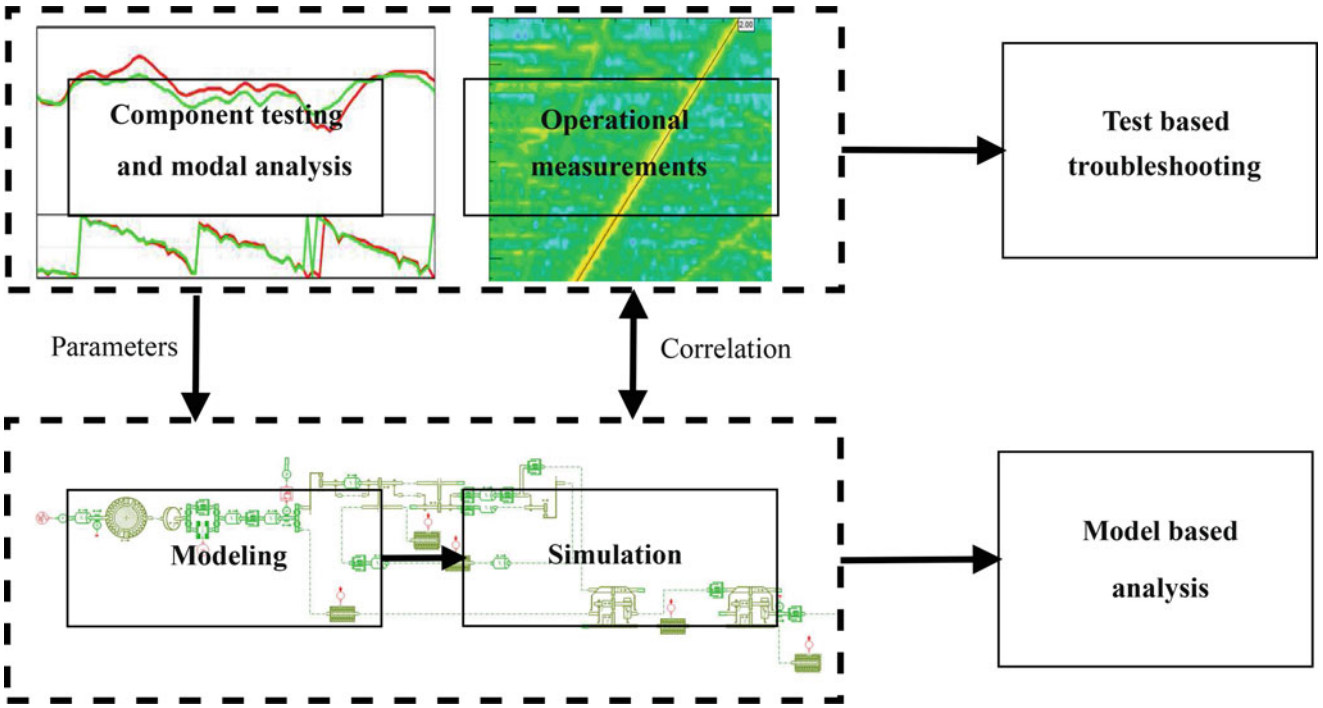

Fig. 9.4 Diagram of test-simulation integration

9.2.1 Testing

Testing has mainly three purposes—to identify physical and dynamic parameters to be used in the model, to obtain operational data that can be used to validate and correlate simulation results, and also provide test based diagnosis and troubleshooting, providing additional insight into the system. In this way, the test phase can be divided in four parts:

- Instrumentation
- Static, component measurements and modal analysis
- Operational measurements
- Diagnosis

The instrumentation phase is defined based on the requirements of the other tests. It is important to measure as many physical quantities as possible, but at the same time, using too many sensors can dramatically increase the cost of the test campaign. Figure 9.5 shows some typical measured quantities in a test campaign, for each of the subsystems.

Static and dynamic measurements are crucial for the modeling phase, providing parameters such as shaft stiffness, mass and inertia properties of the vehicle body and engine, as well as the dynamic and static stiffness of mounts, as shown in Fig. 9.6.

The operational data is used for model correlation and updating, as well as for troubleshooting and diagnosis, to better understand the underlying problems in the vehicle. Figure 9.7 shows the seat vibration and microphone measurements obtained from operational data, using different throttle positions. In this case, the second order components of the measurements is shown.

9.2.2 Simulation

The simulation phase consists in using the parameters and data obtained in the test phase, together with knowledge about the vehicle and its subsystems, to model and validate the low-frequency using 1-D modeling simulation. Essentially, the simulation step can be divided in three phases, as previously shown in Fig. 9.4:

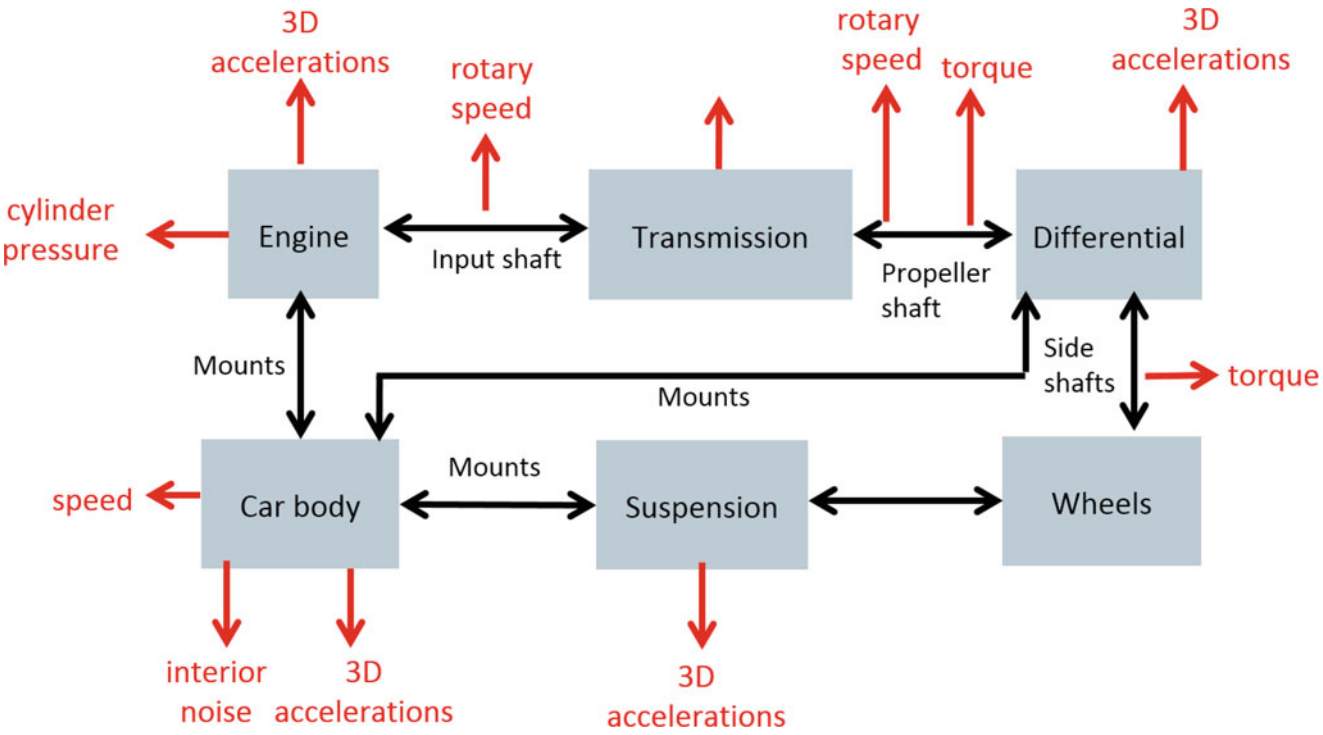

Fig. 9.5 Diagram with vehicle subsystems and measurements

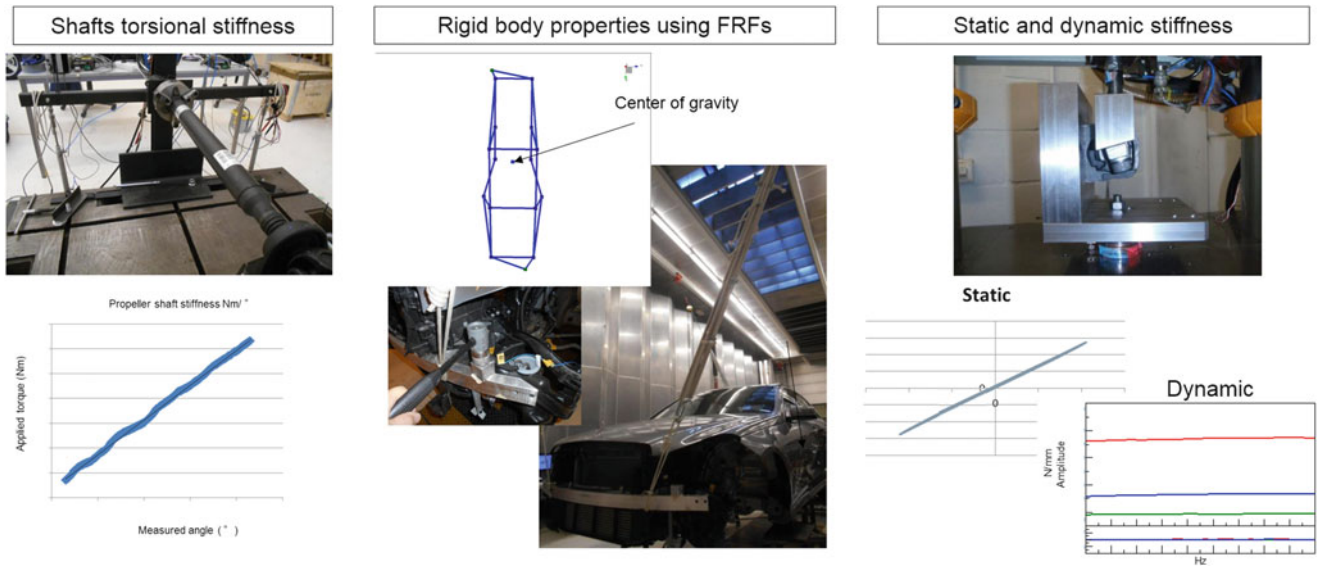

Fig. 9.6 Component static and dynamic measurements

- Vehicle modeling
- Validation
- Model based analysis

The modeling is the most important part of the simulation step—it consists in gathering data obtained from the test phase and use them to appropriately include them in the model parameters. Figure 9.8 shows the model and its subsystems. It is composed of the powertrain, damper and flywheel, transmission, driveline, car body and suspension subsystems.

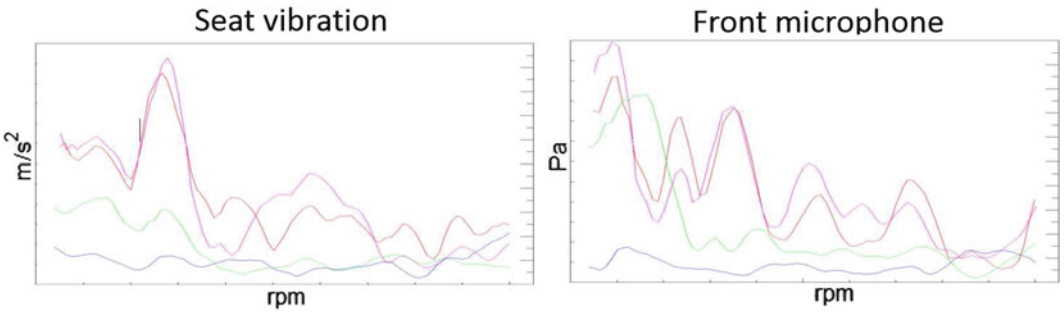

Fig. 9.7 Operational data: example second order components for seat acceleration and microphone measurements for different throttle positions

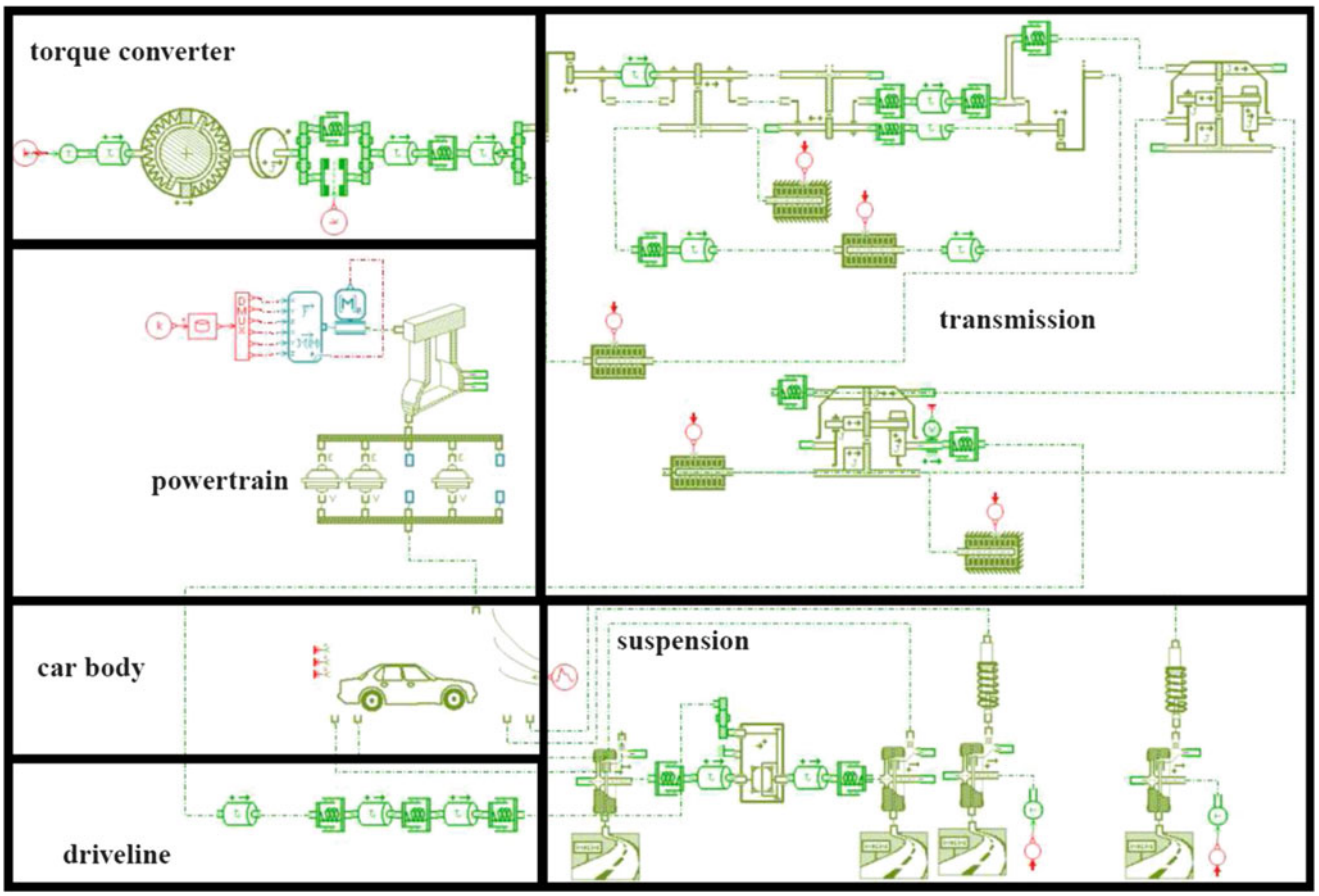

Fig. 9.8 Model overview with subsystems

For the powertrain block, the most important parameters obtained from tests are the block's position and inertia, as well as the mount stiffness values. Moreover, the model itself receives as input the measured engine vibration, which propagates to the vehicle body through the mounts. The vehicle body subsystem contains the inertial parameters obtained in the test phase.

The lock-up damper and flywheel subsystem's most important parameters are related to the flywheel itself, and include torsional stiffness and inertia parameters. As an input, this subsystem receives rotational speed measured in operational conditions. Its output is connected to the transmission subsystem, which can have different complexities, but should usually include an equivalent torsional stiffness and inertia, as well as the gear transmission ratio. Then, the driveline subsystem is modeled as a series of interconnected inertias and stiffnesses, representing the propeller shaft, driveshaft, differential, etc.

Finally, the last subsystem is the suspension, and it contains the properties necessary to properly model the suspension and tire dynamics that lead to booming noise. It includes suspension longitudinal and vertical stiffness and tire torsional stiffness, obtained from the testing phase. The suspension subsystem is connected to the vehicle body subsystem, and to the driveline subsystem, closing the loop in the system.

The model can then be validated by comparing simulated quantities at each of the subsystems with the measured operational data. Since the input data is coming from operational measurements, correlation at each subsystem should be possible, also making it easier to validate the models. In case model and test data don't correlate well, a model updating step can be carried out, where some parameters can be modified to obtain better correlation with the test data.

In the final part of the simulation phase, the validated model can be used to predict changes in the system, that can be used to improve vibration induced from the booming mechanisms.

9.3 Conclusions

This paper introduced how torsional vibration can be an important source of noise in vehicles, especially with the advent of downsized engines and efficiency increasing technologies, that tend to lead to higher noise and vibration perceived by the occupants. Then, it was shown how a combination of testing and 1-D simulation can be used to analyze and predict driveline torsional oscillations and their effect on low frequency booming noise and vibration. It was shown how the approach makes use of test data not only for troubleshooting analysis, but also to provide parameters and input for the model.

The test and simulation phases were explained in detail—for the testing, typical sensor locations was shown, as well as the most important component and operational measurement types. For the simulation phase, the model subsystems were presented, detailing the most important parameters to be used for the simulations, and how the model can be validated and improved.

Acknowledgements The research presented in this paper was partly performed in the context of the O and O project 150394 ECO-Powertrain. The authors gratefully acknowledge the support of VLAIO, The Flemish agency for Innovation and Entrepreneurship.

References

1. Mauch, D.-I.A., Tophoven, D.-I.J., Trzebiatowski, D.-I.T., Raatz, I.T.: Potentials and limits of downsizing a diesel engine. MTZ Worldwide eMagazine **72**(7–8), 4–9 (2011)
2. Wellmann, T., Govindswamy, K., Tomazic, D.: Integration of engine start/stop systems with emphasis on NVH and launch behavior. SAE Int. J. Eng. **6**(2013-01-1899), 1368–1378 (2013)
3. Stoffels, H., Schroeer, M.: NVH aspects of a downsized turbocharged gasoline powertrain with direct injection. Technical report, SAE Technical Paper (2003)
4. Leone, T.G., Pozar, M.: Fuel economy benefit of cylinder deactivation-sensitivity to vehicle application and operating constraints. Technical report, SAE Technical Paper (2001)
5. Abe, H., Tsuruoka, M., Muto, A., Kato, M., Fujiwara, H.: Development of super ultra flat torque converter with multi plate lock-up clutch. SAE Int. J. Eng. **2**(2009-01-0141), 48–55 (2009)
6. Hage, A., Szatkowski, A., Li, Z.: Improving low frequency torsional vibrations NVH performance through analysis and test. Technical report, SAE Technical Paper (2007)
7. Wellmann, T., Govindswamy, K., Braun, E., Wolff, K.: Aspects of driveline integration for optimized vehicle NVH characteristics. Technical report, SAE Technical Paper (2007)
8. Heylen, W., Lammens, S., Sas, P.: Modal Analysis Theory and Testing. Katholieke Universteit Leuven/Departement Werktuigkunde, Leuven (2006)
9. Hermans, L., Van der Auweraer, H.: Modal testing and analysis of structures under operational conditions: industrial applications. Mech. Syst. Signal Process. **13**(2), 193–216 (1999)
10. Allemang, R.J., Brown, D.L.: A correlation coefficient for modal vector analysis. In: Proceedings of the 1st International Modal Analysis Conference, vol. 1, pp. 110–116. SEM, Orlando (1982)
11. Mottershead, J.E., Friswell, M.I.: Model updating in structural dynamics: a survey. J. Sound Vib. **167**(2), 347–375 (1993)
12. Storck, H., Sumali, H., Pu, Y.: Experimental modal analysis of automotive exhaust structures. Technical report, SAE Technical Paper (2001)
13. Van der Auweraer, H., Anthonis, J., De Bruyne, S., Leuridan, J.: Virtual engineering at work: the challenges for designing mechatronic products. Eng. Comput. **29**(3), 389–408 (2013)
14. Cai, W., Pillay, P., Tang, Z., Omekanda, A.M.: Low-vibration design of switched reluctance motors for automotive applications using modal analysis. IEEE Trans. Ind. Appl. **39**(4), 971–977 (2003)
15. Ozdoganlar, O.B., Hansche, B.D., Carne, T.G.: Experimental modal analysis for microelectromechanical systems. Exp. Mech. **45**(6), 498–506 (2005)
16. Samin, J.-C., Brüls, O., Collard, J.-F., Sass, L., Fisette, P.: Multiphysics modeling and optimization of mechatronic multibody systems. Multibody Sys. Dyn. **18**(3), 345–373 (2007)

17. Naets, F., Cuadrado, J., Desmet, W.: Stable force identification in structural dynamics using Kalman filtering and dummy-measurements. Mech. Syst. Signal Process. **50**, 235–248 (2015)
18. Hwang, J.-S., Kareem, A., Kim, W.-J.: Estimation of modal loads using structural response. J. Sound Vib. **326**(3), 522–539 (2009)
19. dos Santos, F.L.M., Pastorino, R., Peeters, B., Faria, C., Desmet, W., Góes, L.C.S., Van Der Auweraer, H.: Model based system testing: bringing testing and simulation close together. In: Structural Health Monitoring, Damage Detection and Mechatronics, vol. 7, pp. 91–97. Springer, New York (2016)

Chapter 10
Structural Coupling Analyses of Experimental Models in a Virtual Shaker Testing Environment for Numerical Prediction of a Spacecraft Vibration Test

S. Waimer, S. Manzato, B. Peeters, M. Wagner, and P. Guillaume

Abstract The paper addresses the methodologies required to derive a reliable and representative simulation environment for virtual shaker testing to predict the outcome of Spacecraft vibration tests numerically prior to its physical execution. The simulation environment needs to comprise the coupled dynamical models of the testing facility, structure under test and control system active during test. Especially, the paper focuses on modelling and experimental validation techniques for coupled test specimen models using the coupled head expander and beam test specimen system as validation test case. The main focus is set on the derivation of experimental test structure models which will be used in the future for modal coupling by applying Component Mode Synthesis and to assess the added value against alternative sub structuring techniques w.r.t. frequency bands and residual compensation, analysis of the measurement of required interface and connection point degrees-of-freedom and consideration of damping. Consequently, those experimental results are used to derive preliminary methodologies and guidelines to couple structural sub component models, and use them in further numerical closed-loop vibration control simulations. Consequently, the developed and experimentally derived structural dynamic models are coupled with a multi-physical electrodynamic shaker and sine controller model to virtually replicate sine control tests, followed by a validation with experimental test results and to be used in preliminary numerical investigations for vibration control performance enhancement.

Keywords Environmental spacecraft testing • Multiphysical system • Modelling and simulation • Experimental system identification • Active control

10.1 Introduction

In spacecraft (S/C) engineering, environmental testing is a crucial part to ensure and demonstrate the spacecraft integrity against the dynamical launch environment, to screen the flight hardware for quality of workmanship and to validate mathematical models [1, 2]. Hence, vibration testing is performed on big electrodynamic or hydraulic shaker testing facilities which are often one of its kind test setups, e.g. the six degree-of-freedom (DoF) hydraulic shaker HYDRA at the European Space Research and Technology Centre (ESTEC) in Noordwijk or multiple electrodynamic shaker configurations for vibration testing of large S/C in lateral and vertical directions [2–4]. Examples of the latter case are given by the left and centred pictures of Fig. 10.1 where the BepiColombo Mercury Composite S/C (MCS) is tested on ESTEC's QUAD Shaker in vertical direction and lateral by using the 160 kN DUAL shaker slip table configuration [5]. Those test campaigns are a mandatory part in the S/C development process to qualify the mechanical designed S/C structure for launch as defined in the 'Spacecraft mechanical loads analysis handbook' of the European Cooperation for Space Standardisation (ECSS)

S. Waimer (✉)
Siemens Industry Software NV, Researchpark 1237, Interleuvenlaan 68, 3001 Leuven, Belgium

Vrije Universiteit Brussel, Pleinlaan 2, 1050 Brussels, Belgium
e-mail: steffen.waimer@siemens.com

S. Manzato • B. Peeters
Siemens Industry Software NV, Researchpark 1237, Interleuvenlaan 68, 3001 Leuven, Belgium

M. Wagner
European Space Agency, ESA/ESTEC, Keplerlaan 1, NL-2200 AG Noordwijk, The Netherlands

P. Guillaume
Vrije Universiteit Brussel, Pleinlaan 2, 1050 Brussels, Belgium

N. Dervilis (ed.), *Special Topics in Structural Dynamics, Volume 6*, Conference Proceedings
of the Society for Experimental Mechanics Series, DOI 10.1007/978-3-319-53841-9_10

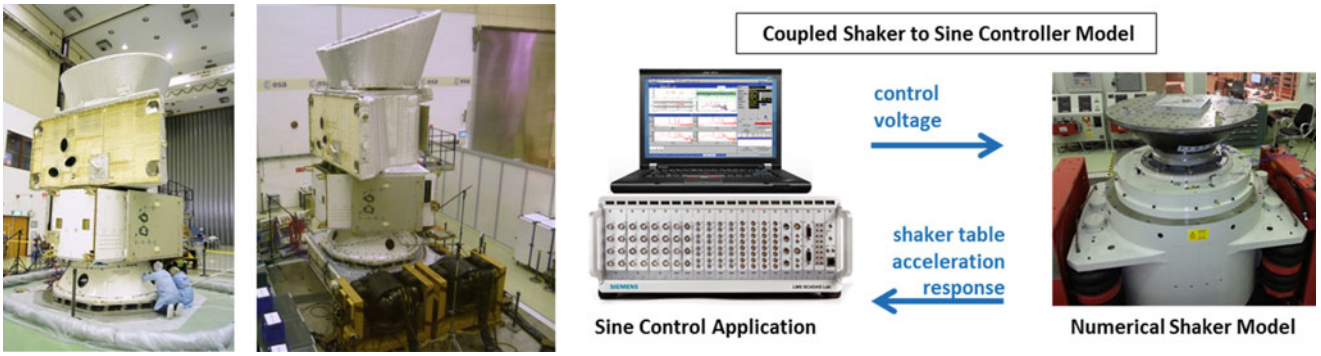

Fig. 10.1 *Left and centre*—BepiColombo Mercury Composite S/C (MCS) on ESTEC's QUAD shaker and DUAL shaker slip table configuration, courtesy of ESA [5] . *Right*—principal sketch indicating the closed-loop control between the LMS Test.Lab sine control model coupled to the numerical model of ESTEC's 160 kN shaker

[2] to experimentally simulate the low frequency structural and mechanical-borne transmission loads through the launcher-spacecraft interface to the test specimen. While testing, especially of large S/C with misalignments in the Centre-of-Gravity (CoG) between the testing facility and test specimen, the interaction between the structure under test, the vibration controller and the hardware used to perform the test is a critical issue. The dynamics of the testing facility couples with that of the test specimen in the frequency range of interest. This can lead to violation of test specifications and undesired challenges while testing, e.g. beating phenomena which usually occur at structural resonances, and can result in over- or under testing, or even damage of the S/C [2–8]. A solution to these problems and limitations can be achieved by simulating the test in advance to its physical execution which is often called virtual shaker testing [2]. The main objective is to predict the outcome of the vibration test numerically to optimise control parameter and apply notching strategies to tackle these issues. Therefore, the simulation environment needs to comprise the main contributors of the vibration test chain:

- the S/C or structure being tested including all test brackets and adapters,
- the excitation system (electrodynamic or hydraulic vibration system), and
- the vibration control system active during test.

The corresponding dynamical coupling between those components is indicated by the schematic sketch on the right of Fig. 10.1 showing the interaction between the vibration control system and the 160kN electrodynamic shaker at ESTEC. An important part of this environment is the shaker generating the vibrations, but in practice, a detailed and validated electrodynamic numerical simulation model of a shaker is not readily available. Therefore, the first part of this paper presents the current status of the virtual shaker testing simulation environment in Sect. 10.2. It summarises the work which has been performed to derive and implement an enhanced five DoF electrodynamic shaker model coupled to a vibration controller to conduct sine control tests for S/C qualification testing as shown by the right sketch of Fig. 10.1. The work is based on previous publications [6, 9, 10] and a continuation study to derive methodologies for a virtual shaker testing simulation environment. Subsequently, a first step for the dynamical coupling of test structures is investigated by performing modal analysis of the shaker Head Expander (HE) and a beam test structure in Sect. 10.3. The experimental hammer impact test results of both structures alone and in coupled configuration in free-free boundary conditions are presented in Sect. 10.3.1 and analysed to determine an experimental data set as basis to apply dynamical substructuring techniques in the frequency and modal domain in the future. The main goal of this study which is still under research is the investigation and evaluation of preliminary coupling techniques and guidelines to comprise coupled dynamical structural test specimen models and the electrodynamic shaker model in further numerical simulations. Therefore, Sect. 10.3.2 comprises a preliminary numerical coupling analysis and Sect. 10.3.3 shows how the experimentally derived FRFs can be applied for a preliminary since control prediction. In Sect. 10.4 the coupled HE/beam structure is mounted on an electrodynamic shaker and vibration testing in open-loop random application and closed-loop sine control is performed. The results are compared and interpreted to the modal analysis investigations presented in Sect. 10.3 and subsequently applied for numerical sine control predictions based on low level open-loop random testing data.

10.2 Electrodynamic Shaker and Sine Controller Model

The coupled electrodynamic shaker to vibration controller model and its dynamical interaction defines a major part in the numerical vibration test simulation. A principle sketch of the coupled shaker to vibration controller model is shown in the right of Fig. 10.1. The shaker facility (right) interacts with the vibration test controller (left) by a closed-loop acceleration feedback control system to be capable of controlling the shaker table acceleration w.r.t. required test specifications. Due to its large number of installations at vibration space testing centres, LMS Test.Lab Sine Control is implemented and used to conduct controlled virtual sine sweep tests. The sine controller model has been derived and extensively validated to the existing hardware and software implementation [11, 12] as reported in previous works [6, 7]. An important part of this environment is the shaker generating the vibrations, but in practice, a detailed and validated electrodynamic numerical simulation model of a shaker is not readily available. Hence, a lumped-parameter shaker model according to [9] is implemented in Matlab/Simulink. It represents a common and simplified electromechanical model valid under a large variety of numerical shaker models and constitutes one crucial part for virtual shaker testing. It is intended that the modelling approach considers experimental system identification data to derive and update model parameters and to improve the entire dynamic system performance.

The left sketch in Fig. 10.2 shows the principle mechanical and electrical parts of a lumped-parameter, one-dimensional, three DoFs, electromechanical shaker model as mentioned in [10] and describes a basic model of a Modal shaker which has already been introduced in detail in previous research activities [6, 7, 9, 10]. The assembly of coil and table is often called armature and represents the moving elements of the electrodynamic shaker. The compliant connection between the armature assembly and the body forms a mass, spring and damper system defining a single DoF system. Adding two more DoFs completes the mechanical model: firstly, the armature structure is modelled as being elastic and not rigid by treating the coil and table as separate masses, connected by a spring and damper system, and secondly, the isolation system of the shaker to the ground is modelled with a second spring and damper system. When an electrical current i is conducted through the coil, an axial force, according to the electromagnetic Lorentz force, is produced and transmitted through the suspension system to the table structure resulting in a vertical motion.

The system identification is applied to real test data gathered at the system identification test campaign using the 160 kN shaker at ESTEC. The results are summarised in [13] using a global approach and a combination of sine and random control data to enhance the quality of the estimated parameter of the entire frequency band up to 2000 Hz. In this case, the experimental results of the first two loading configurations (Empty shaker table and Interface disc) are applied to determine the shaker parameters and used to predict the test performance of the third loading configuration (Interface disc and cuboid) as shown by the right picture of Fig. 10.2.

Test and simulation results are shown by the acceleration-over-electrical current FRFs in the left part of Fig. 10.3. The plot shows the system dynamics of ESTEC's 160 kN shaker facility calculated from a sine control simulation considering the Interface disc and cuboid (measured—blue, predicted—dashed green) and Interface disc and HE (measured—black, predicted—dashed red) loading configuration. The numerical predictions are calculated by using the three DoF shaker model and the global parameter approach. It is obvious that the major system characteristic such as suspension and coil mode can be predicted for both cases. But for the Interface disc as well as the HE configuration, an additional structural resonance occurs

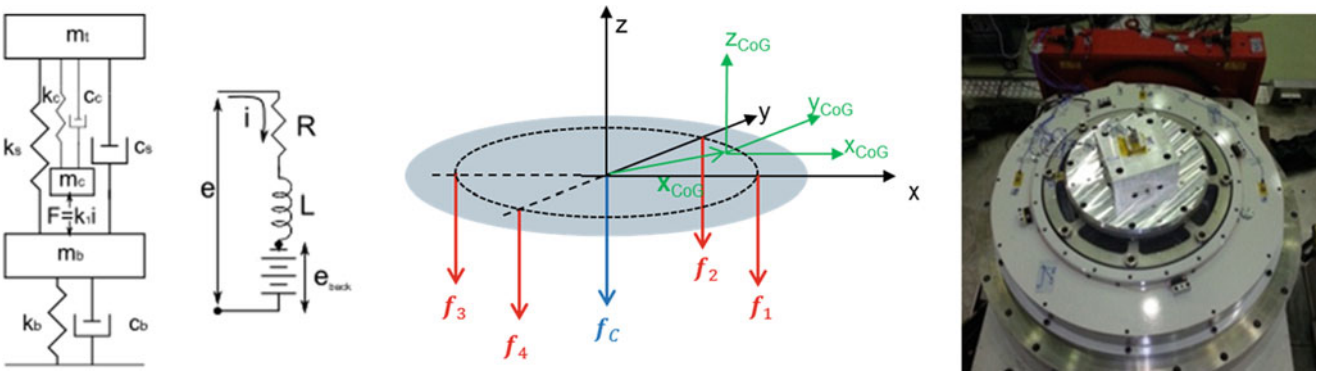

Fig. 10.2 *Left*—electrodynamic shaker lumped parameter model [1, 10]. *Centre*—shaker table modifications to add rotational shaker table dynamics [14]. *Right*—top view to ESTEC's 160 kN shaker with sensor instrumentation and test masses for system identification [5]

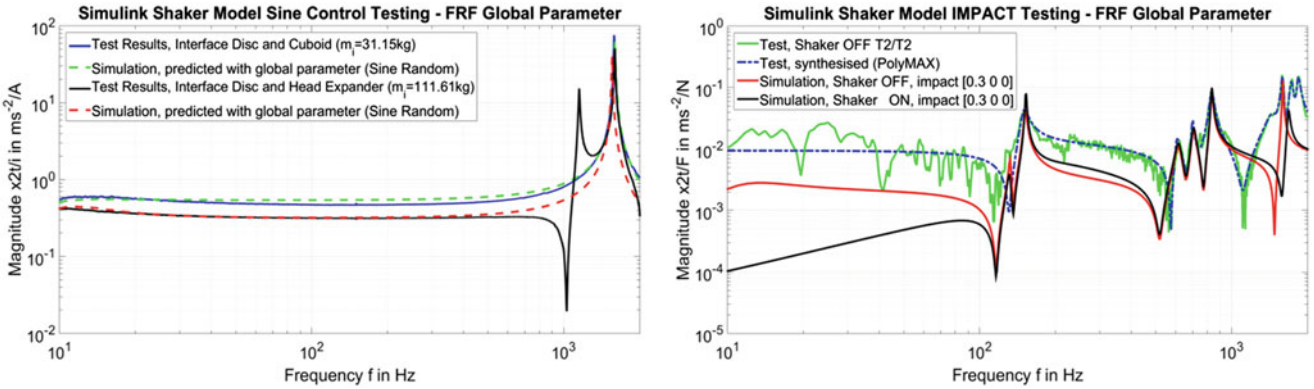

Fig. 10.3 160 kN shaker of ESTEC. *Left*—correlation between experimental test results (*blue*—Interface disc/cuboid, *black*—Interface disc/Head Expander) and sine control simulations using the simplified shaker model and the estimated global set of parameter. *Right*—correlation between hammer impact excitation test results on impact location T2 (−x-axis) and simulated results with enhanced shaker model

because of the flexibility of these components and, therefore, it cannot be anymore represented by a rigid lumped mass or ideal loading case. Consequently, this paper focuses in Sect. 10.3 on the coupling of structural models.

Summarising, at the current status, the shaker table specifically consists of one translational DoF which is capable of representing the shaker's dynamical characteristic for the idealised test. For these cases the current shaker model can be used to recalculate and predict test results in open- and closed-loop random and sine control operations as shown by the dashed green FRFs in Fig. 10.3. However, considering idealised and centred loading and sensor conditions some deviations occur between the test and simulation results. In practice, these deviations will increase, if complex test structures are attached to the shaker and idealised conditions cannot be applied anymore. Especially for S/C vibration testing, the CoG of the S/C and shaker table is rarely aligned to each other w.r.t. the main vertical axis of motion. As consequence, the entire system tends to be subjected to undesired rotational and lateral dynamical movements during test. A first main problem is the dynamical coupling between the first bending mode of the structure under test and the rocking (rotational) mode of the shaker table. This is a main reason, for virtual shaker testing and to follow a multi-domain modelling and simulation approach, including the test structure, excitation system and control system in order to assess the global performance [2].

To predict this, in a previous publication [14] an enhanced shaker model with two additional rotational DoF is derived. A principal sketch is presented in the centred picture of Fig. 10.2 assuming the suspension system to be spatially distributed, the Lorentz force acting on the centre without rotational dynamics and the rotation point to be equal to the CoG of the coupled system. More information is presented in [14].

As a first application, the enhanced shaker model is implemented and verified against hammer impact results of the Interface disc and cuboid loading configuration as presented by the right plot of Fig. 10.3. Therefore, the hammer impacts are numerically approximated and simulated by defining an input moment M_{in} as excitation on the shaker table, similarly to the experimental conditions. The results show a good agreement between the experimental and numerical results, although some deviations are observable which will be investigated in more detail in the future. Additionally, the simulation model is used to show the dynamical differences if the shaker is switched off/on. The main differences are that the suspension mode is highly damped and it is only observable with the shaker turned off, the rocking modes are unchanged and the coil mode is slightly increased if the shaker is switched on as reported in [15].

10.3 Experimental and Numerical Coupling Analysis of Structural Models

10.3.1 Experimental Modal Analysis on Test Specimen Models

The current research activities are focused on the derivation of numerical and experimental structural test specimen models representing the third major part of the virtual shaker testing simulation environment. The main questions are related to the dynamical coupling between the structural test models and the shaker model, and the coupling between different dynamical sub structures of the test specimen and hardware included in the test. The latter is part of this section. Especially, it is of interest to derive experimental and numerical models of the shaker head expander (HE), a beam test structure and the coupled system as shown by the pictures in Fig. 10.4.

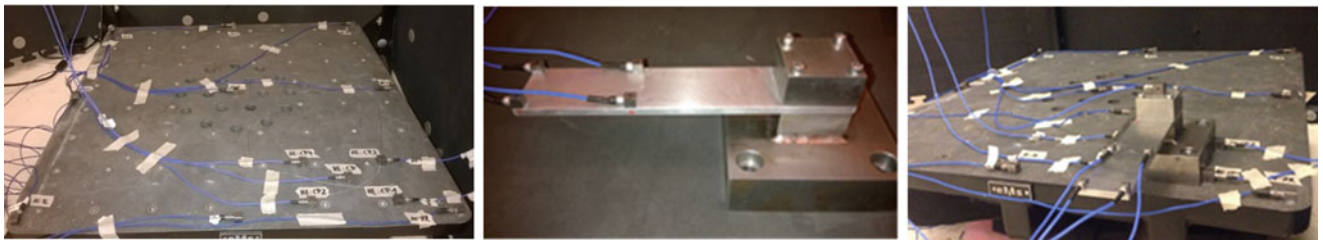

Fig. 10.4 Pictures of the structural components of the Head Expander (*left*), beam test structure (*centre*) and coupled system equipped with acceleration sensors for experimental modal analysis

The shaker HE is a structural component which is usually used in vibration testing to enlarge the mounting interface between the shaker table and the real test specimen to maximise the versatility of the testing facility. Figure 10.4 shows on the left side a picture of the HE for impact testing equipped with multiple acceleration sensors. Nine one-axial acceleration sensors sensitive in z-direction are mounted on the frame of the HE and five tri-axial acceleration sensors are glued at the mounting positions (indicated with CP) of the intended beam test structure. The beam test structure and its acceleration sensor instrumentation are shown by the centred picture of Fig. 10.4. The advantage of the beam structure is that it can be numerically approximated by a clamped beam to derive a first systems insight and determine modal parameter prior to the test. Additionally, the beam presents a test structure with a high flexibility which is intended to be used later on to verify the control performance in a closed-loop shaker control application. The beam is equipped with four miniature tri-axial acceleration sensors and five tri-axial connection point acceleration sensors mounted on the bottom of the base plate which correspond to the intended mounting positions CP on the HE. The beam's four lightweight miniature accelerometers are selected to avoid any mass loading effect induced to the flexible beam's dynamics.

In a modal analysis survey the dynamics of the two structures separately and in coupled condition are identified in free-free boundary conditions to derive structural model dynamics, to review methodologies and preliminary guidelines to couple the two structures to be included in the simulation model. Therefore the HE and the coupled HE and beam test structure are suspended by foam to simulate free-free boundary conditions during impact testing with excitations at all sensor locations, including HE and connection point sensors. The beam test structure is hung by a flexible cord from a frame during test and is excited especially along the beam and connection points at the base structure with hammer impacts. Some major results of the modal analysis campaign are shortly summarised hereafter, whereas a more detailed view on the experimental test results is presented in [16].

The major FRFs which are acquired during impact testing with the main objectives to identify the structural dynamics of each system and in coupled configuration, and to measure a reliable data set which can be later on used for coupling exercises are summarised in Fig. 10.5. Reciprocity checks and system FRFs of the uncoupled beam test structure and HE are presented by the FRFs on the top left and top right, respectively. The coupled system FRFs are given by the figure on the bottom left. For all cases the reciprocity criteria is fulfilled in an agreeable manner over the considered frequency range. The FRFs shown in the bottom right plot verify the assumption that the beam's plate behaves as rigid body for frequencies below 3000 Hz since the driving point FRF HE:CP4/HE:CP4 (black) is almost equal to B:CP4/HE:CP4 (red) representing the base plate sensor's B:CP4 response. Figure 10.6 shows the first and most distinctive mode shapes of the HE (left), beam test structure (centre) and coupled system (right) estimated from the acquired FRFs. As main results the following statements are drawn based on the experimental analyses:

- The beam's 1st bending mode is reduced from the uncoupled case of 185.8 Hz to the coupled case of 155.2 Hz. Additionally the damping is increased from 2.06 to 4.89%.
- Higher order beam modes are difficult to distinguish since, there is a strong coupling between the modes and the mode shapes are dominated by the head expander eigenvectors.
- The saddle mode of the head expander is decreased from 904.3 to 842.1 Hz. The damping is also increase from 0.11 to 0.16%.
- The 1st bending mode of the head expander is decrease from 1192.6 to 1135.1 Hz. The damping is also increase from 0.11 to 0.27%.

For all other modes a similar characteristic is observable: the frequency of the modes of the coupled system is decreased whereas the damping is (slightly) increased.

In the future, it is intended to use theoretical techniques to couple numerical and or experimental subcomponents [17] by methods relying on measured FRFs directly or on a set of identified modes. The experimental campaign described in

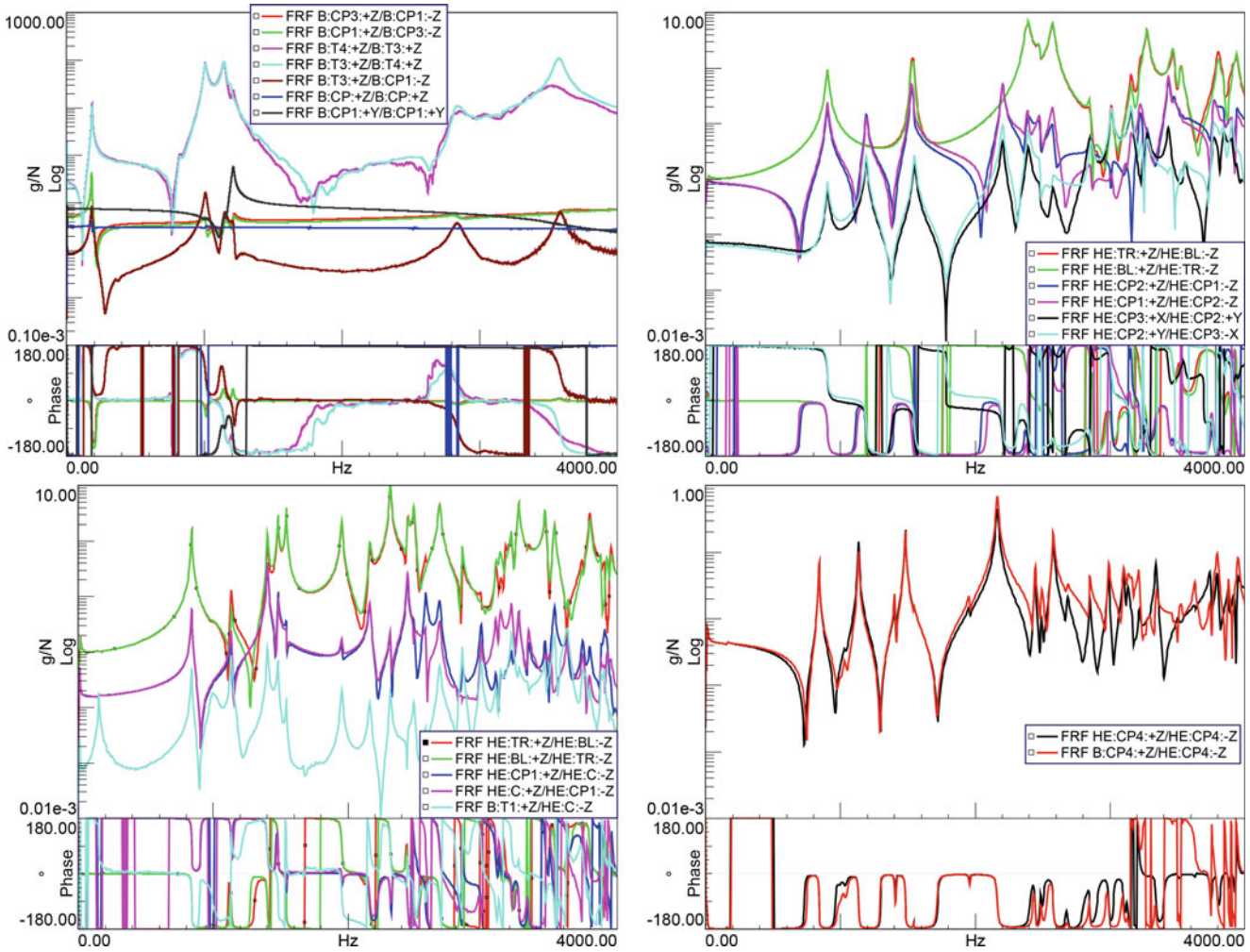

Fig. 10.5 Impact Testing FRFs. *Top-left*—beam test structure. *Top-right*—Head Expander. *Bottom-left*—coupled HE/beam test structure. *Bottom-right*—coupled HE/beam test structure connection point FRFs

the previous paragraphs targeted the latter method, where the response of the assembled system is obtained from the modal model identified on the two subcomponents tested in free-free conditions. This is an important step in the modelling of the vibration test to verify and simulate interactions between the test specimen and shaker testing facility while testing.

10.3.2 Numerical Coupling Analysis

As already discussed, one of the main objectives of a virtual shaker testing environment is the possibility to couple substructures and predict the dynamic response of the whole system starting from the knowledge of the separated components. In literature, several techniques exist to couple numerical and or experimental subcomponents [17] and a first distinction can be made between methods relying on the measured FRFs directly or on a set of identified modes. The experimental campaign described in the previous paragraph targeted the latter method, where the response of the assembled system is obtained from the modal model identified on the two subcomponents tested in free-free conditions. However, before applying Experimental Modal Coupling to the experimental models, some preliminary numerical simulations are performed to understand how assumptions made on the connection between the two substructure influence the predicted results. For this reason, numerical FE models of the beam and head expander are built and the modes up to 4000 Hz are calculated. The two models are not validated with the experimental results, but a qualitative comparison of the results confirmed that the models are sufficiently valid for this preliminary analysis.

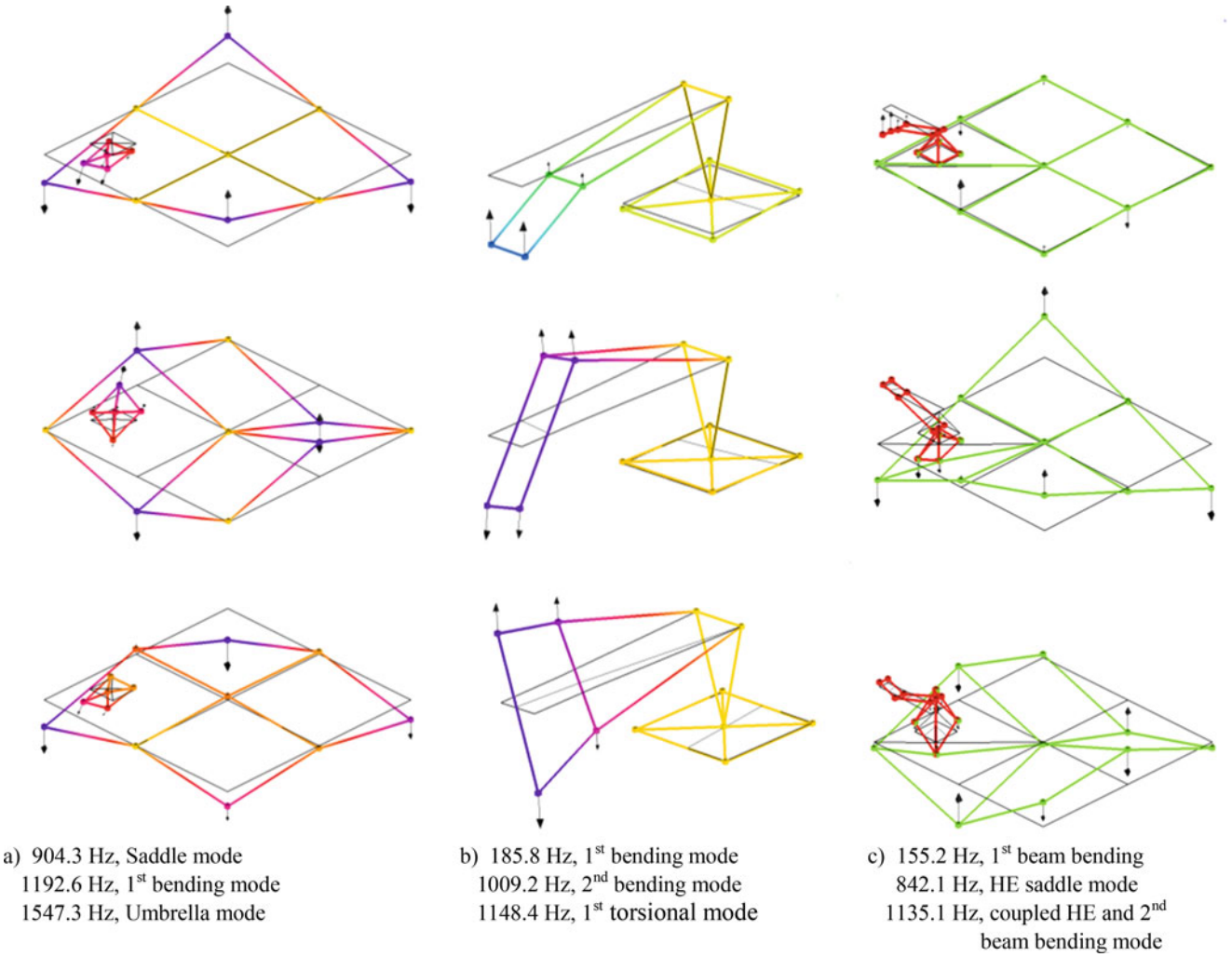

Fig. 10.6 First representative modes shapes of Head Expander (**a**), beam test structure (**b**) and coupled HE and beam test structure system (**c**) in ascending order from top to bottom

Modal coupling is performed by imposing compatibility and equilibrium conditions at the interface between the sub structures in the modal domain. In a first instance, the connection is assumed to be rigid. In principle at each connection six DoFs should be considered. However, measuring (and exciting) rotational DoFs is impractical and in most cases impossible, so in this case only translational DoFs are used for coupling. To verify the coupling results, two modelling assumptions are made (Fig. 10.7). In the first case, being considered as the reference one, the model of the two substructures are connected via a family of rigid nodal connections across the whole surface of contact. This result in a connection stiffer than the actual one, but the model should be valid enough at lower frequencies. On the other hand, when coupling two subsystems, only measured DoFs can be connected, which means that at each corner of the base and on both structures the three translational DoFs are rigidly coupled. In this case, modes are only considered at the points that would have been measured during the actual test.

On the right Fig. 10.7, the correlation between the two models in terms of Modal Assurance Criterion (MAC) is shown. As expected, because of the difference between the connection properties in the two models, differences in the predicted responses can be observed, in particular at frequencies at which the modes of the two systems couple significantly at the connection. The modes on the top left part of the MAC matrix are pure modes of the beam and the table, with limited coupling effects. The higher the frequencies, the higher the local deformation of the HE and beam, and consequently the more different the modes are. On the other hand, a difference in the predicted natural frequencies is observed for all modes.

These observations will need to be taken into account when the results of modal coupling will be compared with the measured modal response. Although the model on the left in Fig. 10.7 is closer to reality, it will be impossible to replicate it exactly when coupling substructures.

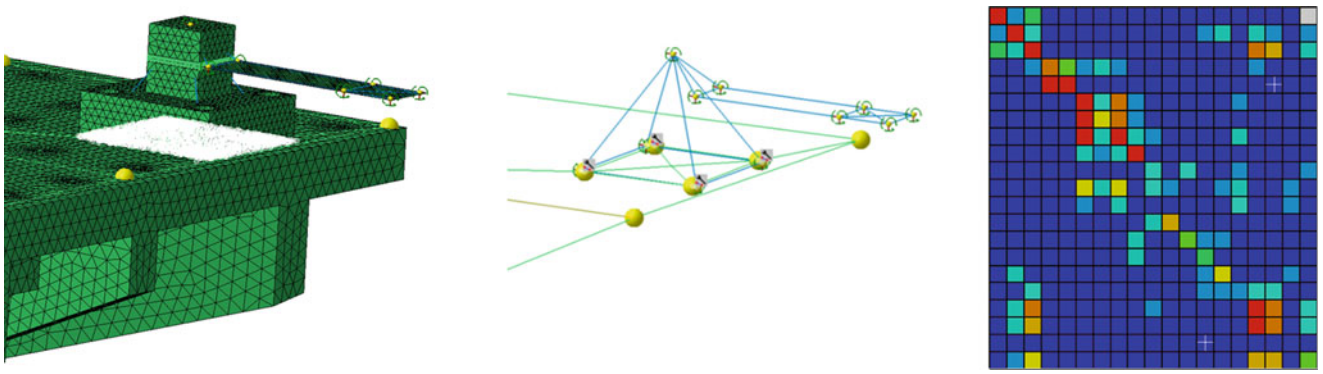

Fig. 10.7 *Left*—FE model of the assembled structure with distributed rigid connection over the whole surface. *Centre*—coupled FE model with rigid connection between the translational DoFs at four interface points. *Right*—MAC matrix between the modes calculated from the two models up to 3000 Hz

10.3.3 Preliminary Sine Control Prediction using Experimental Dynamic Models

Taking advantage of the availability of experimentally measured FRFs of the coupled head expander and beam test structure system, some preliminary analysis to numerically predict the outcome of a sine control vibration test can be performed. As the coupling algorithm to connect the different structural subcomponents with each other and with the shaker model is still being investigated, the derived sine controller model is at this stage directly coupled with the acquired FRFs during modal analysis neglecting the shaker dynamics. This introduces the assumption that the sine controller output voltage (shaker drive signal) is defined to be proportional to the shaker current driving the coil of the electromagnetic shaker and the introduced force. In practice, this assumption is not valid and, secondly, neglecting the entire shaker dynamics will introduce deviations, too. However, this preliminary experimentally data driven approach offers the possibility to qualitatively predict responses, spectra and system behaviour as it can be expected in a real test (simulation). Hence, the approach is applied to determine first qualitative test predictions.

The simulations are performed considering the FRFs between the HE centred sensor HE:C and the connection point sensor HE:CP1 and for the coupled case the beam accelerometer B:T1 mounted at the tip of the beam structure respectively. The impact is chosen to be at HE:C to assume a centred excitation at the HE approximating real test conditions. In principle the modelling and sine control prediction is realised by two basic system identification and simulation approaches as explained in [18]. The first approach presents a direct data driven method by using experimental and/or synthesised FRFs in a look-up-table (LUT) simulation comprising frequency and complex FRF values. While simulating, the correct complex FRF values according to the sweep frequency are selected by applying an interpolation between the sine control sweep frequency and the frequencies in the LUT. The second methodology derives a discretised model conversion of the estimated PolyMAX [19] model. Consequently, the derived discrete-time dynamic system model (polynomial z-domain or discrete state-space model) is directly used in the simulation loop replacing the LUT approach and simultaneously neglecting the need of an interpolation algorithm in the simulation. It is also obvious that the accuracy and correlation of the discretised models w.r.t. the measured models relies on the quality of the PolyMAX estimation and the parameters used for the discretisation, e.g. sampling times/frequencies and conversion methods such as zero order hold, triangle approximation, impulse variant or bilinear discretisation [20].

The FRFs used in the simulation are shown on the left of Fig. 10.8. The measured FRFs of the HE in blue, the measured FRFs of the coupled system in green and the corresponding synthesised FRFs as dashed red and magenta curves. The derived discrete dynamical model representations, z-domain transfer function and discrete state-space model, are shown by the dotted black FRFs and are equal to the synthesised s-domain transfer function model in dashed magenta. Here it is obvious that in the coupled configuration the head expander's umbrella and 1st bending modes are decreased and more excited than in the uncoupled case. Additionally, the beam's first bending modes in coupled conditions occur in the measured (green) and synthesised (dashed magenta) FRFs. The sine control simulation results with a control reference spectrum of 1 g over the entire frequency range of 10 to 1200 Hz applying a frequency sweep rate of 1 Hz/s is presented on the right of Fig. 10.8. The figure shows the acceleration spectra for both cases: coupled HE and beam structure in green using the measured FRFs and dashed magenta applying the synthesised FRFs, and the HE separately using the synthesised FRF in blue.

The results by using the synthesised FRF (spectra in dashed magenta) show much smoother and clearer predictions than the measured FRF (spectra in green) by applying the direct data driven approach using the LUT. This is influenced by the

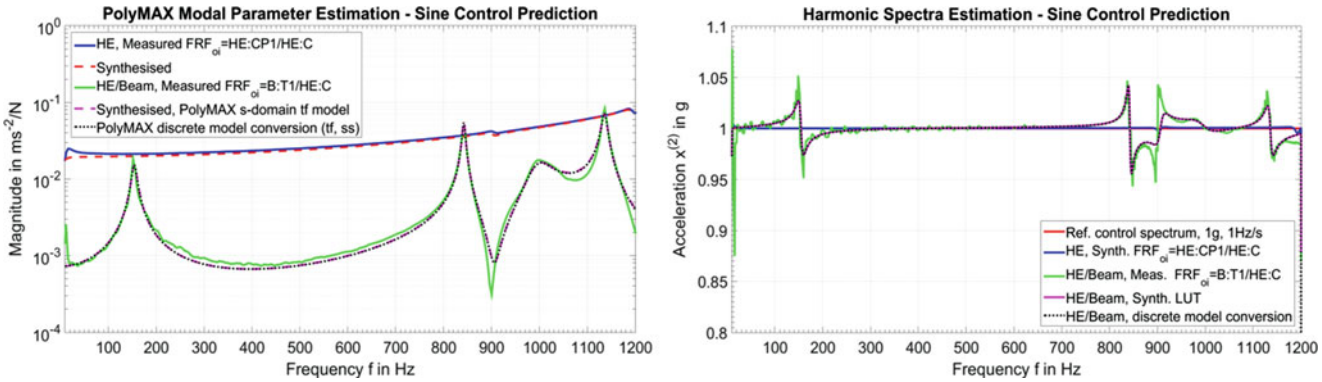

Fig. 10.8 *Left*—experimental and synthesised FRFs for data driven simulation model of HE and HE/beam structure coupled models in free-free boundary conditions. *Right*—acceleration spectra simulation results for preliminary sine control prediction using the experimental and synthesised FRFs and model from the left

coarse frequency resolution of 4 Hz of the measured FRF in combination with the interpolation and the frequency sweep rate. Consequently, the synthesised FRFs result in a smoother control since the frequency resolution of the FRF can be chosen arbitrarily and adapted to the sine control parameter, and no noise occurs. Despite this improvement, a deviation is also observed at the anti-resonance around 900 Hz. This is a result of the modal parameter estimation and the resulting models (dashed magenta and dotted black) which do not fully approximate the measured FRF (green) on the left of Fig. 10.8. Consequently, the resulting and predicted acceleration control spectra show this effect as a deviation in the control performance, too. The simulation results based on the dynamical models in z-domain transfer function and discrete state-space representation derived from the estimated s-domain PolyMAX model are equal to each other and show the same dynamic results as the data driven approach by using the synthesised LUT approach. All sine control predictions overlap and exhibit an equal characteristic. Consequently, it is summarised for this application and with the given settings, that both modelling approaches, either direct data driven LUT or the dynamic model approach are capable of generating a preliminary reliable sine control prediction. The deviations occurring at the anti-resonance are still being investigated but can be minimised by adapting the modal parameter estimation.

10.4 Experimental Results and Numerical Analysis for Coupled Shaker and Test Specimen Models

This section highlights the results and effects which are investigated if the coupled head expander and beam test structure is coupled to an electrodynamic shaker and different tests (impact, open-loop random and controlled closed-loop sine testing) are performed.

An overview and comparison of important results from impact testing is presented in Fig. 10.9. The plot comprises some of the major FRFs of the coupled HE and beam test structure system in free-free boundary conditions (dashed curves) acquired in the modal analysis survey in Sect. 10.3.1, as well as in fixed-free boundary conditions if the coupled test system is mounted on the shaker (solid curves). It needs to be mentioned that the sensor configuration and setup was different compared to the experimental tests introduced in Sect. 10.3.1, and this is the reason why at this stage the comparison can only be made qualitatively. The beam sensor B:T1 of the modal analysis survey is mounted on an approximately similar position than the corresponding beam sensor Beam:B3 of the coupled HE/beam and shaker configuration. The same can be assumed for the HE sensors HE:BR and HeadExp:RB which are glued close to the HE's corner at the bottom right. It is obvious that due to the different boundary conditions, mass loading effects and coupling between the shaker and coupled HE/beam test structure some modes are shifted or changed in frequency and damping but also that new modes occur as shown in Fig. 10.9 and modal analysis results. Main investigations are summarised below:

- Especially, the results show clearly that the 1st bending mode of the beam is not or just slightly affected by testing the coupled system in free-free condition or fixed-free clamped on the shaker. The frequency and mode shape is approx. at 155–160 Hz and is clearly visible on sensors on the beam structure (B:T1 in dashed blue and Beam:B3 in magenta) but also affects sensors on the HE (HE:BR in dashed green and HeadExp:RB in red).

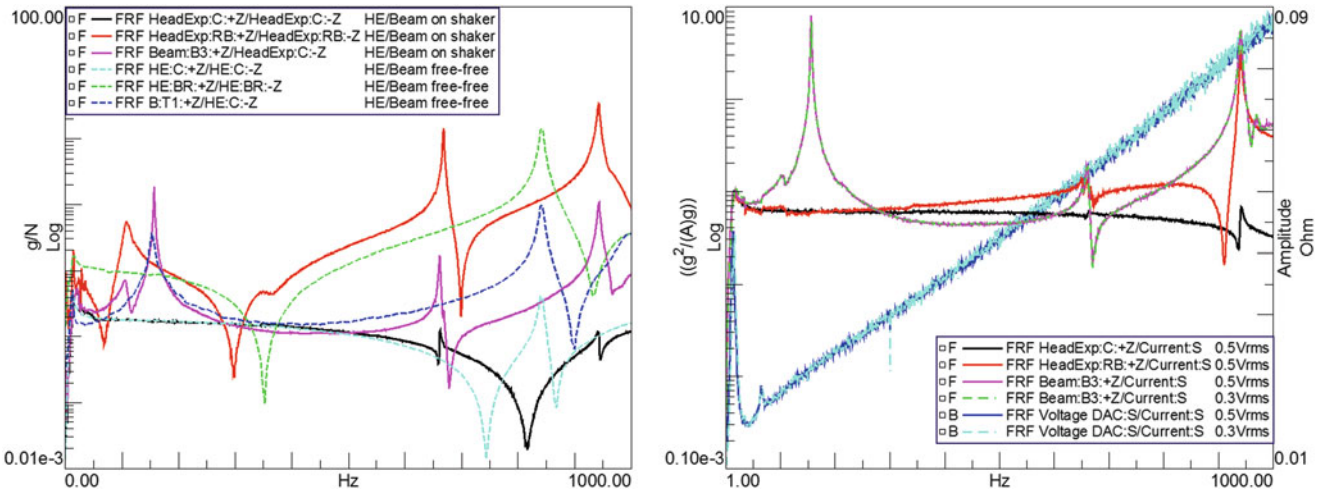

Fig. 10.9 *Left*—impact testing FRFs of coupled Head Expander and beam structure in free-free and fixed-free (mounted on shaker table) boundary conditions. *Right*—open-loop random testing FRFs of coupled system.

- Additionally, first shaker table rotational (rocking) modes are excited during test in the fixed-free case and occur as additional resonance peaks in the HE sensor HeadExp:RB (red) and beam sensor Beam:B3 (magenta) FRFs at low frequencies at approx. 34 and 66 Hz, and a dominating mode at 100 Hz prior to the 1st beam bending mode as shown in Fig. 10.9.
- The high frequency range is dominated by higher order modes at 660 and 960 Hz as clearly indicated by HeadExp:RB (red) and Beam:B3 (magenta) whereas for the free-free case only the clearly identified saddle mode at approx. 842 Hz is detected and shown by the dashed FRFs.

This shaker to test structure interaction will increase if heavier test specimens are tested and can lead to major challenges while performing a controlled closed-loop vibration test.

To asses such interactions and coupling effects low level open-loop random tests (0.3 Vrms and 0.5 Vrms over the entire frequency range <1000 Hz) are performed and presented in the right plot of Fig. 10.9. The results show acceleration-over-current and voltage-over-current FRFs acquired during open-loop random testing. The modes which are identified by impact testing are clearly excited and well presented in the acquired FRFs. The FRFs of the two different excitation levels totally overlap and show now presence of structural non-linearities besides of the low frequency suspension mode (shaker table and coil move in phase w.r.t. the shaker body). This mode shows a softening effect which is decreased in frequency by increasing the excitation level (0.3Vrms: 14.6 Hz, 0.5Vrms: 12.8 Hz) and can be related to the guidance system of the shaker. In the future it is intended to investigate this occurrence more in detail.

The open-loop random tests are performed to generate a data set for system identification purposes as it is used during the self-check phase which is performed prior to a closed-loop sine control execution. A schematic sketch is given on the left of Fig. 10.10. A test structure model is coupled to the electrodynamic shaker system and to the vibration controller $C(s)$. The shaker facility and test specimen interacts with the vibration test controller by a closed-loop acceleration feedback control system to be capable of controlling the shaker table acceleration w.r.t. required test specifications by driving the electrodynamic shaker with an appropriate voltage signal. This voltage signal is calculated by the control algorithm based on the test specifications and internal vibration control parameter, e.g. sweep rate for sine sweep testing, to perform the controlled test execution.

Since, hereafter, an alternative method is presented to derive a coupled shaker and test specimen model to numerically predict sine vibration tests without the need to physically couple an electrodynamic shaker model (refer to Sect. 10.2) with structural model representations but to use experimental test results in a data driven approach instead.

To validate the subsequent numerical sine control simulations, Fig. 10.10 on the right, shows experimental sine control test results of a logarithmic sweep of 4 oct/min up to 1000 Hz with a control reference spectrum of 1 g of the coupled HE/beam structure in blue and the HE without beam structure in red.

Subsequently, the open-loop random results are used to calculate acceleration-over-voltage transfer functions, estimate discrete model representations based on a PolyMAX modal parameter estimation approach and to use the derived z-domain models in a closed-loop simulation coupled to the sine control model. Consequently, this approach follows the equivalent steps as introduced in Sect. 10.3.3 but instead of using the modal models, the coupled electrodynamic shaker and test structure

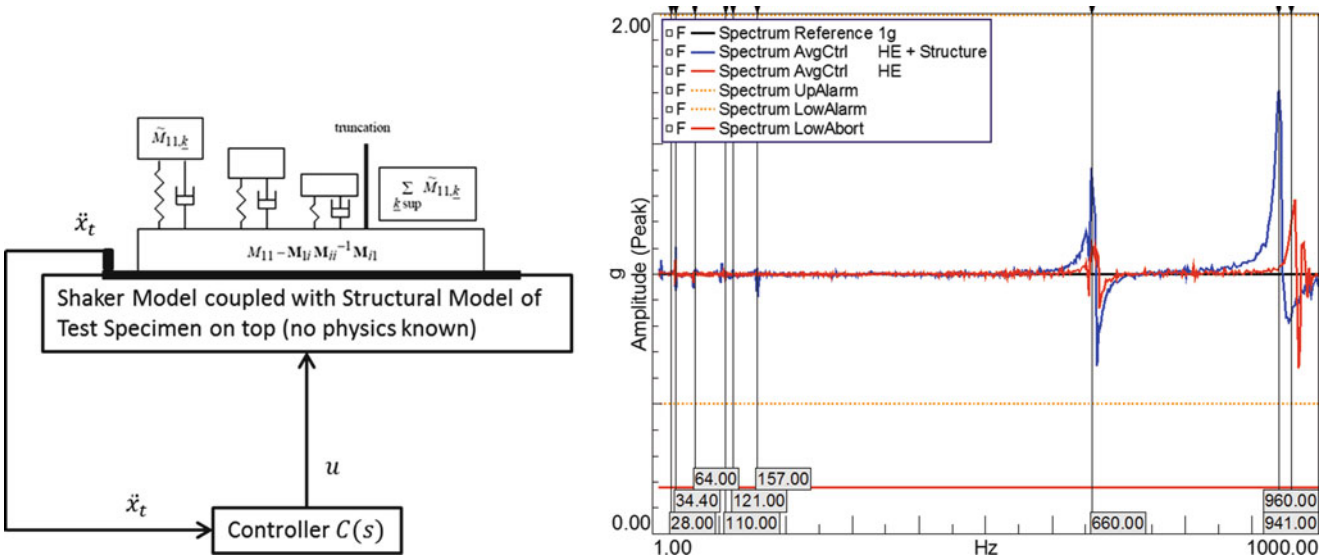

Fig. 10.10 *Left*—sketch of coupled shaker and test specimen to vibration controller for system identification purposes. *Right*—experimental sine control test results (reference control spectrum: 1 g, sweep rate: 4 oct/min) of shaker system loaded with HE (*red*) and coupled HE/Beam (*blue*) system

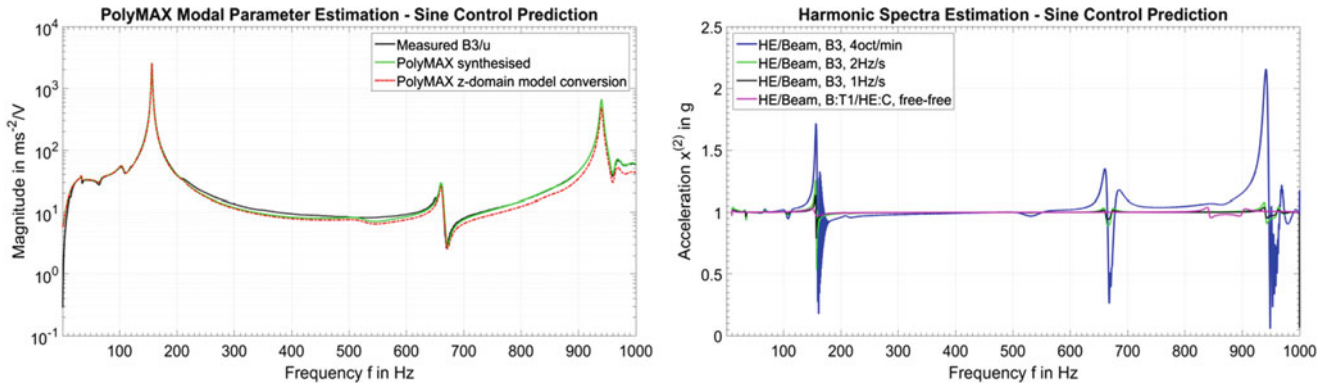

Fig. 10.11 *Left*—experimental and synthesised acceleration-over-voltage FRFs calculated from open-loop random excitation tests of Fig. 10.9 (*right*). *Right*—numerical closed-loop sine control predictions (reference control spectrum: 1 g, sweep rate: various) using the estimated z-domain model on the left and comparison to predicted results of Fig. 10.8 using the free-free model representation

dynamics is comprised in the discrete model representation of the acceleration-over-voltage transfer function (left sketch of Fig. 10.10). The measured (black), synthesised (green) and z-domain polynomial model (red) of the transfer function between the beam sensor B3 and the electrical voltage are presented in the left plot of Fig. 10.11.

The following numerical sine control predictions with a control reference spectrum of 1 g over the entire frequency range of 10 to 1000 Hz are presented on the right of Fig. 10.11. The figure shows the acceleration spectra for different sine sweep rates: in blue a logarithmic sweep rate of 4 oct/min equivalent to the real experimental sine test results as shown in the right of Fig. 10.10, in green and black linear sweep rates of 2 Hz/s and 1 Hz/s, and in magenta it reviews the results of Sect. 10.3.3 considering the estimated modal models in free-free boundary conditions. It needs to be mentioned that different control sensors were selected.

Nevertheless, the comparison between the numerically simulated and predicted results (Fig. 10.11 right) to the real physical test results (Fig. 10.10 right) can be used to draw some preliminary observations. By comparing the blue acceleration spectra of both figures similar control deviations in terms of amplitude and frequency occur at structural modes and coupled structural and shaker modes even if different sensors are used for control. The experimental results use the maximum signal of all HE acceleration sensors whereas the numerical model is based on the beam sensor B3. Consequently the simulations show the presence of the beam's 1st bending mode clearly as control deviation at 157 Hz whereas the experimental results are less influenced. All other modes which have been detected while impact and open-loop random testing occur as control deviations in the acceleration spectra of the experimental test and numerical predictions in an equivalent manner.

Additionally, the numerical simulations can be used to simulate beating phenomena influenced by the sine control sweep rate as shown by the blue, green and black predictions with different sweep rates of 4 oct/min, 2 Hz/s and 1 Hz/s, respectively. According to ECSS [2] and industrial publications of Thales Alenia Space [8, 21] the beating effect occurs if the sweep rate is not sufficiently slow, then the dynamic and coupled system response is no longer stationary (steady-state) at each instant of time and spectral sine excitation. Consequently, it results in a modification of the shape and position of a resonance followed by a ringing effect as a function of the sweep rate and direction. These beating phenomena can be clearly observed after the beam's first resonance at 157 Hz. It is clearly shown that with decreasing sweep rate (from blue to black) the beating phenomena and control deviations decrease at structural resonances. In practice, it is usually not possible to apply very low sweep rates to provide better control in this way, since the risk of damaging the structure under test increases as well as the testing time. Consequently, it is of major importance to include the virtual shaker testing approach in the S/C vibration testing procedure for being capable of including and predicting sweep rate effects and to avoid misinterpretations during tests.

If a preliminary sine control prediction is performed as explained in Sect. 10.3.3 and represented by the magenta control spectrum in Fig. 10.11 a significant deviation at shaker modes (34 Hz, 66 Hz and 100 Hz) or coupled HE structural modes (660 and 960 Hz) is detected compared to simulation approach considering the coupled shaker and structural dynamics. In contrary, the two approaches show similar results for the unchanged 1st beam resonance mode at 156 Hz and can be used as a fast methodology to assess the control performance in this frequency range. Considering the entire frequency range of testing and the increasing model and modal complexity the investigations clearly show that the virtual shaker simulation environment needs to comprise all three major contributors of the vibration test chain to predict the outcome of a S/C vibration test and to assess possible challenges which can occur during the test execution.

10.5 Conclusions

The paper reviews the work of the modelling and derivation of an enhanced electrodynamic shaker model based on experimental results and the coupling to a dedicated sine vibration controller in the first part of the paper. Furthermore, the paper concludes experimental test data and modal analysis results of the shaker head expander and a dedicated beam test structure, both in uncoupled and coupled configuration under free-free boundary conditions. Consequently, the experimentally estimated models are numerically coupled to the sine controller model neglecting the shaker model to calculate first preliminary test predictions and are compared against a more physical approach considering the coupled shaker, controller and test structure model. The calculations are qualitatively evaluated against physical test data of a different test campaign with a diverse sensor setup and boundary conditions, e.g. free-free to fixed-free interface and the dynamical interaction between the electrodynamic test facility, vibration controller and test specimen models. The numerical calculations show that the virtual shaker simulation environment needs to comprise all three major contributors of the vibration test chain to reliably predict the outcome of a S/C vibration test. Additionally, the derived numerical models are used to study the occurrence of beating phenomena as a function of the sine sweep rate and their effect to the control performance. In the future, it is intended to use those results to derive methodologies to couple experimentally derived structural models and to use them in further numerical closed-loop simulation analysis comprising the electrodynamic shaker and sine controller model. The objective is to derive clear guidelines to successfully develop and execute virtual vibration control tests and to identify the advantages that this process can bring in de-risking test execution and successfully achieve product certification.

Acknowledgements The authors of this work gratefully acknowledge the European Space Agency under the Network/Partnering Initiative PhD programme (contract No. 4000110039/14/NL/PA) in collaboration with Siemens Industry Software NV and Vrije Universiteit Brussel. A special thank you also to Alessandro Cozzani, Matteo Appolloni and Steffen Scharfenberg from ESTEC for their support and discussions. This research was also performed in the frame of the project IWT 130936 ADVENT (Advanced Vibration Environmental Testing). The financial support of the IWT (Flemish Agency for Innovation by Science and Technology) is gratefully acknowledged.

References

1. NASA: Technical Handbook, Spacecraft Dynamic Environments Testing, NASA-HDBK-7008. NASA, Washington DC (2014).
2. ESA-ESTEC: European Cooperation for Space Standardization, Space Engineering, Spacecraft Mechanical Loads Analysis Handbook, ECSS-E-HB-32-26A. ESA-ESTEC, Noordwijk (NL) (2013)
3. M. Appolloni, A. Cozzani, Virtual testing simulation tool for the new quad head expander electrodynamic shaker. In: Proceedings of the 6th International Symposium on Environmental Testing for Space Programmes, ESA-ESTEC, 12–14 June 2007

4. M. Appolloni, A. Cozzani et al.: Multi-degrees-of-freedom vibration platform with mimo controller for future spacecraft testing: an application case for virtual shaker testing. In: Aerospace Testing Seminar 2015, Los Angeles, October 2015
5. European Space Agency (ESA), www.esa.int
6. S. Ricci, B. Peeters, R. Fetter, D. Boland, J. Debille: Virtual shaker testing for predicting and improving vibration test performance. In: Proceedings of the IMAC 2009, Orlando (FL), USA, 9–12 February 2009.
7. ESA-ESTEC study: TN-3: Assessment of the Shaker Performance in Presence of Non-linear Dynamic Effects, LMS International in framework of ESA Study Advancement of Mechanical Verification Methods for Non-linear Spacecraft Structures. TEC-MCS/2007/1558/ln/AN.
8. A. Bettacchioli: Simulation of satellite vibration test. In: Proceedings of the 13th European Conference on Spacecraft Structures, Materials and Enviromental Testing, Braunschweig, Germany, 1–4 April 2014
9. S. Manzato, F. Bucciarelli, M. Arras, G. Coppotelli, B. Peeters, A. Carrella: Validation of a Virtual Shaker Testing approach for improving environmental testing performance. In: Proceedings of the ISMA 2014, Leuven, Belgium, September 2014
10. G. Fox Lang, D. Snyder: Understanding the physics of electrodynamic shaker performance, Sound & Vibration, October 2001
11. Siemens Industry Software NV, LMS Test. *Lab Environmental*, www.siemens.com/plm/lms, Leuven, Belgium, 2015
12. Siemens Industry Software NV, *LMS SCADAS III Data Acquisition Front-end*, www.siemens.com/plm/lms, Breda, The Netherlands, 2015
13. S. Waimer, S. Manzato, B. Peeters, M. Wagner, P. Guillaume: Derivation and implementation of an electrodynamic shaker model for virtual shaker testing based on experimental data. In: 29th Aerospace Testing Seminar, Los Angeles, CA, USA, October 2015.
14. S. Waimer, S. Manzato, B. Peeters, M. Wagner, P. Guillaume: A multiphysical modelling approach for virtual shaker testing correlated with experimental test results. In: Proceedings of the 34th International Modal Analysis Conference IMAC, Orlando, USA, January 2016
15. McConnell, K.G., Varoto, P.S.: Vibration Testing: Theory and Practice. Wiley, New York (1995)
16. S. Waimer, S. Manzato, B. Peeters, M. Wagner, P. Guillaume: Modelling and experimental validation of a coupled electrodynamic shaker and test structure simulation model. In: Proceedings of the ISMA 2016, Leuven, Belgium, September 2016
17. De, K., Rixen, D., Voormeeren, S.N.: General framework for dynamic substructuring: history, review and classification of techniques. AIAA J. **46**(5), 1169–1181 (2008)
18. S. Waimer, S. Manzato, B. Peeters, M. Wagner, P. Guillaume: Numerical modelling and simulation of a closed-loop electrodynamic shaker and test structure model for spacecraft vibration testing. In: Proceedings of the European Conference of Spacecraft Structures, Materials and Environmental Testing, Toulouse, France, September 2016
19. Peeters, B., Auweraer, H.V.D., Guillaume, P., Leuridan, J.: The PolyMAX frequency-domain method: a new standard for modal parameter estimation. Shock Vibration. **11**, 395–409 (2004)
20. Bart Cauberghe: Applied frequency-domain system identification in the field of experimental and operational modal analysis. PhD thesis, Vrije Universiteit Brussel (2004)
21. A. Bettacchioli, P. Nali: Common issues in S/C sine vibration testing and a methodology to predict the sine test responses from very low level run. In: Aerospace Testing Seminar 2015, Los Angeles, October 2015

Chapter 11
Establishment of Full-Field, Full-Order Dynamic Model of Cable Vibration by Video Motion Manipulations

Lorenzo Sanchez, Huiying Zhang, Alexander Roeder, John Bowlan, Jared Crochet, Yongchao Yang, Charles Farrar, and David Mascareñas

Abstract In-service cables such as stay cables and suspenders of cable-stayed bridges and suspension bridges, are subjected to dynamic loads (e.g., the vehicle loads and wind excitation). Performing vibration measurements and subsequently identifying the dynamic properties and establishing a dynamic model of cable vibration are essential for their dynamic analysis, condition assessment, and performance prediction. For example, based on the taut-string theory, the cable tension, as a critical indicator of cable performance and health state, can be computed using its frequency that can be identified from the measured cable vibration responses. Traditional contact-type wired or wireless sensors, such as accelerometers and strain gauge sensors, require physically attaching to the structure for vibration measurements, which could induce the mass effect. In addition, installing these sensors on structures is costly, time-consuming, and allows instrumentations at a limited number of places. On the other hand, digital video cameras have emerged as a cost effective and agile non-contact vibration measurement method, offering high-resolution, simultaneous, measurements. Recently, digital video camera measurements processed by advanced computer vision and machine learning algorithms have been successfully used for experimental and operational full-field vibration measurement and modal analysis. This study develops a video measurement and processing based technique that can autonomously and blindly extract the full-field dynamic parameters of cable vibration from the video measurements. In addition, by exploiting the taut string theory, full-order (as many modes as possible) dynamic parameters are also extracted. Therefore, a full-field, full-order dynamic (modal) model of cable vibration is established. Laboratory experiments are conducted to validate the developed approach.

Keywords Mode shape matrix • Cable dynamics • Video measurement • Dynamic model • Taut string theory

11.1 Introduction

11.1.1 Motivation

Cables are prevalent in many structures including suspension bridges, cable stayed roofs and cable stayed bridges. Monitoring the health of these cable structures could be essential to the overall condition and operational lifetime of the entire bridge or building. This application of a novel algorithm to estimate modal information from a video is motivated by drawbacks

L. Sanchez
Department of Mechanical Engineering, Brown University, Providence, RI 02912, USA
e-mail: lorenzo_sanchez@brown.edu

H. Zhang
Department of Applied Math, Columbia University, New York, NY 10027, USA
e-mail: hz2315@columbia.edu

A. Roeder
Department of Mechanical Engineering, Georgia Institute of Technology, Atlanta, GA 30332, USA
e-mail: akalex9@gmail.com

J. Bowlan • J. Crochet
Los Alamos National Laboratory—Physical Chemistry and Applied Spectroscopy, Los Alamos, NM 87545, USA
e-mail: jbowlan@lanl.gov; jcrochet@lanl.gov

Y. Yang (✉) • C. Farrar • D. Mascareñas
Los Alamos National Laboratory—Engineering Institute, P.O. Box 1663, MS T001, Los Alamos, NM 87545, USA
e-mail: yyang@lanl.gov; yangyongchaohit@gmail.com; farrar@lanl.gov; dmascarenas@lanl.gov

N. Dervilis (ed.), *Special Topics in Structural Dynamics, Volume 6*, Conference Proceedings
of the Society for Experimental Mechanics Series, DOI 10.1007/978-3-319-53841-9_11

to traditional methods, such as accelerometers, strain gauges and anchored load cells, of vibration measurements and modal analysis. These methods can only provide low spatial resolution measurements caused by mass effects from the loading of the dense array of sensors on the cable. There is also financial drawbacks in using the traditional sensors as there are costs from installing the sensors. Alternative methods exist that also use video cameras to capture the vibrating structure but require the use of speckle paint or other markers on the structure. The benefit of using this particular algorithm developed in [1] is that it is completely non-contact without structural surface preparation and can be implemented in a relatively automated and efficient manner.

11.2 Background

11.2.1 Taut String Theory

Cable dynamics is well understood from taut string theory [2] as well as prior experimental work [3]. The tension/natural frequency relationship of cables is given by

$$T = \frac{\mu L^2}{\pi^2}\left(\frac{\omega_i}{i}\right)^2 \tag{11.1}$$

where T, the tension, can be calculated from knowing μ, the mass density per unit length; L, the length of the cable; and ω_i, the ith modal frequency. In addition to this relation, taut string theory dictates that the natural frequencies of a cable fall in a linear progression, thus

$$\frac{\omega_i}{i} = \frac{\omega_j}{j} \tag{11.2}$$

holds for any two integers, i and j.

11.2.2 Video Processing: Automated Video Extraction

An algorithm based on unsupervised machine learning and computer vision techniques for estimating modal frequencies and mode shapes has been established by [1]. The application of this algorithm, along with knowledge of cable dynamics, can help establish a full field and full order dynamic model of the cable with a novel non-contact method. This algorithm utilizes phase based optical flow to extract a time history of phase values at each pixel in the video [4, 5]. This high dimensional motion matrix is then condensed using principal component analysis to project this matrix onto fewer principal components [6]. The last tool of this algorithm is using blind source separation (BSS) to obtain the individual modes from the principal components [7]. In the BSS model

$$x(t) = As(t) = \sum_{i=1}^{n} a_i s_i(t) \tag{11.3}$$

the observed mixtures $x(t)$ are linear combinations of the unknown sources $s_i(t)$. Assuming that all $s_i(t)$ are statistically independent for all t, it is possible to find $s(t)$ given $x(t)$ [6]. The output of this video processing algorithm is the modal frequencies and mode shapes (in the video space) of the structure of interest estimated from a video of the vibrating structure.

11.3 Experimental Setup and Results

11.3.1 Laboratory Setup

The structure of interest was a 1.75 m long braided, stainless steel cable with a diameter of 2.38 mm (3/32 in.) held in place within a Unistrut frame. One end of the cable was attached to a load cell which outputted voltage readings to a multimeter. The other end of the cable was connected to a turnbuckle, allowing the tension in the cable to be adjusted. Three separate data collection systems were used: (1) a load cell connected to a high-sensitivity multimeter; (2) PCB accelerometers with a National Instruments data acquisition unit; and (3) a Sony digital video camera set up facing the cable to capture a video of the vibrating structure. The video was set to collect at 480 fps with an ISO setting of 10k (Fig. 11.1).

11.3.2 Automated Filtering

A video motion processing algorithm was used to 'filter' the original video's pixel phases to extract the vibration video of the mode shape for each specific modal frequency, which is automatically specified by the taut string theory. This algorithm can extract the mode shape videos for each modal frequency up to the Nyquist frequency, which in this case is 240 fps.

11.3.3 Mode Shape Estimation

Another algorithm was used to break down the mode shape videos into mode shape vectors. These mode shape vectors can be used to create a mode shape matrix of the size n by m where n is the number of pixels along the length of the cable and m is the number of modal frequencies. The algorithm breaks down the mode shape video into many frames by using the canny edge detection algorithm. See Fig. 11.2 for the procedures.

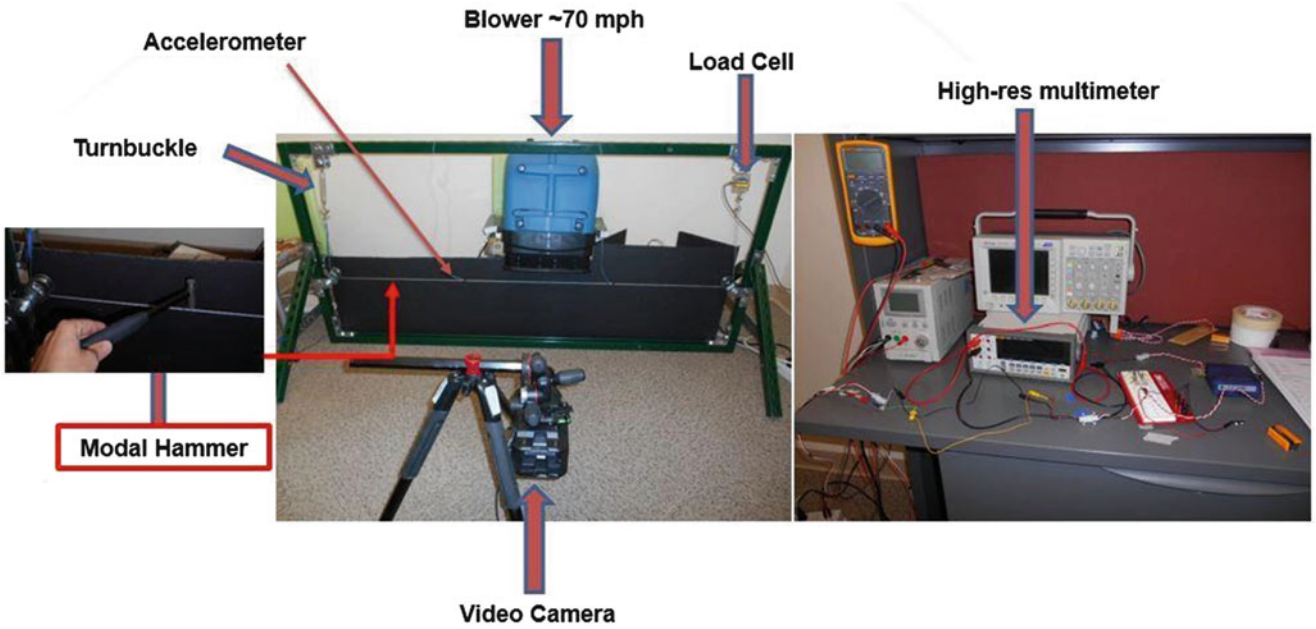

Fig. 11.1 Experimental setup

11.3.4 Results

11.3.4.1 Compare Tension with Accelerometers

Since the video estimated frequencies play a central role in the construction of the frequency response function, two different methods are used to verify them. First, taut string theory provides a relationship between the tension in a cable and the cable's natural frequencies, thus it is possible to find the cable tension from the video estimated frequencies. By taking advantage of this relation the video estimated frequencies can be compared to the accelerometer estimated frequencies and the cable tension as measured by the Futek load cell.

Figure 11.3 below compares the video estimated tensions with the accelerometer estimated tensions for both the impact and wind excitation data from 42 different trials. In both cases, the video estimated tensions match the accelerometer estimated tensions with a max error of 37 and 38 N for wind and impact data, respectively.

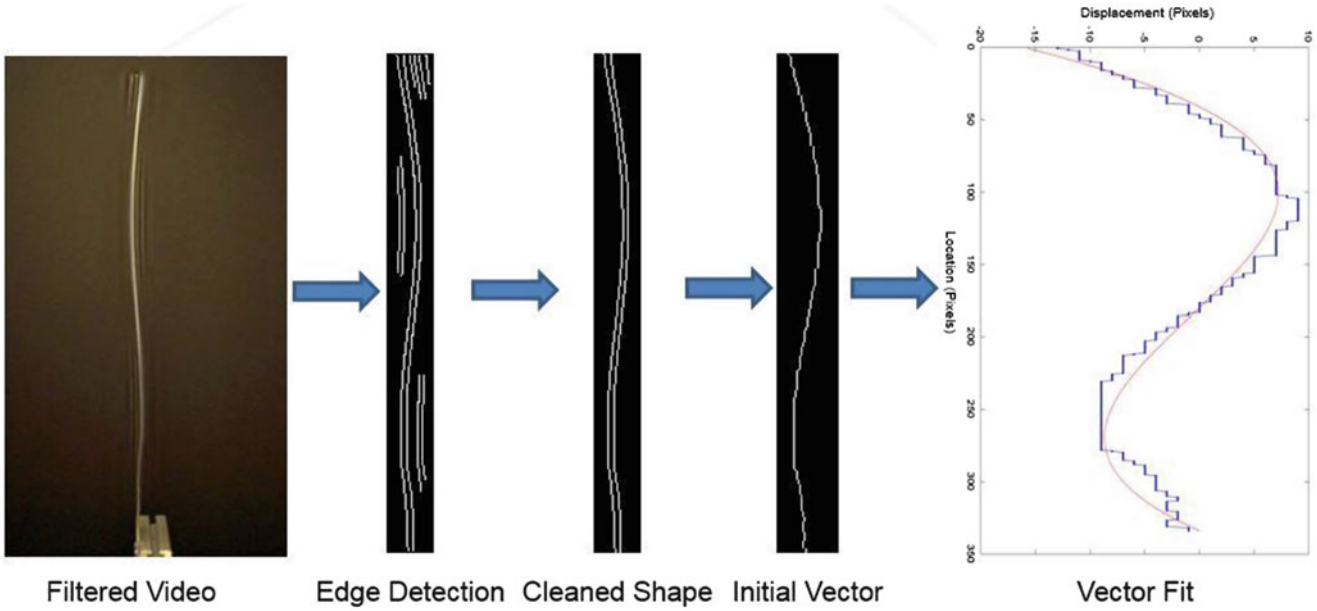

Fig. 11.2 Process for converting the filtered mode shape videos to mode shape vectors

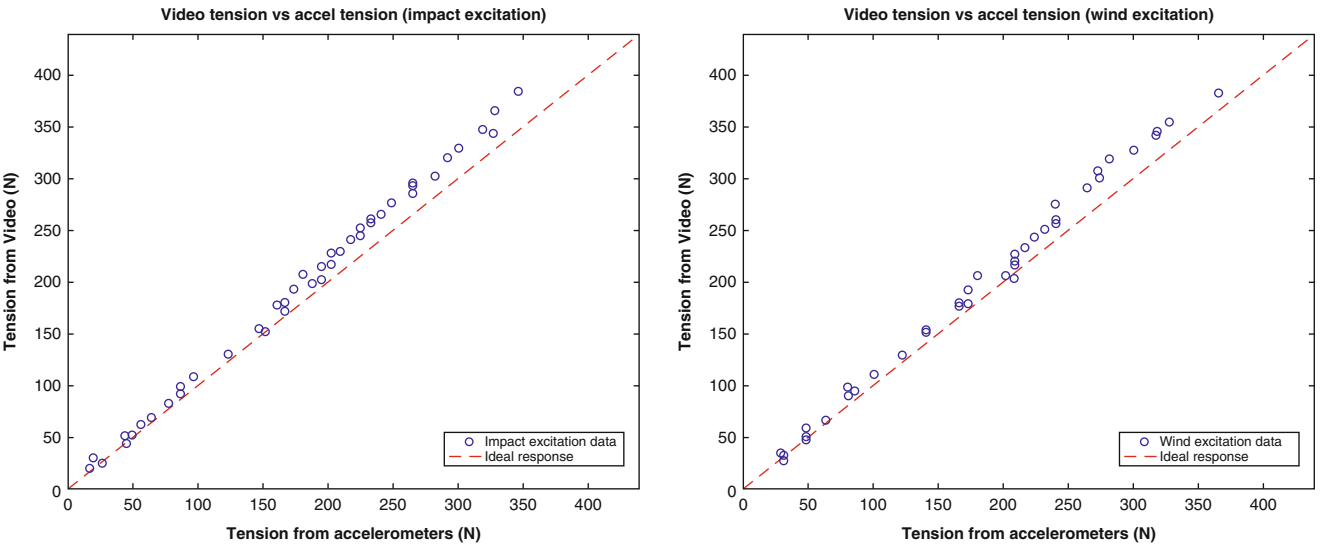

Fig. 11.3 Comparing tension estimated from video to tension estimated using acceleration data from PCB accelerometers

11.3.4.2 Compare Tension with Load Cell

Figure 11.4 below compares the video estimated tensions with tension values estimated from the load cell for both the impact and wind excitation data from 90 different trials. Again, tension in the cable is calculated from the video estimated fundamental frequency and the relation given by taut string theory. Tension values from the load cell are determined after careful calibration of the load cell with weights spanning the entire range of 0.06–440 N. In both cases, the video estimated tensions match the load cell estimated tensions with a max error of 36 and 41 N for wind and impact data, respectively.

11.3.4.3 Linear Progression of Frequencies

From taut string theory the natural frequencies are expected to follow a linear relation and this fact is confirmed experimentally by plotting the progression of frequencies estimated from videos (Fig. 11.5).

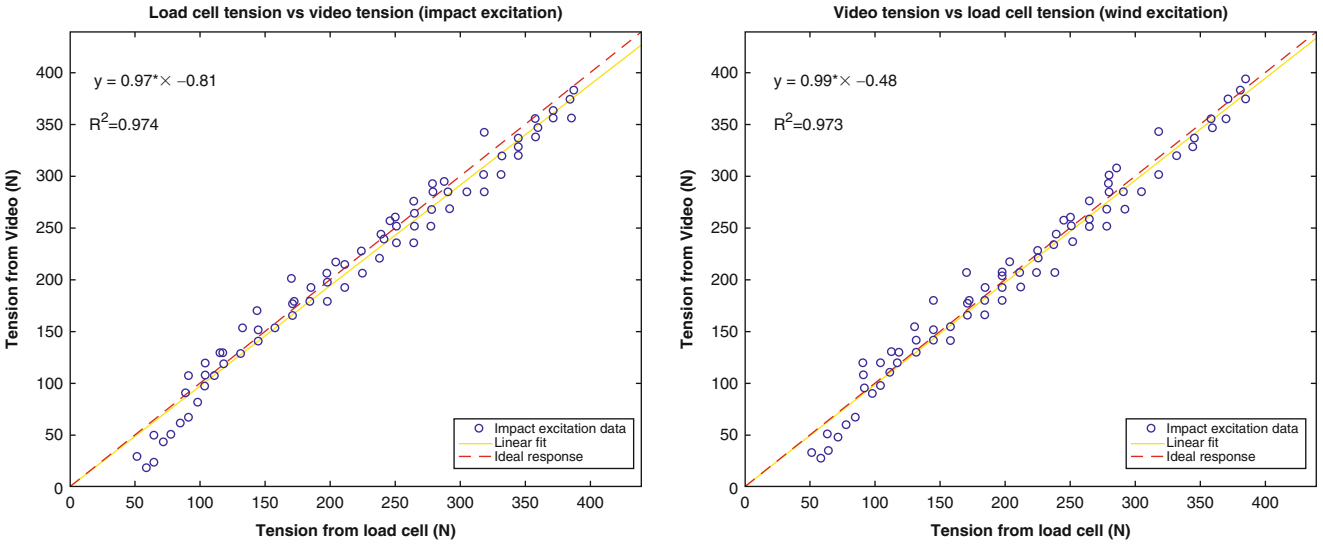

Fig. 11.4 Comparing tension estimated from video to tension estimated with Futek load cell (model LSB302)

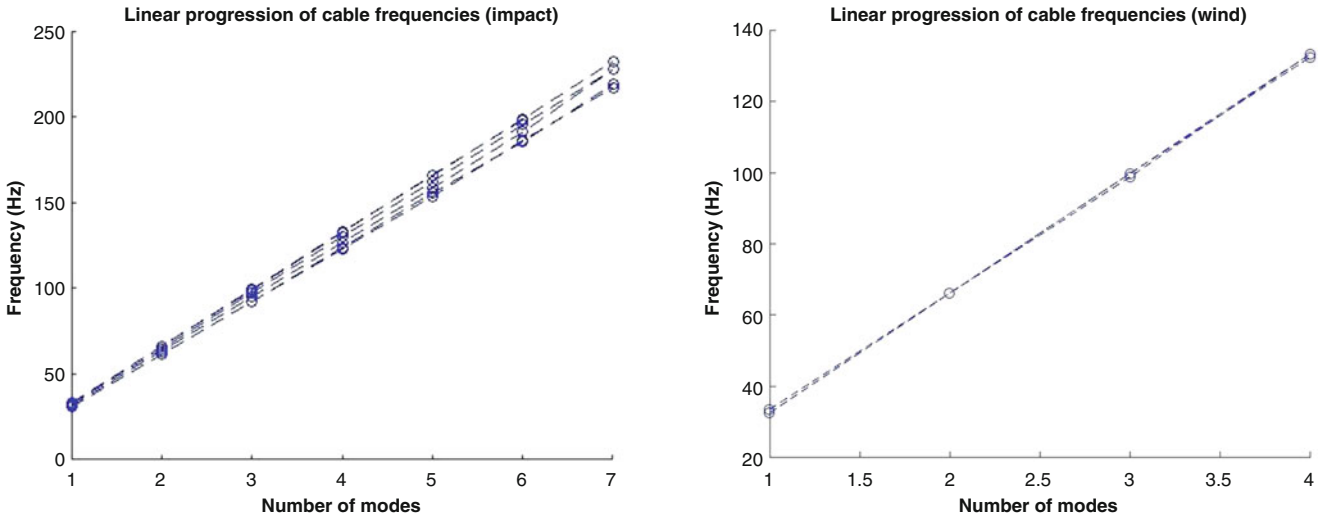

Fig. 11.5 First modal frequencies from six videos with impact excitation and six videos with wind excitation

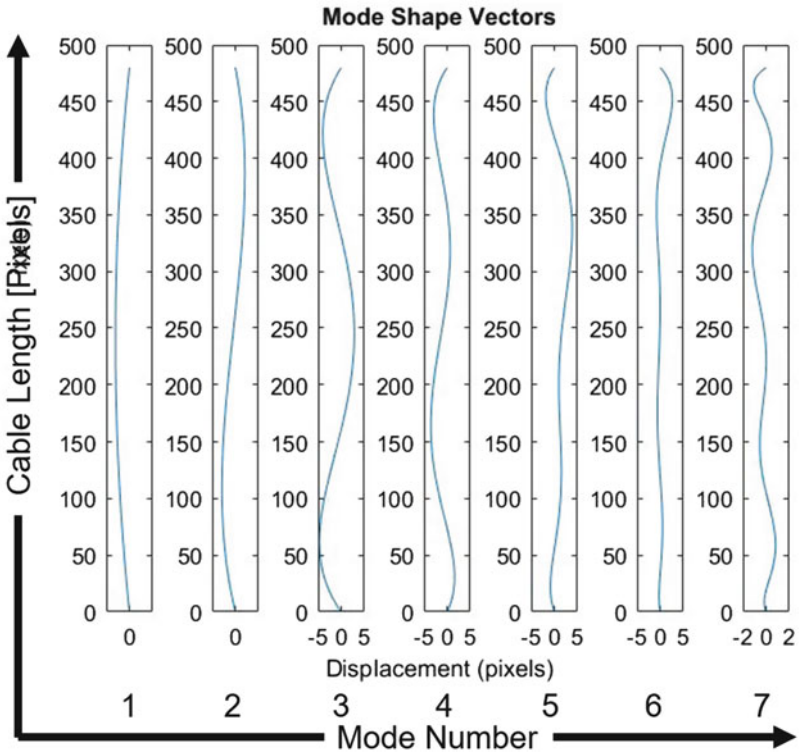

Fig. 11.6 Mode shape vectors for seven modal frequencies

11.3.4.4 Mode Shape Vector

The following figure shows the mode shape vectors of seven modal frequencies extracted by using the algorithms discussed in Sect. 11.3.3. These seven modal frequencies are the full field, full order dynamic model of a cable at a tension of 241 N. The value carried in the mode shape vectors are the pixel displacement along the pixel length of the cable (Fig. 11.6).

11.3.4.5 Comparison with High Speed Camera

A high speed camera with a high sampling rate (thus more modes) was used to compare the extracted modal frequency results measured from the standard camera (Sony). While there are advantages to extracting more vibration modes (Fig. 11.7), there were problems with using a very high-cost high speed camera. First, high speed cameras need extra light sources to perform correctly, which hampers practical use in the proposed manner. Second, the extracted modal frequency data from the standard camera did better, in most cases, than the high speed camera's data (comparing to the accelerometers and load cell) because of the lighting issues from the first problem.

11.3.4.6 Establishing Dynamic Model

Given the smoothed mode shapes and the estimated natural frequencies, a full field and full order dynamic model of the cable can be established via

$$[H(\omega)]_{N\times N} = [\phi]_{N\times m}\left[\left(\lambda_i^2 - \omega^2\right)\right]^{-1}_{m\times m}[\phi]^T_{m\times N} \tag{11.4}$$

where the FRF matrix, $[H(\omega)]_{N\times N}$, depends on a mode shape matrix $[\phi]_{N\times m}$ and a diagonal matrix of the difference of squares between each natural frequency, λ_i, and ω [8].

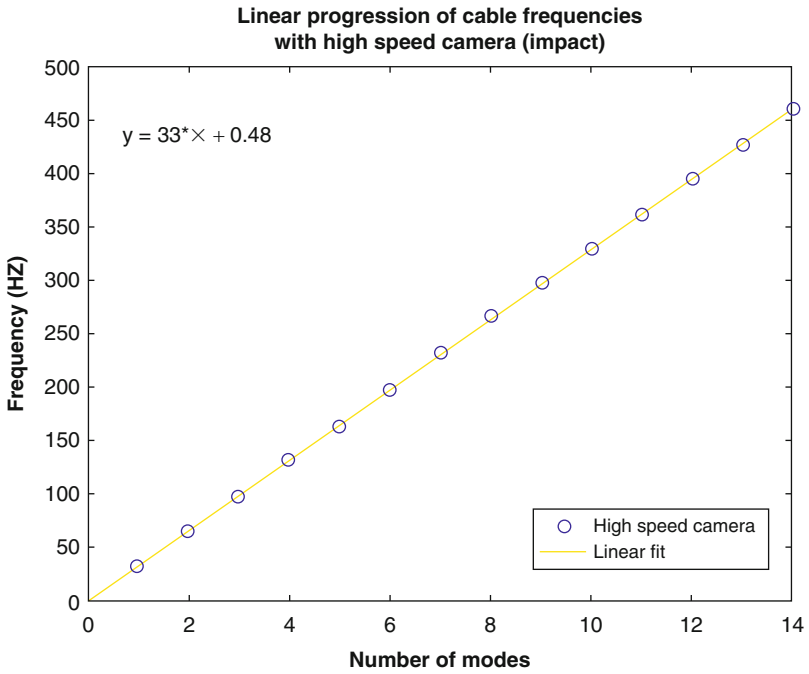

Fig. 11.7 First 14 frequencies from video with high speed camera of vibrating cable after impact

11.4 Conclusion

This work leverages a novel method previously developed to perform output-only modal analysis using phase-based video motion processing, Blind Source Separation (BSS), and principal component analysis techniques. By applying this method to a cable structure and taking advantage of taut string theory, it is possible to establish a full field, full order dynamic model while simultaneously determining the tension in the cable.

References

1. Yang, Y., Dorn, C., Mancini, T., Talken, Z., Kenyon, G., Farrar, C., Mascarenas, D.: Blind identification of full-field vibration modes from video measurements with phase-based video motion magnification. Mech. Syst. Signal Process. **85**, 567–590 (2017)
2. Warnitchai, P., Fujino, Y., Susumpow, T.: A non-linear dynamic model for cables and its application to a cable-structure system. J. Sound Vib. **187**(4), 695–712 (1995)
3. Yang, Y., Li, S., Nagarajaiah, S., Li, H., Zhou, P.: Real-time output-only identification of time-varying cable tension from accelerations via complexity pursuit. ASCE J. Struct. Eng. **142**(1), 04015083 (2015)
4. Fleet, D.J., Jepson, A.D.: Computation of component image velocity from local phase information. Int. J. Comput. Vis. **5**(1), 77–104 (1990)
5. Wadhwa, N., Rubinstein, M., Durand, F., Wadhwa, N.: Phase-based video motion processing. ACM Trans. Graph. **32**(4), 1 (2013)
6. Hyvarinen, A., Oja, E.: Independent component analysis: algorithms and applications. Neural Netw. **13**(4), 411–430 (2000)
7. Antoni, J.: Blind separation of vibration components: principles and demonstrations. Mech. Syst. Signal Process. **19**(6), 1166–1180 (2005)
8. Ewins, D.: Modal Testing. Research Studies Press, Philadelphia, PA (2000)

Chapter 12
Analyses of Target Definition Processes for MIMO Random Vibration Control Tests

Umberto Musella, Giacomo D'Elia, Simone Manzato, Bart Peeters, Patrick Guillaume, and Francesco Marulo

Abstract In Random Vibration environmental testing, it is a common practice to specify the requirements as acceleration power spectral densities (PSDs) that need to be reproduced at user-defined control channels. Such a test is typically performed in a single-axis setting, where the test article is subjected to vibrations in one direction only. If more than one direction is of interest sequential single-axis tests are performed after rotating the test article or using a slip table configuration. This way to perform multi-axial Random Vibration tests is out of date: there is definitely some lack of realism in sequential single-axis testing, as the stress loading and boundary conditions will significantly differ from the true three-dimensional environment. For very heavy structures, often the excitation level safely reachable by a single shaker is not even sufficient, the limitation being the risk of damaging the sometimes very expensive and fragile test articles due to high concentrated stresses. All these limitations are overcome if a Multiple-Input-Multiple-Output (MIMO) Random Vibration Control test is performed. Even though the benefits of MIMO tests are clear and accepted by the environmental engineering community, their practice still needs to grow. This is mainly due to the high degree of expertise needed to perform these tests. The challenges of MIMO Random Control start even before the actual test, in the test definition phase. The target that needs to be reached during the test is a full Spectral Density Matrix where the cross terms are as important as the diagonal ones. Defining this matrix with no a-priori knowledge of the cross-correlation between control channels is very challenging: filling in the off-diagonal terms, in fact, must guarantee that the target has a physical meaning. This is translated in the algebraic constraint that the target matrix needs to be positive (semi)-definite. On the other end the pushing driver of any Random Vibration Control test is to be able to replicate specific PSDs, given, for instance, by qualification specifications or optimal profiles (in terms of fatigue damage or comfort requirements). In defining the target matrix the main challenge is to guarantee a physically realizable full target spectral density matrix that has fixed PSD terms. Several authors tackled the problem of defining the best target possible (in terms of minimum drives energy, in terms of control performances,) even though few works can be addressed that tackle the problem of defining a realizable target first. This leads to a gap in the standards about a generally accepted and robust procedure to define the MIMO Random target matrix. The purpose of this work is to investigate different target generation procedures pointing out the advantages and the challenges in terms of physical meaning and their impact on the random control strategy. Alternative solutions based on on-going research topics will also be considered to propose alternative robust target definition routines in order to aim to a well-defined automatic procedure to include in the standard practice.

Keywords Environmental vibration testing • MIMO random vibration control tests • MIMO reference matrix • Positive semi-definite matrix • Minimum drives requirements

U. Musella (✉)
Siemens Industry Software NV, Interleuvenlaan 68, 3001 Leuven, Belgium

Acoustics and Vibration Research Group, Vrije Universiteit Brussel, Pleinlaan 2, 1050 Elsene, Belgium

Department of Industrial Engineering, University of Naples Federico II, Via Claudio 21, 80125 Naples, Italy
e-mail: umberto.musella.ext@siemens.com

G. D'Elia
University of Ferrara, Via Saragat 1, 44122 Ferrara, Italy

S. Manzato • B. Peeters
Siemens Industry Software NV, Researchpark 1237, Interleuvenlaan 68, 3001 Leuven, Belgium

P. Guillaume
Acoustics and Vibration Research Group, Vrije Universiteit Brussel, Pleinlaan 2, 1050 Elsene, Belgium

F. Marulo
Department of Industrial Engineering, University of Naples Federico II, Via Claudio 21, 80125 Naples, Italy

N. Dervilis (ed.), *Special Topics in Structural Dynamics, Volume 6*, Conference Proceedings
of the Society for Experimental Mechanics Series, DOI 10.1007/978-3-319-53841-9_12

12.1 Introduction

Multiple-Input Multiple-Output (MIMO) vibration control (vibco) tests are performed to subject a unit under test to a realistic three-dimensional dynamic environment. Nowadays the common practice, when multiple directions are required for testing the exposure of a structure to a given vibration environment, is to perform sequential single-axis tests. This practice has known drawbacks: on one hand there is certainly a lack of physical meaning in replicating in-service conditions with a single axis test due to the fact that the in-service stress loading is typically multi-axial; on the other hand sequential single-axis applications can be time consuming and dangerous, since the test set-up has to be changed multiple times with the additional unacceptable risk of damaging the structure. In case of testing heavy slender structures to high overall levels, a single input could also lead to high concentrated loads with the consequence of entering the non-elastic range of the material properties. MIMO tests overcome these limitations and the recent updates to include tailoring guidelines for multi-exciter testing in the United States Military Standards [1] highlight the necessity to improve the knowledge of this innovative practice. While the benefits of MIMO Vibration Control tests are clear and accepted, the current industrial practice is still to a very large extent relying on SISO control. This is basically due to the control and stability problems that could arise during the multi-axial excitation and the inherent level of expertise needed to run these tests.

There are several types of Multi-Axial Vibration Control qualification tests (1) MIMO Random Test, (2) MIMO Time Waveform Replication and (3) MIMO Sine Control Test, differing from the nature of the excitation environment the specimen needs to be subjected to. Random vibco tests are used to simulate the response of the unit under test to a random vibration environment; typical scenarios are the road excitation or the payload and avionic equipment responses during a spacecraft launch. These test specifications are given in terms of Power Spectral Densities (PSDs) of the acceleration *control channels* recordings. For the MIMO case, additional information about the cross-talk between these channels is also included. This information must be provided in terms of Cross Spectral Densities (CSDs) between the control channels defining, for instance, desired phases and coherences. The *target* for a multi-exciter random control test is thus a full reference Spectral Density Matrix (SDM). There are several procedures to define the PSD specifications and generally these terms are given to the environmental test engineer as test requirements. Defining then the full MIMO reference matrix with no a-priori knowledge of the cross-correlation between control channels is very challenging. Filling in the off-diagonal terms, in fact, must guarantee that the reference matrix has a physical meaning. This is translated in the algebraic constraint that this matrix needs to be positive semi-definite, without neglecting the pushing constraint that the test has still to guarantee the required levels at the control locations. In this work, a positive semi-definite SDM is said then to be *physically realisable*. The solution of a physically realisable reference matrix with fixed PSD terms is not unique and not all the possible solutions can be exactly reproduced in the laboratory for a given specimen. In this sense, the best information an environmental test engineer could use is a target originated from real life recordings or field data. However, even in this case, when trying to replicate the target on the test rig, there will be inevitable impedance mismatches between the in field and the laboratory conditions [1–3]. There is thus always the risk of trying to force the test item to an unnatural motion that could lead to poor control results and performances. A target with the *best control performances* can then be achieved by minimizing the aforementioned impedance mismatch on top of using field data (IMMAT procedure, [3, 4]). Other considerations could also drive the choice of a reference matrix. For instance a desirable condition would be to minimize (maximize) the energy provided to the shakers to reach the given target levels. A reference that minimizes (maximizes) the input power is said to match the *Minimum (Maximum) Drives* (or *Inputs*) *Requirements* [1, 5] and in the following will be addressed as *Extreme Drives* (or *Extreme Inputs*) *Target*. Minimizing required drives power to reach fixed output levels is an attractive solution that can increase the reachable levels during the test, avoiding the data acquisition system drives overload and preserving the exciters nominal power limits (that sometimes are very limiting thresholds for MIMO Random Control tests). This problem has been tackled by Smallwood in [5] and the method is also mentioned in the standard practice for multi-exciter vibration tests [1].

Even if several authors tackled the problem of defining the best target possible (in terms of minimum drives energy [5], in terms of control performances [2, 3], few works can be addressed that tackle the problem of defining a physically realizable target first [6]. This leads to a clear gap in the procedures about a generally accepted and robust method to define a full MIMO Random reference matrix. The purpose of this work is to investigate different target generation procedures pointing out the advantages and the challenges in terms of physical meaning and their impact on the random control strategy. Possible solutions based on on-going research topics will then be considered to assess alternative robust target definition routines in order to aim a well-defined automatic procedure to include in the standard test tailoring.

In this work most of the derivations are in the frequency domain hence all the arrays are functions of the frequency f ([Hz]), if not specified otherwise. Vectors are denoted by lower case bold letters, e.g. $\mathbf{a}$, and matrices by upper case bold letters, e.g. $\mathbf{A}$. An over-bar is used to indicate the complex conjugate operation and the apex $\square^H$ to indicate the complex conjugate transpose of a matrix, e.g. $\bar{\mathbf{b}}$ and $\mathbf{B}^H$ are the complex conjugate and the complex conjugate transpose of the vector $\mathbf{b}$ and the matrix $\mathbf{B}$, respectively.

12.2 MIMO Random Vibration Control Process

The block scheme of a general MIMO Random Vibration Control test is illustrated in Fig. 12.1. The structure under test is excited driving m electrodynamic or hydraulic shakers and the system's response is recorded in $\ell \geq m$ control points. In the hypothesis of the structure under test behaving linearly and being time invariant, the system is represented by the Frequency Response Function (FRF) matrix $\mathbf{H} \in \mathbb{C}^{\ell \times m}$

$$\mathbf{Y} = \mathbf{H}\mathbf{U} \tag{12.1}$$

where $\mathbf{Y} \in \mathbb{C}^{\ell \times 1}$ and $\mathbf{U} \in \mathbb{C}^{m \times 1}$ are the spectra of the control channels recordings $\mathbf{y}(t) = \{y_1(t), \ldots, y_\ell(t)\}^T$ and the input drives $\mathbf{u}(t) = \{u_1(t), \ldots, u_m(t)\}^T$, respectively. In case of rectangular systems, i.e. $\ell \geq m$, the impedance matrix $\mathbf{Z}$ is generally obtained via a Moore-Penrose pseudo-inverse, $\mathbf{Z} = \mathbf{H}^\dagger \in \mathbb{C}^{m \times \ell}$. In all the vibration control tests, a System Identification pre-test phase is needed to estimate the system transfer function; this is usually performed by running a low-level random test and using the so called H_1 estimator

$$\hat{\mathbf{H}} = \hat{\mathbf{S}}_{\mathbf{yu}} \hat{\mathbf{S}}_{\mathbf{uu}}^{-1} \tag{12.2}$$

where $\hat{\mathbf{S}}_{\mathbf{yu}} \in \mathbb{C}^{\ell \times m}$ and $\hat{\mathbf{S}}_{\mathbf{uu}}^{-1} \in \mathbb{C}^{m \times m}$ are spectral density matrices estimated via the Welch's averaged periodogram.

The Objective of MIMO Random Control vibration tests is to replicate a full Power Spectral Density matrix $\mathbf{S}_{\mathbf{yy}}^{\mathbf{ref}}$. Theoretically the test target could be directly achieved by sending the input drives that have the specified input spectral density matrix

$$\mathbf{u}(t) = \text{ifft}(\mathbf{U}) : \mathbf{S}_{\mathbf{uu}} \triangleq E[\mathbf{U}\mathbf{U}^H] = \hat{\mathbf{Z}}\mathbf{S}_{\mathbf{yy}}^{\mathbf{ref}}\hat{\mathbf{Z}}^H \tag{12.3}$$

Nevertheless, due to the possible non-linear behaviour of the unit under test and noise in the measurements, the system estimated in the pre-test phase will inevitably differ from the actual one ($\mathbf{H}\hat{\mathbf{Z}} \neq \mathbf{I}$, where $\mathbf{I}$ is the $\ell \times \ell$ identity matrix)

$$\mathbf{S}_{\mathbf{yy}} = (\mathbf{H}\hat{\mathbf{Z}})\mathbf{S}_{\mathbf{yy}}^{\mathbf{ref}}(\mathbf{H}\hat{\mathbf{Z}})^H \neq \mathbf{S}_{\mathbf{yy}}^{\mathbf{ref}} \tag{12.4}$$

and a control action is needed to reduce the error

$$\mathbf{E} = \mathbf{S}_{\mathbf{yy}}^{\mathbf{ref}} - \mathbf{S}_{\mathbf{yy}} \tag{12.5}$$

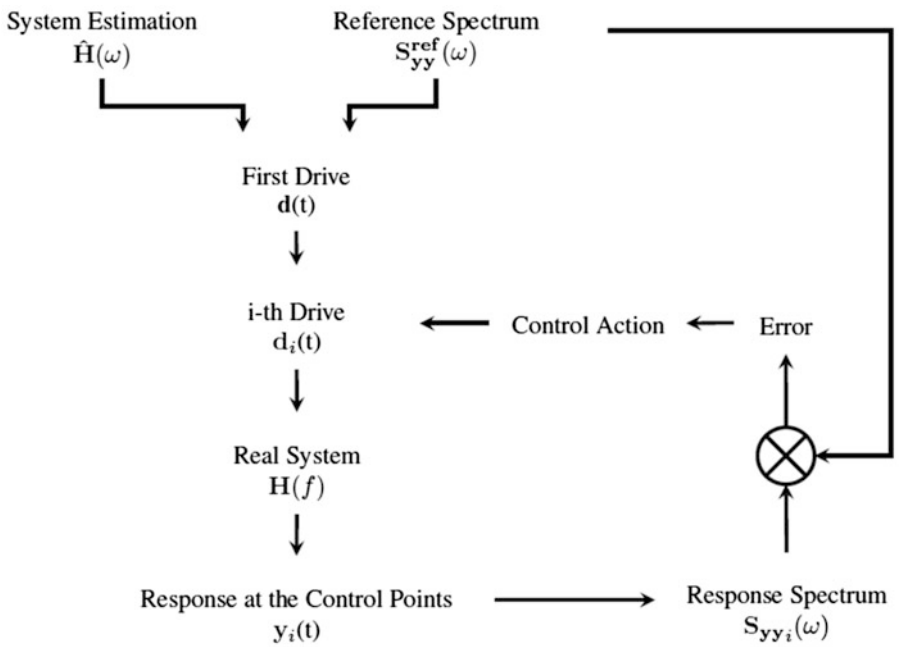

Fig. 12.1 MIMO random control general block scheme

All the error correction strategies for MIMO Random Vibration Control tests (mainly due to the work of Peeters [6], Smallwood [7] and Underwood [8]) rely on the possibility of apply the so called *Cholesky Decomposition* to one of the spectral matrices in the game (either $\mathbf{S}_{\mathbf{yy}}^{\mathbf{ref}}$ or $\mathbf{S}_{\mathbf{uu}}$) and then iteratively correct the resultant *Cholesky Factor*. This operation, as pointed out in Sect. 12.3, is perfectly allowed because of the positive semi-definite nature of the spectral density matrices.

12.3 Building the MIMO Random Vibration Control Reference Matrix

The reference matrix $\mathbf{S}_{\mathbf{yy}}^{\mathbf{ref}}$ to set as target of a multi-exciter random control test must be positive semi-definite to have a physical meaning. Beside the algebraic definition, there are some important properties to consider for practical applications. Particularly, the following statements are equivalent to $\mathbf{S}_{\mathbf{yy}}^{\mathbf{ref}}$ being positive semi-definite [9, 10]:

(a) all the eigenvalues of $\mathbf{S}_{\mathbf{yy}}^{\mathbf{ref}}$ are semi-positive;
(b) $\mathbf{S}_{\mathbf{yy}}^{\mathbf{ref}}$ has a unique Cholesky Decomposition, meaning that it can be decomposed in the product of two triangular hermitian matrices, referred as the Cholesky Factors: $\mathbf{S}_{\mathbf{yy}}^{\mathbf{ref}} = \mathbf{L}\mathbf{L}^H$;
(c) the *Sylvester's Criterion* is respected, i.e. all the *principal minors* of $\mathbf{S}_{\mathbf{yy}}^{\mathbf{ref}}$ have positive determinants. The principal minors are the square sub-matrices that share the diagonal with the full matrix.

Moreover, if $\mathbf{S}_{\mathbf{yy}}^{\mathbf{ref}}$ is positive semi-definite then

(d) the trace of $\mathbf{S}_{\mathbf{yy}}^{\mathbf{ref}}$ is real and semi-positive, being the matrix trace the sum of its eigenvalues;
(e) the determinant of $\mathbf{S}_{\mathbf{yy}}^{\mathbf{ref}}$ is real and semi-positive, being the matrix determinant the product of its eigenvalues;
(f) also $\mathbf{S}_{\mathbf{uu}} = \mathbf{Z}\mathbf{S}_{\mathbf{yy}}^{\mathbf{ref}}\mathbf{Z}^H$ is positive semi-definite.

The diagonal terms of $\mathbf{S}_{\mathbf{yy}}^{\mathbf{ref}}$ are usually known levels for the environmental test engineer, provided as test specifications. Most of the MIMO vibco software have the possibility of defining element-wise the CSDs in terms of coherence and phase profiles. For computational reasons linked to the control process stability [1, 8], coherences values of 0 and 1 are usually avoided. Typical values of low coherence and high coherence are 0.05–0.08 and 0.95–0.98, respectively. No information is available to set this profiles and sometimes an open loop test is run to get a meaningful values. All the CSDs are then easily computed via

$$CSD_{ij} = |CSD_{ij}| \exp(j\phi_{ij}) = \gamma_{ij}\sqrt{PSD_i PSD_j}\exp(\mathrm{i}\phi_{ik}) \tag{12.6}$$

where i is the imaginary unit and i and j are the i-th and the j-th control channels.

12.3.1 Phase Pivoting Method

Filling in the MIMO matrix *element by element* in terms of the $\ell(\ell+1)/2-\ell$ coherence and phase profiles could result in $\mathbf{S}_{\mathbf{yy}}^{\mathbf{ref}}$ being non positive semi-definite, following the fact that none of the properties (a), (b) or (c) have been taken into account in the completion process. Starting from the property (c), Peeters in his work [6] gives a rule to define meaningful coherence choices to get a physical realisable target in case of three control channels. The Sylvester Criterion is, in fact, fully fulfilled if (1) the coherence between two control channels is between 0 and 1 and (2) if the determinant of the full reference spectral matrix is semi-positive. Stated that (1) is the only physical option, to get a meaningful reference matrix is sufficient (and necessary) that

$$det(\mathbf{S}_{\mathbf{yy}}^{\mathbf{ref}}) = 1-\gamma^2-\gamma_{13}^2-\gamma_{23}^2+2\cos(\phi_{12}-\phi_{13}+\phi_{23})\sqrt{\gamma_{12}^2\gamma_{13}^2\gamma_{23}^2} \geq 0 \tag{12.7}$$

where 1,2 and 3 are the control channels. For the special case of the phase between all the control channels being zero, it is possible to fix two of the three coherences and retrieve the allowed values for the last one. For instance, fixing γ_{12} and γ_{13}, Eq. (12.7) allows all the γ_{23} values between the boundaries

$$\gamma_{23,min} = \sqrt{\gamma_{12}^2\gamma_{13}} - \sqrt{(1-\gamma_{12}^2)(1-\gamma_{13})^2} \tag{12.8a}$$

$$\gamma_{23,max} = \sqrt{\gamma_{12}^2\gamma_{13}} + \sqrt{(1-\gamma_{12}^2)(1-\gamma_{13})^2} \tag{12.8b}$$

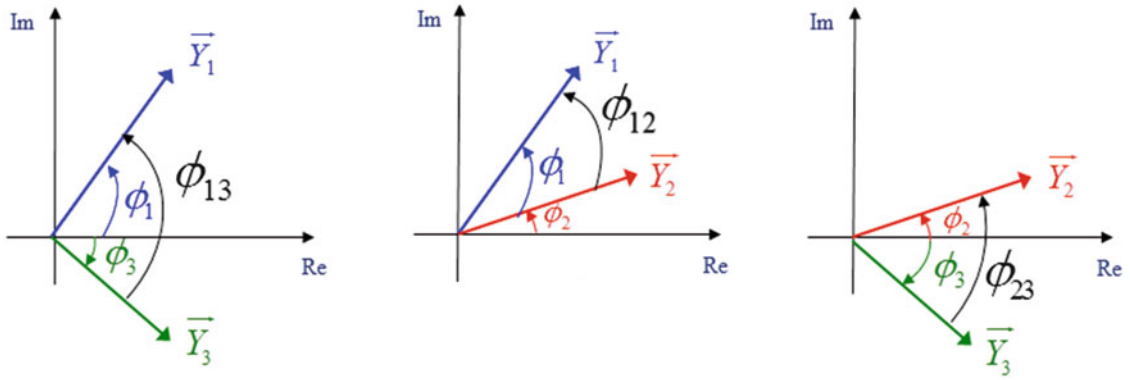

Fig. 12.2 *Phase Pivoting* principle. Given the phases between two pairs of control channels (e.g. ϕ_{13} and ϕ_{12}), the phase between the remaining pair (ϕ_{23}) is automatically defined

The conditions (12.8) can be extended to a more general set of phases by noticing that the two limits (12.8a) and (12.8b) are valid for all the phases combinations that nullify the cosine argument. A general signal processing consideration can drive a meaningful choice of phases that will accomplish this requirement. In the generic CSD term is contained, in fact, the phase difference between pairs of control channels recordings spectra. These phase profiles cannot be independently set in case all the pairs are fully coherent. In Fig. 12.2 three control channels (1, 2 and 3) are taken as example: setting the phases ϕ_{12} and ϕ_{13} means to set a *relative constraint* in the phase information carried by the recorded signals, i.e. that between control 1 and 2 and control 2 and 3 there are phase shifts of ϕ_{12} and ϕ_{13}, respectively. Thus the phase shift between the control channels 2 and 3 is unequivocally defined as the difference between ϕ_{13} and ϕ_{12}. Following this principle, in case of fully coherent control pairs, the user can independently set the $\ell - 1$ element of the first row (but the same could be done by picking other elements) and automatically retrieve the remaining phases by using the first row as a *phase pivot*

$$\phi_{i,j} = \phi_{1,j} - \phi_{1,i} \tag{12.9}$$

To notice that, by following the phase pivoting principle, Eq. (12.7) returns always the conditions (12.8) and a positive semi-definite matrix could then always easily be obtained by choosing an appropriate coherences set. Then to obtain a positive semi-definite reference target for the three control channels case is sufficient to set two phases and two coherences and then retrieve the third phase with the relation (12.9) and the third coherence in the interval defined by (12.8). An extension to the general $\ell \times \ell$ reference matrix is not straightforward because on top of the condition (12.7), $\ell(\ell - 3)/2 + 1$ additional conditions need to be included to get allowable coherence boundaries These will be given, according to (c), by the $\ell - 2$ remaining determinants. Even if a mathematical proof is still pending, in case all the control channels are fully coherent, the phase pivoting method has been proven via simulation to always lead to a physically realisable reference matrix. This can be intuitively explained by noticing that, on top of any mathematical demonstration, there is a physical consideration driving the choice of the phases between control channels.

12.3.2 Eigenvalues Substitution

According to the property (a), in case the phase and coherence profiles filled in the MIMO reference matrix will result in a non positive semi-definite matrix, it means that the eigendecomposition

$$\mathbf{S}_{\mathbf{yy}}^{\mathbf{ref}} = \mathbf{Q}\boldsymbol{\Lambda}\mathbf{Q}^H \tag{12.10}$$

will return some eigenvalues that are negative in the frequency band of interest [9]. A quick solution would then be to force this matrix to be positive semi-definite substituting the negative eigenvalues with semi-positive ones.

$$\mathbf{S}_{\mathbf{yy\ new}}^{\mathbf{ref}} = \mathbf{Q}\hat{\boldsymbol{\Lambda}}\mathbf{Q}^H \tag{12.11}$$

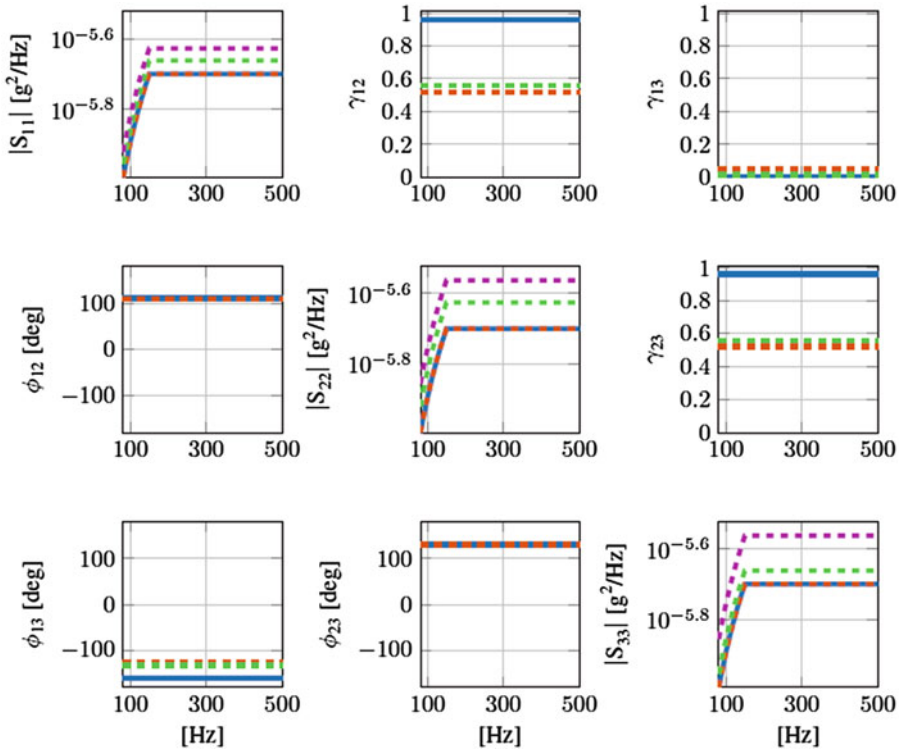

Fig. 12.3 Negative definite reference matrix (*solid blue*), positive semi-definite matrix obtained by substituting the negative eigenvalues with zero (*dashed green*) and its absolute value (*dashed magenta*). Positive semi-definite reference matrix obtained from the *dashed magenta curves* by further replacing the PSDs with the required levels (*dashed red*)

where $\hat{\mathbf{\Lambda}}$ is obtained from $\mathbf{\Lambda}$ by replacing the negative eigenvalues. This operation would however corrupt the PSD levels that the user wants to achieve. In this sense, a minimal modification from the original matrix would be given by replacing with zeros the negative eigenvalues, paying a rank loss equal to the number of original negative eigenvalues. Another option to preserve the rank of the original matrix would be replace the negative eigenvalues with their absolute value. Regardless of any rank-related consideration, the strong limitation of this procedure is that after having modified the eigenvalues, the newly defined reference matrix has diagonal terms that differ from the starting ones. The only option available would be to replace the PSD values with the original reference PSD levels and check if the matrix is still positive semi-definite. If this is not the case, the process can be repeated but the convergence to a positive semi-definite matrix is not guaranteed. In Fig. 12.3 it is shown an application example of the proposed procedure. In the figure the blue curve represents a target obtained by randomly selecting values of coherences and phases between the control channels. The matrix is non positive semi-definite as shown from in Fig. 12.4 where an eigenvalue is negative in the whole frequency range. The green and magenta curves represent the modified matrix by substituting the negative eigenvalue with a zero and its absolute value, respectively. It is worth to notice that substituting the eigenvalue with a zero means a minimal modification to the original matrix. This can be seen in Fig. 12.3 where the green levels are closer to the original target, compared with the magenta ones. However after substituting the PSD values with the required levels, only the substitution with the absolute value brings to a positive semi-definite target. This is shown in Fig. 12.4 where one the dashed green curve is negative in the whole frequency bandwidth.

12.3.3 Smallwood's Extreme Inputs Method

A possible method to derive a Minimum (Maximum) Drives Target has been proposed by Smallwood in [5] and has been referenced as possible method do define the MIMO Random reference matrix in the US Multi-Exciter Test tailoring [1]. The idea of the Smallwood's *Extreme Inputs Method* is to find, with fixed PSD levels, the set of coherences and phases between the control channels that minimize the trace of the drives SDM, i.e.

$$\text{given} \quad \boxed{diag(\mathbf{S}_{yy}^{ref})} \quad \text{find} \quad \boxed{\mathbf{S}_{yy}^{ref}} \quad \text{so that} \quad \boxed{Tr(\mathbf{S}_{uu} = \mathbf{Z}\mathbf{S}_{yy}^{ref}\mathbf{Z}^H)} \quad \text{is minimum/maximum}$$

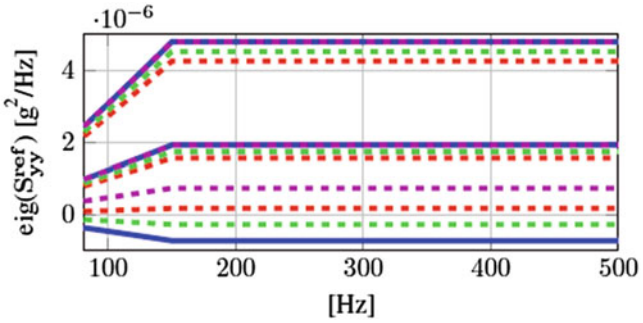

Fig. 12.4 Eigenvalues of the matrices represented in Fig. 12.3. The *dashed green curve* refers to the reference matrix obtained by replacing the original negative eigenvalue with a zero and further replacing the PSDs with the required levels

By considering the basic equations for a linear time invariant system

$$\mathbf{S}_{yy}^{ref} = \mathbf{H}\mathbf{S}_{uu}\mathbf{H}^H \tag{12.12}$$

$$\mathbf{S}_{uu} = \mathbf{Z}\mathbf{S}_{yy}\mathbf{Z}^H \tag{12.13}$$

it is possible to write the diagonal terms of Eq. (12.13) as

$$S_{uu,ii} = \sum_{j=1}^{\ell}\sum_{k=1}^{\ell} Z_{jk} S_{yy,jk} \bar{Z}_{ik} \qquad \forall i = 1:m \tag{12.14}$$

The trace of the drives SDM is the sum of the diagonal terms

$$P \triangleq Tr(S_{uu,ii}) = \sum_{i=1}^{m}\left(\sum_{j=1}^{\ell}\sum_{k=1}^{\ell} Z_{jk} S_{yy,jk} \bar{Z}_{ik}\right) = \sum_{j=1}^{\ell}\sum_{k=1}^{\ell} S_{yy,jk} \sum_{i=1}^{m} Z_{jk} \bar{Z}_{ik} \tag{12.15}$$

By defining the hermitian matrix $\mathbf{F} \triangleq \mathbf{Z}^H\mathbf{Z}$ and noticing that $\mathbf{S}_{yy}^{ref}$ needs to be hermitian too, Eq. (12.15) can be rewritten as

$$\begin{aligned} P &= \sum_{j=1}^{\ell} S_{yy,jj} F_{jj} + 2\sum_{j=1}^{\ell-1}\sum_{i=k+1}^{\ell} |S_{yy,ji}||F_{ji}|\cos(\phi_{ji} - \theta_{ji}) \\ [-3pt] &= \sum_{j=1}^{\ell} S_{yy,jj} F_{jj} + 2\sum_{j=1}^{\ell-1}\sum_{i=k+1}^{\ell} \gamma_{ji}\sqrt{(S_{yy,j} S_{yy,i})}|F_{ji}|\cos(\phi_{ji} - \theta_{ji}) \end{aligned} \tag{12.16}$$

where ϕ_{ji} and θ_{ji} are the phase angles (in radians) of the ji-th off-diagonal terms of $\mathbf{S}_{yy}^{ref}$ and $\mathbf{F}$, respectively. Since the PSD terms are fixed, for a given structure, the first term on the right hand side of Eq. (12.16) is always positive and fixed. The second term contains the unknown quantities ϕ_{ji} and γ_{ji}, and can be negative because of the cosines contained in the double sum. The theoretical minimum (maximum) trace, as pointed out in [5], is obtained when the second term is minimum (maximum), i.e. when the coherences are unitary and the cosines all equal -1 (1). This observation leads to the following conditions that guarantee the theoretical minimum (maximum) drive traces

$$P \text{ is minimum} \iff \begin{cases} \gamma_{ji} = 1 \\ \phi_{ji} = \theta_{ji} + \pi \end{cases} \tag{12.17a}$$

$$P \text{ is maximum} \iff \begin{cases} \gamma_{ji} = 1 \\ \phi_{ji} = \theta_{ji} \end{cases} \tag{12.17b}$$

All the other possible combinations of coherences and phases will return drive traces that fall in the range between the minimum and the maximum value.

12.4 Test Cases

The methods illustrated in Sect. 12.3 have been tested using the Siemens LMS Multi-Axis Random Vibration Control. As unit under test the Siemens LMS FRF BOX hardware has been used. The hardware is an electro-mechanic system with up to 4 tunable resonances, 4 drives and 4 output channels. It is the best first step testing scenario since it does not require any instrumentation and various multi-input test configurations can be easily reproduced without the need of having access to a multi-axial shaker or to connect multiple shakers to a specimen.

12.4.1 Application of the Extreme Inputs Method

As first application case the Extreme Inputs Method has been tested with 2 control channels and using 2 drives (2×2 system). For this system, illustrated in Fig. 12.5, the Minimum (Maximum) Drives Targets are the ones shown in Fig. 12.6.

According to the Extreme Inputs Method, the coherence between pairs of control channels is always unitary and thus, every 2-controls reference matrix retrieved by the method is always positive semi-definite. This allows to run an actual test by setting the matrices as test targets. The control results for the reference matrix of Fig. 12.6 at the 0 dB level are shown in Fig. 12.7. The corresponding drive traces are shown with drive traces of other possible combination of coherences and phases between the control channels. As illustrated in Fig. 12.8, all the curves in fall in the range between the minimum and the maximum drive traces, as expected.

Despite this encouraging result, unfortunately the extreme input method cannot be used to fill in a general $\ell \times \ell$ matrix.

In fact, although the conditions (12.17) will generally return hermitian targets with the minimum/maximum drive traces, they do not guarantee that these matrices will also be positive semi-definite, since this general hypothesis is never taken into account in the conditions (12.17) mathematical derivation.

This limitation could be better shown by looking at the theoretical drive traces in Fig. 12.9, obtained for a 4×4 system. In this plot, in logarithmic scale, the minimum drive trace assumes negative values in the bands [200–315] Hz and [410–1024] Hz. According to the condition (d) this is sufficient to state that some eigenvalues are negative that the reference matrix is not positive semi-definite. To derive the condition (12.17a), in fact, all the second terms in the double summation of Eq. (12.16) are forced to assume the biggest possible negative values (unitary coherences and cosines equal to -1) and eventually overcome in module the first term in the right hand side (fixed and defined by the reference PSDs and the system

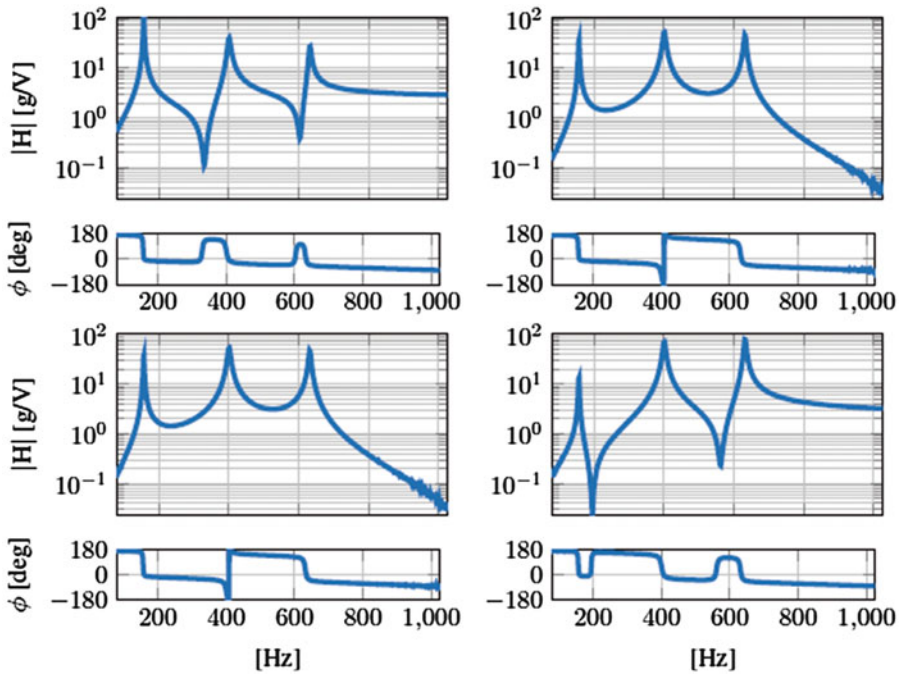

Fig. 12.5 FRF matrix of the 2×2 system

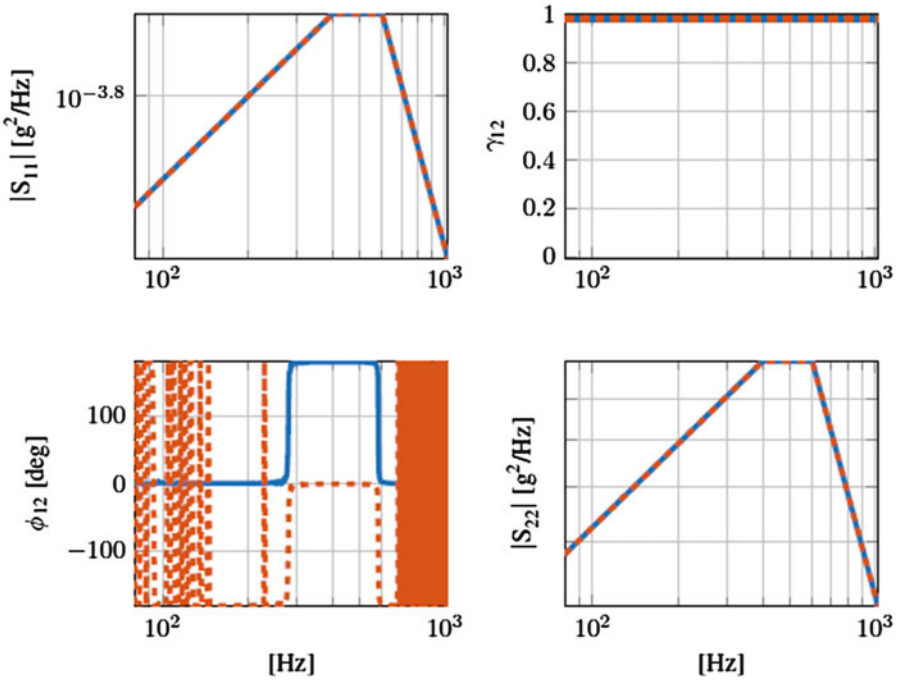

Fig. 12.6 Minimum (*solid blue*) and maximum (*dash red*) drives references for the system of Fig. 12.5

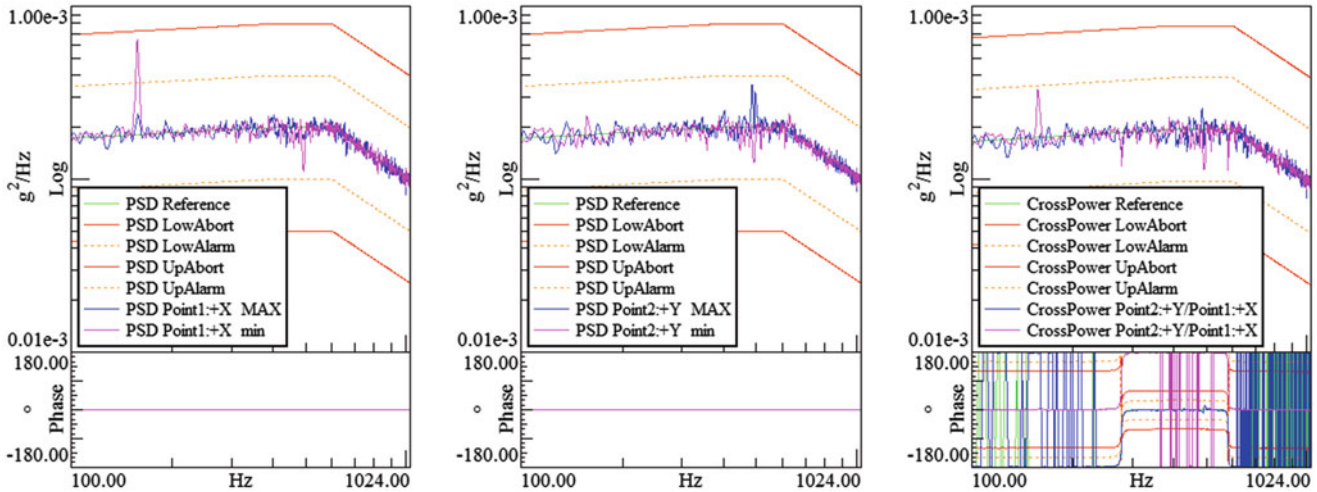

Fig. 12.7 Control results for the Extreme Inputs Target of Fig. 12.6

FRFs). This will force the resulting drives SDM to be non positive semi-definite and this property will be inherited by the reference SDM, according to the condition (f).

The matrix obtained via the application of the method cannot be used to run an actual test because is not physically realisable.

An additional observation can be made on the phases between the control channels. According to the Extreme Inputs Method these phases are derived from the phases of the matrix $\mathbf{F} = \mathbf{Z}^H\mathbf{Z}$ and thus they are not necessary following the principle explained in Sect. 12.3.1, which should hold since the conditions (12.17) impose also that the control channel recordings must be fully coherent.

Starting from these observation a procedure obtained modifying the Extreme Inputs Method in order to a physically realisable target has been implemented.

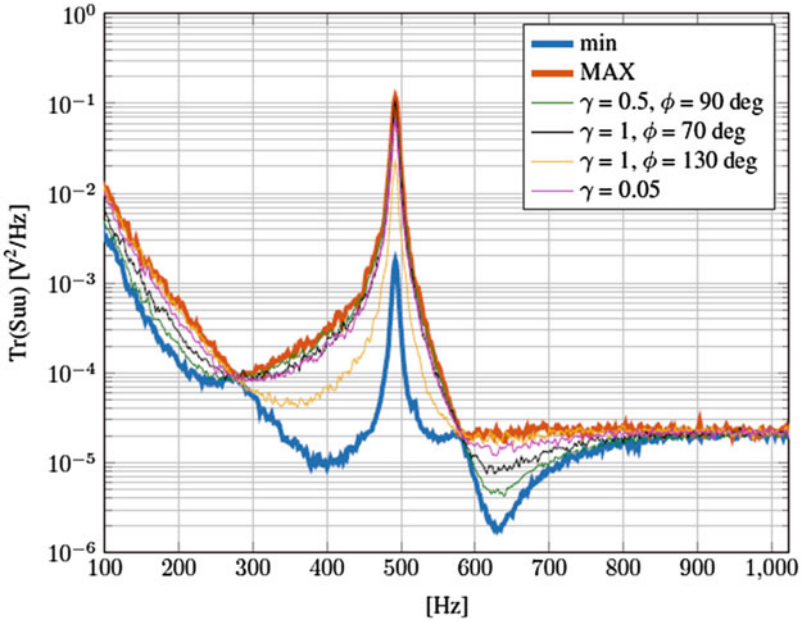

Fig. 12.8 Drives traces for different references for the 2 by 2 system of Fig. 12.5

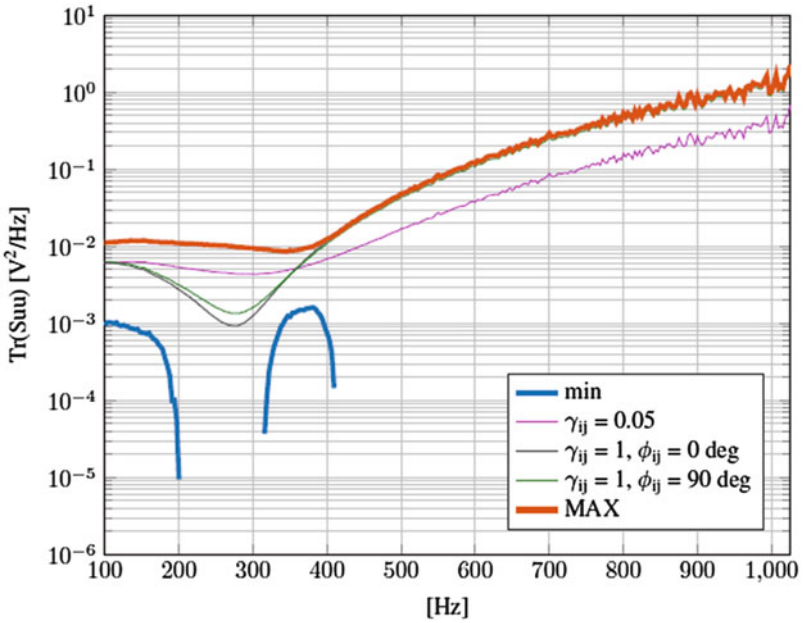

Fig. 12.9 Theoretical drive traces for a 4 × 4 system

12.4.2 Modified Extreme Inputs Method

A positive semi-definite target can be obtained starting from the Extreme Inputs Method and applying the principle explained in Sect. 12.3.1. The system studied has 3 controls and 3 drives; the FRF matrix is shown in Fig. 12.10.

The positive semi-definite matrix illustrated in Fig. 12.11 can be obtained choosing as phase pivot the phases of the first row coming from the application of the Extreme Inputs Method. Such a matrix will be positive semi-definite, as pointed out in Sect. 12.3.1 because the phases are obtained according to the relation (12.9) and the control channels are fully coherent. The condition (12.7) is thus fulfilled.

As pointed out in Sect. 12.4.1, the direct application of the Extreme Inputs Method will return a reference matrix that is not positive semi-definite, as shown in Fig. 12.12 where one of the matrix eigenvalues is negative in the whole bandwidth.

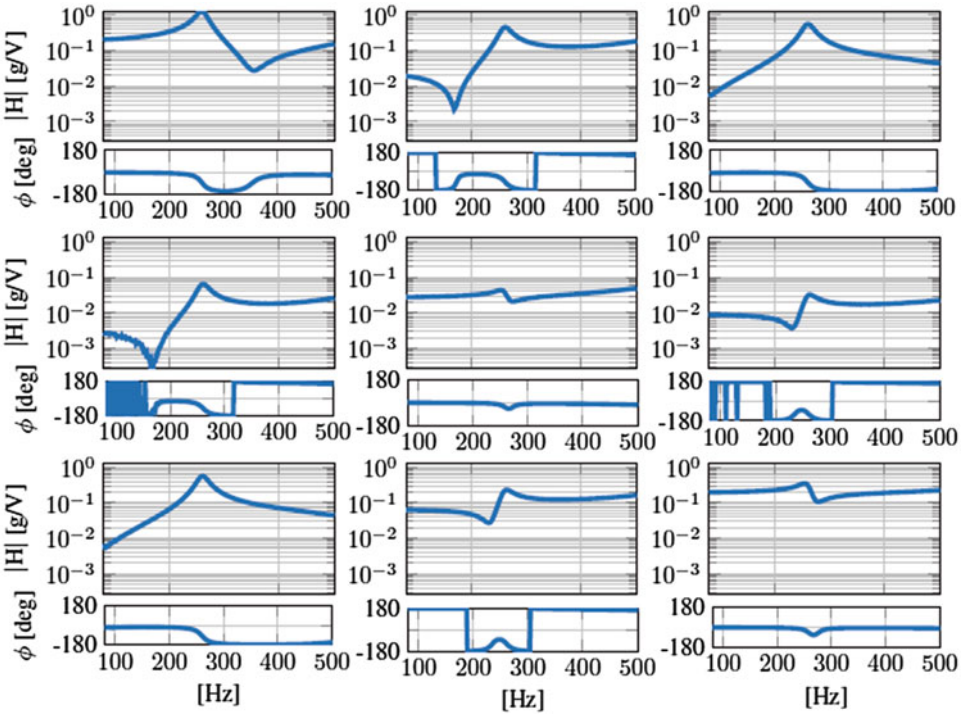

Fig. 12.10 FRF matrix of the 3 × 3 system

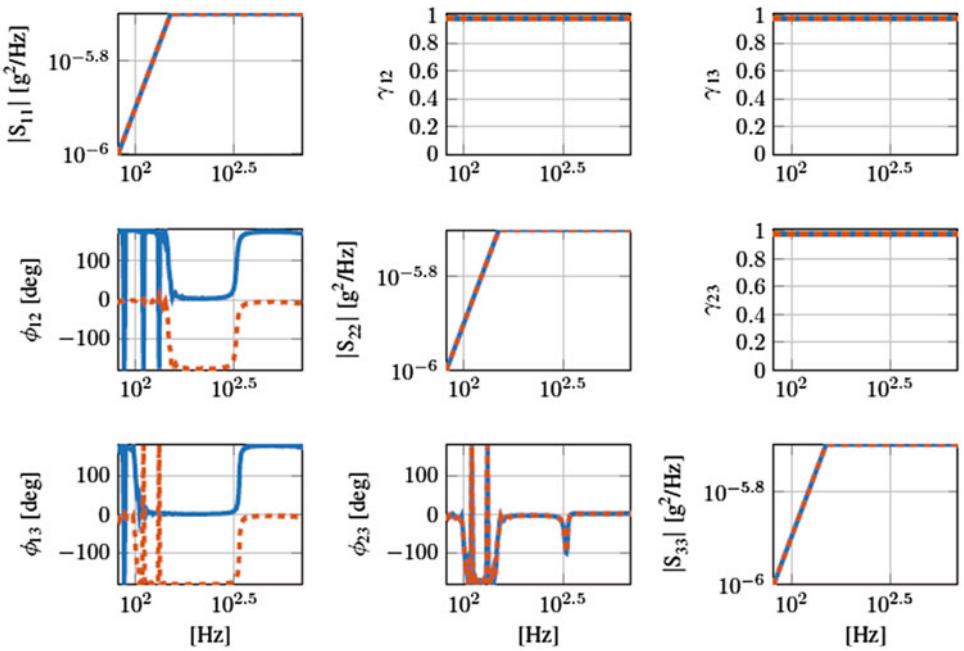

Fig. 12.11 Modified minimum (*solid blue*) and maximum (*dash red*) drives references for the system of Fig. 12.10

The reference matrix in Fig. 12.11 has been used as target of an actual MIMO Random Vibration Control test. The control results in terms of PSDs and CSDs, are shown in Figs. 12.13 and 12.14, respectively.

To demonstrate that the phase pivoting method returns a positive semi-definite matrix also in the general $\ell-$dimensional case, an extra control has been added to the configuration used. The additional PSD profile has been chosen identical to the ones previously considered and high coherence has been set between the additional control channel and the remaining ones. The reference matrix can be easily built by including the additional phases information of Fig. 12.15, obtained considering also ϕ_{14} from the Extreme Inputs Method and using again the first row as a phase pivot.

The resultant reference matrix is positive semi-definite and can be used to run an actual test.

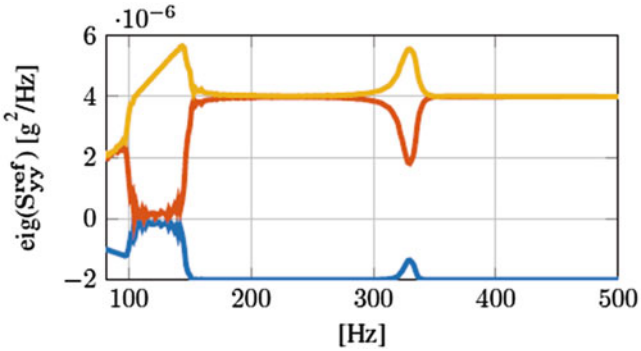

Fig. 12.12 Eigenvalues of $\mathbf{S}_{yy}^{ref}$ retrieved applying the Extreme Inputs Method to the system of Fig. 12.10

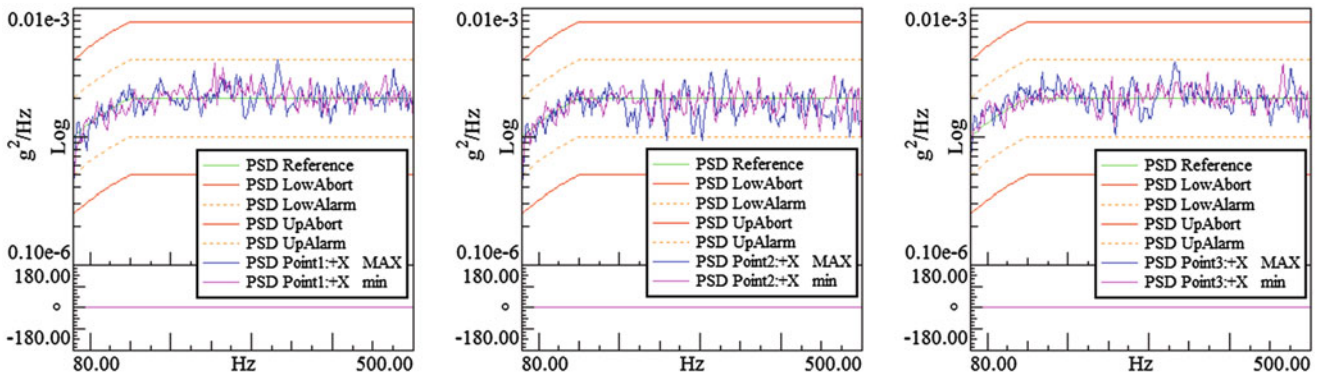

Fig. 12.13 Control results for the target obtained via the Modified Extreme Inputs Method (3 × 3 system), PSDs

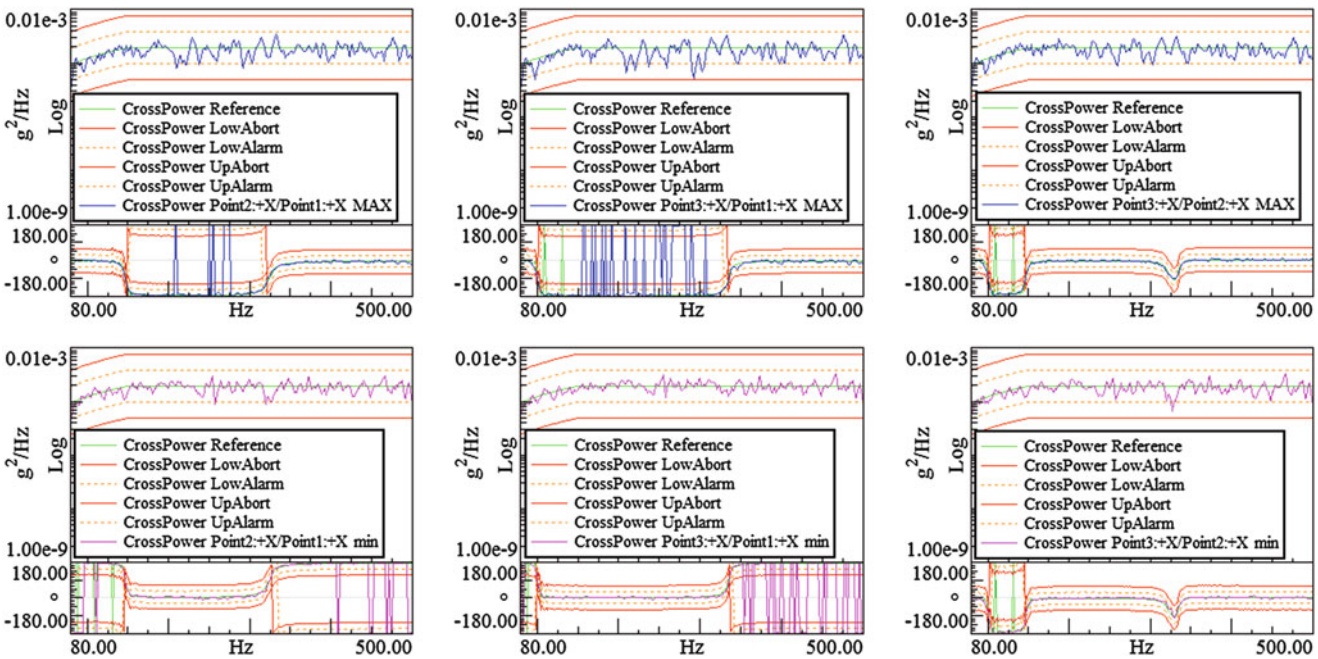

Fig. 12.14 Control results for the target obtained via the Modified Extreme Inputs Method (3 × 3 system), CSDs

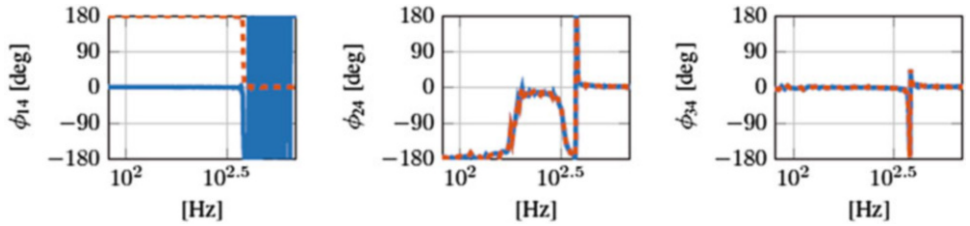

Fig. 12.15 Relative phases between control 4 and control 1,2,3 obtained modifying the Minimum (*solid blue*) and Maximum (*dash red*) Drives Targets (4 × 4 system)

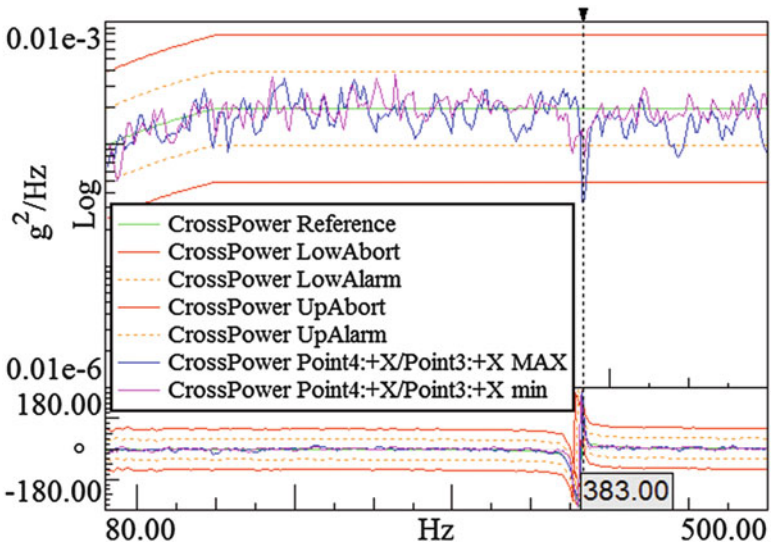

Fig. 12.16 Control results for the target obtained via the Modified Extreme Inputs Method (4 × 4 system), CSD between control channels 3 and 4

Even if the test results show good control performances, the presence of few cross-terms spectral lines out of the alarm limits (an example in Fig. 12.16) shows that the target is not optimal for the MIMO random control test, even if it is physically realisable. A physical interpretation of this behaviour is not straightforward due to the test set-up. Moreover, the targets defined with the modified Extreme Inputs Method do not return minimum and maximum drive traces. A reformulation of the whole problem is needed to tackle this attractive challenge.

12.5 Conclusions

This work aims to find a general solution to one of the challenging questions behind the multi-axial Random Vibration Control tests: how to fill in the full MIMO random reference matrix in case the Power Spectral Densities are fixed and known levels? Before investigating possible advanced target definition scenarios, there is the need to guarantee that the operation of filling in element by element the off-diagonal terms will return a matrix that has a physical meaning. This is translated in the algebraic requirement that the reference spectral density matrix must be positive semi-definite. As first solution, is possible to force the matrix to be positive semi-definite, replacing the negative eigenvalues. However this operation will not guarantee that the resulting PSDs will match the given levels. With respect to this problem, the Extreme Inputs Method, proposed by Smallwood, is able to return a full reference matrix with the given PSD levels and add the additional attractive feature to be able to return the target matrices that minimize (maximize) the drive traces. However the method, which needs the responses to be fully coherent, does not always return positive semi-definite reference matrices. Nevertheless, in case of fully coherent responses, the *phase pivoting* method can be used to obtain positive semi-definite reference matrices, as shown modifying the Extreme Inputs Method for three and four control channels. In case of three control channels the algebraic demonstration of what has been shown via tests, is also available. In this particular case, also a generalization to a set of meaningful coherences can be derived. The promising results achieved in this work leave room to further proceed in improving and combining the

proposed methodologies toward more advanced MIMO Random Vibration Control target definition procedures. First of all, the method needs to be able to return an optimal target for control by including, in the defined target, information derived from the system FRFs. Subsequently, focus can be given to the attractive possibility of enhancing the available methods to obtain a physically realisable target that minimizes (maximizes) the drives power required.

Acknowledgements The financial support of VLAIO is gratefully acknowledged (research grant *ADVENT*: ADvanced Vibration ENvironmental Testing).

References

1. United States Standard 810G: Method 527.1: multi-exciter tests (2008)
2. Underwood, M., Ayres, R., Keller, T.: Filling in the MIMO matrix Part 1 - performing random tests using field data. Sound Vib. (2011)
3. Daborn, P.M., Ind, P.R., Ewins, D.J.: Enhanced ground vibration testing for aerodynamic environments. Mech. Syst. Signal Process. **49**, 165–180 (2014)
4. Daborn, P.M., Ind, P.R., Ewins, D.J.: Next-generation random vibration tests. Topics Modal Anal. II **8**, 397–410 (2014)
5. Smallwood, D.O.: Multiple-input multiple-output (MIMO) linear system extreme inputs/outputs. Shock. Vib. **14**(2), 107 (2007)
6. Peeters, B., Debille, J.: Multiple-input-multiple-output random vibration control: theory and practice. Proc. Int. Conf. Noise Vib. Eng. **1**, 507–516 (2002)
7. Smallwood, D.O.: Multiple shaker random vibration control - an update. In: Proceedings of Institute of Environmental Sciences and Technology (1999)
8. Underwood, M.: Multi-exciter testing applications, theory and practice. In: Proceedings of Institute of Environmental Sciences and Technology (2002)
9. Meyer, C.D.: Matrix Analysis and Applied Linear Algebra. Society for Industrial and Applied Mathematics, Philadelphia (2000)
10. Golub, G.H., van Loan, C.: Matrix Computation. The Johns Hopkins University Press, Baltimore (1996)

Chapter 13
Material Characterization of Self-Sensing 3D Printed Parts

Derya Z. Tansel, Jennifer A. Yasui, Benjamin J. Katko, Alexandria N. Marchi, and Adam J. Wachtor

Abstract Additive manufacturing has seen a resurgence in recent years, mainly driven by its ability to produce parts with complex designs and incorporate multiple components into a single manufactured part. However, additive manufacturing still needs improvements to fabricate consistent and reliable parts. Some of the shortcomings of the process include the effects of build orientation on the material properties. Current structural health monitoring methods, such as visual photography and thermography, provide limited data to quantify the quality and reliability of printed part. In this study, 3D printed novel sensors were embedded within a part and were evaluated as an alternative method for structural health monitoring. The embedded sensors were composed of conductive filament and are intended as a non-intrusive method to monitor the structural health of the part during its service life. Filaments using novel materials, e.g. conductive polylactic acid, were evaluated for their material characteristics and suitability for sensor verification and validation. Specifically, the novel conductive filaments were evaluated for their performance in terms of mechanical and electrical properties. The Young's modulus of the additively manufactured, polylactic acid part was determined by both tensile testing and cantilever testing; and temperature sensitivity was determined by resistance measurements during thermal cycling. Embedding of the sensor into the service part during the printing process can reduce the cost and production time for structural health monitoring and provide a new application area for additive manufacturing.

Keywords Strain gauge • Fused deposition modeling • Structural health monitoring • Conductive filament • Embedded sensors • Polylactic acid

13.1 Introduction

Additive manufacturing (AM) is used to produce parts by laying down successive layers of material to form a 3D shape specified from a computer-aided design (CAD) model. Additive manufacturing was initially developed for prototype production; however, its ability to produce complex parts in an efficient and time-effective manner quickly streamlined its resurgence in recent years [1]. The versatile build material options (e.g., ceramics, polymers, metal alloys) and customization of AM allows for applications over a wide range of fields including engineering, medicine, aerospace, and aeronautical engineering [1]. Fused deposition modeling (FDM) is a type of AM that extrudes material layer by layer to create thermoplastic parts [2]. The process of FDM begins by slicing a CAD model into layers stacked on each other, with the

D.Z. Tansel
Department of Electrical Engineering, University of Florida, Gainesville, FL 32611, USA
e-mail: derya.tansel@gmail.com

J.A. Yasui
Department of Civil Engineering, University of Southern California, Los Angeles, CA 90089, USA
e-mail: jyasui@usc.edu

B.J. Katko
Department of Mechanical Engineering, New Mexico Institute of Mining and Technology, Socorro, NM 87801, USA
e-mail: katko.ben@gmail.com

A.N. Marchi
Materials Physics and Applications, Los Alamos National Laboratory, Los Alamos, NM 87545, USA
e-mail: amarchi@lanl.gov

A.J. Wachtor (✉)
Applied Engineering and Technology, Los Alamos National Laboratory, Los Alamos, NM 87545, USA
e-mail: ajw@lanl.gov

N. Dervilis (ed.), *Special Topics in Structural Dynamics, Volume 6*, Conference Proceedings
of the Society for Experimental Mechanics Series, DOI 10.1007/978-3-319-53841-9_13

thickness of the layers specified by the user, and developing a path to produce each layer of the product. The combination of the extruder parameters (e.g., nozzle temperature, print speed, layer height, etc.) and bed temperature allow each successive layer to be partially fused together to yield one solid product. FDM provides the user the freedom to specify the filament along with the print parameters used throughout the production of the part. However, the print is susceptible to failure from inconsistencies within the filament, uneven bed temperature distribution, inconsistent extrusion of the material, as well as poor orientation of the part. Another shortcoming of AM is the variations in the quality of the parts produced by different printers.

Structural health monitoring (SHM) aims to provide insight into the state of a structure throughout its service life [3]; therefore, sensor data from the part is needed for SHM. Embedding a sensor within the part can result in data that better represents the characteristics of the material itself and not the environmental factors that would affect the sensor's condition [1, 4].

Embedded sensors can provide reliable data from within a material; however, their use for SHM is challenging [4]. Some of the challenges of using embedded sensors for SHM include presence of the sensor itself, which may affect the behavior of the material surrounding it in the part [4]. In addition, embedding a commercial sensor in an AM part increases the manufacturing time and necessary control, as the 3D printing process must be paused to embed the sensor. Some methods to resolve these issues include visual photography and thermography, which provide limited data on the quality of the part.

The objective of this study was to use the FDM process to print polylactic acid (PLA) with embedded sensors printed from conductive PLA. However, since material properties of AM parts can vary based on the printer used, print parameters, and environmental conditions, experiments were conducted to measure the material properties of PLA and conductive PLA for experimental setup described below to demonstrate the development of an AM sensor which may ultimately be used for SHM.

13.2 Materials and Methods

13.2.1 3D printing of the Embedded Sensors

The 3D printing of the parts and the sensors were performed with a LulzBot TAZ 5 printer which was upgraded with a LulzBot TAZ Dual Extruder Tool Head v2 (Fig. 13.1a). Painter's tape was applied to the print bed to enhance adhesion during the build process. Strain gages (C2A-06-125LW-350) were acquired from Vishay Precision Group (Northvale, NJ). Embedded sensors were printed using PLA and conductive PLA. In-PLA PLAdium Natural filament (2.85 mm diameter) was purchased from Taulman3D (Saint Peters, MO) and black conductive PLA filament (2.85 mm diameter) was purchased from Proto-Pasta (Vancouver, WA). Conductive PLA is composed of Natureworks 4043D PLA, a dispersant, and conductive carbon black [5].

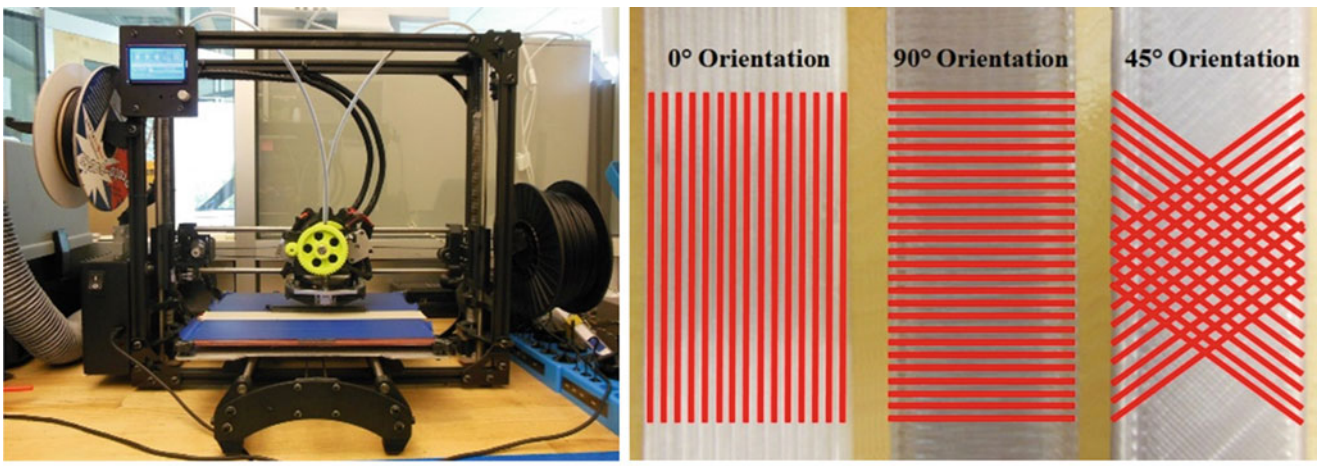

Fig. 13.1 Experimental setup: (**a**) 3D printer setup, (**b**) Print orientations used during the testing

Table 13.1 Print parameters used to print the specimens

Parameter	Test setting
Filament diameter	2.85 mm
Infill	50% and 75%
Layer height	0.5 mm
Layer thickness	0.5 mm
Nozzle diameter	0.5 mm
Nozzle temperature	215°C
Perimeter thickness	1.0 × 1.5 mm
Print bed temperature	60°C
Print speed	50 mm/s

To ensure repeatability during the fabrication of specimens, the print parameters were fixed throughout the study. The print parameters used are summarized in Table 13.1. The specimens were printed at the 0°, 90°, and 45° orientations (Fig. 13.1b), where each layer for the 0° and 90° orientations were printed the same (longitudinal for 0° and transverse for 90°) and the layers for the 45° orientation switched between 45° and −45°. The purpose of testing the materials at these orientations was to satisfy the material property components of the composite laminate theory equations for the Hanshin failure criteria [6].

13.2.2 Testing of 3D Printed Sensor

Currently, there is no standard failure criterion accepted by industry designers for composites under general loading conditions [7]. Therefore, the Hanshin failure criteria are required for evaluating initial, subsequent, and final failure while the printed test specimens are under axial and bending loading. Hanshin failure criteria apply for in-plane ply failure modes and are compatible with the shells, or the outer perimeter layer, of the print specimens [6]. Therefore, the shell thickness is assumed to be a continuation of the composite ply. Through experimental testing, mechanical properties can be measured for Hanshin failure criteria evaluation of 3D printed parts. These mechanical properties include the Young's modulus (E) in the extrusion direction (E_0) and 90° from the extruded direction (E_{90}), Poisson's ratio (ν) in the 0°–90° direction (ν_{0-90}), and the in-plane shear modulus (G_{0-90}) [6]. These properties are necessary to determine the failure of fiber rupture in tension, fiber buckling and kinking in compression, matrix cracking under transverse tension and shearing, and matrix crushing under transverse compression and shearing [6]. While the Hanshin failure criteria requires mechanical properties in the 0° and 90° orientations, this study also investigates the 45° orientation since it is often the default layup in many 3D printing programs.

13.2.2.1 Electrical Properties

Temperature Sensitivity

The electrical properties of the conductive PLA were analyzed to determine the characteristic response of the printed sensors. The sensor developed was a strain gauge (referred to as a U-Gage). Fig. 13.2a presents an industry standard strain gauge (left) and the additive manufactured U-Gage (right). The filament manufacturer (Proto-Pasta) characterized the conductive PLA with a volume resistivity of 30 Ohm-cm for printed parts with perpendicular layers and a volume resistivity of 115 Ohm-cm for printed parts along the Z axis [8]. However, it was not clear under which conditions (i.e., fill density, layer thickness, orientation, other print parameters) these specifications were determined. Therefore, these characteristics were not able to be validated. Due to the lack of adequate information about the print parameters from the manufacturer, tests were conducted to determine the electrical characteristics of the conductive PLA specific to the print parameters used throughout the project.

To measure the temperature coefficient, three U-Gages were placed in a laboratory oven and their resistances were measured with respect to the change in temperature using a multimeter, as shown in Fig. 13.2b. Additionally, due to the conductive PLA being highly hygroscopic, the humidity of the testing environment was monitored throughout the tests. The oven temperature and relative humidity were measured using the Omega RH820U Humidity Temperature Meter. Resistance measurements were taken 10 minutes after the desired environment temperature was reached to ensure thermal equilibrium and the resistances of the U-Gages were stabilized. The resistances were measured during temperature increases and decreases four times to be able to monitor for a hysteresis effect.

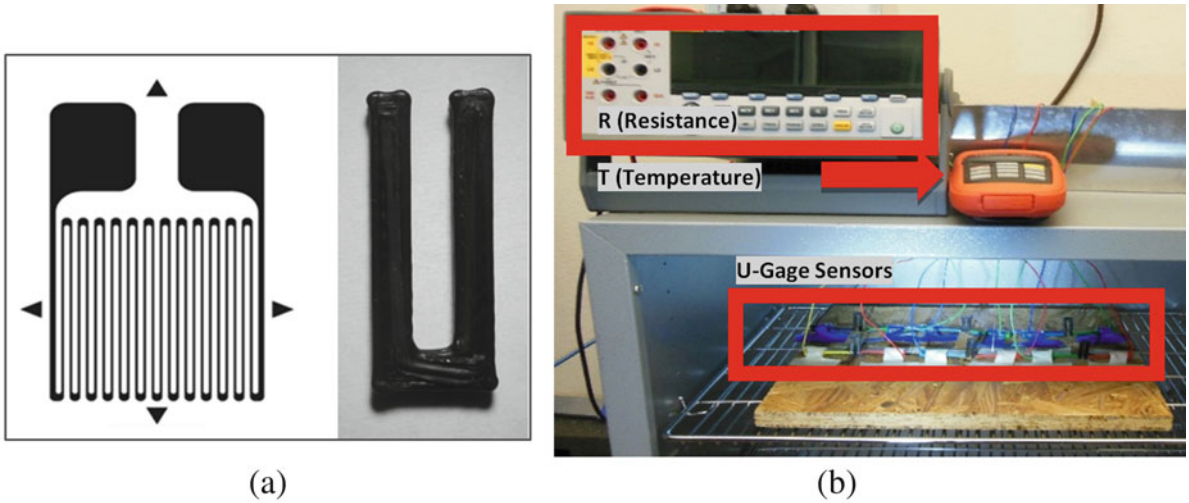

Fig. 13.2 Testing to determine the temperature coefficient: (**a**) Industry standard strain gauge (*left*) and an additive manufactured U-Gage (*right*), (**b**) Experimental setup for the temperature coefficient tests

Fig. 13.3 Tensile testing setup to determine the Young's modulus under axial loading

13.2.2.2 Mechanical Properties

Determination of Young's Modulus by Tensile Testing

Tensile tests were performed on conductive PLA coupons for sensor mechanical characterization as well as PLA coupons for the base material mechanical properties required for analyzing the Hanshin failure criteria. These tests obtain the Young's modulus under axial loading in the longitudinal and transverse directions at 50% and 75% infill. ASTM standard D3039/D3039M for polymer matrix composite materials was adhered to [9]. All tensile tests were performed on a Mark-10 test stand (Fig. 13.3), the grips for the Mark-10 test stand were of type G1061-2, and the max allowable load was 1100 N.

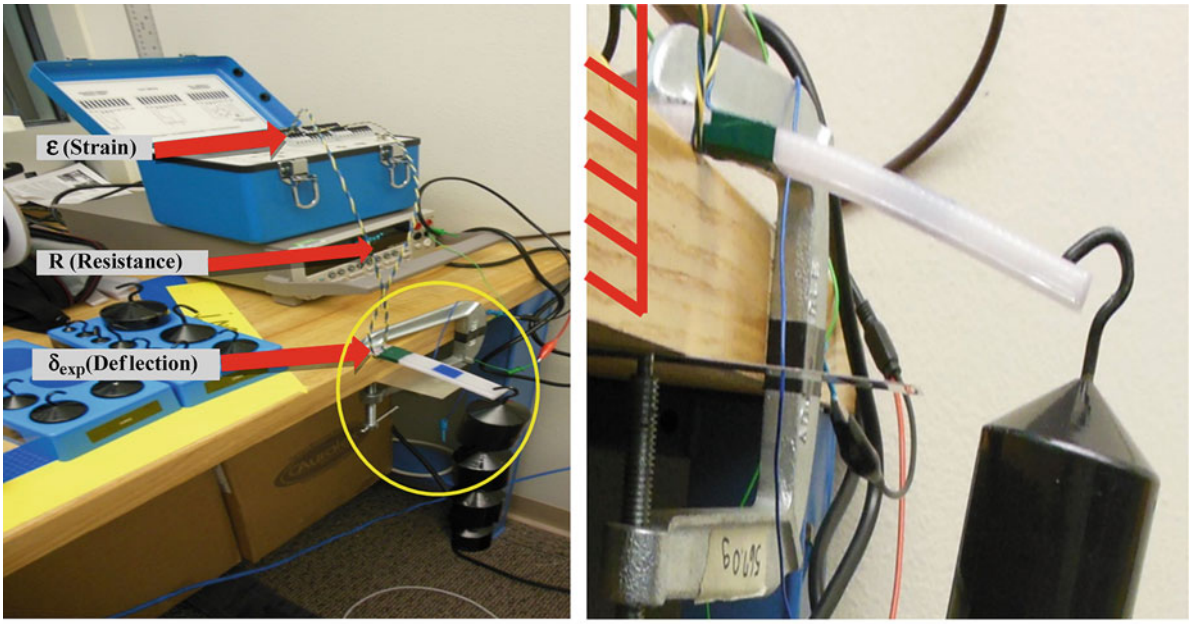

Fig. 13.4 Cantilever beam testing: (**a**) Experimental setup, (**b**) Load being applied to the beam

Determination of Young's Modulus by Cantilever Beam Testing

The Young's modulus under bending load, gauge factor, and Poisson's ratio of PLA at 50% and 75% infill was obtained from a cantilever beam experiment. At each increment of applied load, the strain, resistance, and deflection from a strain gauge was recorded with a P3 Strain Indicator (Vishay Precision Group), multimeter, and micrometer (Fig. 13.4). Two commercial strain gauges were adhered to a PLA beam specimen; these strain gauges were attached on the top and bottom of the beam as well as applied perpendicular to each other to calculate the Poisson's ratio. The CAD model of the PLA beam includes a 4 mm diameter extruded cut hole from the top of the beam, 7.75 mm away from the cantilever end. This hole serves as a consistent location for an incremental load to be applied. To ensure the Young's modulus was obtained from the elastic region of this experiment, the maximum load applied was 1 kg (9.81 N). After testing concluded, a final visual check of strain approaching zero was conducted to verify elasticity within the tested specimen.

13.3 Results and Discussions

13.3.1 Temperature Sensitivity

Experimental evaluation of the electrical properties of the U-Gage showed that the resistance increased with increasing temperature and generally followed a similar path as the temperature decreased (Fig. 13.5a). It should be noted, that Fig. 13.5a represents the data collected for 1 run (i.e., increasing and decreasing the temperature). The other three runs showed similar results. The temperature coefficient was used to quantify the sensitivity of the conductive PLA to temperature using the following equation [10]:

$$R = R_0 \left[1 + a \left(T - T_0\right)\right], \tag{13.1}$$

where R is resistance at temperature T in ohms, R_0 is the resistance at T_0 in ohms, a is the temperature coefficient in units of 1/°C, T is temperature in °C, T_0 is the reference temperature in °C.

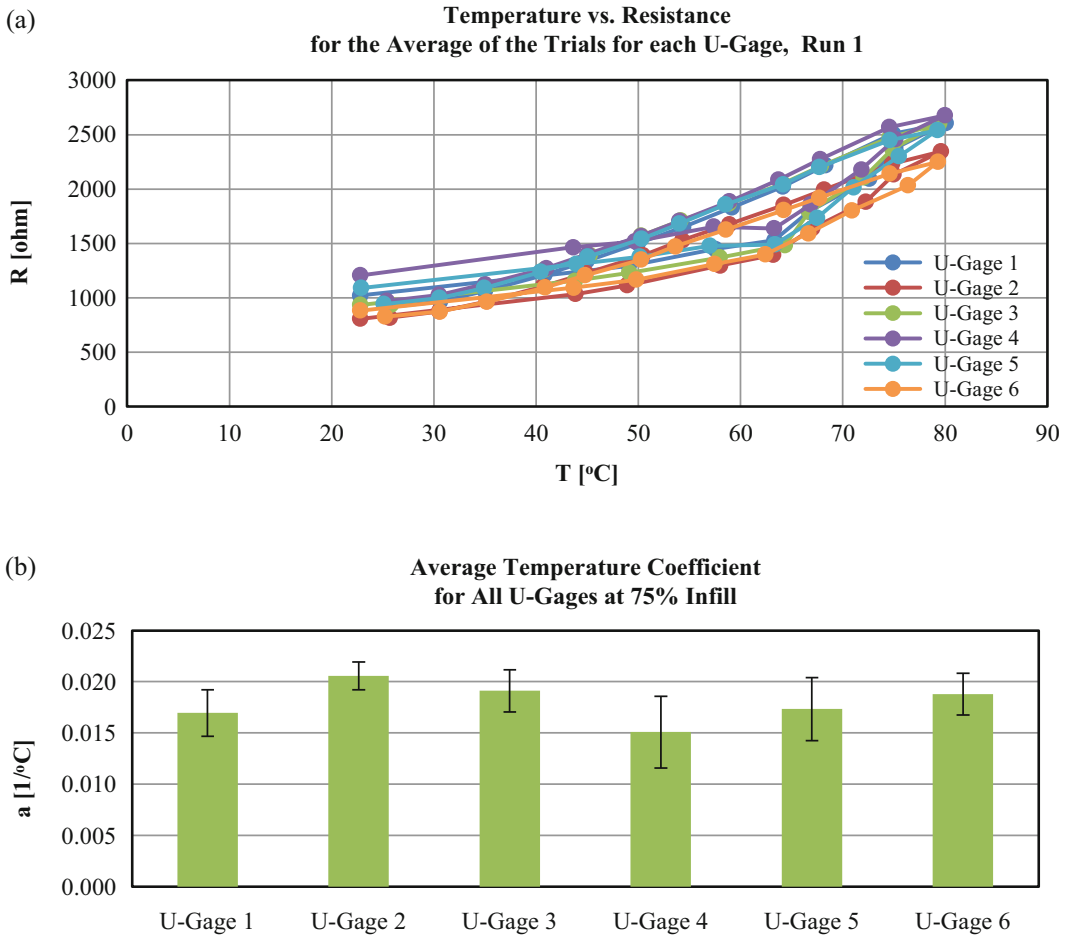

Fig. 13.5 Temperature sensitivity of the U-Gage: (**a**) Change in resistance with increasing and decreasing the temperature, (**b**) Average temperature coefficient of the U-Gage determined from the experiments

Table 13.2 Comparison of the temperature coefficient of conductive PLA with other conductive materials

Material	a (1/°C)
Conductive PLA	0.0179 ± 0.00239
Nickel [11]	0.005866
Copper [11]	0.004041
Zinc [11]	0.003847

Although the general trend of the U-Gages (shown in Fig. 13.5a) did not demonstrate a linear trend with an average R^2 value of 0.8846 (for Run 1), the average temperature coefficient of the conductive PLA was determined as 0.0179 ± 0.00239 per °C (Fig. 13.5b). When compared with other conductive materials, the conductive PLA exhibited a higher sensitivity to temperature (3–5 times higher) as presented in Table 13.2. Commonly used conductive materials, such as copper, are selected based on their stability over time, their low resistance value, and their negligible temperature coefficient. However, conductive metals experience corrosion and their weight is a factor in their application. Due to the high temperature coefficient of conductive PLA, the U-gage should be limited to use in steady temperature environments. The sensitivity of the U-Gage would need to be re-calibrated when applied to a different temperature environment.

Table 13.3 Average Young's modulus under axial loading results and statistics

Material	Orientation	Infill	E (MPa)
Conductive PLA	0°	50%	390 ± 11.8
Conductive PLA	90°	50%	142 ± 7.03
PLA	0°	50%	902 ± 32.3
PLA	0°	75%	908 ± 14.4
PLA	90°	50%	276 ± 10.8
PLA	90°	75%	764 ± 12.2

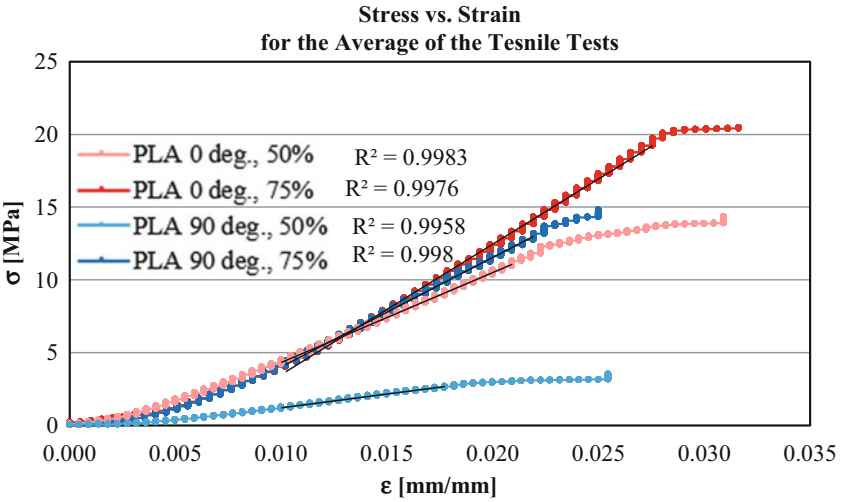

Fig. 13.6 Young's modulus under axial loading: Stress-strain relationship of PLA

13.3.2 Mechanical properties

13.3.2.1 Tensile Test Results

Young's modulus was calculated from the slope of the stress-strain curve in the elastic region from the tensile test data using Hooke's Law [12]:

$$E = \frac{\sigma}{\varepsilon}, \tag{13.2}$$

where E is Young's Modulus in Pascals, σ is stress in Pascals, and ε is strain in mm/mm.

The results of the tensile tests for conductive PLA and PLA are summarized in Table 13.3. From Fig. 13.6, the stress and strain are plotted for the PLA at 50% and 75% infill; a linear fit is applied to each stress–strain curve. Additionally, the R^2 values as shown in Fig. 13.6 are indicative of strong linear fits.

The conductive PLA coupons have a Young's modulus that is approximately two times smaller than that of their PLA counterparts printed at 50% infill. The smaller Young's modulus for these specimens indicates the conductive PLA prints were brittle compared to PLA prints. Conductive PLA's brittle behavior may be attributed to the carbon black dispersed in the PLA.

The PLA coupons printed at 0° have approximately the same Young's modulus at the two infills tested. This phenomenon most likely occurred because the individual fibers are aligned with the axial load, thus the infill doesn't seem to have a significant effect on the Young's modulus for the 0° orientation. This also explains why the 0° coupons are globally stiffer compared to the 90°, as the 90° coupons are transverse to the axial load and the individual fibers are subject to de-bonding during testing which globally makes the coupon less stiff. Additionally, the infill significantly affects the Young's modulus of the 90° coupons. For the 90° coupons, the Young's modulus at 75% is almost three times larger than at 50%. Because the 90° coupons are transverse to the axial load, the infill greatly determines the bonding between fibers which affects the Young's modulus and global stiffness of the coupon. These results demonstrate how better adhesion through increasing infill percentage will yield a higher Young's modulus value.

13.3.2.2 Cantilever Beam Test Results

Young's modulus under bending load was obtained from the stress-strain relationship of the adhered strain gauge and applied load via Eq. (13.2). The stress can be determined from the following equation [13]:

$$\sigma = \frac{6P\,(l-x)}{wt^2}, \tag{13.3}$$

where P is the load applied, l is the length of the cantilever beam, x is the distance from the fixed end of the cantilever beam to the midpoint of the strain gage, w is the width of the beam and t is the thickness of the beam. This equation provides the stress of the beam at the center of the strain gage location.

Additionally, the beam deflection is correlated with the Young's modulus, E, by following equation [14]:

$$\delta(x) = \frac{Pa^2}{6EI}\,(3x-a)\,, \tag{13.4}$$

where δ(x) is the maximum deflection at the end of the cantilever beam in meters, P is the applied load in Newtons, x is the distance from the fixed end of the cantilever beam to the center strain gauge in meters, a is the distance from the fixed end of the cantilever beam to the applied load in meters, and I is the mass moment of inertia in m^4. By rearranging Eq. (13.4), the Young's modulus, E, can verify the Young's modulus value obtained from Eq. (13.2):

$$E = \frac{Pa^2}{6\delta_{max}I}\,(3l-a)\,. \tag{13.5}$$

The gauge factor was also calculated for validating the strain gauge with the following equation [15]:

$$GF = \frac{\Delta R}{R\varepsilon}, \tag{13.6}$$

where ΔR is the change in resistance in ohms, R is the original resistance in ohms, and ε is the strain.

Finally, Poisson's ratio, ν, was calculated by the following equation [16]:

$$\nu = \frac{-\varepsilon_t}{\varepsilon_l}, \tag{13.7}$$

where ε_t is the strain in the transverse direction (90°) and ε_l is the strain in the longitudinal direction (0°).

The results from the cantilever tests are presented Table 13.4. The Young's modulus of PLA under bending loading is three to four times more stiff than compared to the Young's modulus under axial loading, with the exception of the PLA specimen printed at 90° with 50% infill. This phenomenon occurs because the bending load response is affected by the direction at which the layers are printed. All specimens were printed flat on the print bed. When subjected to axial loading, the individual fibers experience either elongation (in the 0° orientation) or de-bonding (in the 90° orientation). However, when the specimens are subjected to bending loads, the bonds between fibers and lamina within the PLA composite laminate are affected. Locally, the individual fibers are more brittle compared to the composite laminate which is more stiff, thus explaining the difference in Young's modulus measured from the tensile tests. For the PLA specimens printed at 90° with 50% infill, the difference in Young's modulus when compared to the value obtained from axial loading is ten times larger.

Table 13.4 Summary of results from the cantilever beam tests.

Material	Orientation	Infill	E (MPa)	GF	ν
PLA	0°	50%	2973 ± 271	2.01 ± 0.184	0.234 ± 0.021
PLA	0°	75%	3292 ± 25.4	1.82 ± 0.013	0.355 ± 0.001
PLA	90°	50%	2740 ± 81.4	1.98 ± 0.138	0.233 ± 0.012
PLA	90°	75%	2612 ± 25.6	1.82 ± 0.029	0.285 ± 0.005
PLA	±45°	50%	2463 ± 165	2.31 ± 0.104	0.372 ± 0.027
PLA	±45°	75%	2631 ± 32.8	1.80 ± 0.025	0.327 ± 0.003

As mentioned earlier, the Young's modulus for the 90° specimens experiencing axial loading are significantly affected by the infill. Thus, when comparing the Young's modulus for 90° specimens under axial load and bending load, the infill is again a significant factor. However, comparing the 90° specimens experiencing bending load, the Young's modulus is relatively close to one another despite the difference in infill. Like the Young's modulus under axial loading results, the Young's modulus under bending load for the PLA specimens at 0° are more stiff amongst all specimens tested. Additionally, the Poisson's ratio for the specimens printed at 0° is higher than at $\pm 45^{o}$ and 90°, which again is explained by the local behavior of the printed layers.

The gauge factor of the attached Vishay strain gage was calculated to validate Vishay Precision Group's reported gauge factor. For the C2A-06-125LW-350 strain gage, Vishay Precision Group noted the gauge factor to be $2.16 \pm 0.5\%$ on the packaging label. The 50% infill specimens tested have a smaller gauge factor error, ranging from 6.93% to 8.13%, when compared to the 75% infill specimens error, ranging from 15.6% to 16.8%. These differences in percent errors may be attributed to the strain the specimens experience at 50% and 75% infill. At the same stresses, the 50% infill specimens experience smaller strains than at 75% infill. Since the gauge factor is based off resistance and strain, the smaller strain values from 50% infill yield a gauge factor closer to the reported Vishay Precision Group gauge factor. Additionally, these percent errors can be used compare future data collected when implementing a U-Gage sensor into a PLA printed part for cantilever testing.

13.4 Conclusions

The mechanical and thermal performance of PLA and conductive PLA were measured to characterize their performance for use as embedded sensors during 3D manufacturing. PLA and conductive PLA exhibited stable performance during repeated testing for electrical and mechanical properties.

The angle of placement of the sensor on the parts significantly affects its sensitivity. Depending on the application, sensitivity can be controlled by the orientation of the sensor. Embedding the sensor into the part during the 3D printing process may reduce the cost and production time while allowing ability to monitor the structural health of the part. Using the Hanshin criteria for the tensile parameters may have some limitations for the two materials tested. Hanshin criteria was developed for unidirectional polymeric composites, and hence, applications to other types of polymeric composites with additives may result in deviations from unidirectional properties requiring significant approximations.

The type of loading the part experiences significantly effects the stiffness of the part. In general, the conductive PLA was overall less stiff and more brittle when compared to the regular PLA. The individual fibers and composite laminate of each specimen may experience elongation or de-bonding depending on the type of loading and infill combination.

13.5 Future Work

The temperature sensitivity of the resistance is related to the difference in the coefficient of thermal expansion between the strain gauge and the material used to make the strain gauge. By conducting measurements of the coefficient of thermal expansion from a dilatometer, a more in-depth understanding of the material properties for the conductive PLA and PLA can be attained. Additionally, due to project time constraints, shear modulus testing via ASTM D3518, tensile testing of the PLA coupon printed at 45°, and tensile testing of the conductive PLA coupon printed at 75% infill were not completed. Future work will detail how the mechanical properties required by the Hanshin failure criteria can be applied to the application of the U-Gage sensor embedded into a cantilever beam.

Acknowledgments The authors gratefully acknowledge support of the research by Los Alamos National Laboratory through the Los Alamos Dynamic Summer School Program led by Charles Farrar. The authors would also like to thank members of the Applied Engineering and Technology (AET-1) team for lending and helping setup instrumentation.

References

1. Baere, D.D., Strantza, M., Hinderdael, M., Devesse, W., Guillaume, P.: Effective Structural Health Monitoring with Additive Manufacturing. Nantes, France (2014)
2. ASTM Standard F2792-12a: Standard Terminology for Additive Manufacturing Technologies. ASTM International, West Conshocken, PA (2013)

3. Balageas, D.: Introduction to structural health monitoring. In: Structural Health Monitoring, pp. 13–29. ISTE Ltd, London (2006)
4. W. Lang, D. Boll and T. Schotzko, Function Scale Integration-Embedding Sensors in Materials for Structural Health Monitoring, 6th European Workshop on Structural Health Monitoring-Th.1.A.1, pp. 1–8, (2012).
5. Conductive PLA, ProtoPasta. [Online]. Available: https://www.proto-pasta.com/pages/conductive-pla (2016). [Accessed 9 July 2016].
6. Kim, H.: Composite Laminate Modeling Using ABAQUS FEA: In-Plane Progressive Failure Analysis Using Hanshin Failure Criteria. University of California, San Diego (2014)
7. Camanho, P.P.: Failure Criteria for Fibre-Reinforced Polymer Composites. Porto, Portugal (2002)
8. Proto-Pasta Conductive PLA −3.00 mm (500 g), MatterHackers Inc. [Online]. Available: https://www.matterhackers.com/store/3d-printer-filament/proto-pasta-conductive-pla-3.00mm (2016). [Accessed 9 July 2016].
9. ASTM Standard D3039/D3039M: Standard Test Method for Tensile Properties of Polymer Matrix Composite Materials. ASTM International, West Conshohocken, PA (2014)
10. HyperPhysics, [Online]. Available: http://hyperphysics.phy-astr.gsu.edu/hbase/electric/restmp.html (2016). [Accessed 9 July 2016].
11. All About Circuits, EETech Media, LLC, [Online]. Available: http://www.allaboutcircuits.com/textbook/direct-current/chpt-12/temperature-coefficient-resistance/ (2016). [Accessed 9 July 2016].
12. Hibbeler, R.: Mechanics of Materials, 8th edn, pp. 90–91. Pearson Prentice Hall, Upper Saddle River, New Jersey (2011)
13. Bucciarelli, L.: Stresses: beams in bending. In: Engineering Mechanics for Structures, pp. 248–251. Dover Publications (2002)
14. Budynas, R.G., Young, W.C.: Roark's Formulas for Stress and Strain, 7th edn. McGraw-Hill, New York (2002)
15. Measuring Strain with Strain Gages, National Instruments, 25 May 2016. [Online]. Available: http://www.ni.com/white-paper/3642/en/ (2016). [Accessed 1 July 2016].
16. Poisson's Ratio, The Engineering ToolBox, 2016. [Online]. Available: http://www.engineeringtoolbox.com/poissons-ratio-d_1224.html. [Accessed 25 July 2016].

Chapter 14
Trajectory Tracking and Active Vibration Suppression on a Flexible Tower Crane

O.A. Garcia-Perez, G. Silva-Navarro, and J.F. Peza-Solis

Abstract This work deals with a flexible structure modeled as a tower crane, with proper servomechanisms for load manipulation. This type of flexible structure deserves popularity due to well-known advantages as high payload and large workspace. The main challenges, however, are the undesirable endogenous and exogenous vibrations attributed to typical tasks as trajectory tracking, at high speed rates, and inherent structural behavior, of tower and arm, excited by internal as external forces. The overall mechanical structure is modeled by means of finite element methods, experimental modal analysis techniques and some specific criteria are used to select the most appropriate locations of sensors and actuators. In order to attenuate these undesirable vibrations, an active tendon system is implemented, on a specific part of the structure, attaching a PZT stack actuator, on a supporting cable, to regulate its tension and to improve the effective modal damping and closed-loop stability and, as a consequence, improve the quality of the trajectory tracking and also reduce, as possible, the structural vibrations. Two active vibration control schemes are employed during the synthesis of the controller, that is, Multiple Positive Position Feedback (MPPF). Finally, the overall dynamic performance is evaluated and validated by numerical and experimental results on a small-scale mechanical platform.

Keywords Space frame flexible structure • Modal parameters • Multiple positive position feedback • PZT actuator • Vibration control

14.1 Introduction

The large-scale structural analysis has been a very active research area in the last few decades, since a wider range of applications and more demanding environmental conditions require them to improve their dynamical performance for the task at hand. The vast majority of large-scale structures are, most of the times, operating under a wide variety of different sources of dynamic perturbations and because of this, it is mandatory to condition these structures, so that, the effects of the perturbations can be coped with in order to avoid possible structural damage to these systems [1–3]. Among the main problems that have been addressed by researchers, principal attention has been paid to the vibration damping problem, since vibration phenomena are inherent to large-scale structural systems. Most of the large-scale structures are designed in such a way that they are capable to endure the stresses due to loading conditions required by their tasks. However, there are mobile structures that operate not only under very demanding loading conditions but are also structurally affected by the inertial effects due to their motion within their workspaces. Such is the case of flexible-link manipulators and tower cranes among other systems. Over time, tower cranes with larger workspace spans and faster operating motion have been built. Yet, the longer the arm and the faster its motion, the more flexible the behavior of the structure will be. Hence, the presence of unwanted vibrations on the structure of the tower crane is to be expected. There have been several cases in which tower cranes have broken due to wind forces, some other forces due to external sources and most commonly, due to vibratory phenomena, which can be excited by the inherent system motion or any of the aforementioned external forces. This is due to the very low structural damping of the cranes structures.

A crane structure operates under a lot of strong sources of excitation, such as wind, trajectory tracking motion of its own arm and payload oscillations, just to mention a few. Because of this, the crane is usually driven in such a way that its motions are slow, so that, the presence of unwanted, harmonic and/or resonant vibrations can be skipped, thus, allowing the operator to place the payload with accuracy. Nevertheless, with the advent of smart materials, it becomes possible to actively modify

O.A. Garcia-Perez (✉) • G. Silva-Navarro • J.F. Peza-Solis
Departamento de Ingeniería Eléctrica, Sección de Mecatrónica, Centro de Investigación y de Estudios Avanzados del I.P.N,
Av. IPN No. 2508, Col. S.P. Zacatenco, C.P. 07360 Ciudad de México, Mexico
e-mail: ogarciap@cinvestav.mx; gsilva@cinvestav.mx; jpeza@cinvestav.mx

N. Dervilis (ed.), *Special Topics in Structural Dynamics, Volume 6*, Conference Proceedings
of the Society for Experimental Mechanics Series, DOI 10.1007/978-3-319-53841-9_14

certain parameters of a structure, such that, its dynamical performance meet some requirements under specific conditions, thus, providing the structure with several means to adjust whenever a perturbation or some change in its structural parameters occurs. This is indeed the case of piezoelectric materials, which allow to inject forces of great magnitudes in a very large bandwidth [4–6].

One of the challenges arising on large-scale structures, as well as in any distributed parameter system, is the fact that there are always a limited quantity of sensors and actuators, which must be employed to control a system with an infinite number of degrees of freedom. Hence, in order to deal with this problem, it is necessary to find proper locations along the structure where the actuator can have as much influence as possible over the chosen number of degrees of freedom that are useful in modeling the dynamics of the large-scale structure. Modeling by using finite element and modal analysis techniques allow to rapidly evaluate the possible candidate locations for both, sensors and actuators, so that the actuators may have the major influence on the modal shapes which are required to be controlled. Gawronski [1] proposes a method for the positioning of sensors and actuators, which consists of evaluating each one of the candidate positions under the scope of the H_2, H_∞ or Hankel norms and determine the influence of these positions over each one of the modal shapes of interest.

In this work, the damping ratio of a rotatory tower crane is increased by means of an active control technique. Its effects can be observed in a more rapid decay of the vibration amplitudes, which are present in the crane structure when a regulation or trajectory tracking of the central shaft is carried out. Therefore, in the first part of this work, the dynamical model of the rotating arm of the crane is outlined by using the method of Gawronski [1], where the aim is to effectively influence the first vibration modes of the crane arm. In order to obtain the modal parameters of the real structure in an experimental scaled structure, experimental modal analysis techniques are employed. The modal parameters thus identified are then used in the tuning of the control schemes to be applied in this work, as well as to validate the mathematical model obtained via the Finite Element Method (FEM). Finally, experimental results are shown in which the MPPF control technique is applied to get good and robust dynamic performance for this kind of structures.

14.2 Modeling of Arm Structure of Rotary Crane with a PZT Stack Actuator

The mechanical system consists of an arm structure on a rotary crane as shown in Fig. 14.1, where the main shaft is mounted on a rotary-type servomechanism, whose control torque $\tau(t)$ is provided by a dc servomotor and the angular displacement of the overall structure on a horizontal plane is denoted by $\theta(t)$ (see [7]). The mechanical structure is constructed with welded aluminum alloy 6061-T5 using circular and squared cross sectional bars. For vibration control purposes, some specific bar is replaced by a PZT stack actuator.

The overall flexible mechanical structure is modeled using finite element methods, considering a discretization with 451 space frame elements and 186 nodes each with 6 degrees of freedom, as described in Fig. 14.2. Moreover, for asymptotic tracking tasks the rigid and rotary crane is controlled by combining PD with strain feedback control [7], whose dynamics also influence the flexible mechanical structure.

The application of boundary conditions results in the following finite element model

$$M\ddot{q} + D\dot{q} + Kq = Bu_{PZT}(t) + B_a\ddot{\theta}(t), \qquad M, D, K \in R^{1086\times 1086}, \qquad q, B, B_a \in R^{1086}, \quad u_{PZT}, \ddot{\theta} \in R \tag{14.1}$$

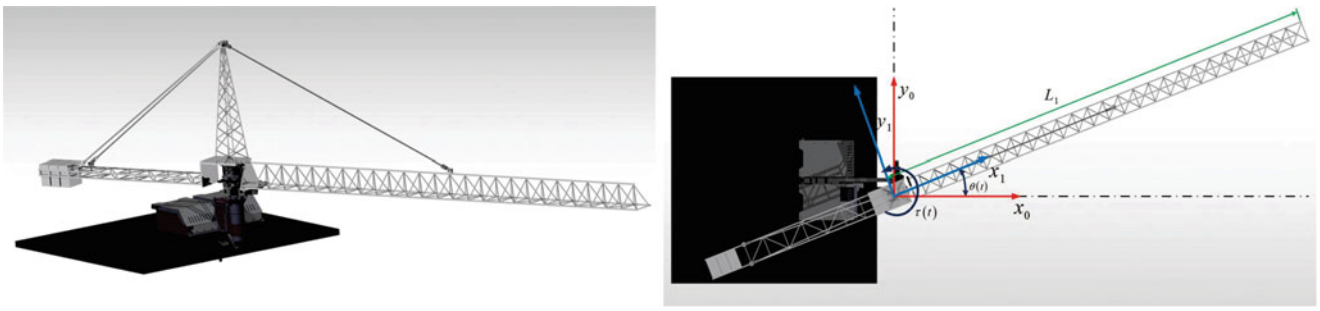

Fig. 14.1 Schematic diagram of arm structure with rotary crane

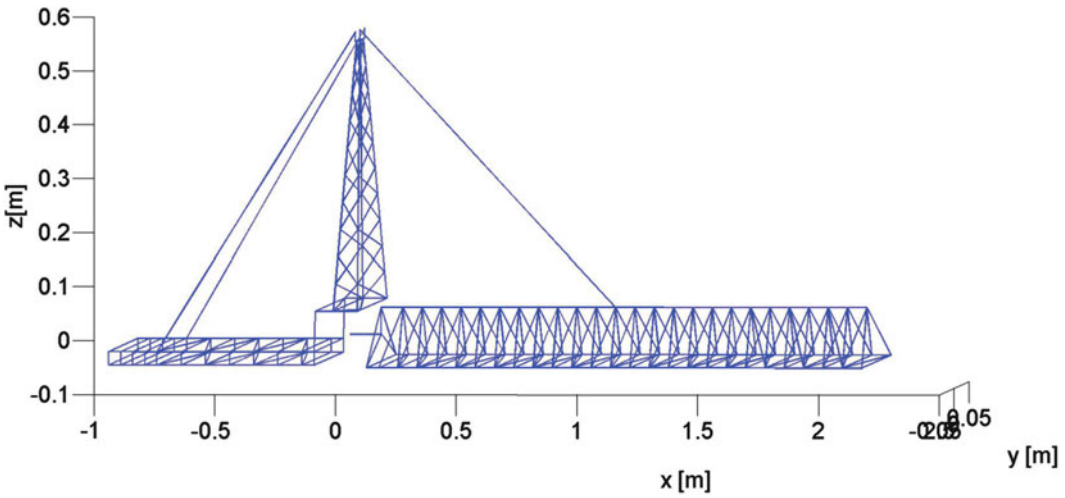

Fig. 14.2 Discretization of arm structure with rotary crane

Table 14.1 First four numerical natural frequencies

Mode	Frequency ω_i [Hz] (FEM in Matlab)	Frequency ω_i [Hz] (ANSYS)
1	4.699	5.422
2	16.066	16.719
3	16.214	20.056
4	20.641	20.946

where q, B_{PZT} and B_a are the displacement vector, influence vector of PZT stack actuator and the influence vector of the angular acceleration on the flexible structure, respectively. Moreover, M, D, K are the global mass, global damping and global stiffness matrices. For modeling purposes is considered proportional (Rayleigh) damping as

$$D = \alpha_1 K + \alpha_2 M, \qquad \alpha_1, \alpha_2 \in R \tag{14.2}$$

The influence vector B is given by the direction cosines on the finite element with respect to the global coordinate frame. Hence, the dynamics of the structure is modified by the influence of PZT stack actuator whose extensions or contractions are represented by δ, which is proportional to the applied voltage $V(t)$ in amount and sign, as shown in the next expression

$$\delta(t) = d_{33} n V(t) = g_a V(t) \tag{14.3}$$

where g_a is the gain of the PZT actuator.

The finite element model can be described in modal coordinates by using the linear transformation

$$q = \Phi q_m \tag{14.4}$$

Thus, assuming modal damping, the equations of motion can be transformed as

$$\begin{aligned} &\ddot{q}_m + 2Z\Omega\dot{q}_m + \Omega^2 q_m = B_m u_{\ddot{\theta}}(t) + B_{mc} u_{PZT}(t), \quad y = C_m q_m, \\ &B_m = {M_m}^{-1}\Phi^T B_a,\ B_{mc} = {M_m}^{-1}\Phi^T B,\ M_m = \Phi^T M \Phi,\ C_m = C_{oq}\Phi \end{aligned} \tag{14.5}$$

where $\Phi = \left[\phi_1\ \phi_2\ \ldots\ \phi_n\right]$, $\Omega = diag\left[\omega_1\ \omega_2\ \ldots\ \omega_n\right]$ are the modal and natural frequencies matrices, respectively.

In Table 14.1 and Fig. 14.3 are shown the first four dominant natural frequencies and modal shapes of the arm structure.

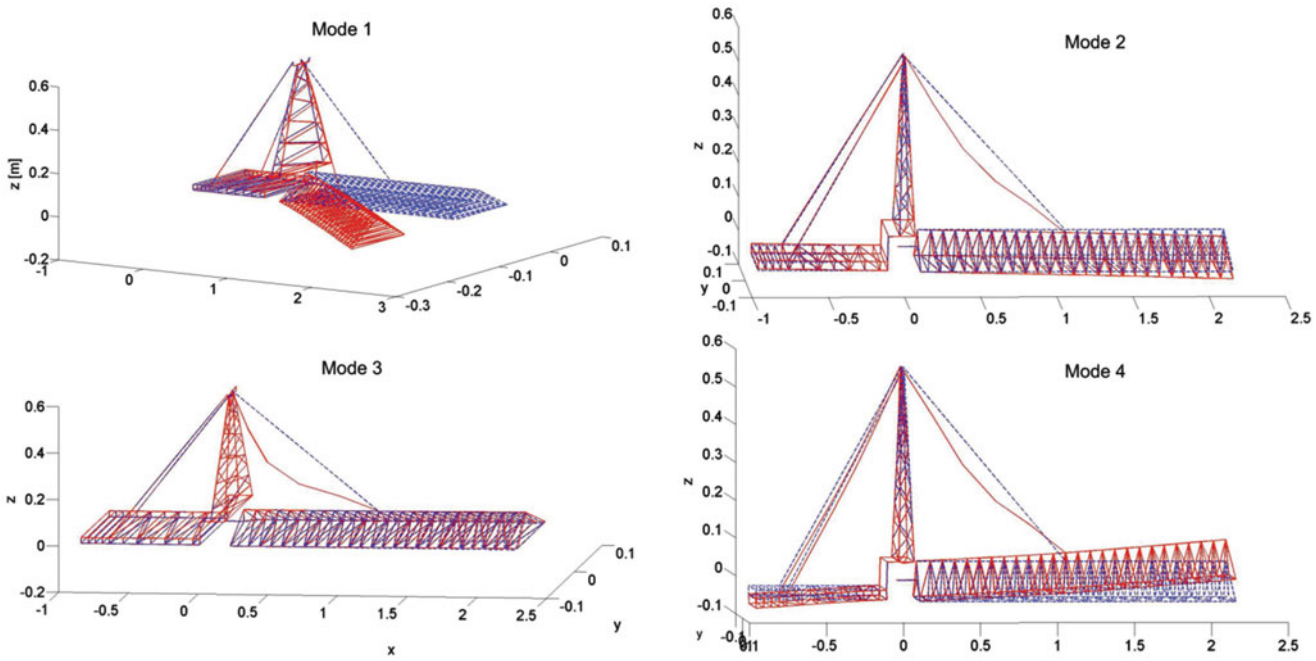

Fig. 14.3 First four modal shapes of the arm structure with rotary crane

14.3 Placement of a PZT Stack Actuator into the Structure

The location of a PZT stack actuator is selected by using a classical approach given in [1]. Thus, evaluation of the H_2 norm, when the vector B is expressed with respect to the direction cosines of the finite element n, leads to a quantitative way to compute the influence of the actuator/sensor on each modal shape. The influence of the PZT stack actuator on the structure is described in Fig. 14.4. For instance, on element 11 the modes 1 and 3 are strongly affected by the actuator and modes 2 and 4 are slight influenced.

The finite element model was also validated using experimental modal analysis techniques. Thus, natural frequencies and damping ratios of the overall structure were evaluated using accelerometers on the structure, impact hammer testing and peak picking techniques. In Fig. 14.5 the Frequency Response Function (FRF) of the structure is shown. In Table 14.2 are summarized the natural frequencies ω_i and modal dampings ζ_i, which were identified using the peak picking technique.

14.4 Application of a MPPF Control Scheme

To attenuate, as possible, the unwanted oscillations on the structure, due to the inherent trajectory tracking tasks of the crane structure, a Multiple Positive Position Feedback (MPPF) control scheme is implemented for the first two dominant modes via the PZT stack actuator. Therefore, the system dynamics in Eq. (14.5) and assuming only the first two vibration modes, a reduced order model is obtained as follows

$$M_r\ddot{q}_m + D_r\dot{q}_m + K_r q_m = B_{m_r}u_{\ddot{\theta}}(t) + B_{mc_r}u_{PZT}(t) \tag{14.6}$$

where $M_r = I\,, D_r = diag[2\zeta_1\omega_1, 2\zeta_2\omega_2]\,, K_r = diag[{\omega_1}^2, {\omega_2}^2]$ are mass (identity), damping and stiffness matrices of the reduced order model associated to the structure, respectively.

The closed-loop system dynamics MPPF control law is then described as follows

$$\begin{bmatrix} M_r & 0 \\ 0 & I \end{bmatrix}\begin{bmatrix} \ddot{q}_{m_r} \\ \ddot{\eta} \end{bmatrix} + \begin{bmatrix} D_r & 0 \\ 0 & 2Z_f W_f \end{bmatrix}\begin{bmatrix} \dot{q}_{m_r} \\ \dot{\eta} \end{bmatrix} + \begin{bmatrix} K_r & -B_{mc_r}GW_f{}^2 \\ -W_f{}^2G^TC & W_f{}^2 \end{bmatrix}\begin{bmatrix} q_{m_r} \\ \eta \end{bmatrix} = \begin{bmatrix} B_{mr} \\ 0 \end{bmatrix} u_{\ddot{\theta}}(t)$$
$$u_{PZT}(t) = GW_f^2\eta \tag{14.7}$$

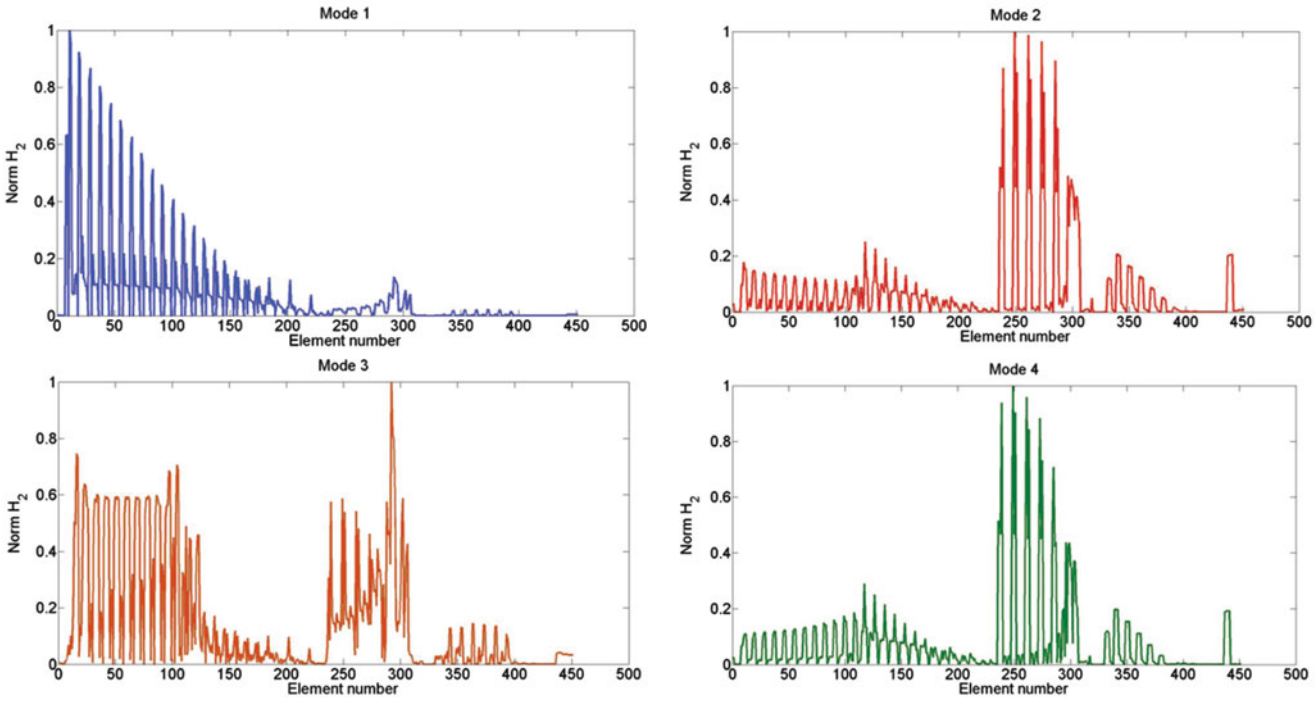

Fig. 14.4 Influence of the PZT stack actuator on different locations along the structure

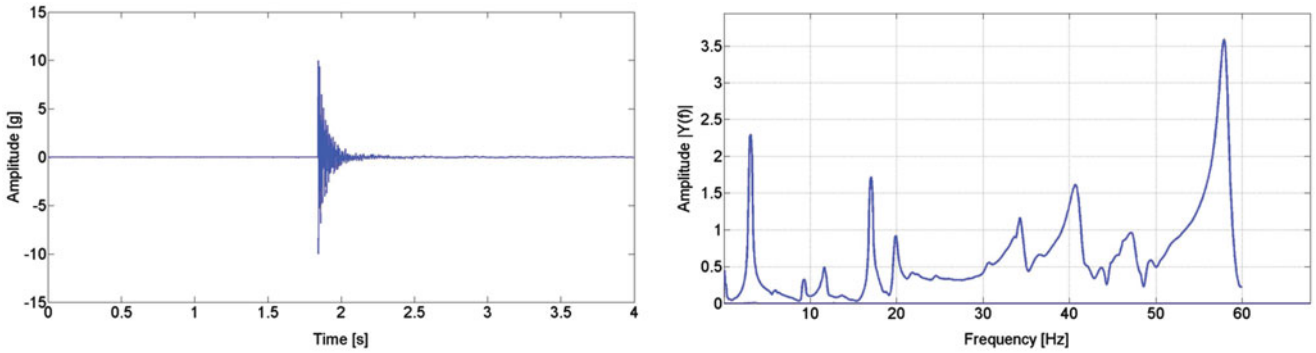

Fig. 14.5 Experimental FRF of the structure

Table 14.2 Natural frequencies and modal damping of the first four modes of the flexible structure

Mode	Frequency ω_i [Hz] (peak picking)	Modal damping ζ_i (peak picking)
1	3.1270	0.051
2	11.63	0.007
3	17.010	0.012
4	19.887	0.013

where $Z_f = diag\left[\zeta_{f_1}, \zeta_{f_2}\right], W_f = diag\left[\omega_{f_1}, \omega_{f_2}\right]$ and $G = [g_1, g_2]$ are matrices with design parameters denoting natural frequencies ω_{fi}, damping ratios ζ_{fi} and control gains g_i, respectively. The overall closed-loop stability can be guaranteed when the equivalent stiffness matrix be positive-definite and the equivalent damping matrix be positive-semidefinite.

14.5 Experimental Results

In order to verify the dynamic performance and effectiveness of the proposed control scheme, an experimental setup was designed and constructed as shown in Fig. 14.6. In addition, a PZT stack actuator and two strain gauges are mounted for monitoring and control purposes of the undesirable vibrations on the overall structure as show in Fig. 14.7.

In order to verify the performance of the MPPF control scheme alone, a free vibration test was conducted in which the structure was disturbed from rest by repeatedly applying forces at the tip of the structure. In Fig. 14.8, strain gauges measurements are shown for both cases: (a) free vibrations with no MPPF control (graph on the left) and, (b) free vibrations using the MPPF scheme (graph on the right), in which it is seen that MPPF causes the structural vibrations to damp out faster indeed.

In Fig. 14.9 are shown the frequency responses of the crane structure when the MPPF control is tuned at the two first natural frequencies of the crane structure. Both, Fig. 14.9 and Table 14.3, show that the damping ratio is increased up to 300%, thus, resulting in a faster decay of vibration amplitudes.

Rotary tower cranes are designed to perform many different tasks, being the position regulation the most common, so that, a payload can be delivered with accuracy. Yet, a far more demanding task is to have the same rotary crane tracking a prescribed trajectory since more dynamical effects take place under this new situation, because in general, no resting times are allowed for the crane structure to damp out vibrations. Hence, more structural modes are to be excited in which amplitudes get greater than they usually do for the typical regulation problem, since inertial effects tend to be more severe. The dynamic performance of the system under a trajectory tracking task using a typical PD controller is shown in Fig. 14.10, in which (a) the left-hand graph shows a good tracking of a sinusoid at the servomechanism level, and (b) the right-hand graph shows the strain measurements on the structure without MPPF vibration control.

Fig. 14.6 Experimental setup

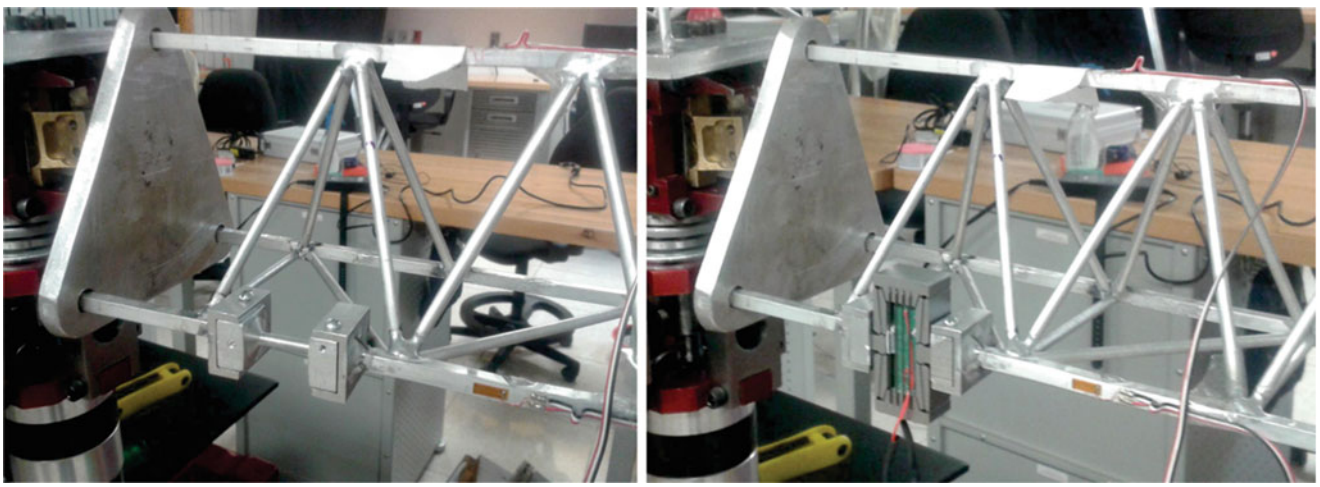

Fig. 14.7 PZT stack actuator and two strain gauge on crane structure

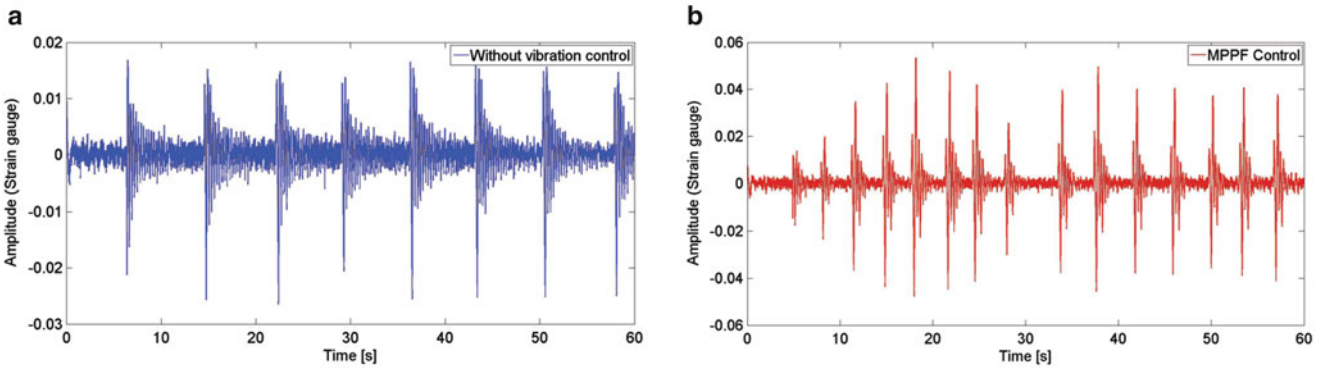

Fig. 14.8 Strain gauge measurements for free vibration test (**a**) without vibration control, (**b**) with MPPF control

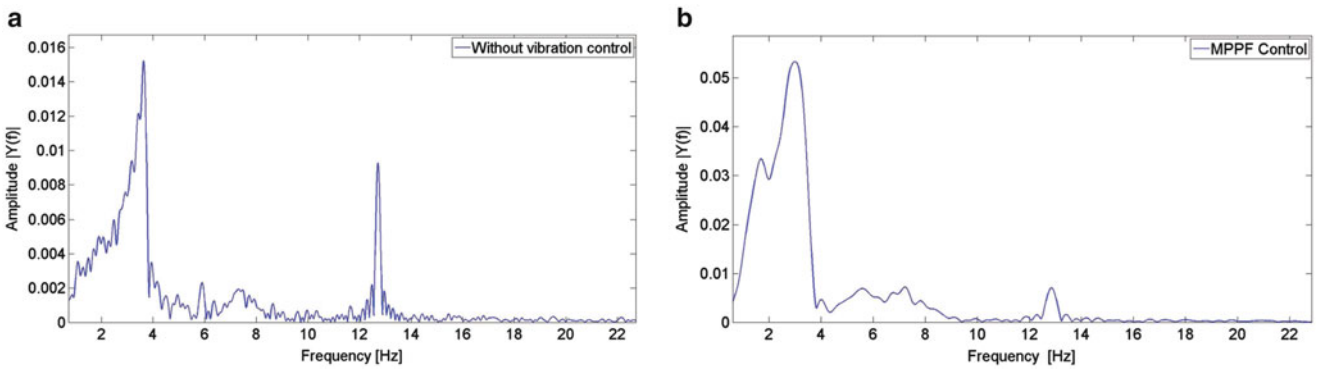

Fig. 14.9 Frequency responses of the crane structure. (**a**) Without vibration control, and (**b**) with MPPF control

Table 14.3 First two natural frequencies and the corresponding modal damping factors for the crane structure

Mode	Frequency ω_i [Hz] (without control)	Modal damping ζ_i (peak picking)	Frequency ω_i [Hz] (MPPF control)	Modal damping ζ_i (MPPF control)
1	3.63	0.051	2.99	0.161
2	12.71	0.005	12.84	0.013

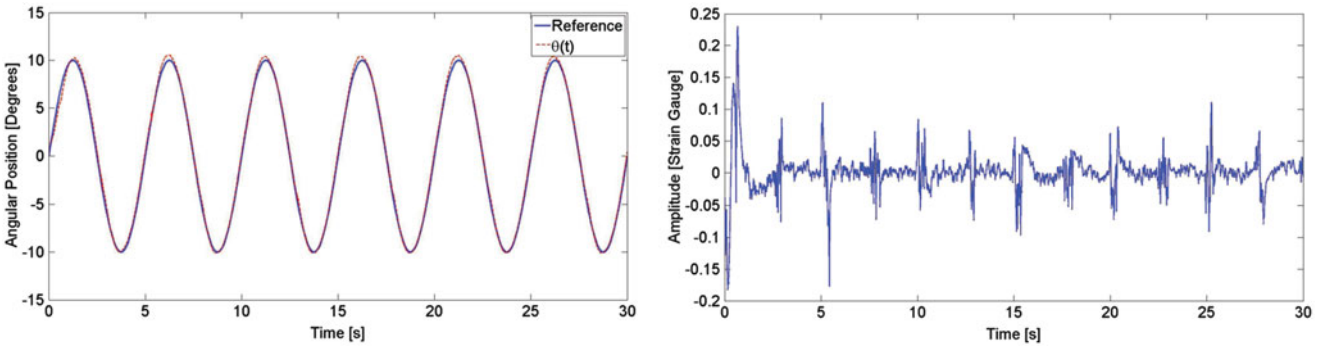

Fig. 14.10 Trajectory tracking of angular position with PD control and its corresponding strain measurements

For vibration control purposes the structure has two different actuators, that is, the main servomotor (PD with strain feedback control), which can be employed to guarantee asymptotic trajectory tracking, with sufficiently smooth acceleration profiles on the rotary crane in order to minimize those residual vibrations. To evaluate the dynamic performance using the PD with strain feedback control (without MPPF vibration controller), a similar test was performed on the structure (Fig. 14.11), thus resulting a better dynamic behavior on the residual lateral vibrations.

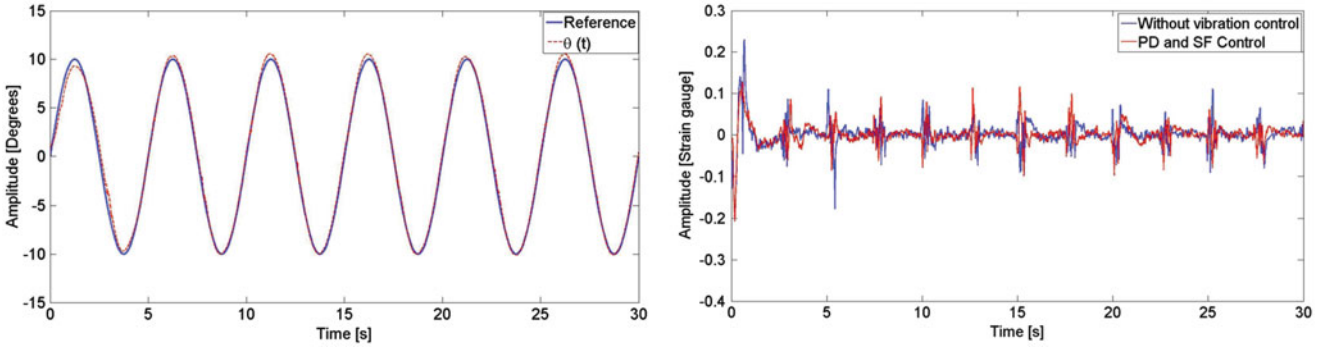

Fig. 14.11 Trajectory tracking using PD with Strain Feedback control (without MPPF vibration control)

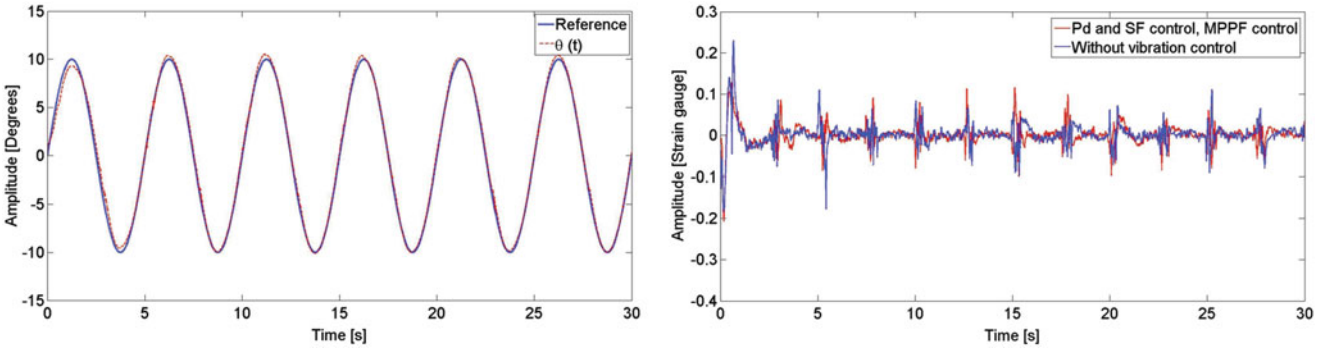

Fig. 14.12 Implementation of PD with Strain Feedback and MPFF vibration control schemes

Finally, as part of the experimental testing, the structure was tested using PD with strain feedback control for trajectory tracking combined with a MPPF vibration control on the PZT stack actuator (see Fig. 14.12). In fact, it is evident the effect of the additional damping injection provided by the MPPF control, which reduces the lateral vibrations on the structure.

14.6 Conclusions

This work describes the application of a PD with Strain Feedback control combined with a MPPF vibration control to perform trajectory tracking tasks on a rotary crane with a long and flexible structure. The overall mechanical structure employs a servomechanism with a dc servomotor for the manipulation of the structure and an additional PZT stack actuator embedded into the space flexible structure to reduce, as possible, the residual lateral vibrations excited by the inherent trajectory tracking motion on the mechanical structure. In general, the MPPF control scheme significantly increases the damping of the first two dominant modes of the structure, employing small control efforts. The results were validated on an experimental platform.

References

1. Gawrosnki, Q.K.: Advanced Structural Dynamics and Active Control of Structures. Springer, New York, NY (2004)
2. Preumont, A.: Vibration Control of Active Structures, 2nd edn. Kluwer Academic Publishers, Dordrecht (2002)
3. Preumont, A., Seto, K.: Active Control of Structures. Wiley, Cornwall (2008)
4. Flatau, A.B., Chong, K.P.: Dynamic smart material and structural systems. Eng. Struct. **24**, 261–270 (2002)
5. Song, G., Sethi, V., Li, H.-N.: Vibration control of civil structures using piezoceramic smart materials: a review. Eng. Struct. **28**, 1513–1524 (2006)
6. Hurlebaus, S., Gaul, L.: Smart structure dynamics. Mech. Syst. Signal Process. **20**, 255–281 (2006)
7. Garcia-Perez, O.A., Silva-Navarro, G., Peza-Solis, J.F.: Vibration control on a space flexible structure with a PZT stack actuator using strain and MPPF Control. In: Wicks, A., Niezrecki, C. (eds.) Structural Health Monitoring, Damage Detection and Mechatronics, The Society for Experimental Mechanics, vol. 7, pp. 111–119. Springer, New York, NY (2016)

Chapter 15
On a Grey Box Modelling Framework for Nonlinear System Identification

T.J. Rogers, G.R. Holmes, E.J. Cross, and K. Worden

Abstract In machine learning, black box models are often used to make excellent predictions of system behaviour. They are especially useful where the physics of a system is unknown or hard to model. This paper examines whether prior knowledge of certain physical properties of a system, encoded in a white box model, can be incorporated into black box methods to improve predictive performance. A combination of genetic algorithm optimisation of the white box model and Gaussian process regression on the residual error is presented as an improved method for system identification. This approach retains physical insight into the behaviour of the system while also reducing the error. Comparisons are made between pure white and black box models and the combined grey box model for several test applications. It is found that the combined model has significant advantages in predictive accuracy. This is especially seen in the case of nonlinear models. Here the full physics of the system is often too complicated or inaccessible to be modelled accurately with a white box method, but also the state space relationships are sufficiently complicated to make black box modelling equally challenging. The use of the proposed grey box method can reduce the complexity of the relationship that the black box is attempting to represent, leading to gains in accuracy. As a bonus, training time is reduced, as less complicated techniques are required to identify the process accurately.

Keywords Nonlinear system identification • White box • Black box • Grey box • Gaussian processes

15.1 Introduction

The problem of nonlinear system identification continues to be of foremost interest across a range of engineering disciplines including structural dynamics [1, 2]. In many cases, the aim of system identification is to allow prediction of system behaviour. The approaches to system identification can be separated into two broad areas: white box and black box models. The white box approach aims to model the underlying physics of a system and ascertain the parameters associated with the physical behaviour of the model, such as stiffness or damping. The black box philosophy sets aside the desire for the model to reflect the physics in a meaningful way, in favour of a more flexible set of modelling tools [3].

15.1.1 White Boxes

The white box method [4] is dependent on an informed prior model which can accurately model the physics of a given system. The parameters of this model can then be optimised with respect to the known input and output data. Provided there is an accurate physical model and the problem is well defined, this method will return results which will perform well even in an extrapolation scenario. However, there are two major challenges associated with implementing an effective white box model for system identification. The first is the determination of the physical model. In a simple system within a small operating range, this may be trivial, however, for the majority of engineering use cases the systems have complex physical behaviour or hidden states which cannot be easily modelled. This sort of system is encountered regularly in engineering problems, for example a physical model of a cantilever beam is easy to establish, but for a full bridge structure this may be more difficult. Limitations on sensor choice and placement may also make states unobservable; even a single degree of freedom oscillator measured with an accelerometer has its displacement and velocity as hidden states.

T.J. Rogers (✉) • G.R. Holmes • E.J. Cross • K. Worden
Dynamics Research Group, Department of Mechanical Engineering, University of Sheffield, Mappin Street, S1 3JD Sheffield, UK
e-mail: trogers3@sheffield.ac.uk

N. Dervilis (ed.), *Special Topics in Structural Dynamics, Volume 6*, Conference Proceedings
of the Society for Experimental Mechanics Series, DOI 10.1007/978-3-319-53841-9_15

The second challenge is that of parameter estimation. This usually revolves around the optimisation of a fitness function (most commonly a normalised mean-square error between the model prediction and the true output of the system on a training set). Not only is multidimensional optimisation a difficult and costly exercise, which increases with the number of dimensions, but it is also vulnerable to converging to local minima in the error surface, resulting in incorrect parameters. Selection and usage of an appropriate optimisation technique with well-tuned control parameters is a key stage in the use of white box models. Correctly implemented white box models have an advantage in that they will not overfit [5] a given dataset provided that the physical model is a true representation of the physical behaviour. When wrong parameters are fitted, this should be a failure of the optimisation technique not of the model itself. For this reason it is important that attention is paid to developing an accurate model. This need for an accurate model informed by the physics necessitates an experienced operator to observe the structure and derive its physical behaviour; this can be a time consuming and expensive task which requires expert knowledge relating to that particular use case.

15.1.2 Black Boxes

The black box philosophy aims to develop data-driven general models which can characterise the state space relationships between many variables which are related in arbitrary ways. For this purpose the methods chosen must be universal approximators. The aim of the general model, therefore, is to be able to represent any relationship without prior knowledge, so no user input is required to model a system. The generality of black boxes tends to lead to higher model complexity than a white box approach. The models will also only be able to predict behaviour within regions of the state space which are present in the training data leading to poor extrapolation performance. They are also vulnerable to overfitting; by adopting a model structure that is more complex than the physics being represented, the performance of the model can be poor without some form of cross validation during training.

As computing power, data availability, and flexibility of machine learning techniques has increased, so has the prevalence of black box methods. This fact is at least in part driven by the generality of many of these methods, meaning that these models can be used with very little or no knowledge of the system they are modelling. There are a variety of powerful methods which are available to perform this type of modelling including artificial neural networks (ANNs) and support vector machines (SVMs), each with their own advantages and drawbacks, a useful introduction can be found in [6]. In recent years, ANNs with a deep architecture have become more popular and are producing very promising results [7], especially in image processing applications; however, the complexity of these methods usually demands very large training data sets.

In this paper, Gaussian Process Regression (GPR) is chosen for black box modelling. GPR is a machine learning method in which a model is fitted based upon known input and output data which can then be used to predict the output given a different set of input data. A full explanation of GPR can be found in [8]. GPR is a nonparametric model which is commonly introduced as a distribution over functions when a prior, over functions, is used to allow the data to shape the relationship between the inputs and outputs. This information is contained in the covariance matrix between the input and output training data, which is generated by means of a covariance function (commonly a squared-exponential function). This allows the GP to be a universal approximator and, as the method is Bayesian, GPR returns confidence intervals automatically. Predictions can then be made on new input data assuming a normal distribution using the mean and covariance matrix determined in the training step with an added zero mean i.i.d. Gaussian noise.

The layout of the paper is as follows; first a description of the grey box methodology used is presented, this is followed by a case study based on a two state nonlinear system where the predictive accuracy of white, black and grey box methods is compared. Finally conclusions are made with comment on the role of grey boxes in modern nonlinear system identification.

15.2 A Grey Box Framework

It is clear that both the white box and black box approaches have their benefits and limitations. Here, it is proposed that both methods are combined to provide a more powerful system identification process. In the grey box framework a white box is constructed based on known physics of the system, usually in the form of an incomplete model of the system. This white box model is optimised with respect to the training data. The output of this white box can then be used as additional information for the black box model, alongside the known inputs to the system. It can be incorporated either as a mean function for the black box model or as an additional input dimension.

The white box is assumed to be noise-free and contains terms with physical meaning. The black box is used to account for physics that cannot be easily modelled in the white box and also allows correction for noise. In the case where the white box is used to generate a mean function for the black box process, this can be viewed as making a prediction with the black box serving as the noise model.

$$\mathbf{y_p} = \overbrace{f(X)}^{\text{white box}} + \overbrace{\epsilon(X)}^{\text{black box}} \tag{15.1}$$

The alternative case is where the output of the white box, $f(X)$, is used as an additional input to the black box.

$$\mathbf{y_p} = g(X, f(X)) \tag{15.2}$$

This form of the grey box carries the prior information of the model forward into the GPR and provides a strongly correlated input. In this way the physical insight of the white box is carried forward into the black box component creating what can be termed a type B [9] grey box where the nonparametric component of the model is strongly linked to the physics of the problem, as opposed to relying on the universal approximation property of any given method.

Although the concept of grey box models for nonlinear systems has been discussed in literature previously [10, 11], the use of the white box output as an informative input to a machine learning technique, such as GPR, represents an update of this method in light of modern tools available. The use of the white box as an informative input to the black box is a key difference to many other grey box models where the black box is used as a noise model to the predictions made from the white box.

15.3 Case Study with a Cascaded Tanks Problem

15.3.1 The Problem

The method in the form of Eq. (15.2) was tested on benchmark data provided by Schoukens et al. [12] as part of a workshop on nonlinear system identification which took place at the Vrije Universiteit Brussel in Belgium from 25–27 April 2016. Data was collected from a rig which consisted of two nominally identical tanks, water is pumped into the top tank, flows through an aperture, into the bottom tank and then through another aperture into the reservoir. The input controls the pump voltage and thus the rate at which the top tank fills.

The system is given inputs such that the top tank will sometimes overflow causing the behaviour to be nonlinear. This overflow causes a saturation nonlinearity where a proportion of the overflow will be transferred into the lower tank and the rest will return to the reservoir. It is also possible for the lower tank to be forced into an overflow condition, in this case all of the water overflowing is returned to the reservoir. A picture of the setup can be seen in Fig. 15.1. As well as the saturation nonlinearity present in the system, the cascaded tanks also contain a hidden state, the height of the top tank, since this is not observed. The initial level of this tank, which is unknown, has significant impact on the system behaviour, and therefore, increases the challenge in modelling this system.

When no overflow occurs, a model of the system can be constructed based on Bernoulli's Principle,

$$\dot{x}_1(t) = -k_1\sqrt{x_1(t)} + k_4 u(t) + w_1(t) \tag{15.3}$$

$$\dot{x}_2(t) = k_2\sqrt{x_1(t)} - k_3\sqrt{x_2(t)} + w_2(t) \tag{15.4}$$

$$y(t) = x_2(t) + e(t) \tag{15.5}$$

When the overflow case is considered, the model can be described by the following equations:

$$\dot{x}_1(t) = -k_1\sqrt{x_1(t)} + k_4 u(t) + w_1(t) \tag{15.6}$$

$$\dot{x}_2(t) = \begin{cases} k_1\sqrt{x_1(t)} - k_3\sqrt{x_2(t)} + w_2(t), & x_1(t) \leq 10 \\ k_1\sqrt{x_1(t)} - k_3\sqrt{x_2(t)} + k_5 u(t) + w_3(t), & x_1(t) > 10 \end{cases} \tag{15.7}$$

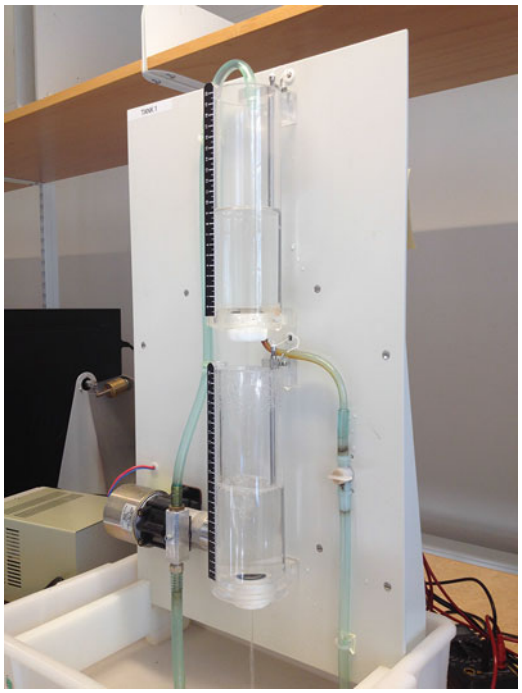

Fig. 15.1 Figure showing cascaded tank setup used to generate the benchmark data. Image taken from [12]

In both these cases, $u(t)$ is the input to the system, k_n represents the nth parameter of the system and w_n and e are the noise terms. These noise terms are assumed zero in the white box model, allowing the black box to compensate for noise and avoiding any distortion of the physics by the noise model.

15.3.2 White Box Model

This model was implemented as a continuous model that could return values indicating the height of the top or bottom tank. Successive discrete points were calculated for a given time step, Δt, such that:

$$\begin{aligned} x_1(t + \Delta t) &= x_1(t) + \Delta t\, \dot{x}_1(t) \\ x_2(t + \Delta t) &= x_2(t) + \Delta t\, \dot{x}_2(t) \end{aligned} \tag{15.8}$$

Four different optimisation schemes were compared: a differential evolution (DE) [13] using the classic random binary crossover; a particle swarm (PSO) [14] using sigmoid decreasing inertia weights [15]; a quantum behaved particle swarm (QPSO) [16], and a krill herd (KH) optimisation [17]. The latter two methods represent more recent approaches in optimisation which will be briefly described. The QPSO method is based on the same principles as the regular particle swarm but the dynamics of each particle is changed from the classic formulation to one where every particle is treated in a quantum manner. In terms of the optimisation this means the trajectory of the particles is now dependent upon, both, an attractor that is a random combination of the global best and previous best position for each particle, and a term relating to the particles' potential fields. This change in the position update procedure encourages better exploration properties for the QPSO over the PSO. The krill herd is another population-based optimiser which aims to mimic the behaviour of Antarctic krill, it has been shown that the krill move according to three factors the movement of neighbouring krill: a foraging action, and physical diffusion [18]. This leads to the updates of the particle positions in the KH algorithm being a combination of vectors modelling these three factors. The particles are affected by; the motion of neighbouring particles and the global best particle, a weighted average of the global best solution and the centre of mass of all individuals (food location) which relates to the foraging motion; the physical diffusion is modelled by a random perturbation on particle positions.

Each optimiser was run 50 times and the best run and average run results were compared using the normalised mean-square error measure (NMSE) shown in Eq. (15.9). This gives a value of zero for a perfect model or 100 if the predictions, $\mathbf{y}^*$, are set to the mean of the true outputs.

$$\text{NMSE} = \frac{100}{N\sigma_y^2}\sum_{i=1}^{N}(y_i^* - y_i)^2 \tag{15.9}$$

The optimisers were all run with a population size of 500 for 1500 generations to ensure that the algorithms converged. Stopping criteria could be applied to check for average change in function values or for stalling. This was not done to allow fair comparison of the models. The errors used for comparing the optimisation schemes were chosen to be the training error, since there was no validation set and the outputs of the white box were carried forward, this allowed a true test on the grey box output. The lack of a validation set was one of the challenges of the benchmark, which was limited to two short data records of only 1024 points each. This allowed selection of the best set of parameters which were then used to make a model prediction. The errors associated with these predictions are shown in Table 15.1.

The mean convergence curves can be seen Fig. 15.2, and the convergence of the best run of each optimiser in Fig. 15.3. Considering only the training and testing errors, the performance of each method is very similar. However, the convergence curves show significantly faster convergence for the QPSO method over the others tested.

The model of the system was then extended to include a more accurate physical model of the losses in the fluid flow.

$$\dot{x}_1(t) = -k_1\sqrt{x_1(t)} + k_5 x_1(t) + k_4 u(t) + w_1(t) \tag{15.10}$$

$$\dot{x}_2(t) = \begin{cases} k_1\sqrt{x_1(t)} - k_5 x_1(t) + k_6 x_2(t) - k_3\sqrt{x_2(t)} + w_2(t), & x_1(t) \leq 10 \\ k_1\sqrt{x_1(t)} - k_5 x_1(t) + k_6 x_2(t) - k_3\sqrt{x_2(t)} + k_5 u(t) + w_3(t), & x_1(t) > 10 \end{cases} \tag{15.11}$$

Here k_5 and k_6 are coefficients related to losses in the system due to friction or geometry. The losses are proportional to the velocity of the fluid squared and, therefore, proportional to the height of the fluid in each tank. For comparison, all four optimisation schemes were run in the same manner and compared as before.

Table 15.1 Normalised mean-square errors for each optimisation scheme during its best run in training and the model prediction error on the test set for that best set of parameters

Optimiser	Training	Testing
DE	4.5815	6.8107
PSO	4.2276	5.9309
QPSO	4.2276	5.9313
KH	4.2447	5.9329

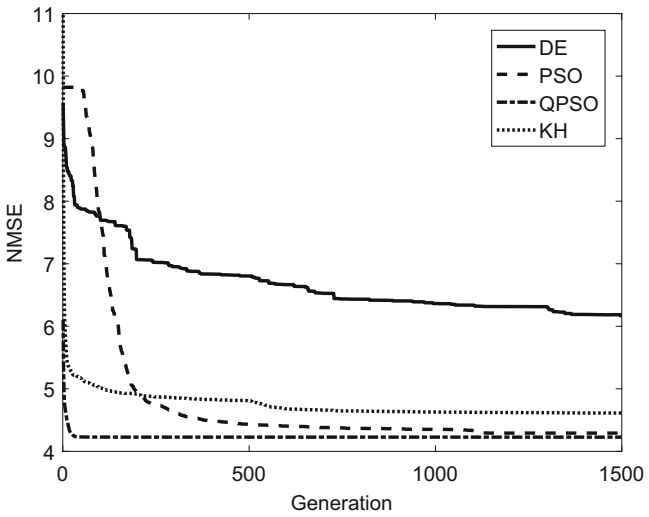

Fig. 15.2 Figure showing mean convergence curves for the four optimisation techniques tested on the white box model

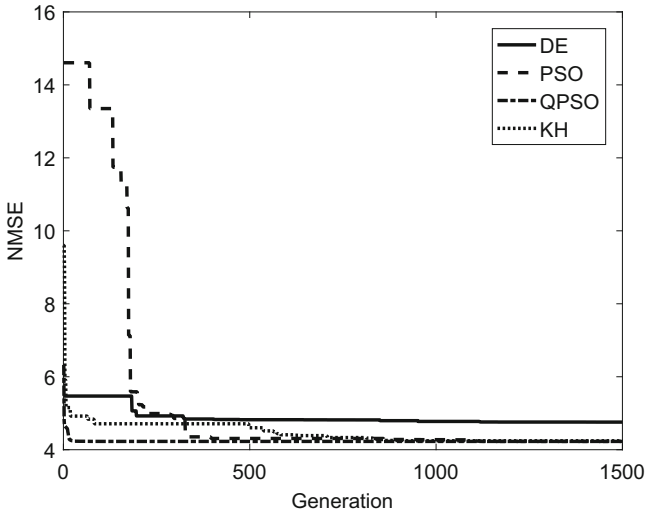

Fig. 15.3 Figure showing convergence curves for the best run of the four optimisation techniques tested on the white box model

Table 15.2 Normalised mean square errors for each optimisation scheme during its best run in training and the model prediction error on the test set for that best set of parameters using the extended physical model

Optimiser	Training	Testing
DE	2.5116	3.9537
PSO	1.7416	3.1210
QPSO	1.0174	1.7759
KH	1.0804	1.7816

The addition of these parameters showed a significant improvement of over 4% points in training and model prediction error, shown in Table 15.2. Since these additional model terms have physical meaning, an improvement in model behaviour was expected but not to the extent seen, given the relatively small effect the friction and geometry losses have on the system. As stated, the model was unlikely to overfit in the traditional sense of an overcomplicated model due to the additional terms being directly related to physical phenomena. If the terms relating to these losses had been negligible, this should have led to the optimisation scheme returning very small values for these parameters and little improvement in NMSE would be seen. The more accurate the model of the physics used, the better the performance of that model, provided the model incorporates true physical behaviour.

Again the convergence curves are plotted for the four optimisers (Figs. 15.4 and 15.5) these plots confirm the choice of the QPSO method for this problem. This also shows that as the dimensionality of the problem increases, the requirement for optimisation schemes more resistant to local minima increases.

It should be noted at this point that, although a normalised mean-squared error is used to compare the effectiveness of the models in a predictive task, this does not fully encompass the value of the model. One of the key advantages in the white box model used here is that the physical meaning associated with each of the parameters retains an intuitive and informative meaning within the engineering context. This insight into the physical behaviour of the system beyond just the prediction of the system output can be invaluable, especially when it gives additional information regarding hidden states such as the top tank level in this case study.

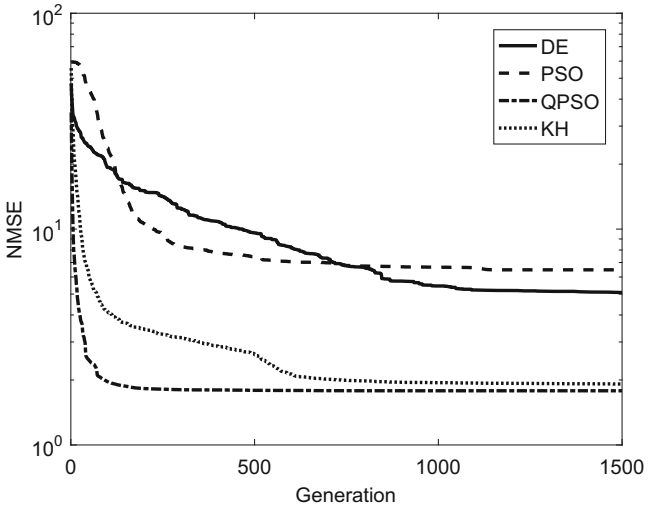

Fig. 15.4 Figure showing mean convergence curves for the four optimisation techniques tested with the extended physics model

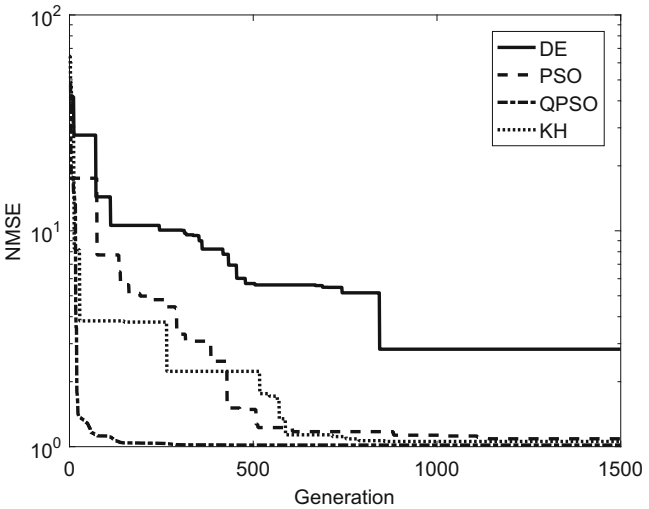

Fig. 15.5 Figure showing convergence curves for the best run of the four optimisation techniques tested with the extended physics model

15.3.3 Black Box Model

In order to allow comparison with the grey box model, the system was modelled using a fully black box method. A Gaussian Process Regression model was trained using the GP-NARX framework [19]. Since this is a nonlinear auto-regressive with exogenous (NARX) model, there are additional hyperparameters, associated with the lags in the NARX model, to be determined. A manual search identified these to be 15 lags in both input and output with a lag multiplier of two. The lag multiplier allows increases in spacing of the points by taking points that are not consecutive but instead leaving out intermediate points which can be useful if the data is oversampled. In this case the lag multiplier was two, therefore, inputs were taken at $x_t, x_{t-3}, \ldots, x_{t-30}$ and at $y_{t-1}, y_{t-3}, \ldots, y_{t-31}$. A squared exponential kernel with automatic relevance determination was used for the GP covariance structure; the hyperparameters for this were optimised using a conjugate gradient descent [20, 21].

The GPR model was then used to make both a one-step-ahead prediction and a full model predicted output. In the one-step-ahead (OSA) case the model outputs, at time t, are calculated based on the true observations of the system inputs up to time t and the outputs to $t-1$, see Eq. (15.12).

$$y_i^* = F(y_{i-1}, \ldots, y_{i-n_y}; x_{i-1}, \ldots, x_{i-n_x}) \tag{15.12}$$

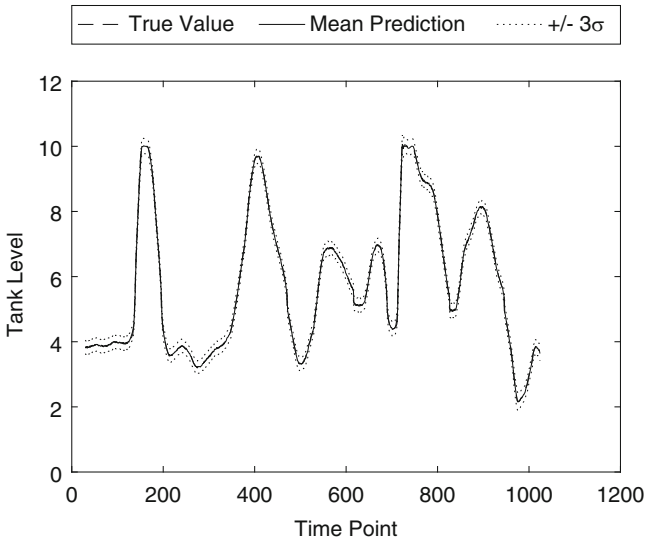

Fig. 15.6 One-step-ahead prediction made by the black box model with an overall NMSE of 0.0565

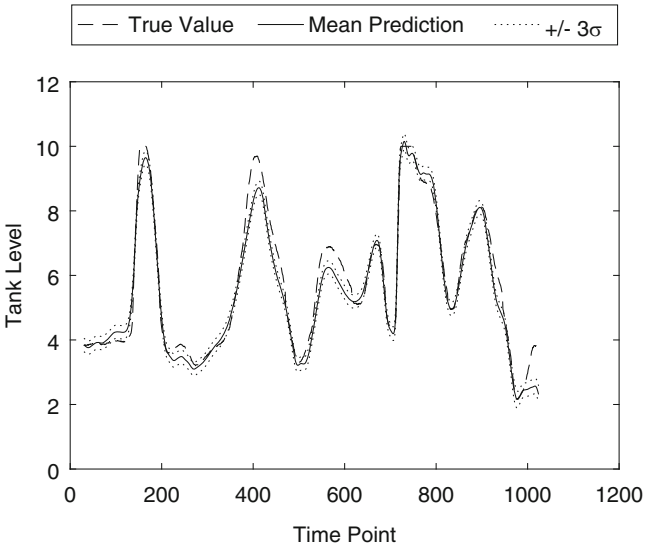

Fig. 15.7 Full model prediction made by the black box model with an overall NMSE of 4.6174

A more rigorous test of the model is to use the full model predicted output (MPO). In this case the model is not fed any additional output information once the predictions have begun, only information regarding the inputs. This is sometimes referred to as a simulation test, but that terminology is not adopted in this paper. The MPO can be expressed as in Eq. (15.13).

$$y_i^* = F(y_{i-1}^*, \ldots, y_{i-n_y}^*; x_{i-1}, \ldots, x_{i-n_x}) \tag{15.13}$$

Plots of the predictions can be seen in Figs. 15.6 and 15.7 with a one-step-ahead error of 0.0565 and a model prediction error of 4.6174. It is interesting that for this problem, where the physics is relatively simple and can be modelled with confidence, the extended white box model outperforms GPR. If, however, the original reduced physics model is used, GPR produces a lower prediction error for the model predicted output.

15.3.4 Grey Box Model

The output from the white box model, is used as an additional input to a black box, again chosen to be a Gaussian Process model. If there is structure in the residuals of the white box output this can be modelled by the Gaussian Process and leads to a reduction in prediction error while maintaining the physical insight from the white box model.

To assess whether a simplified physics model can produce the same level of prediction accuracy, a grey box model was trained using the outputs from both of the white box models. The inputs to the GPR were lagged measurements from both the known input readings and also the output vector from the white box models.

Taking the outputs of the first model, the NARX hyperparameters were determined to be a lag of two on the inputs and ten on the outputs with a lag multiplier of two. After training the GPR model with this additional input, the OSA error is 0.0529 which is not a notable improvement. However, the more rigorous MPO gives an error of 2.4621. This represents an improvement of approximately 2.2 points over the black box and 3.5 points over the white box model using the NMSE measure. As discussed earlier, while improvement in mean-squared error is a well established measure of model superiority, there is additional value in the physical insight retained by use of the white box model. This value is not encapsulated in the MSE, and to quantify it is difficult, as a more subjective fitness model would need to be established.

Using the outputs from the extended physical model in the same manner, the NARX hyperparameters were determined to be the same as for the first grey box. This would indicate that the model structure for the two grey box models is the same. This in turn implies that the structure in the residuals is the same. Therefore, both white box models fail to identify a particular area of the state space, which means their physics is incomplete. The GPR improves the prediction behaviour of the white box models by modelling this missing area of the state space with inaccessible physics; this is seen when the second grey box is trained and the OSA error falls to 0.0442 and the MPO to 0.8178 (Figs. 15.8, 15.9, 15.10 and 15.11). An improvement of almost 4 points over the black box and 1 point over the improved white box model in the MPO case. With this extended model, more physical information about the behaviour of the system is retained which contains information valuable in an engineering context.

A section of the test data is plotted along with predictions from the two grey boxes and the black box in Fig. 15.12, here the improvement that the grey boxes give can be seen more clearly. On the first peak the improvement in prediction as the prior information contained in the white box becomes more accurate can be easily seen. In addition to this, two features in the response also become more clear; close to time points 470 and 610, sharp drops in the measured tank level can be seen. This response is believed to be due to water collecting on the capacitive sensor used in drops which then fall giving rise to the sudden falls in tank level. As the prior model of the white box becomes more informative the method becomes more robust to this noise affecting the training of the black box component.

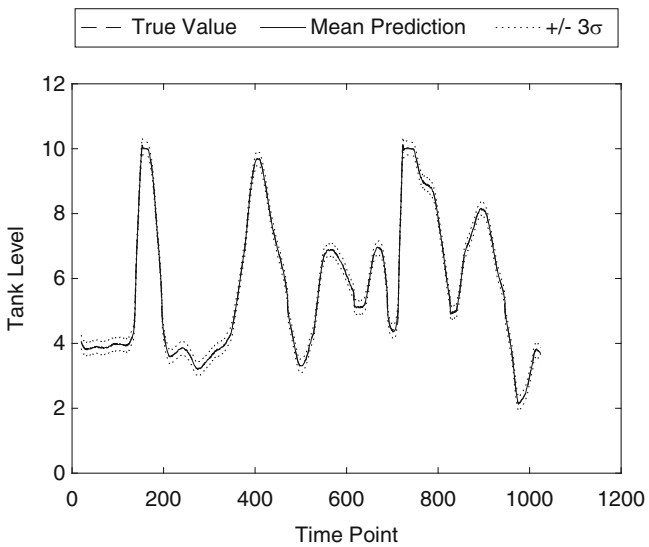

Fig. 15.8 One step ahead prediction made by the grey box model, using the initial white box, with an overall NMSE of 0.0529

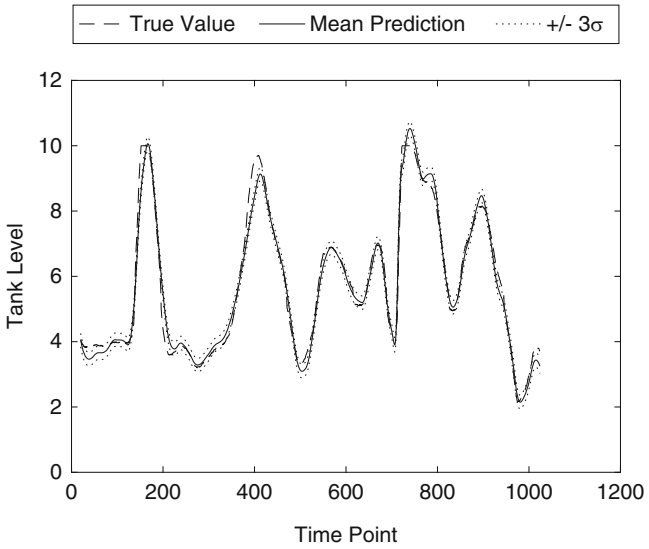

Fig. 15.9 Full model predicted output of the grey box model, using the initial white box, with an overall NMSE of 2.4621

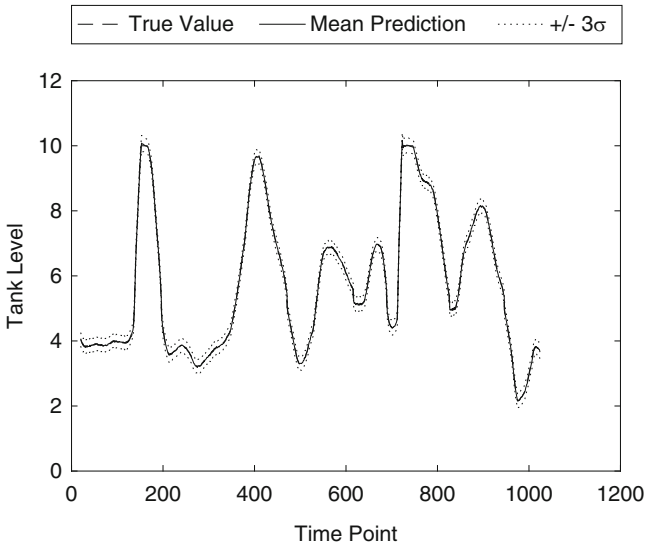

Fig. 15.10 One-step-ahead prediction made by the grey box model, with the results of the extended physics white box, with an overall NMSE of 0.0442

15.4 Conclusions

This paper presents strong motivation for attempting to combine physics-informed white box models with state of the art black box models from the machine learning literature. Using Gaussian processes regression in this case, it has been shown that, even for an idealised physics model in the white box, a grey box model can lead to significant reduction in NMSE prediction error, while retaining physical insight.

The use of GPR has been shown to be effective in modelling structured residuals in the white box. These correspond to missing physics and thus facilitate good prediction performance even when complete physical models may be inaccessible or too complicated to optimise. The results presented here also show, however, that an improvement in the quality of the white box model (a more realistic physical model), not only yields a lower prediction error in the white box, but also improves the performance of the grey box overall.

The results shown here suggest that machine learning approaches to system identification should not too quickly replace the role of physical insight into a system. However, machine learning methods offer a powerful tool to enhance the system

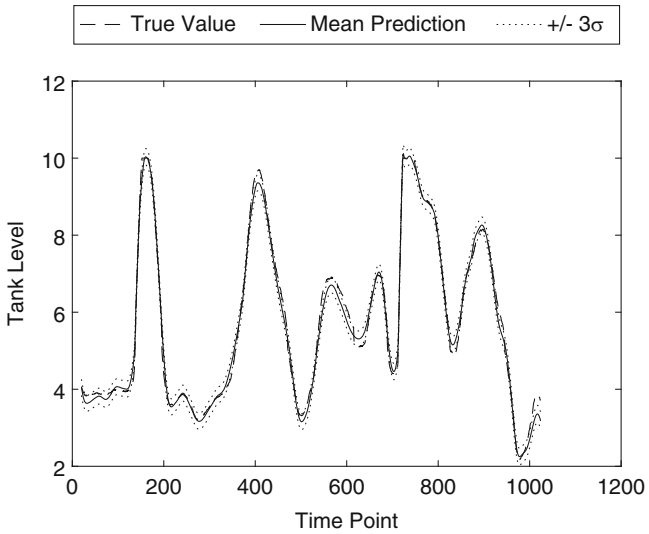

Fig. 15.11 Full model predicted output of the grey box model, with the results of the extended physics white box, with an overall NMSE of 0.8178

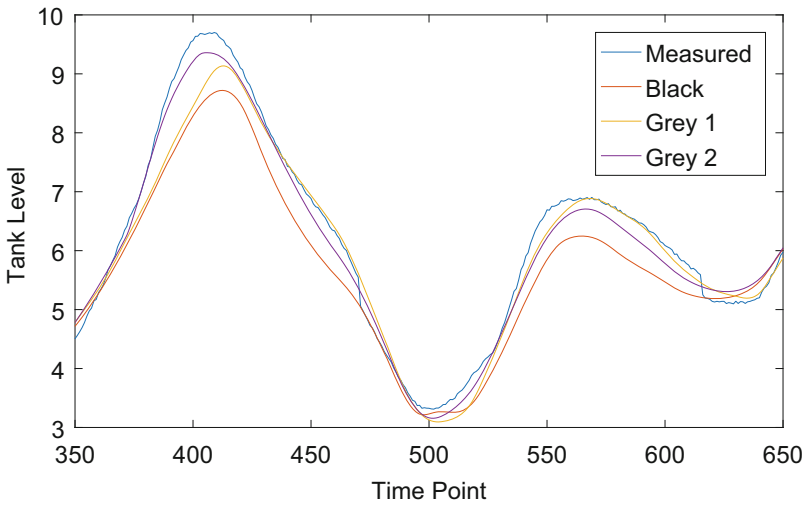

Fig. 15.12 Figure showing performance of the two grey box models compared to the black box in the middle section of the time series where all models struggled to fit in the testing set

identification process and can offer significant increases in predictive performance when combined with prior knowledge contained in a white box model. This motivates the adoption of a grey box framework when approaching system identification tasks from an engineering perspective.

Acknowledgements The authors wish to thank Ramboll for providing funding for this work and in particular Ulf Tyge Tygesen whom they are working with directly.

References

1. Kerschen, G., Worden, K., Vakakis, A., Golinval, J.: Past, present and future of nonlinear system identification in structural dynamics. Mech. Syst. Signal Process. **20**(3), 505–592 (2006)
2. Noël, J., Kerschen, G.: 10 years of advances in nonlinear system identification in structural dynamics: a review. In: Proceedings of ISMA 2016-International Conference on Noise and Vibration Engineering (2016)

3. Sjoberg, J., Zhang, Q., Ljung, L., Benveniste, A., Delyon, B., Glorennec, P., Hjalmarsson, H., Juditsky, A., et al.: Nonlinear black-box modeling in system-identification-a unified overview. Automatica **31**(12), 1691–1724 (1995)
4. Nelles, O.: Nonlinear System Identification: from Classical Approaches to Neural Networks and Fuzzy Models. Springer Science & Business Media, Berlin (2013)
5. Hawkins, D.: The problem of overfitting. J. Chem. Inf. Comput. Sci. **44**(1), 1–12 (2004)
6. Bishop, C.: Pattern Recognition and Machine Learning (Information Science and Statistics), 1st edn. 2006, Springer (2007)
7. Schmidhuber, J.: Deep learning in neural networks: an overview. Neural Netw. **61**, 85–117 (2015)
8. Rasmussen, C., Williams, C.: Gaussian Processes for Machine Learning. MIT Press, Cambridge (2006)
9. Worden, K.: Is system identification just machine learning? Workshop on Nonlinear System Identification Benchmarks (2016)
10. Tulleken, H.J.: Grey-box modelling and identification using physical knowledge and Bayesian techniques. Automatica **29**(2), 285–308 (1993)
11. Bohlin, T.: A case study of grey box identification. Automatica **30**(2), 307–318 (1994)
12. Schoukens, M., Mattsson, P., Wigren, T., Noël, J.P.: Cascaded tanks benchmark combining soft and hard nonlinearities (2016)
13. Storn, R., Price, K.: Differential evolution - a simple and efficient heuristic for global optimization over continuous spaces. J. Glob. Optim. **11**(4), 341–359 (1997)
14. Eberhart, K.J., et al.: A new optimizer using particle swarm theory. In: Proceedings of the Sixth International Symposium on Micro Machine and Human Science, vol. 1, pp. 39–43, New York, NY (1995)
15. Malik, R., Rahman, T., Hashim, S., Ngah, R.: New particle swarm optimizer with sigmoid increasing inertia weight. Int. J. Comput. Sci. Secur. **1**(2), 35–44 (2007)
16. Sun, J., Feng, B., Xu, W.: Particle swarm optimization with particles having quantum behavior. Congress on Evolutionary Computation (2004)
17. Gandomi, A., Alavi, A.: Krill herd: a new bio-inspired optimization algorithm. Commun. Nonlinear Sci. Numer. Simul. **17**(12), 4831–4845 (2012)
18. Hofmann, E., Haskell, E., Klinck, J., Lascara, C.: Lagrangian modelling studies of Antarctic krill (Euphausia Superba) swarm formation. ICES J. Mar. Sci. J. du Conseil **61**(4), 617–631 (2004)
19. Worden, K., Manson, G., Cross, E.: Higher-order frequency response functions from Gaussian process NARX models. In: Proceedings of 25th International Conference on Noise and Vibration Engineering, Leuven (2012)
20. Fletcher, R., Reeves, C.: Function minimization by conjugate gradients. Comput. J. **7**(2), 149–154 (1964)
21. Dai, Y., Yuan, Y.: A nonlinear conjugate gradient method with a strong global convergence property. SIAM J. Optim. **10**(1), 177–182 (1999)

Chapter 16
In-Process Monitoring of Automated Carbon Fibre Tape Layup Using Ultrasonic Guided Waves

R. Fuentes, E.J. Cross, N. Ray, N. Dervilis, T. Guo, and K. Worden

Abstract This paper presents an investigation into the inspection of an Automated Tape Placement (ATP) process, which automates the process of laying composite plies on a tool surface. The requirement for monitoring this process is motivated by the need to detect common defects in the process which could compromise the integrity of the structure. An experimental procedure was carried out where the tool surface, where composite is laid during the ATP, was excited with ultrasonic guided waves. Several types of defects were introduced during this process, and a methodology is presented to extract features from the signals acquired, model the process using this data and identify the defects. The main challenge in modelling this process is the cumulative trend throughout the application of the composite plies. A method is presented where wavelet analysis is used to model short-term dynamics while the long term, cumulative trends are eliminated using cointegration. The results show that one can detect various types of defects during an ATP process using the methodology introduced here. The key result is that the trends in the data due to the normal process can be removed using cointegration in order to reveal abnormalities.

Keywords Carbon fibre reinforced plastics • Ultrasound • Guided waves • Wavelets • Cointegration

16.1 Introduction

Monitoring of Carbon Fibre Reinforced Plastics (CFRPs) has attracted significant attention due to their increased use in engineering structural components. In contrast with their metallic counterparts, visual inspection is generally not sufficient to assess the structural integrity of CFRPs, as damage and defects tend to hide within the matrix of the composite. This has led to the development of various Non Destructive Testing (NDT) techniques. Ultrasound testing has emerged as a viable technique for NDT, and there is a wide variety of methods in which one could make use of ultrasound to scan a structure [1, 2]. NDT is critical post-manufacturing, in order to ascertain the quality of the structure. However, in many instances it can be beneficial to monitor the actual composite layup in order to stop if a defect is introduced during the process.

This paper presents an investigation of the inspection of an Automated Tape Placement (ATP) procedure, used for the application of composite plies. An ATP machine allows for a custom layup of CFRP plies to be applied to a complex geometry by means of a multi-axial head that can apply strips, or courses, of composite pre-preg to a tool surface. The ATP machine used for this study is located in the University of Sheffield's Advanced Manufacturing Research Centre (AMRC) with Boeing. The tests carried out involved the application of unidirectional layers of CFRP using the ATP machine, while ultrasonic guided waves were transmitted and received at opposite ends of the tool surface. The objective of this exercise being to attempt to characterise the layup process, with the overall aim of detecting manufacturing defects introduced *during* the tape laying. One simple yet common defect affecting the tape laying process is the introduction of Foreign Object Debris (FOD), which if undetected, could potentially compromise the structural integrity of the composite. Another more subtle type of defect could be delamination or an incorrect placement of the plies. To this end, three tests were carried out and are presented in this paper; A normal tape layup, without any defects, and two layups where various types of defects were introduced; these comprised three steel washers of 20, 9 and 6 mm diameter respectively to simulate more obvious FOD as well as two small square sheets of thin Teflon, to simulate a more subtle incorrect lamination during the process.

The next section presents the experimental procedure in more detail, whilst Sect. 16.3 discusses the data processing methodology used to identify the defects. Section 16.4 presents a discussion of the results obtained and the direction of further investigation and experimental work.

R. Fuentes (✉) • E.J. Cross • N. Ray • N. Dervilis • T. Guo • K. Worden
Dynamics Research Group, Department of Mechanical Engineering, University of Sheffield, Mappin Street, S1 3JD Sheffield, UK
e-mail: ramon.fuentes@sheffield.ac.uk

N. Dervilis (ed.), *Special Topics in Structural Dynamics, Volume 6*, Conference Proceedings
of the Society for Experimental Mechanics Series, DOI 10.1007/978-3-319-53841-9_16

16.2 Experimental Procedure

The ATP lays plies of composite by applying uni-direction strips of ply, or courses, on top of a tool surface that acts as a mold. For this investigation, a special tool surface was used which consisted of a 10 mm thick, 800 × 800 mm aluminium plate on which the ATP machine laid several courses of carbon fibre tape. One layer of ply is comprised of several courses laid parallel to each other. Four piezoceramic transducers were bonded to the surface of the aluminium surface (using cyanoacrylate adhesive); two of them were used as transmitters, and two as receivers. The transmitter-receiver pairs were placed normal to each other, as shown in Fig. 16.1. Guided waves are thus transmitted at both 0° and 90° to the orientation of the ply. A function generator was used to send a tone-burst of 100 cycles at 300 kHz, every 0.25 s. A multiplexer was then used to alternate the excitation source between *A* and *B*. This gives more than enough time for the response of the previous guided wave to attenuate completely before a new one is transmitted. An example of an excitation pulse, and the corresponding responses are shown in Fig. 16.2. Even though, every quarter of a second two channels are recorded, the resulting data set consists of four channels (each pair 0.25 s out of phase), given that when transmitter *A* emits, both receivers and *A* and *B* receive, and vice-versa for transmitter *B*. Different representative defects were introduced throughout the ATP process, namely a 20, 9 and 6 mm steel washer as well as a thin square patch of Teflon sheet. The aim of the Teflon sheet is to simulate an abnormality in the ply.

A total of three tests were carried out. Each test consists of the ATP machine laying six layers of unidirectional ply on the aluminium tool surface, which is excited by the guided waves. The first test was used as a baseline, so no defects were introduced. On the second test, a 20 mm diameter washer was introduced into the layup on the second layer, followed by a Teflon patch on the fifth layer. Both were introduced outside the path of any of the transducer pairs, however after placing the washer, the ATP roller moved it closer to the **BB** path during application of tape. A patch of Teflon was also introduced on the fifth layer of the second test. On the third test 6 and 9 mm washers were introduced on the second and third layers respectively, and a Teflon patch on the fifth layer. From the observation that on the second test the washer was displaced by the ATP roller, a small amount of cyanoacrylate glue was placed on the subsequent washers to avoid movement. In summary, six layers of ply were applied to tests 1, 2 and 3, with the last two containing defects. Approximately 900 pulses per channel were collected for every test.

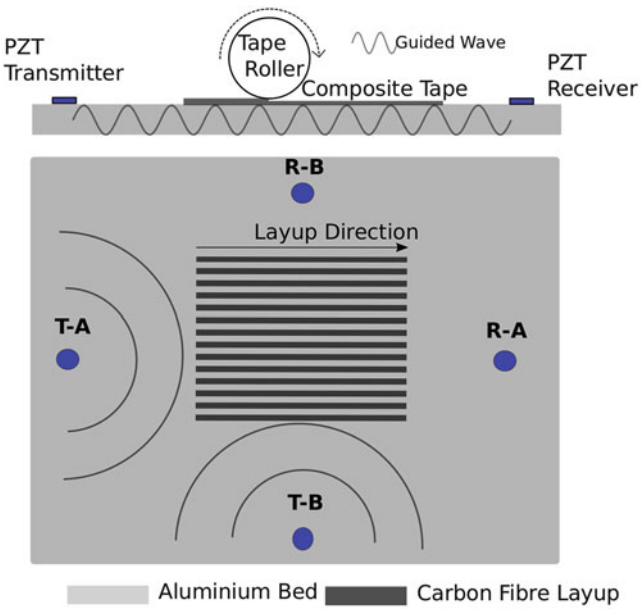

Fig. 16.1 Illustration of experimental setup, outlining positions of transmitting (**T-A**, **T-B**) and receiving (**R-A**, **R-B**) transducers

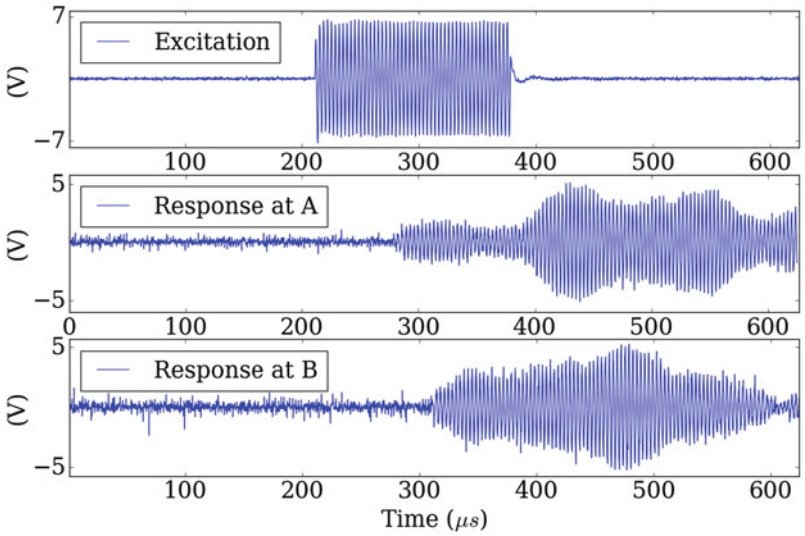

Fig. 16.2 Illustration of emitting and receiving waveforms

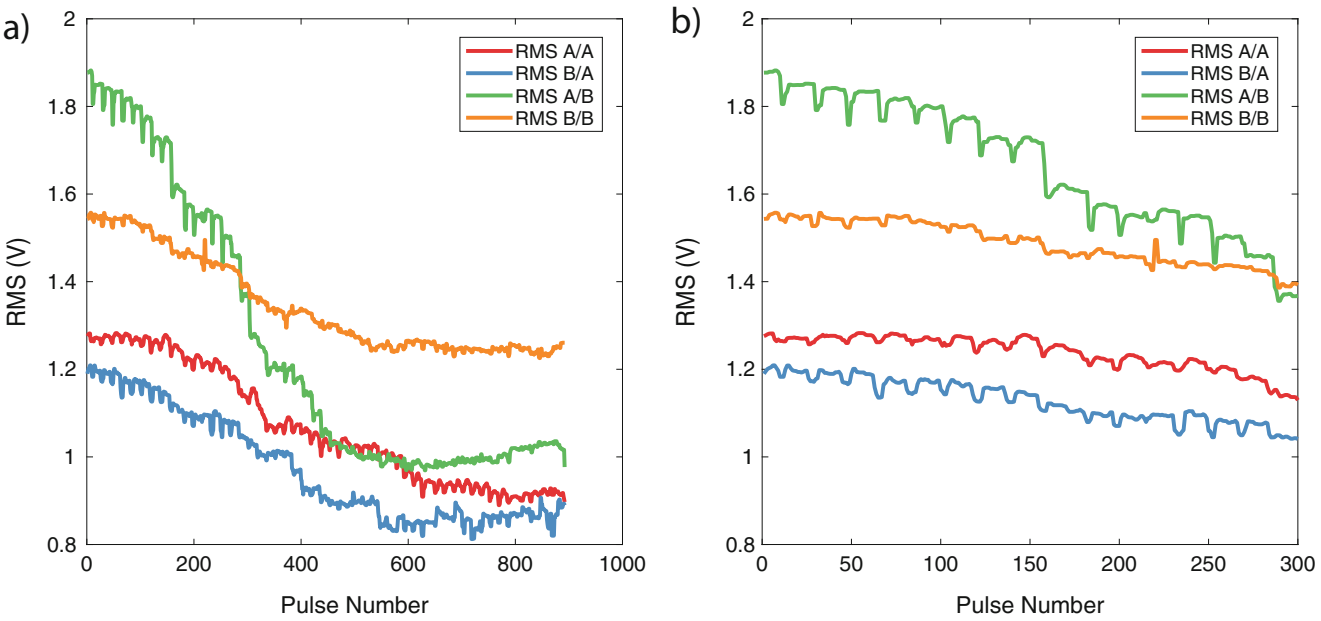

Fig. 16.3 RMS from the four receiving channels throughout the layup of six layers of ply. The overall test is on the (*left*, **a**) while (*right*, **b**) zooms in on the periodicities created by the roller contact

16.3 Defect Detection Methodology

The problem of identifying a change in the data set is a novelty detection problem, which can be solved via density estimation. If the process was stationary, spotting such a change may be a trivial process now, as outlier analysis is a rather well established procedure within the Structural Health Monitoring (SHM) literature [3]. The novelty detection process is not carried out directly on the raw data, but on a more informative feature space, which normally requires some pre-processing of the data to derive damage sensitive features. In this case, the energy in the obtained pulses could be considered as one of the simplest features, and can be represented by the Root Mean Square (RMS) of each pulse. The RMS illustrates the process very well, and it is shown in Fig. 16.3 for the baseline test with no defects.

The main challenge in this dataset is introduced by the fact that the process is constantly changing with time. In this case, two main trends arise; one from the contact of the ATP roller with the tool surface, and one from the application of carbon

fibre tape. The former generates a trend that is periodic and would be easily modelled using an Auto Regressive (AR) model, or in this case, since the problem has several dimensions (4 sensing channels, with multiple features each), a Vector Auto-Regressive (VAR) model may be more appropriate. Unfortunately, the constant application of carbon fibre tape introduces a cumulative change in the process. As more tape is applied, the composite matrix absorbs more energy, and thus less energy will be observed at the receiving sensors. Furthermore, the resin in the material could be described as a highly viscous fluid and the amplitude and phase of the guided wave is subject to change according to the fluid properties [4]. Throughout the layup process, the viscous properties of the resin may start to change, thus modifying its sound absorption characteristics. These effects are illustrated clearly in Fig. 16.3 where the Root Mean Squares (RMS) are shown for the four channels, for the first test consisting of 6 unidirectional plies. Note the long and short-term trends corresponding to the roller contact and tape layup. One could think of this process as having three different time scales at which different dynamics play a role; short medium and long. In the short-scale, the dynamics of the guided wave propagation play the main role, characterised by the amplitude modulation of the 300 kHz tone—the periods of this modulation are on the order of 50 µs. Arrivals of different wave modes, as well as reflections of the wave at the boundaries of the plate will all shape the modulation of the response. This short-scale has been decomposed using a Continuous Wavelet Transform (CWT). More specifically, the envelopes of the CWT have been used, as these capture the amplitude modulation of the pulse. An illustration of a wavelet envelope is shown in Fig. 16.4a for a representative guided wave response. In the medium scale, the periodicities introduced by contact of the ATP machine with the tool surface play the main role, with periods on the order of 5 s. This is shown in Fig. 16.3b. Figure 16.4b illustrates the time evolution of the short-scale dynamics, over the medium and long scales. If close attention is paid to Fig. 16.4, it can be noticed that although the energy in the pulses decreases over time (indexed by pulse number), different peaks contain different trends, and the presence of a defect could be apparent in any one of the points on the short-time axis of Fig. 16.4. This could be indicative of the scattering of waves from a defect. Multivariate time series analysis methods are needed to model the medium and long time scales.

The medium scale could be modelled as a Vector Auto Regressive (VAR) process which models the time evolution of a feature vector $\mathbf{y}_t$ as a function of its past values; it is essentially linear regression of the feature vector with lagged versions of itself:

$$\mathbf{y}_t = \sum_{p=1}^{P} \Pi_p \mathbf{y}_{t-p} + \boldsymbol{\epsilon} \tag{16.1}$$

where P is the number of lags, and Π_p is the regression coefficient matrix between $\mathbf{y}_t$ and its lagged value $\mathbf{y}_{t-p}$. The process is assumed to be corrupted with zero mean Gaussian noise $\boldsymbol{\epsilon}$ with covariance Q. One caveat in representing the wavelet envelopes as features in a multivariate time series model is that the dimensions of $\mathbf{y}$ will be the number of points in the envelope; at full sample rate, this is 10,000. Truncating the pulse and decimating it can reduce this to 330 points without much loss of information. However, as will be shown in Sect. 16.3.2, around 25 lags are required to capture the VAR process

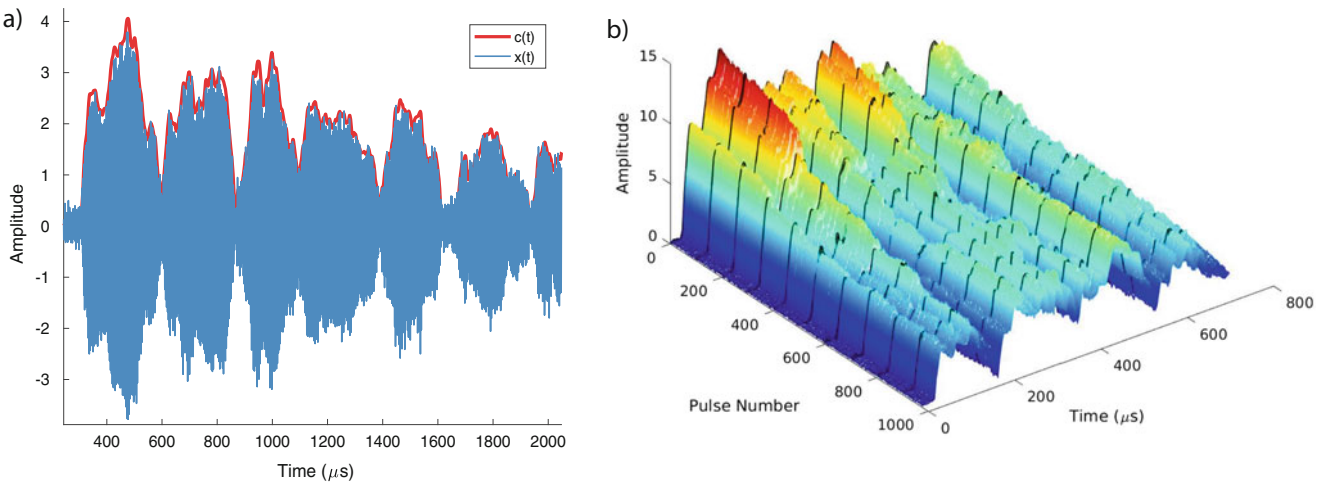

Fig. 16.4 (**a**) Wavelet envelope evaluated on one pulse response. Note that it clearly captures the amplitude modulation of the various reflections contained within the pulse. (**b**) Evolution of wavelet envelopes through time, each pulse is separated by 0.5 s. Note the decay in amplitude, and the change in relative shape

in this specific case (this corresponds to just over one period of roller contact). Given that only up to 900 pulses are recorded on each test, 330 dimensions is too many for the regression problem of Eq. (16.1), where only about 100 training points will be available, and this is only considering one channel. For this reason, Principal Component Analysis (PCA) has been used to reduce the dimensions of the wavelet envelopes from 330, to 3, whilst still preserving most of the variance encoded in the envelopes. The use of PCA is outlined in Sect. 16.3.1.1.

Lastly, the long time scale corresponds to the slow changing trends given by the cumulative process of tape laying, and this is captured and removed through cointegration. This is a methodology for removing common trends in multivariate time series analysis rooted in econometrics [5], but more recently introduced in an engineering context as a method for removing environmental trends in SHM data [6]. Note that there are other methods that may be well suited to this problem; PCA has also been used on its own to remove environmental trends in SHM data [7], and more recent methods have been developed based on robust regression to separate operational and environmental trends [8]. However, cointegration is well suited to the problem of modelling common cumulative trends such as this one. There have been some studies that have used cointegration on guided wave features to detect structural damage under changing environmental conditions [9]. The entire methodology presented here is summarised in Fig. 16.5, and the following sections describe each step in more detail. Note that in this process, the main output is the residual of the cointegration model, defined using Johansen's procedure [10], which implicitly assumes an underlying VAR model on the first difference, $\Delta \mathbf{y}_t$, of $\mathbf{y}_t$. This is discussed in Sect. 16.3.2.

16.3.1 Wavelet Enveloping

The response pulses are amplitude modulated 300 kHz sine tone-bursts, therefore lending themselves to enveloping analysis. Enveloping can be done relatively straightforward with a Hilbert transform, or a Continuous Wavelet Transform (CWT). Although both approaches have been compared, only the results based on a CWT envelope are presented here, as they tend to be better, while removing unwanted noise from lower frequency vibration (which was heavily present in these tests). This is achieved by the selection of a wavelet with a scale parameter appropriate to the carrier frequency of the pulse. Wavelet analysis is a well established signal processing tool for SHM [11, 12]. The CWT of the signal $x(t)$ is defined as its convolution with a wavelet function $\psi(a, t)$,

$$c(a,b) = \frac{1}{|a|^{1/2}} \int_{-\infty}^{\infty} x(t)\psi\left(\frac{t-b}{a}\right)dt \tag{16.2}$$

where a and b are scale and translation parameters respectively. In this investigation, a complex Morlet wavelet was used for ψ, defined as a wave windowed by a Gaussian:

$$\psi(t) = (\pi C)^{-0.5} e^{-t^2/B} e^{2\pi i C t} \tag{16.3}$$

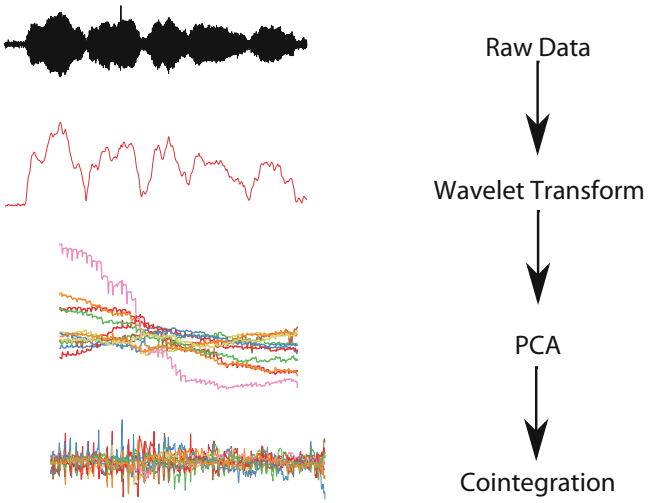

Fig. 16.5 Summary and illustration of the different steps in the data process methodology. Note that the VAR interpretation is inherent in the cointegration analysis

where B and C are bandwidth and centre frequency parameters, respectively. Because this is a complex wavelet, the output of the convolution in Eq. (16.2) is also complex, and is thus able to represent the signal amplitude and phase. Although the phase information has been investigated, the results presented in this paper all make use of the amplitude alone. Because the response of the guided wave is confined to a single frequency of 300 kHz, one can choose an appropriate scale a, to use when performing the CWT [Eq. (16.2)]. In this case $a = 16$ was used, and the wavelet transform was evaluated at varying translations b. Figure 16.4a, gives an illustration of the wavelet envelope defined by the modulus of the CWT evaluated on one pulse. Figure 16.4b illustrates the time evolution of envelopes throughout a layup test.

16.3.1.1 Use of PCA on Wavelet Envelopes

As discussed above, the dimensionality of the wavelet envelope, $c(t)$, is much larger than the number of pulses available and thus not readily suitable for a VAR representation, and thus also generally unsuitable for cointegration. PCA is used as a dimensionality reduction step. The goal of PCA is to represent the original data, in this case $\mathbf{c}$, using a much lower number of variables, $\mathbf{y}$, that can capture a large portion of the variance contained in $\mathbf{c}$. PCA is thus a linear map,

$$\mathbf{c} = C\mathbf{y} \tag{16.4}$$

where $\mathbf{c}$ is the original data, and $\mathbf{y}$ is its lower dimensional representation. The map, C, can be from an eigenvalue analysis of the covariance matrix of $\mathbf{c}$. The eigenvectors with the greatest eigenvalues correspond to those that represent the most variance in the original data. For this data set, it was found that the envelopes of each channel were represented well using only three principal components. PCA was applied to each channel individually, and C is derived using the training dataset. Any new points are projected into the lower-dimensional space using C derived during the training phase. This procedure results in a feature vector of 12 dimensions (three principal components per channel), which is much more suitable to the number of samples available to train the VAR model required by cointegration. The interested reader is referred to [13] for a richer description of PCA.

16.3.2 Cointegration of Feature Vectors

The medium time scale of the process can be described using a VAR model, described by Eq. (16.1). Such a model assumes that the residual is Gaussian distributed, stationary and ergodic. It is a straightforward procedure to estimate the maximum likelihood model parameters $\theta = (\Pi_1, \ldots \Pi_P)$ using least squares regression. It is critical to choose an appropriate model order P in order to capture the process correctly. If P is too low the model may underfit and the residual, $\boldsymbol{\epsilon}$, will not be white Gaussian. If P is too large on the other hand, the model may fail to generalise. A popular procedure to estimate P is to use the Akaike Information Criterion (AIC) or Bayesian Information Criterion (BIC), which use the likelihood of the model, penalised by the number of parameters, in order to choose a model with enough parameters to maximise its likelihood, but not at the expense of an unnecessarily large number of parameters. The reader can refer to [14] for more details. Whilst the VAR, as it stands in Eq. (16.1) is suitable for modelling the medium-scale dynamics of the process, it fails to model long-term trends, as it assumes stationarity, which is not the case in this dataset. This should be clear by examination of Figs. 16.3 and 16.4. Note that a regression term $D\boldsymbol{x}$ can be added to Eq. (16.1) in order to account for external inputs, and this leads to the also well-known VAR with eXogenous inputs (VARX). In the context of the ATP process, this could be the spatial coordinates of the robot head, number of applied courses and plies, temperatures, roller contact pressure, etc. Even if these parameters were available, there will still be unknown trends in the process due to the changing material properties of the polymer in the composite matrix, which are hard to measure directly (one could turn to ultrasound for this [4]). This provides enough motivation for turning to cointegration, which is well suited for the problem of modelling *unknown* cumulative trends in data. What follows is an outline description of cointegration commensurate to this paper, but the interested reader is encouraged to see [10] for a more thorough treatment.

The idea behind cointegration is to use regression in order to find common trends within the dimensions of a multivariate data set. A nonstationary time series $\mathbf{y}$ is cointegrated if a linear combination of itself $\boldsymbol{\beta}'\mathbf{y}$ is stationary.

$$\boldsymbol{\beta}'\mathbf{y}_t = \beta_1 y_{1t}, \ldots, \beta_n y_{nt} \tag{16.5}$$

The goal, is finding a suitable basis of vectors $\boldsymbol{\beta}$ that will reduce the nonstationary, but cointegrated process $\mathbf{y}$, to a zero-mean Gaussian variable, that is stationary. There are two general approaches to cointegration modelling: the Engle-Granger [15], and Johansen's [10]. The Engle-Granger procedure is the regression formulation to cointegration; It selects one variable from the data set as a dependent variable, and performs Ordinary Least Squares (OLS) regression to test whether a vector $\boldsymbol{\beta}$ can be found that produces a stationary process. The Johansen approach, on the other hand presents an autoregressive formulation of the process $\Delta\mathbf{y}_t$ with a correction factor proportional to $\mathbf{y}_{t-1}$. In this work, the Johansen approach [10] has been taken, mainly because it does not require one to hold one dimension out of the time series as dependent and it makes use of the autoregressive nature of the process to model the cointegration relationships. A VAR(p) process is stable if the solution to

$$\det(\mathbf{I}_n - \Pi z - \ldots - \Pi z^p) = 0 \tag{16.6}$$

has all roots outside of a complex unit circle. If Eq. (16.6) has a root on the unit circle, some or all variables in $\mathbf{y}$ are nonstationary, and they could *also* be cointegrated. If the variables are stationary and possibly cointegrated, the standard VAR representation is not suitable as it does not account for the cointegration. The Granger representation theorem, allows for a VAR model to be written in the following form:

$$\Delta\mathbf{y}_t = \Pi\mathbf{y}_{t-1} + \sum_{k=1}^{K} \Gamma_k \Delta\mathbf{y}_{t-k} + \boldsymbol{\epsilon} \tag{16.7}$$

where $\Pi = \sum_p \Pi_p - I_n$ and $\Gamma_k = -\sum_{j=k}^{p} \Pi_j$ for $k = 1, \ldots p-1$. This is referred to as a Vector Error Correction (VEC) model. The matrices are usually referred to as the long-run and short-run impact matrices respectively. The VAR parameters can be also easily recovered from the VEC parameters. Any potential cointegrating relationships are hidden in the $\Pi\mathbf{y}_{t-1}$ process, and since the VEC model assumes that the first derivative of the process $\Delta\mathbf{y}$ is stationary it follows that if $\mathbf{y}$ is cointegrated, the cointegrating relationships will be represented by $\Pi\mathbf{y}_{t-1}$. If the VAR process has unit roots, then Π will be singular which in turn means it has reduced rank: $rank(\Pi) = r < n$. If $r = 0$ then $\mathbf{y}$ is not cointegrated, and the VEC model reduces to a VAR process of $\Delta\mathbf{y}$. If $r < n$ then $\mathbf{y}$ is cointegrated with r linearly independent cointegrating vectors and $n - r$ common stochastic trends. Furthermore, Π can be expressed as a product $\Pi = \boldsymbol{\alpha}\boldsymbol{\beta}'$, where both $\boldsymbol{\alpha}$ and $\boldsymbol{\beta}$ are of rank r. Rows of $\boldsymbol{\beta}$ then become a basis for the cointegrating vectors, while $\boldsymbol{\alpha}$ dictate their impact on $\Delta\mathbf{y}$. The parameters $\theta = \{\boldsymbol{\alpha}, \boldsymbol{\beta}, \Gamma_1, \ldots, \Gamma_K\}$ of the VEC model can be estimated using maximum likelihood. In this paper, the maximum likelihood parameter estimation method that is outlined in [10] is used. Johansen describes a procedure to find the appropriate rank of $\boldsymbol{\beta}$ by starting from $r = 0$ and testing the hypothesis that there exists a matrix with rank higher than r by using a test statistic based on Gaussian likelihood ratio tests (the trace of the eigenvalues of $\boldsymbol{\beta}$), and incrementing this until no higher rank can be found.

Now, once the VEC parameters are found, novelty detection can be performed on the residuals resulting from the long-run relationships of Eq. (16.7), defined solely by the projection on $\boldsymbol{\beta}$,

$$r = \boldsymbol{\beta}'\mathbf{y}_t \tag{16.8}$$

for every feature vector (principal components of pulse envelopes, in this case). One would expect the residual r to remove the trends in the feature matrix $\mathbf{Y} = \{\mathbf{y}_1, \ldots, \mathbf{y}_n\}$ and to project it as Gaussian, distributed with zero mean. The next section shows the results of the application of Johansen's cointegration method outlined here, to the PCA of the wavelet envelopes described in the previous sections. The results are presented in terms of the residual r, evaluated using Eq. (16.8).

16.3.3 Results

The features used in this case were the first three principal components of the modulus of the CWT, for all four channels. The feature matrix, $\mathbf{Y}$ in this case contains 12 rows, and n columns, where n is the number of pulses in each test.

Recall that three tests were carried out, the first one being a normal layup without defects, whilst the second and third contained different types of defects. The maximum likelihood $\boldsymbol{\alpha}$ and $\boldsymbol{\beta}$ parameters for a VEC model with 25 lags (found to be appropriate) were estimated using features from all the pulses of the baseline test. This constitutes the training data set. The residuals of the model were then evaluated using Eq. (16.7) and the estimated model parameters from the training set.

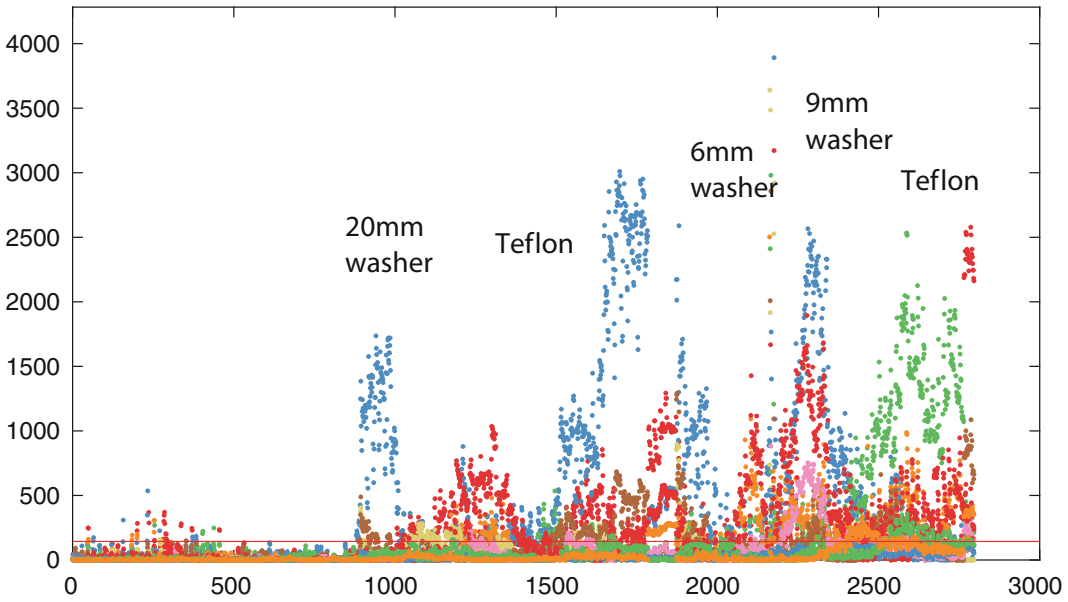

Fig. 16.6 All cointegration square residuals are shown, in *different colours*. Note that most of them succeed at staying under the threshold until point 1000, approximately when the first defect was introduced, some are better than others at highlighting the fault. Figure 16.7 shows the 8th residual in more detail, separated by tests.

The results are shown in Fig. 16.6 for all of the residuals, and all three tests, while Fig. 16.7 shows in more detail one of the cointegrating residuals that performed well at remaining bounded within the 99th percentile threshold of the training set, while highlighting the defect by large excursions of the residuals beyond the threshold.

16.4 Discussion and Conclusions

The results shown in Figs. 16.6 and 16.7 are highly encouraging. First, it is clear that the cointegrated residuals capture the process well, as they remain bounded within a threshold before the defects are introduced, and are also Gaussian (not shown here). The first layer of tests two and three do not contain any defects, and thus act as rigorous validation cases, to test how well the method performs on a different layup than that used to estimate the cointegration parameters. If the model generalises well, one would expect the residuals to remain under the threshold; this seems to generally be the case, except for the first few points on test three. This is reasonable given that, during the training phase, the first few points do not have corresponding lags, and so the $\boldsymbol{\beta}'\mathbf{y}_t$ cointegration relationship may not be strictly applicable for $t < P$. On the rest of the layers of tests two and three, the cointegration residuals clearly show that defects as subtle as a small Teflon patch may be identified well. There are several interesting points to note. In both cases, the Teflon patch was detected only after a further layer of ply was applied to it, hinting that it is the separation between the plies that has caused the change in residuals, and not the Teflon itself. A similar trend seems to appear for the 20 mm washer, which is the most obvious defect introduced. However it should be pointed out that the washer was moved by the roller after it was applied, moving it close to the path *BA*, and possibly explaining why it is detected better in the third layer of the second test. The better detection of the smaller washers is not a surprise. While all the other defects were placed away from the path of any channel pair, the 9 mm washer was placed directly in the **AA** path, and hence its detectability is better. Note also that the best performing cointegrating residual (in terms of good generalisation and excursions during defects) has been examined in the results presented here and it is left as further work to model the entire set of residuals using multivariate statistical methods.

While the procedure implemented here may seem overly complex, the reader is reminded that the process is only modelling the long term trends using cointegration, of features that capture much shorter term trends, such as a wavelet enveloping. The addition of PCA to the wavelet envelopes was introduced in order to reduce its dimensions (from an effective 330, per channel, to 3 per channel) in order to facilitate the use of cointegration. Finally, the long term trends of this process have been shown to be nonstationary, but cointegrated, which is expected from such a cumulative process. Inference of the

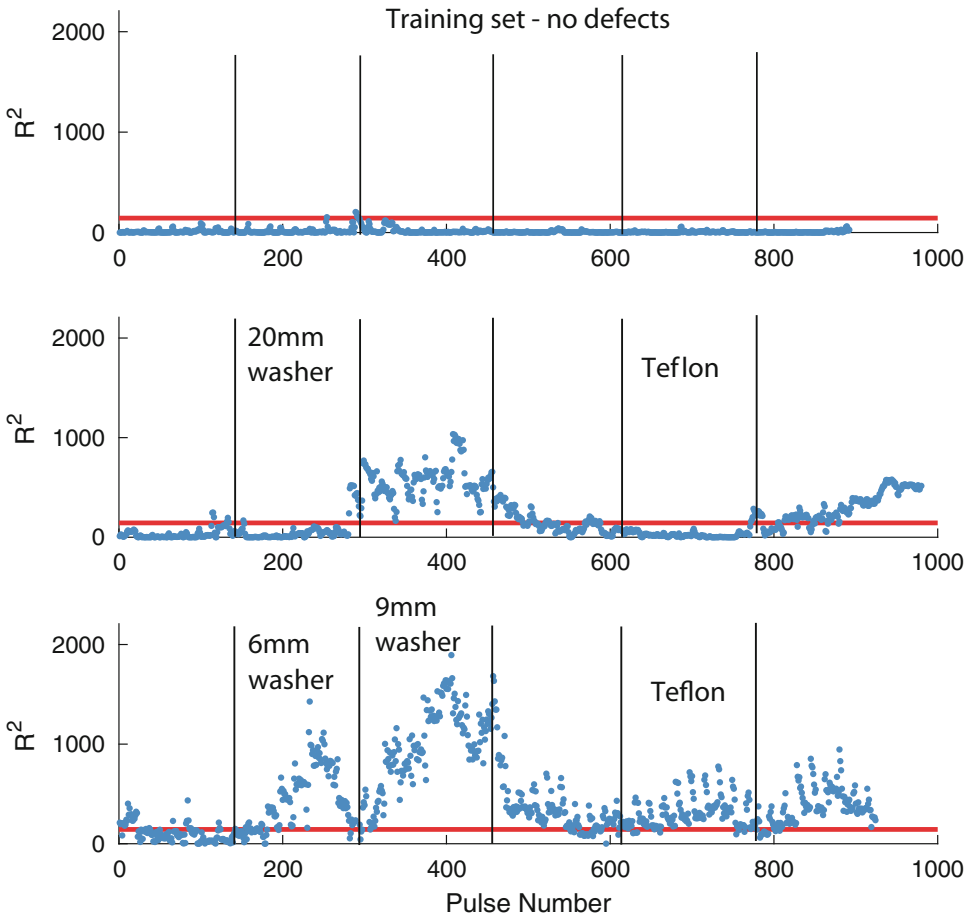

Fig. 16.7 Eighth cointegration squared residual, showing (**a**) the baseline test, (**b**) layup with a 20 mm washer and a Teflon sheet and (**c**) layup with a 9 and 6 mm washers, and a Teflon sheet towards the end. The threshold shown is the 99th percentile of the squared residual of the test set on the baseline condition. Vertical lines divide the layers of ply

presence of defects was carried out using information from four different channels. This study paves the way for a more detailed examination of more subtle, and perhaps more relevant defects under this methodology. A detailed examination of the sensitivity to different levels of defects and their localisation should follow on from the results presented here.

Acknowledgements The authors are very grateful to Richard Smith from AMRC with Boeing, who assisted in the ATP process and data collection, and without whom this study would have not been possible.

References

1. Adams, R.D., Cawley, P.: A review of defect types and nondestructive testing techniques for composites and bonded joints. NDT Int. **21**(4), 208–222 (1988)
2. Scott, I.G., Scala, C.M.: A review of non-destructive testing of composite materials. NDT Int. **15**(2), 75–86 (1982)
3. Worden, K., Manson, G., Fieller, N.R.J.: Damage detection using outlier analysis. J. Sound Vib. **229**(3), 647–667 (2009)
4. Zhu, Z., Wu, J.: The propagation of Lamb waves in a plate bordered with a viscous liquid. J. Acoust. Soc. Am. **98**(2), 1057–1064 (1995)
5. Granger, C.W.J.: Developments in the study of cointegrated economic variables. Oxf. Bull. Econ. Stat. **48**(3), 213–228 (1986)
6. Cross, E.J., Worden, K., Chen, Q.: Cointegration: a novel approach for the removal of environmental trends in structural health monitoring data. Proc. R. Soc. Math. Phys. Eng. Sci. **467**(2133), 2712–2732 (2011)
7. Manson, G.: Identifying damage sensitive, environment insensitive features for damage detection. In: 3rd International Conference on Identification in Engineering Systems, Swansea (2002)
8. Dervilis, N., Worden, K., Cross, E.J.: On robust regression analysis as a means of exploring environmental and operational conditions for SHM data. J. Sound Vib. **347**, 279–296 (2015)

9. Worden, K., Cross, E.J., Antoniadou, I., Kyprianou, A.: A multiresolution approach to cointegration for enhanced SHM of structures under varying conditions - an exploratory study. Mech. Syst. Signal Process. **47**(1–2), 243–262 (2014)
10. Johansen, S.: Likelihood-Based Inference in Cointegrated Vector Autoregressive Models. Oxford University Press, Oxford (1995)
11. Staszewski, W.J., Robertson, A.N.: Time-frequency and time-scale analyses for structural health monitoring. Philos. Trans. A Math. Phys. Eng. Sci. **365**(1851), 449–477 (2007)
12. Worden, K., Staszewski, W.J., Hensman, J.J.: Natural computing for mechanical systems research: A tutorial overview. Mech. Syst. Signal Process. **25**(1), 4–111 (2011)
13. Bishop, C.M.: Pattern Recognition and Machine Learning. Springer, New York (2006)
14. Shumway, R.H., Stoffer, D.S.: Time Series Analysis and Its Applications. Springer, New York (2011)
15. Engle, R.F., Granger, C.W.J.: Co-integration and error correction: representation, estimation, and testing. Econometrica **55**(2), 251–276 (1987)

Chapter 17
Development of a Mathematical Model to Design the Control Strategy of a Full Scale Roller-Rig

Ferruccio Resta, Edoardo Sabbioni, Davide Tarsitano, Dino Deva, Daniele Termini, and Alvaro Fumi

Abstract Roller rigs have been built world-wide to investigate the dynamics of railway vehicles and they have particularly been applied to the development of high-speed trains.

Specifically, the present paper focuses on a roller-rig for testing full scale locomotives/coaches, which is located at the Osmannoro Centre of Experimental Dynamics (Italy). The considered roller rig allows to test vehicles having up to 6 axes and 3 bogies. Aim of the roller-rig is to verify traction systems of locomotives, to test anti-slip/anti-skid control systems, to identify braking performance and to perform electromagnetic tests (radiated emissions and immunity) on the locomotive.

At present, the design of the control strategy allowing to perform the desired tests is under development. To account for roller-rig and vehicle dynamics at a design stage, a numerical model of the complete test bench (including the locomotive/coach, the roller rig, the actuating devices and the corresponding control systems) was developed and interfaced with the control strategy of the test bench. The present paper describes the simulation tool developed on purpose and preliminary experimental results are presented.

Keywords Roller-rig • Multi-body model • Co-simulation • Experimental tests

17.1 Introduction

Roller-rigs, full size and scale, are being used by researchers and railway organizations worldwide to assist the understanding of the behaviour of railway vehicles and the development of faster, safer and more efficient railways [1–6].

In fact, roller-rigs offer the advantage that experiments are independent of weather conditions, individual phenomena can be investigated, experiments and constrains as well as particular conditions are reproducible, experiments are less expansive than track testing. Though considerable differences between the dynamics of railway vehicles on roller-rigs and on real tracks can be found, these rigs have proved to be useful for basic research (models validation [7], running stability analysis), for the development and testing of new concepts of innovative railway design [8], for vehicle components optimization (layout optimization), for the design and testing of active control systems (anti-skid, anti-slip devices, active yaw dampers, etc.) and for further investigations hardly performable on the track for safety reasons (e.g. determination of the performance limits, critical speed, skidding, failure tests, development of health monitoring devices, [1, 9]).

In this paper, the simulation tool developed to design and test the control logic of the roller-rig is described. It is constituted of:

- a mathematical model of the test bench developed in MatLab/Simulink environment, which includes a multi-body representation of the locomotive/coach and a lumped-parameters schematization of the driveline and of the roller-rig;
- the control logic actually present on the test bench developed in LabView environment (the control system is based NI hardware).

F. Resta • E. Sabbioni (✉) • D. Tarsitano
Department of Mechanical Engineering, Politecnico di Milano, Via La Masa 1, Milano (MI), Italy
e-mail: edoardo.sabbioni@polimi.it

D. Deva • D. Termini
Simpro S.p.A., Via Torino 446/A, Brandizzo (TO), Italy

A. Fumi
RFI-Rete Ferroviaria Italiana S.p.A., Via di Portonaccio 175, Roma (RO), Italy

N. Dervilis (ed.), *Special Topics in Structural Dynamics, Volume 6*, Conference Proceedings
of the Society for Experimental Mechanics Series, DOI 10.1007/978-3-319-53841-9_17

A co-simulation is then performed between the two environments. During the co-simulation of this mechatronic system Labview and MatLab/Simulink are running at the same time exchanging inputs and outputs after predefined time steps.

In the following, the developed simulation tool is described. Then preliminary experimental tests carried out with a passenger coach and the developed control strategy are presented.

17.2 Roller-Rig

Figure 17.1 shows the roller-rig located at the Osmannoro Centre of Experimental Dynamics. Aim of the roller-rig is to verify traction systems of locomotives up to 6 axes, to test anti-slip/anti-skid control systems, to identify braking performance, to develop diagnostic/monitoring systems and to perform electromagnetic tests (radiated emissions and immunity) on the locomotive.

Main characteristics of railway vehicles which can be tested on the roller-rig are reported in Table 17.1. As it can be seen, the roller-rig allows to test vehicles having up to 6 axes and 3 bogies.

In the test bench are present 6 rollersets (one for each possible axle). Each of them is constituted of:

- two 950 kW electric motor (one per wheel);
- two torquemeters to measure torques transmitted by the shafts of the roller motors;
- three encoders to measure the angular speeds of the rollers and of the vehicle axle;
- six laser sensors to measure the distance of the wheels from the roller in the longitudinal, lateral and vertical direction.

Fig. 17.1 Osmannoro Centre of Experimental Dynamics roller-rig

Table 17.1 Roller-rig main characteristics

Max. number of axles (−)	6
Max. number of bogies (−)	3
Max. load per axle (kg)	25,000
Gauge (mm)	1435
Max. wheel diameter (mm)	1350
Bogie wheelbase (mm)	1600 ÷ 3200
Max. speed (km/h)	400
Max. traction power (MW)	10
Max. traction force (kN)	500
Max. braking power (MW)	10

17.3 Simulation Tool

In order to design and test the control logic of the roller-rig, a simulation tool was developed based on co-simulation technique.

Figure 17.2 shows the scheme of the roller-rig and the flow of information between its components. A locomotive/coach is placed on the rollers, which are driven by independent electric motors. Roller-rig and locomotive/coach are coupled by means of contact forces between wheels and rollers. The braking system and/or the traction system (only present in the case of a locomotive) provides the vehicle with the drive/brake torques ($u_{m,dem}$) demanded by the simulated test, taking into account anti-slip and anti-skid devices intervention.

Resistant forces acting on the vehicle during the considered test are reproduced by applying proper torques to the rollers (u_{dem}). Coherence between vehicle drive torques, roller resistant torques and roller angular speeds is given by the roller-rig control system. It consists of the regulators controlling speeds/torques of the motors driving the rollers and of a Real Time (RT) simulator of the vehicle longitudinal dynamics. The basic idea behind the control strategy for the roller-rig is to avoid macro-slippage between wheels and rollers in any working condition, even when low adherence tests are simulated [10]. This can be achieved by properly controlling the motors driving the rollers in order to reproduce, in the contact area, the same tangential forces existing between the wheel and the rail during track testing, rather than the same relative velocity. Thus, torques applied to the rollers and their angular speed must be determined by the RT vehicle model according to the simulated test.

The developed simulation tool mimics the real test bench, based on co-simulation technique. The roller-rig including the railway vehicle (comprising the brake/traction system) and the rollersets (comprising rollers, motors and their regulators) has been modelled in MatLab/Simulink environment and it has been interfaced with the control logic actually present in the test bench (developed in Labview environment), so to test its effectiveness.

In the following the elements of the simulation tool are described, making reference to case in which the tested vehicle is a locomotive.

17.3.1 Roller-Rig Mathematical Model (MatLab/Simulink)

The mathematical model [11] includes a multi-body representation of the locomotive (Fig. 17.3) and a lumped parameters schematization of the driveline and of the roller-rig (Fig. 17.4). Concerning the locomotive, carbody and bogies are modelled as rigid bodies, while wheelsets are represented as deformable elastic bodies, using a modal superposition approach in order to take into account their torsional deformability [12]. Carbody, bogies and wheelsets are linked one to the other by means of elastic and damping elements reproducing primary and secondary suspensions. The simulation code accounts for the motion of the locomotive in vertical, lateral and longitudinal direction. The d.o.f.s of the system are shown in Fig. 17.3. The vehicle

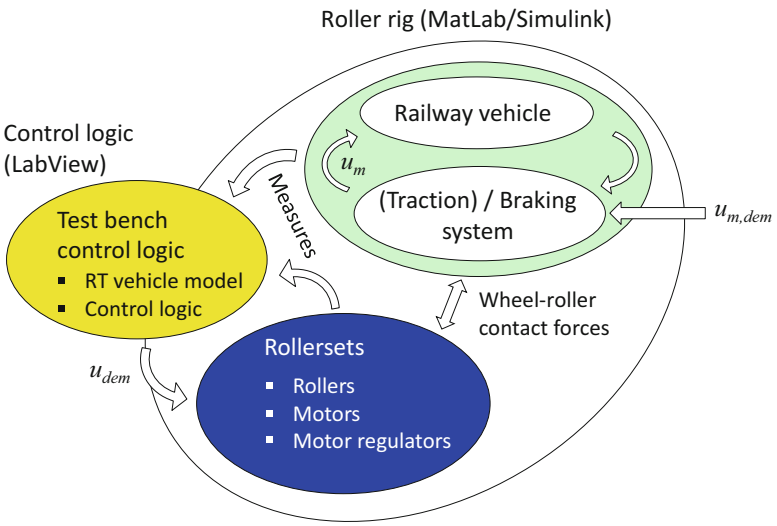

Fig. 17.2 Block diagram of the roller-rig

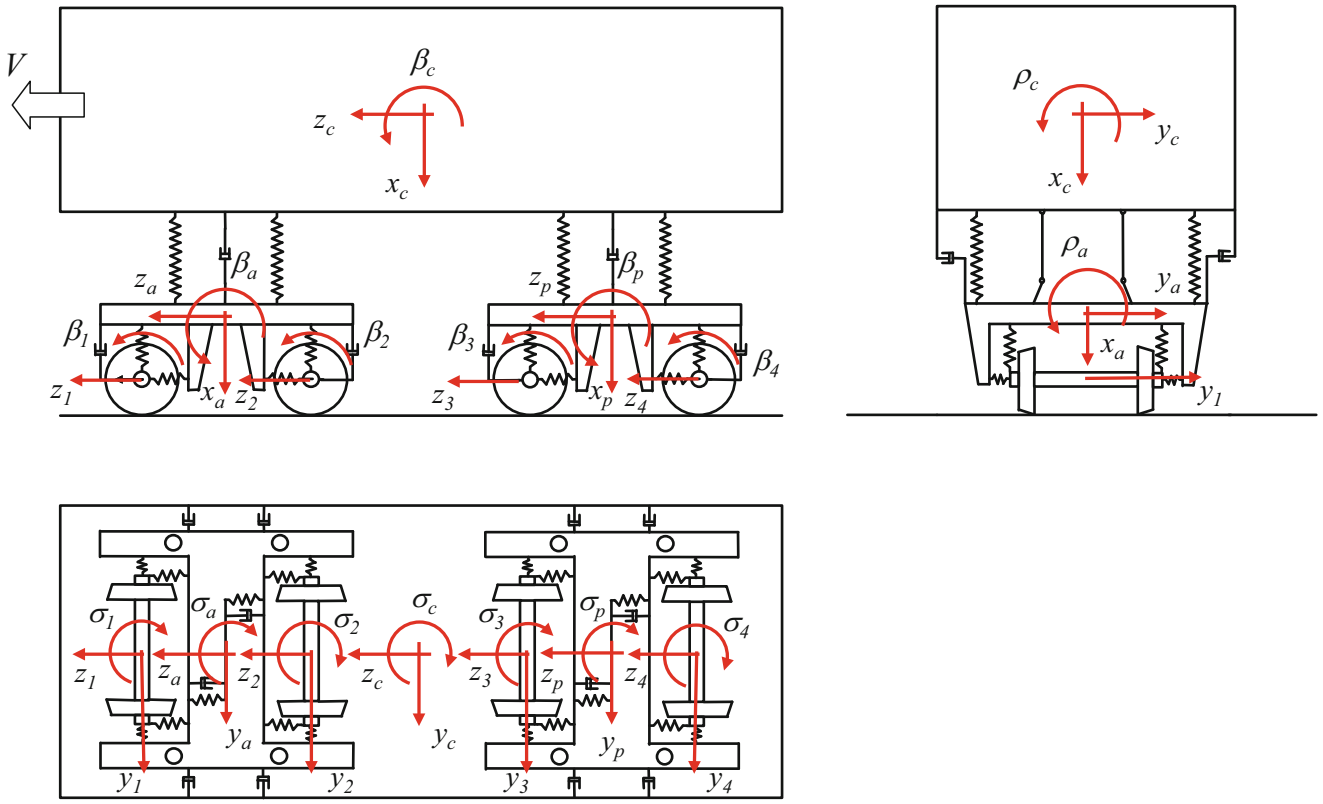

Fig. 17.3 Rail vehicle model

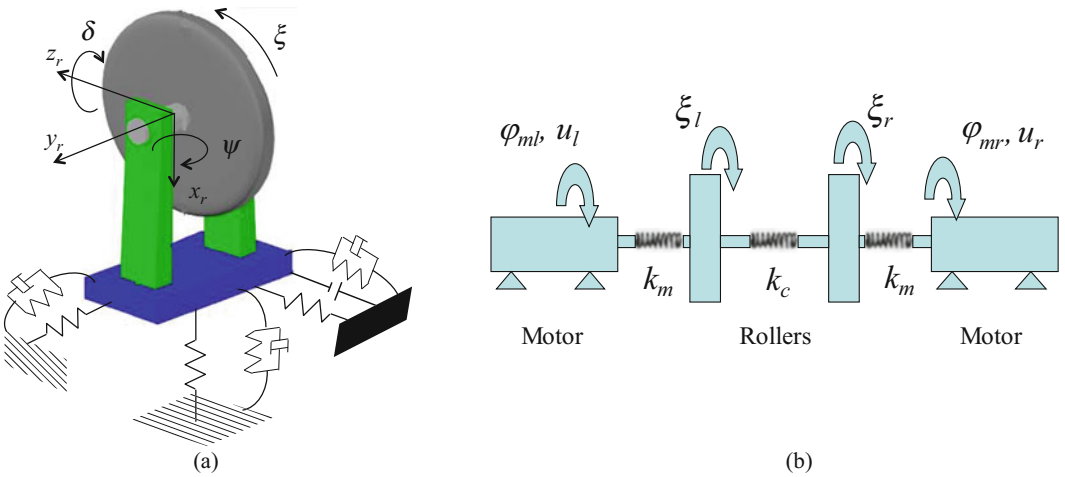

Fig. 17.4 (**a**) Roller. (**b**) Roller-motor connection

equations of motion are written with respect to a moving reference system, traveling along the ideal track centreline, which is a straight line in tangent track.

On the other hand, a lumped parameters schematization has been adopted for the transmission system of the locomotive and for each roller and motor constituting the test bench. In particular, for what concerns the driveline, the torsional flexibility of the connection between the driving electric motors and the wheelsets has been considered and backlash has been included accounting for the clearance between the teeth of the transmission [13].

For each pair of rollers and motors (Fig. 17.4), 14 d.o.f.s have been considered: 6 d.o.f.s for each roller (displacements x_r, y_r, z_r and rotations δ, ξ, ψ) and the rotation φ_m of each motor. As it can be seen from Fig. 17.4, compliance of roller supports

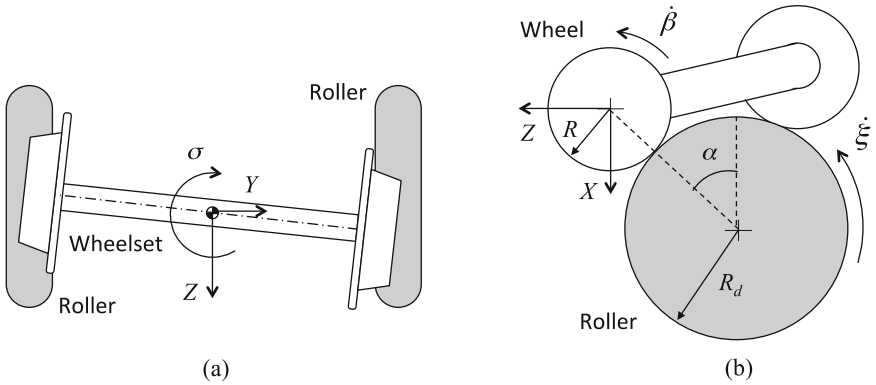

Fig. 17.5 Kinematics of lozenging. (**a**) Top view, (**b**) lateral view

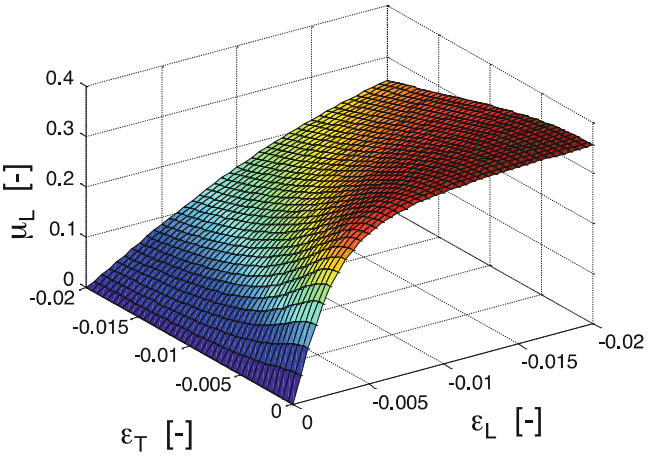

Fig. 17.6 Longitudinal friction coefficient vs. longitudinal and lateral creepage

and torsional flexibility of motor shaft and rollers' connecting shaft have been introduced in order to take into account the influence of the roller-rig dynamics on the tested vehicle. Supports compliance was experimentally identified.

Separate subsets of equations can be respectively written for the locomotive, the driveline and the roller-rig. Wheel-roller contact forces are then introduced as coupling terms between the sets of equation referring to the vehicle and the roller-rig. The equations of motion can thus be expressed as follows:

$$\begin{cases} [M_t]\,\underline{\ddot{x}}_t + [C_t]\,\underline{\dot{x}}_t + [K_t]\,\underline{x}_t = \underline{Q}_{tr}\left(\underline{\dot{x}}_t, \underline{x}_t, \underline{\dot{x}}_r, \underline{x}_r, \underline{u}_{dem}, t\right) + \underline{Q}_{tm}\left(\underline{\dot{x}}_t, \underline{x}_t, \underline{\dot{x}}_m, \underline{x}_m, \underline{u}_m, t\right) \\ [M_r]\,\underline{\ddot{x}}_r + [C_r]\,\underline{\dot{x}}_r + [K_r]\,\underline{x}_r = \underline{Q}_r\left(\underline{\dot{x}}_t, \underline{x}_t, \underline{\dot{x}}_r, \underline{x}_r, \underline{u}_{dem}, t\right) \\ [M_m]\,\underline{\ddot{x}}_m + [C_m]\,\underline{\dot{x}}_m + [K_m]\,\underline{x}_m = \underline{Q}_m\left(\underline{\dot{x}}_t, \underline{x}_t, \underline{\dot{x}}_m, \underline{x}_m, \underline{u}_{m,dem}, t\right) \end{cases} \tag{17.1}$$

where $\underline{x}_t$, $\underline{x}_m$ and $\underline{x}_r$ are the vectors containing the coordinates of the locomotive, of the driveline and of the roller-rig respectively, $\underline{Q}_{tr}$ and $\underline{Q}_r$ represent the Lagrangian components of wheel-rollers contact forces (including components due to wheelset decrowning and lozenging, see Figs. 17.5 and 17.7) with respect of vehicle and rollers d.o.f.s and $\underline{Q}_{tm}$ and $\underline{Q}_m$ include the Lagrangian components of the drive torques (input to the model, $\underline{u}_{m,dem}$) provided by the locomotive traction system with respect of vehicle and driveline d.o.f.s. Finally, vector $\underline{u}_{dem}$ collects the torques computed by the test bench control logic.

The contact model is based on a geometrical analysis of the measured wheel and roller profiles. Contact parameters such as rolling radius, contact angle and decrowning angle (angle α, Fig. 17.5) are reported in table form, as functions of wheel-rail lateral and longitudinal displacements. It must be in fact noted that when the wheelset yaws on a rollerset, the wheels move off the crown of the rollers (Fig. 17.5 and 17.7). As a consequence, the mass of the centre of gravity of the wheelset moves downward and the wheelset lozenges, as shown in Fig. 17.5. Then the point of contact at each wheel on the roller moves away from the top of the rollers and the wheelset is said to decrown, as depicted in Fig. 17.7.

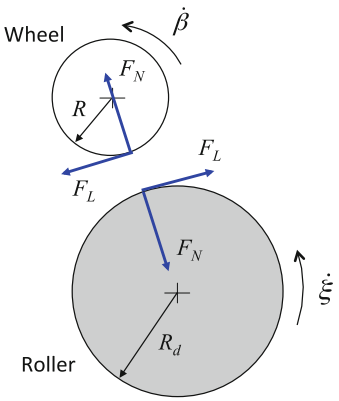

Fig. 17.7 Forces due to decrowning

Wheel-roller contact force ($F_{c,i}$) is assumed to be a non-linear function of the vertical load ($F_{N,i}$) and of the longitudinal and lateral creepages ($\varepsilon_{L,i}$, $\varepsilon_{T,i}$) according to (Fig. 17.6):

$$\begin{aligned} &F_{c,i} = -\mu\left(\varepsilon_{tot,i}\right) F_{N,i}; \qquad F_{L,i} = F_{c,i}\frac{\varepsilon_{L,i}}{\varepsilon_{tot,i}}; \qquad F_{T,i} = F_{c,i}\frac{\varepsilon_{T,i}}{\varepsilon_{tot,i}} \\ &\mu\left(\varepsilon_{tot,i}\right) = \frac{\chi\varepsilon_{tot,i}}{\sqrt{\left(1+\left(\frac{\chi\varepsilon_{tot,i}}{\mu_{\max}}\right)^2\right)}}; \qquad \varepsilon_{tot,i} = \sqrt{\varepsilon_{L,i}^2 + \varepsilon_{T,i}^2} \end{aligned} \tag{17.2}$$

Lateral and longitudinal creepages are then computed as:

$$\begin{cases} \varepsilon_{Li} = \frac{\left(V_{L,i} - \dot{\beta}_i R_i\left(\gamma_{rel,i}\right)\right) + \dot{\xi}_i R_d}{\left|\dot{\xi}_i R_d\right|} \\ \varepsilon_{Ti} = \frac{V_{T,i}}{\left|\dot{\xi}_i R_d\right|} \end{cases} \tag{17.3}$$

where $V_{L,i}$ and $V_{T,i}$ are respectively the longitudinal and lateral velocity of the i-th wheel centre, while R_i and $R_{d.}$ are the i-th wheel and roller radii. As it can be seen, both the locomotive and the roller-rig dynamics are included in the definition of contact forces.

Motors driving the rollers have been introduced into the model through their characteristic curve torque vs. angular speed, while their dynamics has been modelled as a first order time lag, so to account for motors' bandwidth, nonlinearity and torque saturation.

17.3.2 Control Logic (Labview)

The control strategy implemented in the test bench is based on the algorithm proposed in [10]. As already mentioned, the basic idea of the control logic is to regulate the driving torque of the rollers so to reproduce on the rig the same angular speeds the wheels would have on the rail, but avoiding avoid macro-slippage between wheels and rollers. On the purpose, a RT model simulating the longitudinal dynamics of the locomotive is needed.

According to the proposed algorithm, torque demanded by the control logic to the i-th roller is given by:

$$u_{dem,i} = \frac{J_{yr}R}{J_{ys}R_d}\widehat{C}_i - \left(\frac{J_{yr}R^2}{J_{ys}R_d^2} + 1\right) R_d f_{l,i}^{(s)} + \left[k_p\left(\dot{\beta}_i - \dot{\beta}_i^{(s)}\right) + k_i\left(\beta_i - \beta_i^{(s)}\right)\right] \tag{17.4}$$

In Eq. (17.4), R and R_d are respectively wheel and roller radii, J_{yr} and J_{ys} are respectively the roller and the wheel moments of inertia, $\dot{\beta}_i$ is the angular speed of the i-th wheel, while $\dot{\beta}_i^{(s)}$ and $f_{l,i}^{(s)}$ are respectively the angular speed and the longitudinal force of the i-th wheel predicted by the RT model.

The estimate of the driving/braking torque applied by the locomotive to the i-th wheel is given by:

$$\widehat{C}_i = -\frac{R}{R_d} u_{meas,i} + \left(J_{yr} \frac{R^2}{R_d^2} + J_{ys} \right) \ddot{\beta}_i \tag{17.5}$$

being $\ddot{\beta}_i$ the angular acceleration of the i-th wheel (which is estimated based on the measurements of the angular speed of the roller and of the axle) and $u_{meas,i}$ being the torque measured by the torquemeter.

The longitudinal force of the i-th wheel $f_{l,i}^{(s)}$ is calculated by the RT vehicle model simulating the longitudinal dynamics of the locomotive during the considered maneuver:

$$\begin{cases} M\dot{V}^{(s)} = \sum_{i=1}^{8} f_{l,i}^{(s)} + P(t) \\ J_{ys}\ddot{\beta}_i^{(s)} = \widehat{C}_i - f_{l,i}^{(s)} R \end{cases} \qquad f_{l,i}^{(s)} = -\mu\left(\varepsilon_i^{(s)}\right) F_{N,i}^{(s)}; \qquad \varepsilon_i^{(s)} = \frac{V^{(s)} - \dot{\beta}_i^{(s)} R}{V^{(s)}} \tag{17.6}$$

where M is global mass of the locomotive, $V^{(s)}$ is the longitudinal speed of the RT vehicle model cog, $P(t)$ includes the resistant force applied to the vehicle (aerodynamic resistance, rail slope, effect of other coaches attached to the locomotive, etc.), $\ddot{\beta}_i^{(s)}$ and $\varepsilon_i^{(s)}$ are respectively the angular acceleration and the creepage of the i-th wheel of the RT simulator. Note that with the apex$^{(s)}$ the quantities calculated by the RT model are indicated.

It is to point out that, in Eq. (17.4), the torque demanded to the i-th roller includes a PI regulator term based on the error between the angular speed of the wheel of the locomotive and of the RT simulator of the control logic, so to avoid differences between the simulated and the performed maneuver.

17.4 Preliminary Experimental Results

To assess the performance of the developed control logic, preliminary experimental tests were carried out with a passenger coach (Fig. 17.1). It is to point out that, since no motors are installed on the coach, it has to be accelerated simulating a track with a rail gradient.

As an example, Fig. 17.8 shows the results of an experimental test, during which:

- a rail gradient of $-1.5°$ is imposed to accelerate the coach up to 70 km/h (0–60 s);
- after 90 s the coach is braked till standstill. The pneumatic braking system of the coach is used by means of a manual remote control.

The time histories of the imposed rail gradient (input to the RT model simulating the coach longitudinal dynamics), the speed of the coach wheelsets and torques measured by torquemeters are shown.

As it can be seen, during the first part of the test, a driving torque is imposed by the roller-rig motors to accelerate the coach. Then torques become almost equal to zero when the rail gradient is removed. Finally, as the coach is braked, torques provided by roller-rig motors increase to balance the braking torques applied by the coach and so decelerate wheelsets and rollers avoiding macro-slippages between the wheels and the rollers.

17.5 Concluding Remarks

In this paper, the simulation tool developed to design and test the control logic of the roller-rig placed at the Osmannoro Centre of Experimental Dynamics is presented. It is constituted of a mathematical model of the test bench developed in MatLab/Simulink environment and the control logic actually present on the test bench developed in LabView environment. A co-simulation was therefore performed between the two environments.

Results of preliminary experimental tests carried out with a passenger coach proved the effectiveness of the developed control logic before the execution of tests with a locomotive.

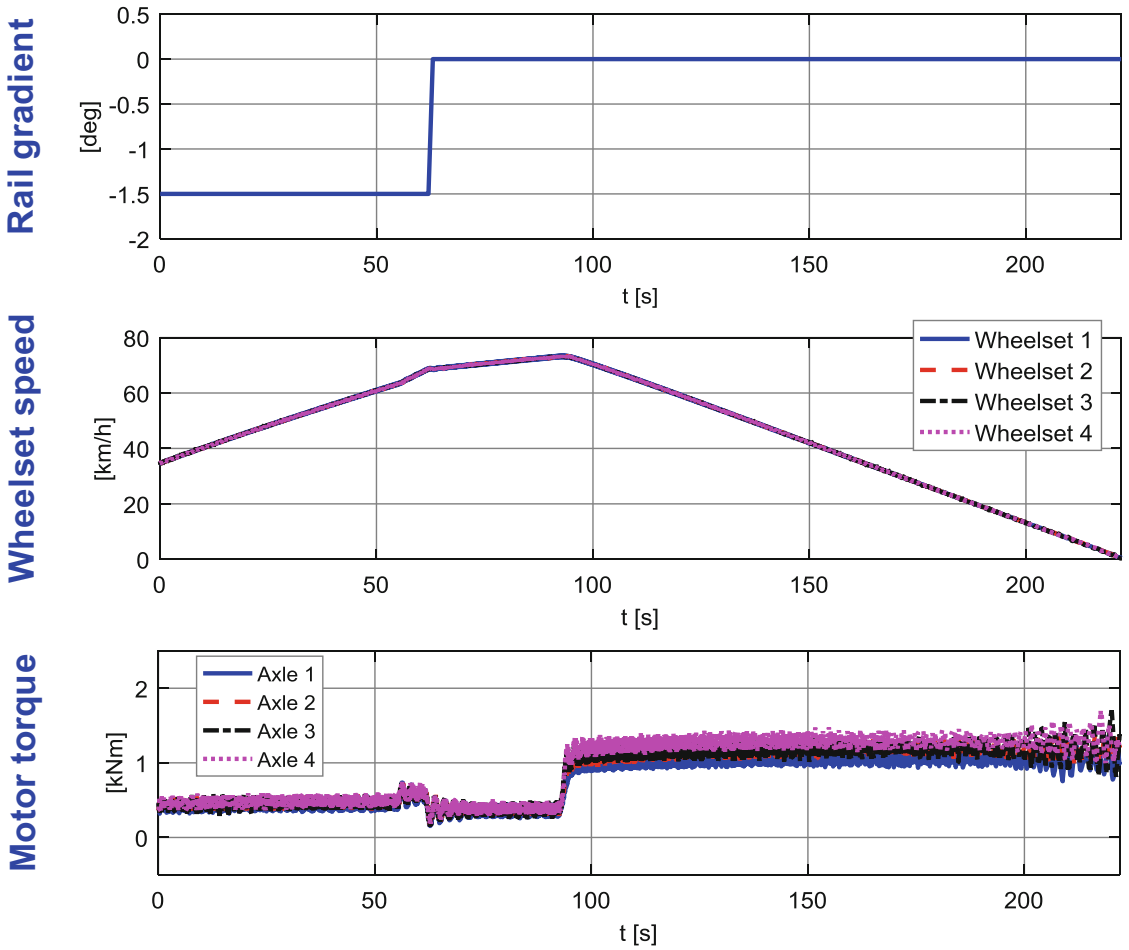

Fig. 17.8 Experimental test: time history of imposed slope (simulation input, *top* part of the figure), wheelsets' speed (*central* part of the figure) and roller-rig motors' torque (*bottom* part of the figure)

References

1. Jaschinski, A., Chollet, H., Iwnicki, S., Wickens, A., Von Wurzen, J.: The application of roller rigs to railway vehicle dynamics. Veh. Syst. Dyn. **31**, 345–392 (1999)
2. Chul Oh, S.: Evaluation of motor characteristics for hybrid electric vehicles using hardware in the loop concept. IEEE Trans. Veh. Technol. **54**(3), 817–824 (2005)
3. Kent, S., Tunley, J.: The evaluation of wheel slide protection equipment. AEA Technol. Rail. **1**, 15 (1997)
4. Bruni, S., Cheli, F., Resta, F.: A model of an actively controlled roller rig for tests on full-size railway wheelsets. Proc. Inst. Mech. Eng. F J. Rail Rapid Transit. **215**(4), 277–288 (2001)
5. Dukkipati, R.V.: A parametric study on lateral stability of rail boogie on a roller rig. Proc. Inst. Mech. Eng. F J. Rail Rapid Transit. **213**, 39–47 (1999)
6. N. Bosso, A. Gugliotta, E. Napoli, A. Somà, Simulation of a scaled roller rig. In: 5th ADAMS/Rail Users' Conference. Haarlem, The Netherlands (2000)
7. Iwnicki, S.D., Wickens, A.H.: Validation of a MatLab railway vehicle simulation using a scale roller rig. Veh. Syst. Dyn. **30**(3), 257–270 (1998)
8. G. Dreher, F. Jobst, G. Gotz, et al., Active hunting control of a wheel/rail vehicle demonstrated up to 530 km/h o the German roller test rig. In: Proceedings of 8th IAVSD Symposium, Cambridge, MA (1893)
9. Manigrasso, R., Mapelli, F.: Requisiti di massima e analisi prestazionali di azionamenti elettrici per un banco a rulli per prove su rotabili. Ingegneria Ferroviaria. **58**(4), 379–382 (2003)

10. Malvezzi, M., Alotta, B., Pugi, L., Rindi, A.: Control of a full scale locomotive roller rig for simulation of wheel sliding. In: Proceedings of AIM07 IEEE/ASME International Conference (2007)
11. F. Cheli, G. Diana, E. Leo, F. Mapelli, E. Sabbioni, Mathematical model of a full scale locomotive roller rig. In: Proceedings of ASME International Mechanical Engineering Congress and Exposition (IMECE2008), October 31–November 6, vol. 17, pp. 445–454. Boston, MA (2008)
12. S. Bruni, A. Collina, G. Diana, P. Vanolo, Lateral dynamics of a railway vehicle in tangent track and curve: tests and simulations. In: Proceedings of the 16th IAVSD Symposium, vol. 33, pp. 464–477 (1999)
13. Litak, G., Friswell, M.: Vibration in gear systems. Chaos Solitons Fractals. **16**, 795–800 (2003)